

**Experimental and Finite Element Investigation on the Flexural
Behaviour of LCA studied Steel-Concrete Composite
Prefabricated Ultra-Shallow Slabs (PUSS)**

Ahmed Abdulla Ahmed Alali

Submitted in accordance with the requirements for the degree of
Doctor of Philosophy

The University of Leeds
Faculty of Engineering
School of Civil Engineering

June, 2025

The candidate confirms that the work submitted is his own, except where work which has formed part of jointly-authored publications has been included. The contribution of the candidate and the other authors to this work has been explicitly indicated below. The candidate confirms that appropriate credit has been given within the thesis where reference has been made to the work of others.

The work in Chapter 3 of the thesis has appeared in the following publication:

Alali, A.A., Huang, Y. and Tsavdaridis, K.D. 2024. Comparative Life Cycle Assessment (LCA) of the Composite Prefabricated Ultra-Shallow Slabs (PUSS) and Hollow Core Slabs in the UK. *Journal of Building Engineering*. 110588.

The work in Chapter 4 of the thesis has appeared in the following publications:

Alali, A.A. and Tsavdaridis, K.D. 2023. Flexural Behaviour of Prefabricated Ultra-Shallow Composite Slabs with Horizontally Oriented Shear Connectors. In: *Proceedings of the 10th Hellenic National Conference of Steel Structures*, 19-21 October 2023, Athens, Greece.

Alali, A.A. and Tsavdaridis, K.D. 2024. Experimental Investigation on Flexural Behaviour of Prefabricated Ultra-Shallow Steel Concrete Composite Slabs. *Journal of Constructional Steel Research*. 217, 108632.

The work in Chapter 5 of the thesis has appeared in the following publications:

Alali, A.A. and Tsavdaridis, K.D. 2021. Flexural Behaviour of Prefabricated Ultra-Shallow Steel-Concrete Composite Slabs. In: *Proceedings of the 9th European Conference on Steel and Composite Structures (EUROSTEEL 2021)*, 1-3 September 2021, Sheffield, UK.

All aspects of the publications above were undertaken by the candidate. However, the candidate benefited from the guidance and suggestions from the named co-authors who played the usual role of supervisor.

This copy has been supplied on the understanding that it is copyright material and that no quotation from the thesis may be published without proper acknowledgement.

The right of Ahmed Abdulla Ahmed Alali to be identified as Author of this work has been asserted by him in accordance with the Copyright, Designs and Patents Act 1988. © 2025 The University of Leeds and Ahmed Abdulla Ahmed Alali.

Dedication

To my beloved wife, whose constant encouragement, support, and patience have been my greatest source of inspiration.

To my little three stars, Amna, Aisha, and Sara, who have filled my life with joy and love, giving me the motivation to keep going, even when I was away pursuing this journey.

Acknowledgements

First and foremost, I would like to express my heartfelt gratitude to Almighty Allah, the All-Knowing and Most Merciful, for granting me the strength and capability to complete this research.

I am deeply thankful to Professor Konstantinos Daniel Tsavdaridis for his invaluable guidance, unwavering support, and patience throughout my research journey. His expertise and constructive feedback have greatly enriched my work.

I extend my sincere thanks to Dr. Ioannis Mitseas and Dr. Yue Huang for their essential contributions and assistance during my PhD programme. I would also like to acknowledge the staff of the Heavy Structures Laboratory at the University of Leeds for their continuous technical support, which was instrumental in the success of my research.

I am truly grateful to SC4 Ltd. and their commercial and technical director, Shay Eddy, for their invaluable technical support and for providing the necessary test materials.

I would like to express my deep appreciation to the University of Bahrain for funding my studies and providing me with this valuable opportunity. Their support has been instrumental in enabling my research and furthering my academic and professional growth.

To my family—my mother and father, Hend and Abdulla; my mother and father-in-law, Suhair and Hafedh; my grandmother and grandfather-in-law, Hessa and Abdulrazzaq; my beloved wife, Fatima; my daughters, Amna, Aisha, and Sara; my brothers, Abdulrahman, Mohammed, and Yousif; my sisters, Aisha, Maryam, and Asma; and my nephews, Reem and Zain—thank you for your endless love and encouragement.

Additionally, I would like to thank my friends and colleagues, Dr. Fahad Almutairi, Dr. Abdulrahman Abbadi, and Dr. Ali Alatas, for their stimulating discussions and generous support throughout this process.

I would also like to express my appreciation to all my friends in Bahrain, whose friendship and support have been a source of strength during this journey.

Lastly, I want to thank everyone who has been part of this journey and sincerely apologise to anyone I may have inadvertently overlooked.

Table of Contents

Dedication	1
Acknowledgements	2
Table of Contents	3
List of Figures	7
List of Tables	14
List of Abbreviations	16
List of Notations	19
List of Publications	26
Abstract	27
Chapter 1 Introduction	29
1.1 Research Background and Motivation	29
1.2 Prefabricated Ultra-Shallow Slab (PUSS®) Flooring System	31
1.3 Problem Statement and Research Aims	32
1.4 Research Objectives.....	33
1.5 Structure of the Thesis	34
Chapter 2 Literature Review	36
2.1 Introduction	36
2.2 Global Environmental Challenges.....	36
2.3 Role of Sustainable Building Design	37
2.3.1 Material Selection for Sustainability	37
2.3.2 Prefabrication and Sustainability.....	39
2.3.3 Life Cycle Assessment (LCA) of Construction Practices.....	40
2.4 Composite Flooring System.....	42
2.5 Shallow Composite Beams	44
2.5.1 Slim Floor Beam (SFB)	45
2.5.2 Asymmetric Slim Floor Beam (ASB)	47
2.5.3 Ultra-Shallow Floor Beam (USFB)	49
2.5.4 Composite Slim Floor Beam (CoSFB)	53
2.5.5 Deltabeam	57
2.5.6 Summary	60
2.6 Prefabricated Slabs.....	61
2.6.1 Prefabricated Ultra-Shallow Slabs (PUSS®)	61
2.6.2 Hollow Core Slabs	65
2.6.3 Modular Steel Channel–Concrete Composite Flooring System (MSCCF).....	68

2.6.4 Real-Life Applications of Composite Prefabricated Slabs	70
2.7 Code of Practice	71
2.7.1 Resistances of Cross-Section of Composite Beams.....	72
2.7.2 Headed Shear Stud Connection	74
2.7.3 Testing of Composite Floor Slabs	78
2.8 Experimental Work on Headed Shear Studs Connections.....	81
2.8.1 Headed Studs Used in Solid Slabs	81
2.8.2 Headed Studs Used with Profiled Decking	82
2.8.3 Headed Studs Used with Lightweight Concrete	83
2.8.4 Horizontally Lying Headed Shear Studs	85
2.9 Summary	86
Chapter 3 Life Cycle Assessment (LCA) Study	88
3.1 Introduction	88
3.2 Methodology	88
3.3 Comparative Study	89
3.3.1 Functional Unit.....	92
3.3.2 System Boundaries.....	92
3.3.3 Impact Categories and Calculation Methodology	95
3.4 Life Cycle Inventory (LCI)	95
3.5 Inventory Results	97
3.5.1 Example of Inventory Results Calculation Methodology	98
3.5.2 Assessment of All Live Load/ Slab Span Scenarios.....	105
3.5.3 Sensitivity Analysis	111
3.6 Results Discussion.....	116
3.7 LCA Study Limitations.....	118
3.8 Conclusions and Recommendations.....	119
Chapter 4 Experimental Four-Point Bending Tests	122
4.1 Introduction	122
4.2 Experimental Program	122
4.2.1 Details of Test Specimens	122
4.2.2 Specimens Preparation.....	126
4.2.3 Materials Properties	127
4.2.4 Test Setup and Loading Protocol.....	131
4.2.5 Instrumentation	133
4.3 Test Results	135
4.3.1 Maximum Moment vs. Mid-span Deflection	135

4.3.2 Stress Distribution in Steel Sections	139
4.3.3 Stress in Concrete Top Surface	143
4.3.4 Crack Development and Failure Mechanism	145
4.3.5 Shear Connectors Failure	147
4.3.6 End-Slip	150
4.4 Concluding Remarks.....	154
4.5 Limitations.....	156
Chapter 5 Finite Element Analysis	158
5.1 Introduction	158
5.2 Modelling Procedure	159
5.3 Material Properties.....	160
5.3.1 Concrete	160
5.3.2 Steel Elements.....	167
5.4 Model Description	169
5.4.1 Interactions and Constraints	170
5.4.2 Boundary Conditions and Load Application	172
5.4.3 Analysis Method.....	173
5.4.4 Meshing and Element Types	174
5.5 FE Model Validation.....	176
5.5.1 Mesh Sensitivity Analysis.....	176
5.5.2 Results Comparison.....	178
5.6 Parametric Investigation	184
5.6.1 Parametric Study Results	185
5.6.2 Effect of Slab Depth	200
5.6.3 Effect of Slab Span	201
5.6.4 Effect of Concrete Type and Strength.....	203
5.6.5 Effect of Degree of Shear connection	205
5.6.6 Comparison of FEA Outcomes and Calculations	208
5.7 Summary	210
5.8 FEA Parametric Study Limitations	211
Chapter 6 Analytical Study of Shear Connectors Capacity.....	213
6.1 Introduction	213
6.2 Shear Capacity of Shear Connectors Formulas.....	213
6.2.1 Existing Formulas for Shear Capacity of Headed Shear Studs.....	213
6.2.2 Existing Formula for Shear Capacity of WWSS and Steel Dowels in PUSS	215

6.2.3 Proposed Formula for Shear Capacity of Shear Connectors in PUSS	215
6.3 Bending Resistance Design of Prefabricated Ultra-Shallow Slabs ..	223
6.3.1 Stress Block Method	224
6.3.2 Linear Interaction Method	230
6.3.3 Quantity and Size of shear Connectors	231
6.4 Analytical Study Limitations	232
6.5 Summary	233
Chapter 7 Conclusions and Recommendations.....	235
7.1 Overview	235
7.2 Research Objectives.....	236
7.3 Research Conclusions	237
7.3.1 Conclusions of the Life Cycle Assessment (LCA) Study	237
7.3.2 Conclusions of the Experimental Four-Point Bending Tests ...	239
7.3.3 Conclusions of the Finite Element Analysis (FEA) Parametric Study	241
7.3.4 Conclusions of the Analytical Study of Shear Connectors Capacity 243	
7.4 Recommendations for Future Research	243
References.....	246
Appendix A LCA Study Detailed Inventory Results for Each Load/ Slab Span Scenario	261
Appendix B Detailed Drawings of Test Specimens	277

List of Figures

Figure 1-1: Placing PUSS units within the depth of CoSFB	31
Figure 2-1: LCA phases (BS EN ISO 14040, 2006a; BS EN ISO 14044, 2006b)	41
Figure 2-2: (a) Typical composite beam arrangement (Nethercot, 2003) (b) Composite downstand beam with steel deck composite slab (Crisinel and Marimon, 2004).....	44
Figure 2-3: Using slim floor beams with hollow core precast slabs (Lawson et al., 2015).....	45
Figure 2-4: Various methods of floor construction using slim floor beams (Mullett, 1992).....	46
Figure 2-5: Asymmetric slim floor beam with precast concrete and concrete topping (Rackham et al., 2006).....	47
Figure 2-6: Concrete slab showing no visible concrete crushing after testing (Sheehan et al., 2018)	49
Figure 2-7: Cross-section configuration of USFB with precast units and metal decking (Tsavdaridis et al., 2009)	50
Figure 2-8: Failure profiles of the (a) concrete-infill-only shear connection, & (b) tie-bar shear connection (Huo, 2012)	51
Figure 2-9: (a) Concrete crushing under loading points in specimens had flexural failure, (b) Specimens with shear failure (Chen et al., 2015) ...	52
Figure 2-10: Composite slim floor beam (CoSFB) (Lawson et al., 2015)	54
Figure 2-11: Observations of failure condition at the completion of the ultimate tests (Baldassino et al., 2018).....	55
Figure 2-12: (a) Deltabeam parts (b,c) The use of Deltabeam with hollow core and composite steel decking slabs (PEIKKO, 2014).....	57
Figure 2-13: Conditions of (a) Type 1 sections and,(b) Type 2 sections at the end of the tests (Kyriakopoulos et al., 2021).....	59
Figure 2-14: Schematic drawing of a 1.6m segment of a standard PUSS flooring unit with steel dowel and WWSS shear connection system (Alali and Tsavdaridis, 2021)	62
Figure 2-15: Grid of PUSS flooring system	64
Figure 2-16: (a) Hollow core floor units (b) Typical cross-sections for floor units (Way et al., 2007)	65
Figure 2-17: Schematic drawings of modular steel channel–concrete composite flooring system (MSCCF) (Fang et al., 2024b)	68
Figure 2-18: (a) Plastic stress distribution of a downstand composite beam with full shear connection in sagging and hogging bending (b) Plastic stress distribution of a downstand composite beam with partial shear connection (CEN, 2004b).....	73

Figure 2-19: Comparison between the plastic stress block method (line 1) and the simplified linear interaction method (line 2) for ductile partial shear connection (CEN, 2004b).....	74
Figure 2-20: Position and geometrical parameters of horizontally lying shear stud connections (CEN, 2005)	77
Figure 2-21: Four-point bending test setup (CEN, 2004b)	79
Figure 2-22: Design relationship for longitudinal shear resistance of the composite floor slab (CEN, 2004b)	80
Figure 2-23: Determination of the degree of shear connection from bending moment test (CEN, 2004b)	81
Figure 3-1: Life cycle stages modules in accordance with BS EN 15804:2012+A2:2019 (BSI, 2019a)	88
Figure 3-2: LCA general life cycle stages of a structural product with LCA study boundaries	89
Figure 3-3: Structure of the LCA model for this study	90
Figure 3-4: System boundaries of the studied flooring systems.....	94
Figure 3-5: Grids of (a) Hollow core flooring (b) PUSS flooring	94
Figure 3-6: GWP results for LL= 3 kN/m ² & span= 8 m (a) by life cycle stage (b) by flooring system	104
Figure 3-7: EE results for LL= 3 kN/m ² & span= 8 m (a) by life cycle stage (b) by flooring system.....	105
Figure 3-8: (a) 3D plot of GWP results (b) 2D plot of GWP results with curve fitting equations.....	107
Figure 3-9: (a) 3D plot of EE results (b) 2D plot of EE results with curve fitting equations	109
Figure 3-10: Floor weight change pattern with increasing spans and live loads	110
Figure 3-11: Floor depth change pattern with increasing spans and live loads	111
Figure 3-12: Sensitivity analysis of transportation distance effect on GWP outcomes	113
Figure 3-13: Sensitivity analysis of transportation distance effect on EE outcomes	114
Figure 3-14: Sensitivity analysis of recycling allocation method effect on GWP and EE outcomes	115
Figure 4-1: 3D view of the details of test specimens.....	123
Figure 4-2: Prepared specimens before casting concrete.....	126
Figure 4-3: Cast specimen	127
Figure 4-4: (a) Slump test (b) Prepared concrete cylinders and cubes	127
Figure 4-5: Average stress-strain curves of cylinder compressive tests for NWC and LWC on the day of the experiments	128

Figure 4-6: (a) NWC concrete cube under compression test; (b) LWC concrete cylinders after splitting tensile test	128
Figure 4-7: (a) Steel rebar during tensile test; (b) Steel section coupons after tensile test.....	129
Figure 4-8: Stress-strain curves of steel section coupons.....	130
Figure 4-9: Stress-strain curves of shear connectors and steel rebars	130
Figure 4-10: Side view sketch of the test setup for 4 m span PUSS slab ..	132
Figure 4-11: 3D view sketch of the test setup for 4 m span PUSS slab on the GEL floor.....	132
Figure 4-12: Test setup.....	133
Figure 4-13: Strain gauges, rosettes strain gauges and LVDTs layout	135
Figure 4-14: Relationship between moment and mid-span deflections (a) for the whole tests (b) for the first three pre-loading cycles.....	136
Figure 4-15: Strains measured in steel section at different locations and different stages of tests.....	142
Figure 4-16: Strains measured along the CL of the top surface of concrete at (a) mid-span (b) 1 m from mid-span	143
Figure 4-17: Horizontal cracks at the end of the tests below loading points in (a) NWC-230-SD, (b) LWC-230-SD, (c) LWC-230-D and (d) NWC-300-SD.....	146
Figure 4-18: Holes broken around shear connectors in specimens (a) NWC-230-SD and (b) NWC-300-SD	149
Figure 4-19: Condition of shear connectors after the tests for (a) NWC-230-SD and (b) LWC-230-SD	149
Figure 4-20: Condition of (a) failed and (b) undamaged shear connectors after the test for LWC-230-D	149
Figure 4-21: Condition of (a) failed and (b) undamaged shear connectors after the test for NWC-300-SD	150
Figure 4-22: Cracks in concrete near the failed shear connectors in NWC-300-SD.....	150
Figure 4-23: Relationship between moment and end-slip at (a) top flange and (b) bottom flange.....	151
Figure 4-24: Separation between steel and concrete at the end of the tests for (a) NWC-230-SD and (b) LWC-230-SD.....	153
Figure 4-25: Separation between steel and concrete at the end of the test for LWC-230-D at the sides (a) near and (b) far from the failed shear connector.....	153
Figure 4-26: Separation between steel and concrete at the end of the test for NWC-300-SD at the sides (a) near and (b) far from the failed shear connector.....	154
Figure 5-1: Response of concrete to uniaxial loading in (a) Tension and (b) Compression (Dassault Systèmes, 2022).....	161

Figure 5-2: Comparison between (a) Linear (Dassault Systèmes, 2022) (b) Bilinear (Hillerborg, 1985) and (c) Exponential (Cornelissen et al., 1986) tension softening models	162
Figure 5-3: Schematic representation of the stress-strain relationship for Concrete in compression ($0,4f_{cm}$ is used for the definition of E_{cm}) (CEN, 2004a).....	164
Figure 5-4: Schematic diagram of stress-strain relationship model established by Almusallam and Alsayed (1995) with its parameters	165
Figure 5-5: Curves of concrete properties used in modelling FE validation models for (a) Specimen NWC-230-SD & (b) Specimen LWC-230-D167	
Figure 5-6: (a) Bi-linear elastic perfectly plastic and (b) Tri-linear stress Strain Curves (Díaz et al., 2018)	168
Figure 5-7: Stress triaxiality damage initiation model for shear connectors	168
Figure 5-8: True stress-plastic strain curves of (a) Shear Studs (b) Steel beams (c) Steel dowels & (d) Steel reinforcement.....	169
Figure 5-9: (a) Parts involved in FE Models (b) Assembled view of FE Models (one quarter) (c) Assembled view of full model.....	170
Figure 5-10: Surface contact pairs and embedded reinforcement	171
Figure 5-11: FE model boundary conditions	172
Figure 5-12: Smooth amplitude for load application.....	174
Figure 5-13: FE model meshing.....	175
Figure 5-14: FE model element types	176
Figure 5-15: Mesh convergence study of mid-span moment vs displacement curves of FE validation models	177
Figure 5-16: Mesh sensitivity analysis of FE validation models	178
Figure 5-17: Comparison of mid-span moment vs displacement curves of FE models and experimental four-point bending tests	179
Figure 5-18: Comparison of cracks at the end of tests beneath specimens in FE models and experiments of (a) NWC-230-SD (b) LWC-230-SD (c) LWC-230-D & (d) NWC-300-SD	181
Figure 5-19: Comparison of deflected shape at the end of the test in FE model and experiment of specimen LWC-230-D	181
Figure 5-20: Comparison of separation between steel beam and concrete slab at the end of the test in FE model and experiment of specimen LWC-230-SD.....	182
Figure 5-21: Comparison of compression cracks below loading beams at the end of the test in FE model and experiment of specimen LWC-230-SD	182
Figure 5-22: Comparison of internal diagonal crack near steel dowel at the end of the test in FE model and experiment of specimen NWC-300-SD ..	182
Figure 5-23: Stress contour plots on steel beam and shear connectors of NWC-230-SD at 100 mm displacement.....	183

Figure 5-24: Stress contour plots on steel beam and shear connectors of LWC-230-SD at 100 mm displacement.....	183
Figure 5-25: Stress contour plots on steel beam and shear connectors of LWC-230-D at 100 mm displacement.....	183
Figure 5-26: Stress contour plots on steel beam and shear connectors of NWC-300-SD at 100 mm displacement.....	184
Figure 5-27: General FEA model arrangement.....	185
Figure 5-28: Comparison between internal energy (ALLIE) and kinetic energy (ALLKE) over analysis time for selected FE models,	187
Figure 5-29: Effect of varying PUSS depth on moment vs displacement curves	200
Figure 5-30: Effect of varying PUSS span on moment vs displacement curves	201
Figure 5-31: Effect of varying PUSS span on the degree of shear connection	202
Figure 5-32: Effect of varying PUSS concrete type on moment vs displacement curves	203
Figure 5-33: Effect of varying PUSS concrete strength on moment vs displacement curves	204
Figure 5-34: Effect of varying PUSS degree of shear connection on moment vs displacement curves.....	205
Figure 5-35: Stress block method curves.....	206
Figure 5-36: Effect of degree of shear connection on depth of concrete in compression	207
Figure 5-37: Effect of degree of shear connection on depth of PNA.....	207
Figure 5-38: Maximum moment FEA/calculation ratio for all FE models....	208
Figure 5-39: Degree of shear connection FEA/calculation ratio for all FE models	209
Figure 6-1: Geometrical parameters of Equation 6-1	217
Figure 6-2: Comparison between the degree of shear connection obtained from Experiment results and predictions calculated using various formulas.....	220
Figure 6-3: Comparison between the degree of shear connection obtained from FEA results and predictions calculated using various formulas	220
Figure 6-4: Comparison between the shear capacity of all shear connectors on one side of PUSS units obtained from Experiment results and predictions calculated using various formulas.....	221
Figure 6-5: Comparison between the shear capacity of all shear connectors on one side of PUSS units obtained from FEA results and predictions calculated using various formulas.....	222
Figure 6-6: Comparison of the moment capacity vs degree of shear connection curves between plastic theory and the simplified method (CEN, 2004b)	223

Figure 6-7: Details of half PUSS unit cross-section used in design methodology example	223
Figure 6-8: Examples of plastic stress distribution in a composite beam with a solid slab with full shear connection in (a) sagging and (b) hogging bending (CEN, 2004b)	224
Figure 6-9: Stress block diagram of PFC 300x100x46 steel section	226
Figure 6-10: Stress block diagram of PFC 300x100x46 steel section with steel reinforcement	227
Figure 6-11: Stress block diagram of PUSS in full shear connection	228
Figure 6-12: Stress block diagram of PUSS in partial shear connection	228
Figure 6-13: Comparison of the variation of MRd between stress block method and linear interaction method	230
Figure 6-14: Shear force (V), bending moment (M) and shear flow (q) diagram of PUSS unit with uniformly distributed load (w)	231
Figure 6-15: Longitudinal shear flow (q) between the concrete slab and steel section of PUSS unit	232
Figure A-1: Results for LL= 2 kN/m ² & span= 6 m (a) GWP by life cycle stage (b) GWP by flooring system (c) EE by life cycle stage (d) EE by flooring system	261
Figure A-2: Results for LL= 2 kN/m ² & span= 8 m (a) GWP by life cycle stage (b) GWP by flooring system (c) EE by life cycle stage (d) EE by flooring system	262
Figure A-3: Results for LL= 2 kN/m ² & span= 10 m (a) GWP by life cycle stage (b) GWP by flooring system (c) EE by life cycle stage (d) EE by flooring system	263
Figure A-4: Results for LL= 2 kN/m ² & span= 12 m (a) GWP by life cycle stage (b) GWP by flooring system (c) EE by life cycle stage (d) EE by flooring system	264
Figure A-5: Results for LL= 3 kN/m ² & span= 6 m (a) GWP by life cycle stage (b) GWP by flooring system (c) EE by life cycle stage (d) EE by flooring system	265
Figure A-6: Results for LL= 3 kN/m ² & span= 8 m (a) GWP by life cycle stage (b) GWP by flooring system (c) EE by life cycle stage (d) EE by flooring system	266
Figure A-7: Results for LL= 3 kN/m ² & span= 10 m (a) GWP by life cycle stage (b) GWP by flooring system (c) EE by life cycle stage (d) EE by flooring system	267
Figure A-8: Results for LL= 3 kN/m ² & span= 12 m (a) GWP by life cycle stage (b) GWP by flooring system (c) EE by life cycle stage (d) EE by flooring system	268
Figure A-9: Results for LL= 4 kN/m ² & span= 6 m (a) GWP by life cycle stage (b) GWP by flooring system (c) EE by life cycle stage (d) EE by flooring system	269

Figure A-10: Results for LL= 4 kN/m ² & span= 8 m (a) GWP by life cycle stage (b) GWP by flooring system (c) EE by life cycle stage (d) EE by flooring system	270
Figure A-11: Results for LL= 4 kN/m ² & span= 10 m (a) GWP by life cycle stage (b) GWP by flooring system (c) EE by life cycle stage (d) EE by flooring system	271
Figure A-12: Results for LL= 4 kN/m ² & span= 12 m (a) GWP by life cycle stage (b) GWP by flooring system (c) EE by life cycle stage (d) EE by flooring system	272
Figure A-13: Results for LL= 5 kN/m ² & span= 6 m (a) GWP by life cycle stage (b) GWP by flooring system (c) EE by life cycle stage (d) EE by flooring system	273
Figure A-14: Results for LL= 5 kN/m ² & span= 8 m (a) GWP by life cycle stage (b) GWP by flooring system (c) EE by life cycle stage (d) EE by flooring system	274
Figure A-15: Results for LL= 5 kN/m ² & span= 10 m (a) GWP by life cycle stage (b) GWP by flooring system (c) EE by life cycle stage (d) EE by flooring system	275
Figure A-16: Results for LL= 5 kN/m ² & span= 12 m (a) GWP by life cycle stage (b) GWP by flooring system (c) EE by life cycle stage (d) EE by flooring system	276
Figure B-1: Transverse cross-section details for tests specimens 1 & 2 (as well as specimen 3 but without WWSS).....	278
Figure B-2: Longitudinal cross-section details for specimens 1 & 2 (as well as specimen 3 but without WWSS)	279
Figure B-3: Transverse cross-section details for specimen 4	280
Figure B-4: Longitudinal cross-section details for specimen 4	281

List of Tables

Table 2-1: Comparative summary of shallow composite beam systems.....	60
Table 2-2: Characteristic shear resistance of headed shear studs in normal weight concrete (BSI, 1990).....	76
Table 3-1: Live load/ slab span scenarios of the LCA study	89
Table 3-2: Characteristics of the flooring systems	90
Table 3-3: Details of concrete mix designs used in the studied flooring systems	90
Table 3-4: GWP Characterisation factors of GHGs (Masson-Delmotte et al., 2021)	95
Table 3-5: Embodied carbon and energy of the materials for production and EOL processes	96
Table 3-6: Embodied carbon and energy for construction equipment and transportation.....	97
Table 3-7: Approximate waste factors of each of the production materials..	97
Table 3-8: Approximate transportation distances at between different life cycle stages	97
Table 3-9: Comparison of total inventory results for design optimisation	99
Table 3-10: Comparison of material quantities in all design alternatives ...	100
Table 3-11: GWP results for LL= 3 kN/m ² & span= 8 m (GWP - kg CO _{2,e} /m ² of slab).....	103
Table 3-12: EE results for LL= 3 kN/m ² & span= 8 m (EE – MJ/m ² of slab)	103
Table 3-13: Comparison of GWP results for all live load/ slab span scenarios (kg CO _{2,e} /m ² of slab)	107
Table 3-14: Constants of curve fitting equations for GWP and EE.....	108
Table 3-15: Comparison of EE results for all live load/ slab span scenarios (MJ/m ² of slab).....	109
Table 3-16: Constants of curve fitting equations for densities and depths of slabs	111
Table 4-1: Specimen test matrix	124
Table 4-2: Concrete properties	128
Table 4-3: Average mechanical properties of steel sections, rebars and shear connectors	129
Table 4-4: Loading cycles	133
Table 4-5: Comparison of load values at specific stages of the tests.....	137
Table 4-6: Evaluation of test results in comparison to calculated capacities using stress block method	138
Table 5-1: Comparison of FE models results and experimental four-point bending tests	180

Table 5-2: FE parametric study matrix	185
Table 5-3: Summary of FE parametric study results for models with depth = 200 mm and span = 3 m	188
Table 5-4: Summary of FE parametric study results for models with depth = 200 mm and span = 4 m	189
Table 5-5: Summary of FE parametric study results for models with depth = 200 mm and span = 6 m	190
Table 5-6: Summary of FE parametric study results for models with depth = 230 mm and span = 4 m	191
Table 5-7: Summary of FE parametric study results for models with depth = 230 mm and span = 6 m	192
Table 5-8: Summary of FE parametric study results for models with depth = 230 mm and span = 8 m	193
Table 5-9: Summary of FE parametric study results for models with depth = 260 mm and span = 6 m	194
Table 5-10: Summary of FE parametric study results for models with depth = 260 mm and span = 8 m	195
Table 5-11: Summary of FE parametric study results for models with depth = 260 mm and span = 10 m	196
Table 5-12: Summary of FE parametric study results for models with depth = 300 mm and span = 8 m	197
Table 5-13: Summary of FE parametric study results for models with depth = 300 mm and span = 10 m	198
Table 5-14: Summary of FE parametric study results for models with depth = 300 mm and span = 12 m	199
Table 6-1: Evaluation of fitting of various formulas to Experiment results ..	219
Table 6-2: Evaluation of fitting of various formulas to FEA results	219
Table 6-3: Results corresponding to various degrees of partial shear connection	229

List of Abbreviations

AASHTO	American Association of State Highway and Transportation Officials
AISC	American Institute of Steel Construction
ANSI	American National Standards Institute
ASFB	Asymmetric Slim Floor Beam
BC	Boundary Condition
BSI	British Standards Institution
C3D8R	Three dimensional eight-node solid element with reduced integration (in ABAQUS)
CAE	Computer-Aided Engineering
CEN	Comité Européen de Normalisation (European Committee for Standardization)
CL	Centreline
CoSFB	Composite Slim-Floor Beams
CV	Coefficient of Variation
DAQ	Data Acquisition system (data logger)
DL	Dead Load
DOF	Degree of Freedom
EC4	Eurocode 4
EE	Embodied Energy
EOL	End-Of-Life
FE	Finite Element
FA	Fly Ash
FEA	Finite Element Analysis
<i>fib</i>	Fédération internationale du béton (International Federation for Structural Concrete)
GEL	George Earle Laboratory

GGBS	Ground Granulated Blast furnace Slag
GHGs	Greenhouse Gases
GPC	Geopolymer Concrete
GWP	Global Warming Potential
HC	Hollow Core precast slab
ISO	International Organization for Standardization
LCA	Life Cycle Assessment
LCI	Life Cycle Inventory
LCIA	Life Cycle Impact Assessment
LL	Live Load
LVDT	Linear Variable Differential Transformer
LWC	Lightweight Concrete
NWC	Normal Weight Concrete
PFC	Parallel Flange Channel steel section
PNA	Plastic Neutral Axis
PUSS	Prefabricated Ultra-Shallow Slab
RC	Reinforced Concrete
RP	Reference Point
R3D4	Three dimensional four-node bilinear quadrilateral element (in ABAQUS)
SCC	Steel-Concrete Composite
SFB	Slim Floor Beam
SLS	Serviceability Limit State
T3D2	Three dimensional two-node truss element (in ABAQUS)
ULS	Ultimate Limit State
ULWC	Ultimate Lightweight Concrete
USFB	Ultra-Shallow Floor Beams

WWSS

Web-Welded Shear Stud

List of Notations

Latin upper case letters

A1-A5	Production and manufacturing LCA modules
A_c	Area of concrete in compression in composite section with full shear connection
$A_{c/f}$	The area of steel section the top flange in compression
$A_{c/w}$	The area of steel section portion of the web in compression
A_q	Area of concrete in compression in composite section with partial shear connection
A_s	Cross-sectional area of the shear connector
$A_{t/f}$	The area of steel section the bottom flange in tension
$A_{t/R}$	The area of steel reinforcement in tension
$A_{t/w}$	The area of steel section portion of the web in tension
B1-B5	Operation and maintenance LCA modules
C1-C4	End-of-life LCA modules
D	Transportation distance per functional unit in LCA calculations or The depth of PNA
D_c	The distance between the PNA and the centroid of area of concrete in compression in composite section with full shear connection
$D_{c/f}$	The distance between the PNA and the centroid of steel section area of top flange in compression
$D_{c/w}$	The distance between the PNA and the centroid of steel section portion of web in compression

D_q	The distance between the PNA and the centroid of area of concrete in compression in composite section with partial shear connection
$D_{t/f}$	The distance between the PNA and the centroid of steel section area of bottom flange in tension
$D_{t/R}$	The distance between the PNA and the centroid of steel reinforcement area of in tension
$D_{t/w}$	The distance between the PNA and the centroid of steel section portion of web in tension
E_0	Initial elastic stiffness of concrete
E_c	Modulus of elasticity of concrete
E_{cm}	Secant modulus of elasticity of normal weight concrete
E_{lcm}	Secant modulus of elasticity of lightweight concrete
E_s	Modulus of elasticity of steel
G_f	Fracture energy of concrete
I	Moment of inertia
K_c	Ratio of the second stress invariant on the tensile meridian to that on the compressive meridian at initial yield for concrete
LCI	Life cycle inventory per unit in LCA calculations
LL	Live load
M	Mass of material per functional unit in LCA calculations or Bending moment
M_a	Contribution of the structural steel section to the design plastic resistance moment of the composite section
M_c	Calculated moment capacity of composite section
$M_{c,Full}$	Calculated moment capacity of composite section at full degree of shear connection

$M_{pl,a,Rd}$	Design value of the plastic resistance moment of the structural steel section
$M_{pl,Rd}$	Design value of the plastic resistance moment of a composite section with full shear connection
M_{Rd}	Design value of the resistance moment of a composite section
M_s	Calculated moment capacity of steel section
M_{Test}	Calculated moment capacity of from test results
N_a	Design value of the normal force in structural steel of composite section
N_c	Design value of the compressive normal force in concrete of composite section
	or
	Longitudinal shear resistance of the shear connectors
$N_{c,f}$	Design value of the compressive normal force in concrete of composite section with full shear connection
$N_{pl,a}$	Design value of the plastic resistance of the structural steel section to normal force
N_s	Design value of the plastic resistance of the steel reinforcement to normal force
P_{Rd}	Shear resistance of shear connector
$P_{Rd,h}$	Shear resistance of horizontally oriented shear connectors in PUSS
$P_{Rd,L}$	Shear resistance of horizontally oriented headed shear stud connector (Annex C of Eurocode 4)
P_s	Shear resistance of headed shear stud connector
P_{sd}	Shear resistance of shear stud or steel dowel
Q	First moment of area

R_c	Compressive resistance of the concrete of composite section with full shear connection
$R_{c/f}$	The compressive resistance of the steel section top flange area
$R_{c/w}$	The compressive resistance of the steel section web portion in compression
R_q	Longitudinal shear resistance of the shear connectors
$R_{t/f}$	The tensile resistance of the steel section bottom flange area
$R_{t/R}$	The tensile resistance of the steel reinforcement in tension
$R_{t/w}$	The tensile resistance of the steel section web portion in tension
S	Slab span
T	Operation time of equipment per functional unit in LCA calculations
V	Shear force

Latin lower case letters

a	Horizontal spacing of studs (Annex C of Eurocode 4)
$a_1 - a_4$	Flooring system-dependent coefficient
a_r	The vertical distance from the edge of the slab to the centre of the stud (Annex C of Eurocode 4)
	or
	The distance from first stud or dowel in PUSS to the top of concrete (Ahmed and Tsavdaridis, 2020)
a'_r	The effective edge distance to the centre of the stud
$b_1 - b_4$	Flooring system-dependent coefficient
c_v	The vertical concrete cover (Annex C of Eurocode 4)
d	Diameter of shear connector or shear stud

d_c	Compression damage parameter of concrete
d_t	Tension damage parameter of concrete
f	Stress
f_0	A reference stress in the stress-strain relationship curve established by Almusallam and Alsayed (1995)
f_c	Compressive stress of concrete corresponding to the strain ε_c
f_{cc}	Peak compressive stress in GPC model
f_{cd}	Design cylinder compressive strength of concrete
f_{ck}	Characteristic compressive strength of concrete
f_{cm}	Mean cylinder compressive strength of normal weight concrete
f_{lcm}	Mean cylinder compressive strength of lightweight concrete
f_{sd}	Design value of the yield strength of reinforcing steel
f_t	Tensile strength of concrete
f_u	Ultimate strength of steel
f_y	Yield stress of steel
f_{yd}	Design value of the yield strength of structural steel section
k	Initial slope of the stress-strain relationship curve established by Almusallam and Alsayed (1995) [equal to modulus of elasticity of concrete (E_c)]
k_p	Final slope of the stress-strain relationship curve established by Almusallam and Alsayed (1995)
k_v	Constant in calculating shear resistance of horizontally oriented headed shear stud connector (Annex C of Eurocode 4)
n	Curve-shape factor of the stress-strain relationship curve established by Almusallam and Alsayed (1995)
q	Shear flow between the composite members

s	The spacing of stirrups (Annex C of Eurocode 4)
w	Crack opening displacement of concrete
w_c	Crack opening displacement of concrete at which stress can no longer be transferred

Greek upper case letters

\emptyset	The resistance factor for the shear connectors = 0.85 (AASHTO, 2020)
\emptyset_s	The diameter of stirrups
Ψ	Dilation angle of concrete

Greek lower case letters

α_v	A partial factor in calculating shear resistance of horizontally oriented headed shear stud connector in PUSS
γ_v	A partial factor in calculating shear resistance of horizontally oriented headed shear stud connector (Annex C of Eurocode 4)
ε	Flow potential eccentricity of concrete (in Damaged plasticity model)
ε	Strain
ε_c	Compressive strain of concrete
ε_{cc}	Compressive strain corresponding to peak stress f_{cc} of concrete
$\varepsilon_c^{\sim pl}$	Compressive plastic strain of concrete
ε_c^{el}	Compressive elastic strain of concrete
ε_{c1}	Compressive strain of normal weight concrete at the peak stress f_{cm}

ε_{cu1}	Compressive nominal ultimate strain of normal weight concrete
ε_{lc1}	Compressive strain of lightweight concrete at the peak stress f_{1cm}
ε_{lcu1}	Compressive nominal ultimate strain of lightweight concrete
ε_r	Strain in steel at which fracture is observed in steel
ε_t	Tensile strain of concrete
$\varepsilon_t^{\sim pl}$	Tensile plastic strain of concrete
ε_t^{el}	Tensile elastic strain of concrete
ε_u	Strain corresponding to ultimate stress f_u of steel
ε_y	Strain corresponding to yield stress f_y of steel
η	Degree of shear connection
μ	Viscosity of concrete
ρ	Oven-dry density of lightweight concrete
σ_{b0}/σ_{c0}	Ratio of initial equibiaxial compressive yield stress to initial uniaxial compressive yield stress for concrete
σ_c	Compressive stress of concrete
σ_{c0}	Compressive initial yield stress of concrete
σ_{cu}	Compressive ultimate stress of concrete
σ_t	Tensile stress of concrete
σ_{t0}	Tensile failure stress of concrete

List of Publications

Part of the findings of this thesis is presented in the journal articles and conference papers listed below.

- Journal Articles:

1. Alali, A.A., Huang, Y. and Tsavdaridis, K.D. 2024. Comparative Life Cycle Assessment (LCA) of the Composite Prefabricated Ultra-Shallow Slabs (PUSS) and Hollow Core Slabs in the UK. *Journal of Building Engineering*. 110588.

DOI: <https://doi.org/10.1016/j.jobe.2024.110588>

2. Alali, A.A. and Tsavdaridis, K.D. 2024. Experimental Investigation on Flexural Behaviour of Prefabricated Ultra-Shallow Steel Concrete Composite Slabs. *Journal of Constructional Steel Research*. 217, 108632.

DOI: <https://doi.org/10.1016/j.jcsr.2024.108632>

3. Alali, A.A. and Tsavdaridis, K.D. 2025. Shear Capacity Assessment of Horizontally Oriented Shear Connectors in Prefabricated Ultra-Shallow Slabs (PUSS). (In-Draft).

- Conference Papers:

1. Alali, A.A. and Tsavdaridis, K.D. 2021. Flexural Behaviour of Prefabricated Ultra-Shallow Steel-Concrete Composite Slabs. In: *Proceedings of the 9th European Conference on Steel and Composite Structures (EUROSTEEL 2021)*, 1-3 September 2021, Sheffield, UK.

DOI: <https://doi.org/10.1002/cepa.1362>

2. Alali, A.A. and Tsavdaridis, K.D. 2023. Flexural Behaviour of Prefabricated Ultra-Shallow Composite Slabs with Horizontally Oriented Shear Connectors. In: *Proceedings of the 10th Hellenic National Conference of Steel Structures*, 19-21 October 2023, Athens, Greece.

Available from:

https://www.researchgate.net/publication/378297980_FLEXURAL_BEHAVIOUR_OF_PREFABRICATED_ULTRA-SHALLOW_COMPOSITE_PUSS_R_SLABS_WITH_HORIZONTALLY_ORIENTED_SHEAR_CONNECTORS

Abstract

This thesis investigates the environmental and flexural performance of the recently developed ultra-shallow flooring system known as Prefabricated Ultra-Shallow Slab (PUSS®). The prefabricated units consists of T-ribbed concrete slabs partially embedded within and connected to two side PFC channel steel beams via a novel horizontally-oriented shear connection system. This connection system incorporates either horizontally-oriented web-welded shear studs (WWSS), horizontal steel dowels welded to the webs, or a combination of both (WWSS with dowels). The unique configuration of the flooring system minimises its structural depth, yielding ultra-shallow floors with a high span-to-depth ratio, surpassing other shallow flooring systems in efficiency. Additionally, it reduces the material usage, and when combined with lightweight concrete, the flooring overall weight (load on beneath structure) and the associated environmental impacts are significantly reduced.

The environmental performance of the flooring system is evaluated through a comparative Life Cycle Assessment (LCA) study, focusing on the global warming potential (GWP) and embodied energy (EE) impacts of PUSS compared with the widely used hollow core precast slabs. The study examines 16 live load/ floor span scenarios and evaluates the benefits and drawbacks of utilising different concrete types in PUSS flooring, namely normal weight concrete (NWC), lightweight aggregates concrete (LWC) and geopolymer concrete (GPC). Results indicate that PUSS outperforms hollow core slabs in all scenarios, regardless of the concrete type used. PUSS with GPC offers the greatest GWP savings, achieving up to 50% reductions compared to hollow core slabs. However, PUSS with LWC demonstrates the best overall performance in terms of both GWP and EE, with up to 35% savings in EE and 46% in GWP, and its lighter weight reduces the load on supporting structural elements, further amplifying the overall environmental benefits.

Furthermore, the research explores the effect of a group of parameters on the flexural behaviour of PUSS and the performance of the implemented shear connectors under bending through a series of experimental and computational studies. The investigated parameters include concrete type, concrete strength, degree of shear connection, span and slab depth. Four full-scale specimens, each with a span of 4 m were constructed and tested under four-point bending

tests at George Earle laboratory (GEL), University of Leeds. The results indicate that PUSS with LWC achieves similar flexural capacity to PUSS with NWC, though it exhibits lower initial stiffness and develops larger cracks. Additionally, the tests reveals that reducing the degree of shear connection lowers the slabs' moment capacity and leads to failure of some shear connectors. Despite this, PUSS units demonstrates ductile behaviour in all cases.

A finite element model resembling the experimental tests was then developed, validated against the experimental results, and used in a comprehensive parametric Finite Element Analysis (FEA) study involving 324 models. The study shows that reducing the degree of shear connection (η) leads to decrease in moment capacity, but the reduction is non-linear due to the parabolic relationship between moment capacity and η . This highlights the complex interaction between shear connectors and overall slab performance. Larger discrepancies are noted between FE-derived moment capacities and hand calculations using existing shear capacity formulas, especially in lightweight concrete (LWC) models, underscoring the need for refinements in the shear resistance equation to achieve more accurate predictions.

The gathered data from both experimental and FEA studies were extensively studied, and analysed through regression analysis, leading to the development of an optimised empirical formula to predict the shear resistance of the shear connectors employed in PUSS and their corresponding degrees of shear connection. This formula provides a more accurate prediction of shear resistance and degree of shear connection compared to existing methods, aligning closely with the results of 328 experiments and FEA models. Additionally, a moment capacity design methodology for PUSS flooring system in accordance with the Eurocode 4 standards is presented. This methodology offers a solid framework for the practical implementation of PUSS in construction, with the potential to inform future revisions of design codes.

Chapter 1

Introduction

1.1 Research Background and Motivation

Steel-Concrete Composite (SCC) structural systems are integral to the advancement of the construction industry and have garnered significant research attention due to their efficiency in material utilisation, cost reduction and ability to provide high strength. SCC involves the combination of steel and concrete into a unified component, creating composite action between the two materials. The integration results in a singular, high-performance entity that surpasses the capabilities achieved by individual materials.

SCC flooring systems represent one of the widespread SCC structural elements, and their evolution over the past decades has contributed to enhancing the quality of the floorings in buildings, the increase of spans, the mitigation of vibrations and the material reduction. This progression commenced with traditional downstand steel beams where concrete slabs positioned on top of the steel beams flange to form a composite beam. Subsequently, developments led to the integration of the slab thickness within the depth of the steel beam forming optimised composite slim floors (Ahmed and Tsavdaridis, 2018). Various slim floor systems have been developed over the years, including slim-floor constructed with deep composite decking, slim-floor constructed with precast concrete slab, ultra-shallow floor beams (USFB) and composite slim-floor beams (CoSFB). These systems share a common advantage of connecting concrete slabs to the steel beams within their structural depth, resulting in a reduced overall depth of the flooring system and thus the overall height of the building. In addition, these systems offer quick construction by using less or no propping and providing large uninterrupted floor areas. This enhances the building's flexibility capacity. As a result, such kind of systems are widely used and gained popularity in the construction sector. However, it has been observed that to achieve spans longer than 10 m, these systems require depths exceeding 300 mm to increase the bending resistance of the slab, even when lightweight concrete is used. The increased depth leads to higher material consumption, increased weight, and the possibility of shear failure. Consequently, there is a need for further improvements to composite flooring systems to make them more economically viable (Tsavdaridis et al., 2009; Hechler et al., 2013; Lawson et al., 2015).

Over the previous decade, considerable attention has been directed towards the performance of the shear connectors in these slim flooring systems capitalising on the connection between the steel and the concrete to control stiffness, strength, and ductility. Several innovative shear connection systems have been introduced and studied while many of them demonstrated favourable outcomes and promising results. Among the trends in the advancement of the shear connectors of slim floors, the utilisation of horizontally oriented shear connectors has gained prominence, moving away from the traditional vertical shear studs. Several types of horizontal shear connectors have been examined in the literature, such as web-welded shear studs, concrete dowels (through web openings) and concrete dowels with steel tie bars (dowels) (Chen and Limazie, 2018; Majdub et al., 2022). The primary research focus has been on the performance of such shear connectors in slim composite beams, loading them experimentally and numerically to direct shear (Hechler et al., 2013; Limazie and Chen, 2017; Hosseinpour et al., 2018; Ahmed and Tsavdaridis, 2020; Coldebella et al., 2022) and flexural loading tests (Hechler et al., 2013; Chen et al., 2015; Baldassino et al., 2019; Sheehan et al., 2019; Dai et al., 2020).

Moreover, the sustainability of structural elements is a crucial consideration that needs to be examined before selecting the appropriate structural system for a project. In the context of residential and office buildings, especially tall ones, floors constitute a significant proportion of the total weight (load) and material consumption, resulting in high environmental impacts (carbon footprint). Studies demonstrated that buildings account for approximately 40% of the global material flow, with the cement industry alone responsible for about 7% of the worldwide CO₂ emissions (Meyer, 2009; Dong et al., 2015). On-site construction is a considerable source of material waste and carbon emissions, primarily from fuel consumption during material transportation and the operation of heavy equipment. Conversely, off-site prefabrication enhances quality control and site safety, and reduces material waste, adverse environmental impacts, labour work, and construction time, which makes it a sustainable construction practice (Jaillon and Poon, 2008). Therefore, innovative designs that facilitate the use of less and lighter materials can significantly contribute to carbon reduction and align with sustainability objectives.

1.2 Prefabricated Ultra-Shallow Slab (PUSS®) Flooring System

This thesis focuses on studying a recently developed composite flooring system known as prefabricated ultra-shallow slab (PUSS). This innovative flooring system was initially introduced in 2017 and the previous research on it revealed its quick and efficient production capabilities and its potential to develop sustainable lightweight and high-strength long-span slim floor systems. Figure 1-1 shows how PUSS units can be integrated within composite slim floor beams such as the CoSFB.

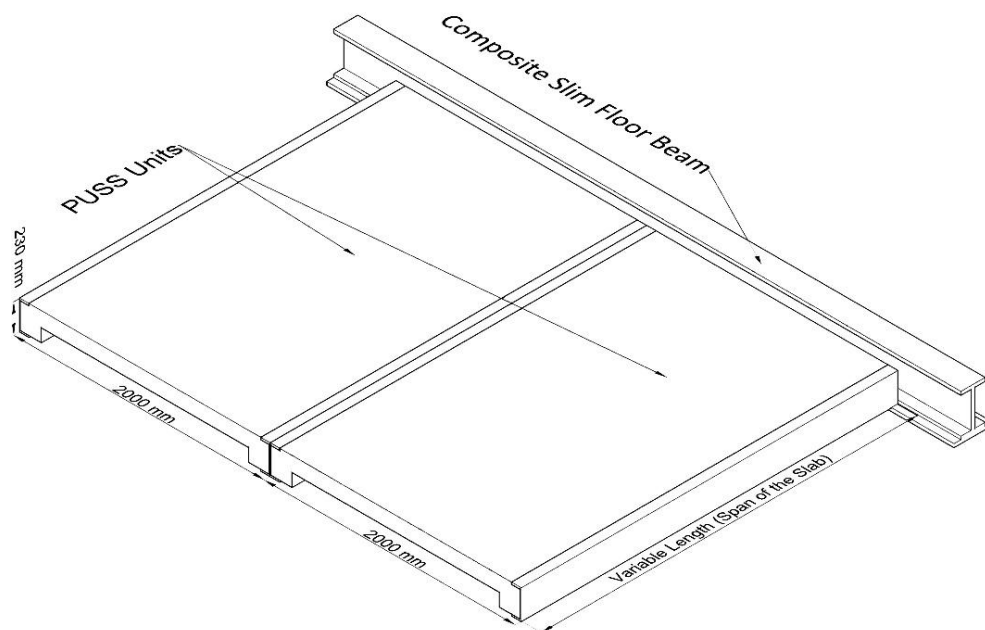


Figure 1-1: Placing PUSS units within the depth of CoSFB

According to BS EN 1992-1-1 (2004a) and SCI P359 (2011), the limiting span/depth ratio for single span slabs is 20. However, the significance of shallow floors lies in their ability to achieve higher span-to-depth ratios, saving both construction materials and overall cost. The unique configuration of PUSS flooring system minimises its structural depth, resulting in ultra-shallow floors, which exhibit larger span/depth ratio compared to other existing flooring systems, such as reinforced concrete (RC) and hollow core precast floors. For instance, a single span PUSS unit with a depth of 230 mm can span up to 8 meters without requiring a finishing layer, providing a span-to-depth ratio exceeding 34, which is of similar ratios to the state-of-art CoSFB.

Previous research has highlighted several advantages of the PUSS system, particularly its lightweight nature, the possibility of integration of building services and reducing the overall building height (Ahmed, 2019). Moreover, Life Cycle Assessment (LCA) and Life Cycle Cost (LCC) studies of PUSS, specifically when

constructed with lightweight aggregate concrete (LWC), have demonstrated significant reductions in Global Warming Potential (GWP), energy consumption, time, and costs compared to other prefabricated flooring systems (Ahmed and Tsavdaridis, 2018). However, these studies have been limited to specific spans, loads, concrete types, and transportation distances.

Additionally, the shear connection system in PUSS was tested experimentally and numerically using the push-out test methodology. As an outcome of the tests, a formula (Equation 2-4) was developed to predict the shear resistance of the system which was derived solely from push-out test observations and did not account for the system's response under bending loads (Ahmed and Tsavdaridis, 2020). A detailed review of these studies, along with the shear connection system employed in PUSS, is provided in Section 2.6.1 of the Literature Review chapter.

1.3 Problem Statement and Research Aims

Previous studies of PUSS have shown promising results, particularly in demonstrating its potential environmental benefits and in the development of a novel horizontally oriented shear connection system. However, the environmental performance of the PUSS has not been fully explored, especially regarding the use of different concrete types and the impact of varying spans, loads, and other key parameters such as transportation distances and EOL allocation methods on the overall environmental footprint of the system. Additionally, earlier experimental and numerical research primarily focused on direct shear push-out tests, which do not provide a comprehensive understanding of the behaviour of slabs and shear connection system under bending. This is crucial for real-world applications, where floors are primarily subjected to flexural loads.

This research seeks to address these gaps by exploring areas not covered in previous studies. The research aims to evaluate the environmental performance of the PUSS flooring system under various live load and span scenarios, comparing it to conventional hollow core slabs. This is achieved through a detailed comparative Life Cycle Assessment (LCA) study, which includes sensitivity analyses of key parameters such as transportation distances and end-of-life allocation methods. The study also investigates the use of different concrete types in PUSS, aiming to identify the option that minimises CO₂ emissions and energy consumption.

Additionally, this research aims to investigate the flexural behaviour of PUSS and the performance of the employed shear connection system under bending through experimental and computational studies, focusing on the effects of various parameters. The ultimate goal is to develop an empirical formula to predict the shear resistance of the horizontally oriented shear connectors employed in PUSS under bending, based on analytical study of the experimental and numerical results. This facilitates the creation of a precise and effective design methodology for calculating the moment capacity of PUSS composite sections.

1.4 Research Objectives

In line with the research aims, the specific objectives of this study are summarised as follows:

1. Conduct a comprehensive literature review on the sustainability of structural systems, shallow flooring systems, shear connectors, and relevant experimental and computational studies.
2. Carry out a comparative Life Cycle Assessment (LCA) to evaluate the global warming potential (GWP) and embodied energy (EE) of the PUSS flooring system, using different concrete types and comparing it to the conventional hollow core slabs. In addition, it studies the pattern of change in environmental impacts with the increase of applied live load or span through exploring several live loads/ spans scenarios.
3. Design and perform full-scale four-point bending tests on four PUSS units to assess the flexural performance of the composite slabs and the employed shear connectors, considering variables such as concrete type, slab depth, and the degree of shear connection.
4. Develop and validate a high-fidelity model of the PUSS system under bending using ABAQUS software, followed by a comprehensive parametric study to examine the effects of key parameters, including concrete type and strength, degree of shear connection, span, and slab depth on the flexural behaviour of PUSS units and the performance of the employed shear connectors.
5. Propose a reliable and optimised empirical formula for predicting the shear resistance of the shear connectors, derived from regression analysis of experimental and FEA data.

6. Develop a design methodology for the moment capacity of the PUSS composite section.

1.5 Structure of the Thesis

The thesis consists of seven chapters, which are briefly summarised below.:

Chapter 1: Introduction

This chapter outlines the background and motivation of the research. It also summarises the research problem as well as its aims and objectives.

Chapter 2: Literature Review

Chapter 2 provides a brief introduction to sustainability of structural systems and explores the composite flooring systems and their components. In addition, it presents an overall review of the previous experimental and numerical investigations relevant to the research topic, along with applicable design codes.

Chapter 3: Life Cycle Assessment (LCA) Study

To assess the environmental benefits of the PUSS flooring system and to identify potential trade-offs, this chapter presents a comprehensive comparative Life Cycle Assessment (LCA) study, focusing on the global warming potential and embodied energy of PUSS flooring compared to widely used hollow core slabs, across a range of live loads, spans, transportation distances and allocation methods. The study includes a comparison of four distinct slabs used in buildings internal floorings: hollow core precast slabs and three PUSS slabs with different concrete types.

Chapter 4: Experimental Four-Point Bending Tests

Chapter 4 discusses the methodology and results of the experimental four-point bending tests performed on a total of four PUSS units. The specimens are designed to investigate the effects of concrete type, shear connection system, and slab depth on the flexural behaviour. Details on specimen design, preparation, test setup, instrumentation, observations and test results are provided.

Chapter 5: Finite Element Analysis

This chapter outlines the methodology followed in developing and validating the FE model that simulates the experimental four-point bending test on PUSS. It

then discusses the results of a comprehensive FE parametric study that investigates the flexural behaviour of PUSS units and the performance of the shear connection system under bending. The study analyses a total of 324 models, considering key parameters such as slab depth, span, concrete type, concrete strength, and degree of shear connection. The aim is to quantify the shear strength of the shear connectors and their influence on the composite action of PUSS units.

Chapter 6: Analytical Study of Shear Connectors Capacity

The focus of this chapter is on analysing the experimental and FE results to develop an empirical formula, using regression analysis, to predict the shear resistance capacity of shear connectors used in PUSS flooring system. This facilitates the calculation of the degree of shear connection provided by the implemented shear connection system. In addition, it is used to evaluate and design the bending capacity of PUSS units.

Chapter 7: Conclusions and Recommendations

The final chapter summarises the key findings and contributions of the research, and offers recommendations for future work that could enhance the PUSS system.

Chapter 2

Literature Review

2.1 Introduction

This chapter provides a comprehensive review of the key topics that are essential to understanding Prefabricated Ultra-Shallow Slabs (PUSS) and related composite flooring systems, and guiding the investigations presented in this thesis. The review is organised into several sections that cover (1) sustainability practices in construction, (2) an overview of existing composite flooring systems, including shallow composite beams; (3) a detailed discussion on the prefabricated slabs included in the study; and (4) a review of the experimental and computational investigations on shear connectors, particularly headed shear studs and horizontally oriented connectors. The aim of this chapter is to provide a thorough background of the existing research, identify gaps in knowledge, in relation to PUSS system and the implemented shear connection system.

2.2 Global Environmental Challenges

Over the previous decades, a continuous degradation of the environment was associated with the accelerated economic growth because of the substantial use of natural resources. Some of the key concerns of environmental impacts linked to this development include the extent of energy usage (embodied energy) and the climate change, primarily attributed to the release of greenhouse gases (GHGs). The rise of the GHGs concentration in the atmosphere is directly correlated with the annual increase of temperature, with carbon dioxide identified as the most significant anthropogenic GHG (Masson-Delmotte et al., 2021).

Since 1980's, the world understood the importance of global collaboration towards controlling and assessing the emissions of GHGs to reduce the harmful environmental impacts. This led to the formation of the United Nations Framework Convention on Climate Change (UNFCCC) in 1994 that acts as a worldwide organization that aims to set goals, measures and strategies to prevent the harmful effects of human activities on the climate change (UNFCCC, n.d.). As a first stage in decreasing the release of GHGs, Kyoto Protocol took place in 1997, in which 37 industrialised countries and economies in transition and the European Union committed to reducing the main six GHGs emissions by an average 5% compared to 1990's level for the period from 2008 to 2012 (UNFCCC, 1997). This

protocol had some amendments that took place in Doha, 2012 and the new commitment increased the average reduction of the GHGs emissions by an average of 18% in comparison to 1990's level for the period between 2013 and 2020 (UNFCCC, 2012). The UK is part of Kyoto Protocol parties and has a legal commitment to achieve its targets. In addition, in 2019, UK became the first major economy to pass a law committing to net zero GHGs by 2050 (UK Export Finance, 2021).

To achieve these goals, researchers and manufacturers are exploring the possibility of implementing more environmentally friendly practices and materials in every industry, including the construction industry. GHGs emissions are more readily quantified compared with other environmental impacts due to the availability of extensive inventory databases. This abundance of data facilitates more detailed and accurate research, making the study of GHGs emissions a prominent focus in environmental research. However, it is just one of several impact categories that should be considered in evaluating the environmental impacts, such as ozone depletion, eutrophication, acidification and human toxicity. Unfortunately, there is some shortage in data and inventories of some of these impact categories for specific construction materials and equipment (Li et al., 2010; Mateus and Bragança, 2011; Van den Heede and De Belie, 2012; Jang et al, 2022; Rey-Álvarez et al, 2022).

2.3 Role of Sustainable Building Design

Achieving the net zero GHGs goal by 2050 is a collective responsibility shared by many stakeholders in the construction sector, starting from government authorities to on-site labours. Designers and engineers play a crucial role in mitigating impacts by focusing on sustainable design and sustainable construction practices of structural elements that lead to the reduction of the consumption of materials, especially materials with high carbon footprint (Ahmed and Tsavdaridis, 2018).

2.3.1 Material Selection for Sustainability

Material selection is one of the main factors affecting the overall energy consumption and GHGs emissions of buildings. Construction industry is a primary consumer of the global materials, counting for around 40% of the global consumption (Dong et al., 2015). Thus, it is responsible for a huge proportion of

the GHGs emissions and other environmental impacts. In addition, the cement industry alone is responsible for about 7% of the worldwide carbon footprint (Malhotra, 2000). Due to the huge demand for cement in construction projects, the world production of this construction material increases by around 7% per annum compared with other materials (Topçu et al., 2014). Therefore, it is necessary to partially replace cement with alternative cementitious materials derived from industrial by-products, particularly ground granulated blast furnace slag (GGBS) and fly ash (FA). Additionally, the use of diverse recycled materials can serve as substitutes for aggregates, thereby diminishing the requirement for extracting aggregates through quarrying (Meyer, 2009).

The utilisation of geopolymer concrete (GPC) within the construction industry represents a promising sustainable practice and an interesting area of research focused on developing innovative products derived from industrial by-products and wastes. GPC is produced by substituting the traditional Portland cement with geopolymer binders, which are made by activating aluminosilicate materials with alkaline solutions, such as sodium hydroxide (NaOH). Industrial materials like FA and GGBS have emerged as primary source materials for GPC due to their abundant alumina-silica compounds (Nath and Sarker, 2014; Neupane, 2016; Suwan, 2016). It is worth noting that the production of GPC is more complex than ordinary concrete, involving a series of controlled processes. Initially, aluminosilicate source materials are blended with fine and coarse aggregates, followed by mixing with an alkaline activator solution to initiate geopolymerization. This process rapidly forms strong polymeric bonds, imparting strength and durability to the geopolymer concrete. The curing of GPC typically occurs at elevated temperatures (40–90°C) to achieve optimal mechanical and durability properties in the final product (Zhang et al., 2020; Cui et al., 2023). Extensive research has explored various geopolymer cements and concrete blends, revealing favourable properties such as high mechanical and chemical performance (Bakharev, 2006; Duxson et al., 2007; Komnitsas et al., 2007; Hardjito et al., 2008; Al Bakri et al., 2013; Ryu et al., 2013). However, it is essential to note that the environmental impact of GPCs can significantly differ based on their specific compositions. Salas et al. (2018) compared different GPC designs documented in the literature. The findings indicated a substantial variation in carbon emissions associated with producing 1m³ of GPC, ranging from approximately 100 to over 300 kg CO_{2,e}.

Kurda et al. (2018) explored the environmental benefits of using high volumes of recycled aggregates and fly ash in concrete. The study showed that replacing coarse natural aggregates with coarse recycled concrete aggregates reduces most of the studied environmental impacts by an average of approximately 20%. More importantly, the study also found that using fly ash as a replacement of up to 60% of cement reduces most the studied impacts by an average of about 45%. In addition, several studies have highlighted the benefits of employing lightweight over heavyweight materials in various construction applications. Mateus et al. (2013) demonstrated the sustainability of lightweight materials in partition walls. The LCA study analysed and compared the environmental, economic, and functional life cycles of ten design alternatives for a new lightweight sandwich membrane (LSM) wall with two conventional partition wall systems: the traditional heavyweight conventional masonry partition wall (HCM) and the lightweight reference plasterboard partition wall (LRP). The comparison revealed the potential of the new lightweight solution to be more sustainable than both traditional systems, reducing the associated GWP by up to 85% and 60% in comparison to HCM and LRP, respectively.

The industry's focus on achieving increased spans with minimal structural depth and flooring weight aligns with architectural and functional requirements, aiming to reduce the number of columns and foundations for a lighter and more sustainable construction, ultimately reducing time and costs. Consequently, different types of flooring systems have emerged, utilising new lightweight materials (Yan et al., 2016).

2.3.2 Prefabrication and Sustainability

On-site construction is another major contributor to energy consumption and CO₂ emissions, primarily for material transportation, heavy machinery, waste, and temporary materials (Dong et al., 2015). Prefabrication is a process that demonstrated efficacy in reducing on-site construction, improving quality control and site safety, and mitigating environmental impacts, construction time, and labour requirements (Meyer, 2009). Dong et al. (2015) conducted a LCA using cradle-to-site approach, comparing the carbon emissions of precast and traditional cast-in-situ construction for a residential building in Hong Kong. The study reported a 10% reduction in carbon emissions for the precast method. Regarding flooring systems, López-Mesa et al. (2009) found similar LCA

outcomes, stating that residential structures with precast hollow core concrete floors have 12.2% lower environmental impacts compared with those with cast-in-situ floors. This reduction is attributed to the diminished use of timber formwork in precasting, leading to reduced waste and carbon emissions compared with cast-in-situ methods (Jaillon and Poon, 2008; Wong and Tang, 2012).

2.3.3 Life Cycle Assessment (LCA) of Construction Practices

Life Cycle Assessment (LCA) is a powerful tool developed in the 1970s to effectively and systematically evaluate the environmental impacts associated with products, processes, or designs. It measures and assesses the effects of the energy use, material consumption and waste generation on the environment through the whole life cycle of the studied product, from raw material extraction to the end-of-life stage (i.e. cradle-to-grave approach). LCA is particularly valuable when comparing alternative options that offer similar performance but differ in ecological impacts (Mateus et al., 2013).

The main part of any LCA is the quantification of all energy and material flows associated with a product or a system to develop an inventory, followed by an impact assessment, which includes calculating and presenting findings in a predefined way that supports comparison or further analysis. The ISO 14040 (International Organization for Standardization (ISO, 2006a) and ISO 14044 (ISO, 2006b) standards of the International Organization for Standardisation (ISO) list the main four phases that must be carried out in any LCA study. The “14040 series” is within the broader ISO 14000 category on environmental management and most of the LCA studies adhere to the principles presented in it (BS EN ISO 14040, 2006a; BS EN ISO 14044, 2006b). Figure 2-1 illustrates the flowchart of the phases of LCA.

These phases are strongly related to each other, and it is a normal practice to go back and forth between phases. The main tasks in steps are as follows:

- a) Defining goal and scope: includes the definition of the boundaries, timeframe and the limitations of the study. These definitions clarify the questions to be answered, and the reliability and precision of data needed to be used in the LCA. If LCA is to be used for comparing products or materials, then an appropriate functional unit must be defined that provides a level-playing field to compare the different products or services.

- b) Life Cycle Inventory (LCI) analysis: includes the collection of the required data and calculation for inventory analysis. This step is considered as the most important and most time-consuming step. It is common that this step leads to redefinition of some of the system boundaries and other methodological choices. In this phase, usually some available life cycle inventory databases for building materials are used.
- c) Life Cycle Impact Assessment (LCIA): in this step, the environmental impacts are evaluated by converting the LCI to pre-defined impact categories based on a series of environmental indicators and selected characterisation models for each impact category. The common steps associated with this phase include the definition of impact categories by selecting a set of categories, classification factors and assigning of LCI results to each impact category, and the choice of a characterisation model to calculate indicator results within each impact category.
- d) Interpretation and conclusions phase: in this step, outcomes from the previous steps are analysed to get conclusions about the environmental impact of the product under investigation within the defined boundaries and limitations towards providing recommendations. In general, LCA results are very useful in finding opportunities to improve the environmental performance of a product or process in the life cycle period, decision-making and marketing.

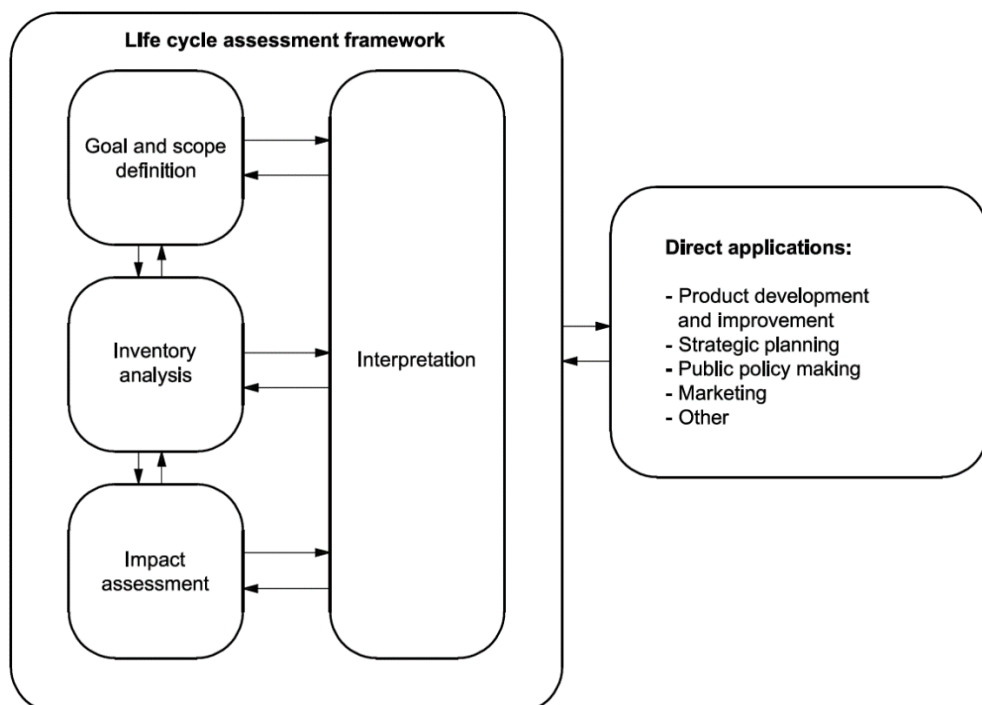


Figure 2-1: LCA phases (BS EN ISO 14040, 2006a; BS EN ISO 14044, 2006b)

LCA has wide applications in structural engineering, enabling the assessment of the environmental impacts of a building's entire life cycle or a specific component. It is also used to evaluate the environmental benefits of incorporating recycled or manufacturing by-product materials into construction. Besides that, independently verified LCA results can be used to label the environmental performance and support marketing of products by giving the knowledge of products' environmental impacts, which enables informed comparison between products fulfilling the same function, such as the comparison going to be carried out between the three flooring systems in this research.

The environmental impact of the construction process is influenced not only by the chosen material but also by factors such as construction procedures, component assembly methods, maintenance needs, transportation, and more. Thus, a thorough LCA study is essential to inform decision-making in material selection and structural design. Comparative LCA studies are widely utilised to assess the environmental impacts of alternative building materials and components based on equivalent functional behaviours. For instance, Anderson and Moncaster (2020) examined the effect of compression resistance and material mix design on the embodied carbon of concretes. Similarly, Hill and Dibdiakova (2018) and Grazieschi et al. (2021) assessed how density and weight influence the environmental footprint of insulation panels with similar thermal resistance. Additionally, Asdrubali et al. (2023) explored how factors like maintenance requirements, disassembly potential, and durability affect the life cycle impacts of walls that share comparable thermal performance and superficial mass. Furthermore, Hahnel et al. (2021) analysed the effects of material selection on the environmental impacts of floors having similar structural performance. These studies underscore the importance of comparative assessments in identifying the most sustainable building practices.

2.4 Composite Flooring System

In recent decades, there has been a growing demand for high-quality flooring systems that can be constructed quickly, provide larger clear floor areas, and offer flexibility in utilising the floor space. One construction approach that showed good performance toward reaching these goals is the steel-concrete composite (SCC) construction. This method combines steel and concrete into a single

composite component, enabling the materials to work together, yielding higher structural performance than if they were used separately.

Since its introduction, composite action has been recognised as an effective way of enhancing structural performance. In steel frame building construction, SCC beams are the most common form of composite elements. These are defined as “elements resisting only flexure and shear that comprise two longitudinal components connected together either continuously or by a series of discrete connectors” (Nethercot, 2003). Typically, SCC beams consist of a slab (either solid concrete slab or SCC slab) attached to a rolled steel I-beam section through shear connectors, with the most common being headed shear studs.

Beams are designed initially for ultimate strength using load factor methods and the ultimate capacity of the composite element will be considered if the full shear connection exists between the components (slab and beam). However, in many cases the connection cannot resist all of the forces applied and considered as partial shear connection. The same pattern is repeated when considering the serviceability limit-state of composite beams. The slabs are designed to carry the floor load spanning between the parallel beams and also take compression perpendicular and along the beam line because it is connected to the steel beam sections with shear connectors. The connection between steel and concrete in the slab must be sufficient to control longitudinal shear and any uplift forces and the longitudinal forces generated by this connection must transfer fully from the steel section into the slab. The typical composite beam arrangement is shown in Figure 2-2 (a).

A common example of composite beams is the composite downstand beam with SCC slabs that are made from steel deck sheets connected to the beam and cast-in-place concrete. A schematic drawing of this composite beam is shown in Figure 2-2 (b). Some disadvantages of this composite beam, which the flooring system under research aims to address, include the high total depth of the floor due to the slabs being placed on top of the beam and the need for on-site construction to install steel sheets, connect them to the beam, and cast concrete. These drawbacks can be avoided by the use of prefabricated slabs.

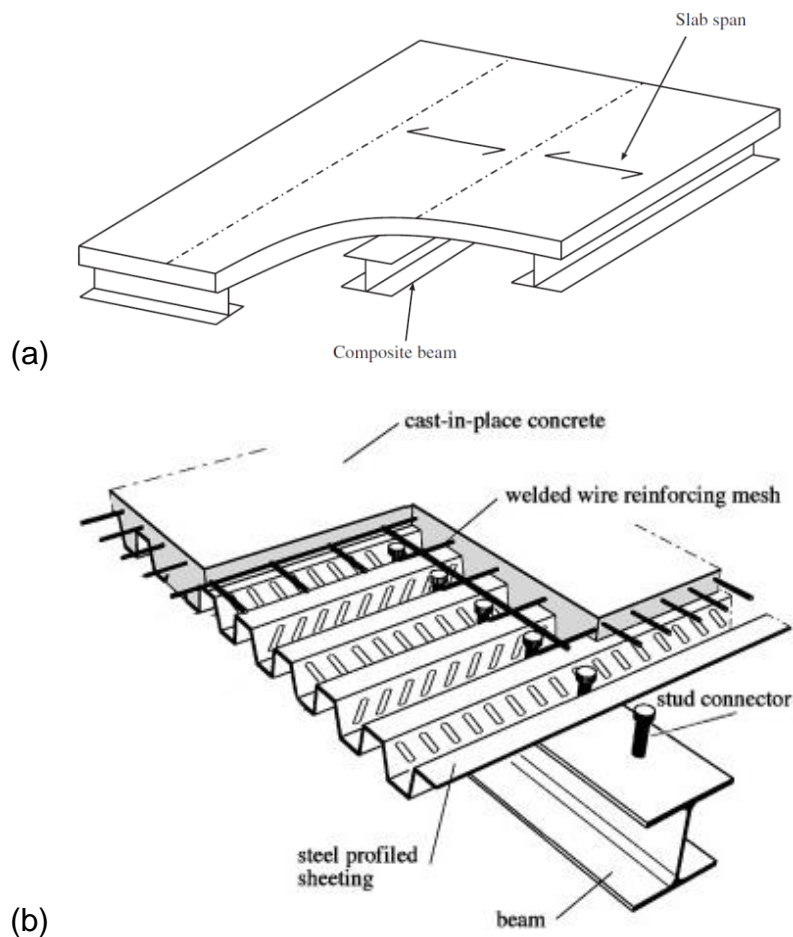


Figure 2-2: (a) Typical composite beam arrangement (Nethercot, 2003) (b) Composite downstand beam with steel deck composite slab (Crisinel and Marimon, 2004)

2.5 Shallow Composite Beams

Flooring systems play a pivotal role in determining building's overall weight and material usage, driving the demand for lighter, more environmentally friendly systems. The current trend in composite flooring construction is transitioning from traditional downstand steel beams to lighter, shallower, and often aka 'plug' composite systems, where the concrete slab sits at the bottom flange (Tsavdaridis et al., 2009; Tsavdaridis et al., 2013; Ahmed and Tsavdaridis, 2019). These systems are called slim floors and many designs have been developed towards achieving this goal by applying some modifications to the beam sections that allows comprising the shear connections and the slabs thickness within the depth of the beam. This section presents an overview of some of the developed slim floor composite beams, that can be integrated with PUSS units to form flooring system. Additionally, it discusses research papers that explore the flexural behaviour of these composite beams and the performance of shear connectors employed to facilitate composite action between the beams and concrete flooring.

2.5.1 Slim Floor Beam (SFB)

Slim floor beams are created by welding a plate to the bottom flange of a universal column section. The floor slabs are placed on this bottom plate, which serves as the slab's support. Various kinds of slabs, including the hollow core precast slabs, have been integrated in that flooring system. They are placed directly on the bottom plates and then in-situ structural concrete with or without shear connectors and steel reinforcement (depending on the requirements) is placed to form a topping layer and a composite connection between the slabs and the beam, as shown in Figure 2-3 and Figure 2-4. A design guidance for SFB with hollow core precast units in agreement with the BS5950: Part 1, was introduced by Mullett (1992). The flexural behaviour of SFB using deep profile decking and hollow core precast slabs was experimentally investigated by many studies over the last 3 decades. Some of these experimental researches are presented below.



Figure 2-3: Using slim floor beams with hollow core precast slabs (Lawson et al., 2015)

The results of full-scale six-point bending test on SFB were discussed by Mullett (1998). The specimen was 7.5 m in span with an overall depth of 300 mm, and made of original CF210 deep decking with no shear connection, but with holes constructed on the web post which provided a passage for short lengths of concrete cylinders. The six-point loading simulating a uniformly distributed load, was discontinued after reaching a total load of 1016 kN, with a mid-span deflection of 150 mm (span/50). The maximum bending moment was calculated to be 925 kN.m, which is 1.68 times the capacity of bare steel. Based on the calculated load intensity of the tests, the specimen could have supported an imposed load of 10.9 kN/m² compared with the design value of 5 kN/m². This increase in moment capacity due to composite action without shear connection led to the development of the Asymmetric Slim Floor Beams (ASB).

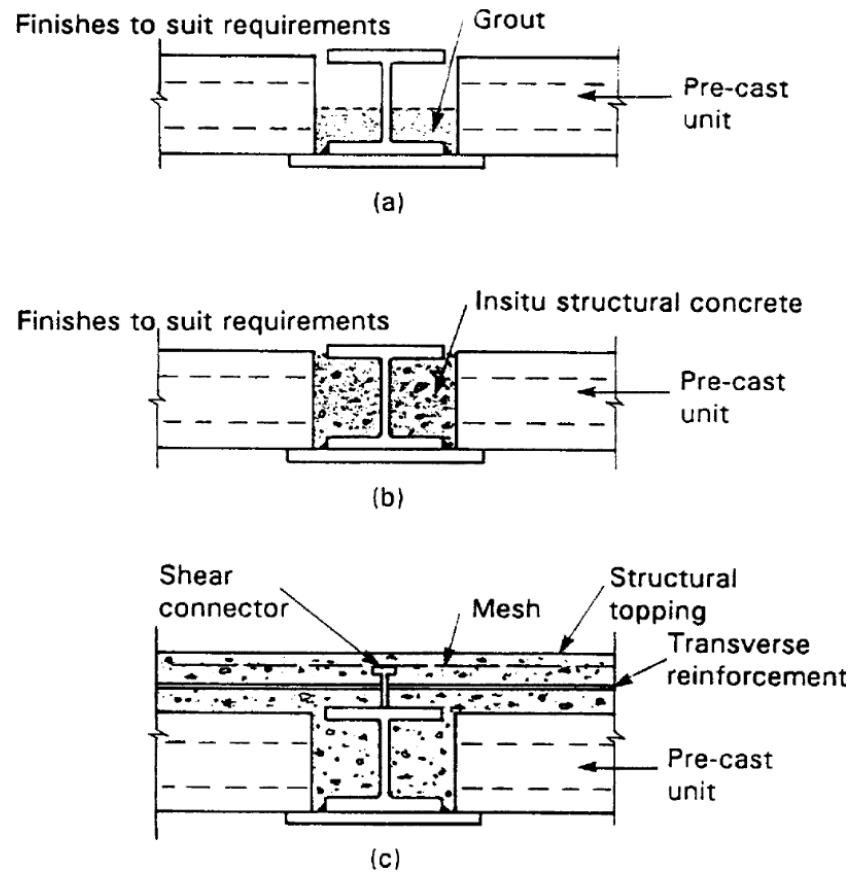


Figure 2-4: Various methods of floor construction using slim floor beams (Mullett, 1992)
 Wang et al. (2009) carried out three-point bending tests on two SFBs using deep decking with fixed end connection to a column frame. The span of the two specimens was 6 m with an overall depth of 290 mm and 0.75 m width of concrete slab. One of the specimens was with a higher reinforcement ratio and that did not show any influence on the stiffness but induced a slight higher failure load, which was 476 kN compared with 446 kN for the other specimen. As an outcome of the study, a formula for moment capacity in the hogging moment region $M_{c,hog}$ was proposed, together with an existing formula for the sagging moment $M_{c,sag}$. The failure load F of the SFBs with span L was derived (Equation 2-1) and verified with test results and FEA.

Equation 2-1

$$F = \frac{4(M_{c,sag} + M_{c,hog})}{L}$$

Hegger et al. (2009) tested the shear capacity and the load bearing behaviour of prestressed hollow core slabs in SFBs by conducting four full-scale tests carried out on continuous two-span floor systems (6 m x 10 m) that consists of a total of 10 slabs. In the middle of the two-span system, the slabs were supported by a SFB. The conclusions of the research showed that large deformations due to

plastification of the supporting beam caused premature failure of the slabs and that on rigid supports, 60-70% of the shear strength of the slabs can be utilised under appropriate boundary conditions.

Despite the practical application of SFBs over previous decades and the robust experimental foundation supporting their use, recent literature indicates a notable decline in research specifically focused on this configuration, particularly concerning their structural behaviour under loading in both experimental and numerical contexts. The inherent limitation in achieving an effective composite shear connection between the steel beam and the concrete slab has redirected attention toward more structurally integrated systems, such as Ultra-Shallow Floor Beams (USFB) and Composite Slim Floor Beams (CoSFB), which offer improved composite action and load transfer capabilities. Nonetheless, some contemporary studies still explore other aspects of SFBs, such as fire resistance, an example being the work by Alam et al. (2021), which investigates their thermo-mechanical response under fire conditions experimentally and numerically. Consequently, the SFB system, while historically significant, is increasingly regarded as a transitional solution in the evolution of shallow composite flooring systems.

2.5.2 Asymmetric Slim Floor Beam (ASB)

ASBs (or ASFBS) are similar in application to SFBs; however, it uses different beam cross-section. The beam is rolled I section with the bottom flange larger than the top flange and therefore, additional plate is not required. Similar to SFB, this type of beams has been integrated with different kinds of floor slabs and an example with precast hollow core slabs is shown in Figure 2-5. A design guidance for ASB with precast hollow core concrete slabs with or without concrete topping was introduced in 2006 (Rackham et al., 2006).

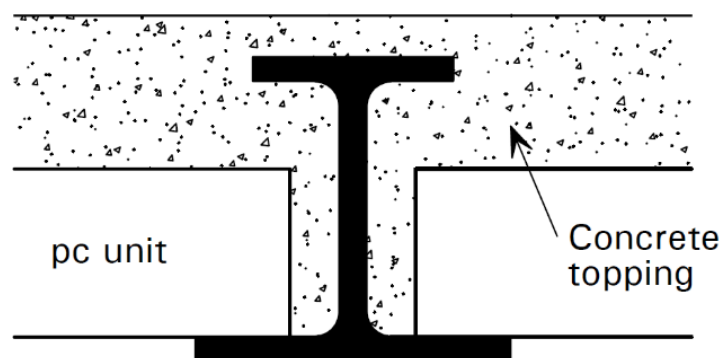


Figure 2-5: Asymmetric slim floor beam with precast concrete and concrete topping (Rackham et al., 2006)

Lawson et al. (1997) and Lawson et al. (1999) presented three full-scale six-point bending tests on 280 ASFB, 300 ASFB and 280 ASFB/100 (light steel) composite beams using deep decking. The first two specimens were with a 7.5 m and 1 m width while the third specimen was with 2 m width. The major difference in the third specimen is that it had a series of elongated web openings (160 mm x 240 mm). The tests were first carried out with 1000 cycles of dynamic loading between 0 and 1.2 times the calculated working load, and then tested with monotonic loading up to the failure. The results of the tests showed that the bending resistance of the ASFB was increased by 30-50% due to the composite action, which did not deteriorate under the repeated loading, and the actual degree of shear connection was between 75-100%. As a result, a design shear bond strength of 0.6 N/mm^2 was concluded. The initial stiffness of the composite section was maintained up to 70% of the failure load and the measured stiffness was very close to the design stiffness based on the uncracked section. The effect of the elongated openings on the performance of the beam was relatively small.

Sheehan et al. (2018) presented the results of a bending test on a 12 m long composite beam subjected to uniformly distributed loading. The composite beam comprised a concrete slab on a steel profiled metal decking forming a composite slab, connected to an ASFB using welded shear studs. The test intended to test the flexural behaviour with degree of shear connection lower than the minimum specified by the Eurocode 4, and therefore, the degree of shear connection applied was equal to 33% whereas the minimum degree of shear connection based on the equations of Eurocode 4 should be 77%. The uniformly distributed load was applied and increased until the failure occurred because of the yielding of the steel beam without an observed concrete crushing or shear stud failure (Figure 2-6). The obtained maximum bending moment of the composite beam was almost equal to the plastic bending resistance according to the Eurocode 4 and the end slips reached 19.2 mm which exceeded 6 mm, the limit for ductile behaviour in Eurocode 4 and hence, the shear connection showed a ductile behaviour. The analysis of the results and the conclusions of the study suggest that the design limits governing the minimum degree of shear connection could be revised to give better match.

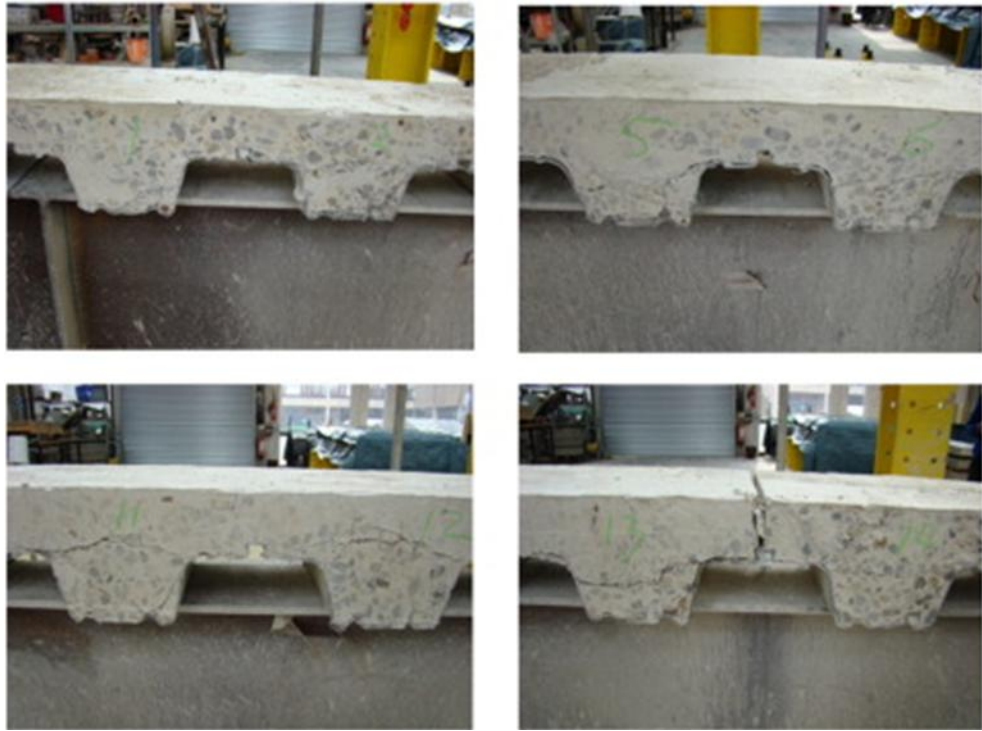


Figure 2-6: Concrete slab showing no visible concrete crushing after testing (Sheehan et al., 2018)

Although ASBs are considered a more recent development compared to traditional SFBs, they serve largely the same structural applications. As a result, most recent research on the behaviour of shallow flooring systems has increasingly shifted focus toward more advanced systems such as Ultra-Shallow Floor Beams (USFB), Composite Slim Floor Beams (CoSFB), and Deltabeams, which offer more effective composite shear connections between the beam and the slab. Nonetheless, there remains some ongoing research addressing specific aspects of ASBs, particularly in areas like fire resistance, such as the study conducted by Duma et al. (2022) which explores the bending resistance of ASB under fire.

2.5.3 Ultra-Shallow Floor Beam (USFB)

Ultra-Shallow Floor Beam is a slim floor perforated beam designed developed by Westok Ltd. It is fabricated by welding two highly asymmetric cellular T sections (one small at the top and a larger one at the bottom) over their webs forming a shape similar to ASB with large bottom flange but with additional web openings. These openings allow forming a strong composite connection with the floor slabs lying on the bottom steel flanges. This system has been used with various types of slabs including precast slabs as shown in Figure 2-7 (Tsavdaridis et al., 2009).

The web openings allow connecting the concrete slabs to the steel beam with concrete dowels and steel bars, which act as shear connectors. These connectors enhance both the longitudinal and vertical shear resistance. The web openings can also be used for passage of building services through the depth of the beam which minimises the overall required depth of the beams and produces lighter members. In this type of beams, and due to the fact that the connection is made at the web and not on the upper flange, the composite action is assured without increasing the beam height or the floor thickness, as would have been required with the use of traditional shear studs welded onto upper flange of the steel profile, and therefore, the concrete cover above the steel section can be reduced to a minimum.

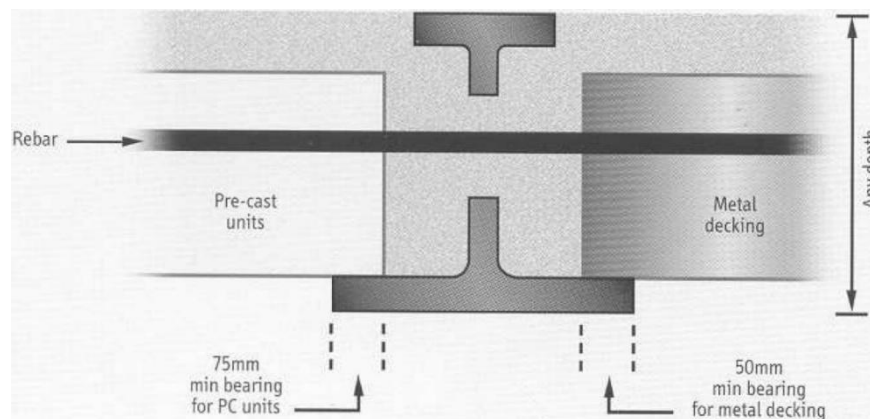


Figure 2-7: Cross-section configuration of USFB with precast units and metal decking (Tsavdaridis et al., 2009)

Huo (2012) tested the shear connection in 16 full-scale USFBs specimens under direct longitudinal shear with push-out tests as well as two flexural tests. Four types of shear connectors were studied in push-out tests, which are concrete infill only shear connectors, tie bar shear connectors, ducting shear connectors and horizontal shear stud connectors with two types of concrete (normal and fibre reinforced concrete) while only the first two types of shear connectors were tested in flexural tests. The push-out test results concluded that uniform behaviour was demonstrated by each type of shear connectors. The use of concrete infill only shear connector showed brittle failure and the use of tie bars and studs increased the shear capacity, slip, and ductility capacity of the shear connectors (Figure 2-8). The shear capacity of the shear connectors increased with increasing diameters of the web opening and with higher strengths of concrete infill. Based on the experimental results and a FEA parametric study, an empirical formula for calculating the shear capacity of the new shear connectors P_{uc} was proposed (Equation 2-2). Where f_{ct} is the tensile splitting strength of concrete, f_{cu} is the

compressive strength of concrete, D is the diameter of the web opening, t is the thickness of the web, R_{add} is the additional resistance of the tie-bar or studs.

Equation 2-2

$$P_{uc} = \frac{1.6758(f_{cu}tD) + 1.4355\left(f_{ct}\frac{\pi D^2}{4}\right) + R_{add}}{1.5}$$

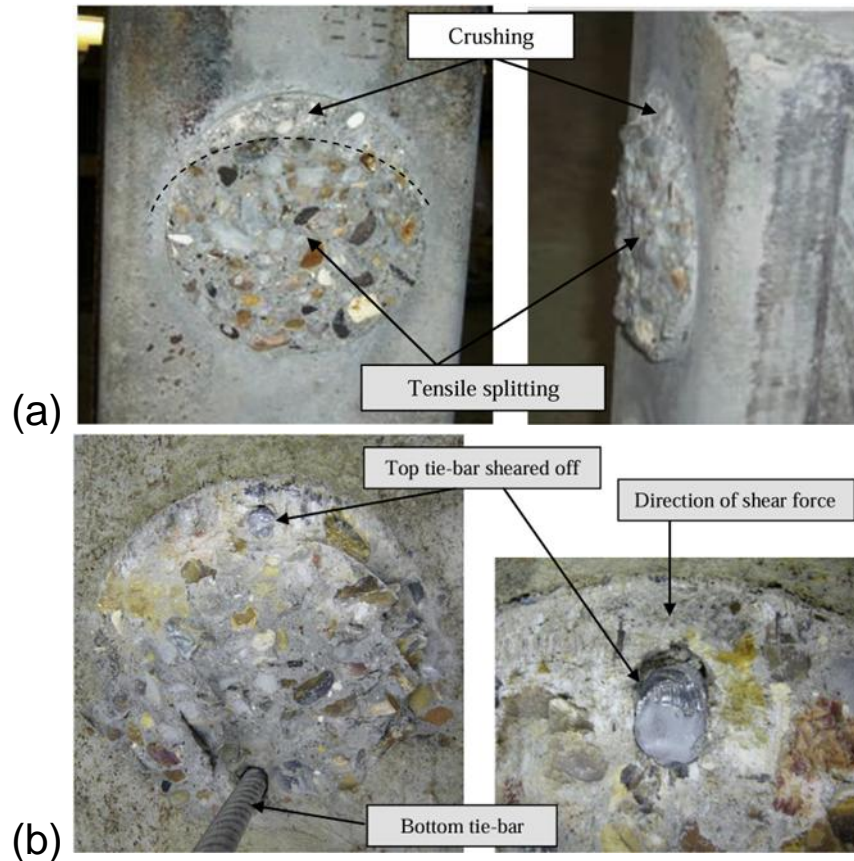


Figure 2-8: Failure profiles of the (a) concrete-infill-only shear connection, & (b) tie-bar shear connection (Huo, 2012)

For the flexural tests, one USFB specimen with 6.2 m span, 1 m width and 230 mm depth was tested under four-point and three-point asymmetric bending test. Half of the specimen had concrete infill only shear connector, and the other half had 16 mm tie bars shear connectors. Four cycles of four-point bending loading was applied first up to reaching the plastification, followed by three cycle of three-point asymmetric loading up to failure. The tests results were consistent with those of the push-out tests, where brittle failure was observed in the region with concrete infill only shear connectors, while ductile failure occurred in the region with 16 mm tie bar connectors. The specimen exhibited a flexural failure mode, and significant composite action was evident, as the measured test moment resistance reached 1.5 times the plastic moment resistance of the steel section.

Chen et al. (2015) examined the flexural behaviour of shallow asymmetric cellular composite floor beams with perfobond-like shear connections using four-point bending tests on four beams with varied web openings and concrete cover thicknesses. In addition, two specimens were without top steel flange. These beams incorporated tie-bars through circular or clothoidal web holes, improving slip capacity and ductility. The 4 m beams, composed of composite steel deck floors and asymmetric steel sections, showed effective composite action and increased shear resistance due to the tie-bar and concrete infill interactions. The findings supported the perfobond shear connection's effectiveness, as beams with this configuration demonstrated substantial horizontal shear resistance and favourable ductile behaviour, crucial for shallow floor applications. In terms of failure mechanisms, two failure modes were observed in the experiments: the specimens with top steel flange had flexural failing with concrete crushing in the compression zone without bond failure (Figure 2-9 (a)), while specimen without top steel flange failed in shear (Figure 2-9 (b)).

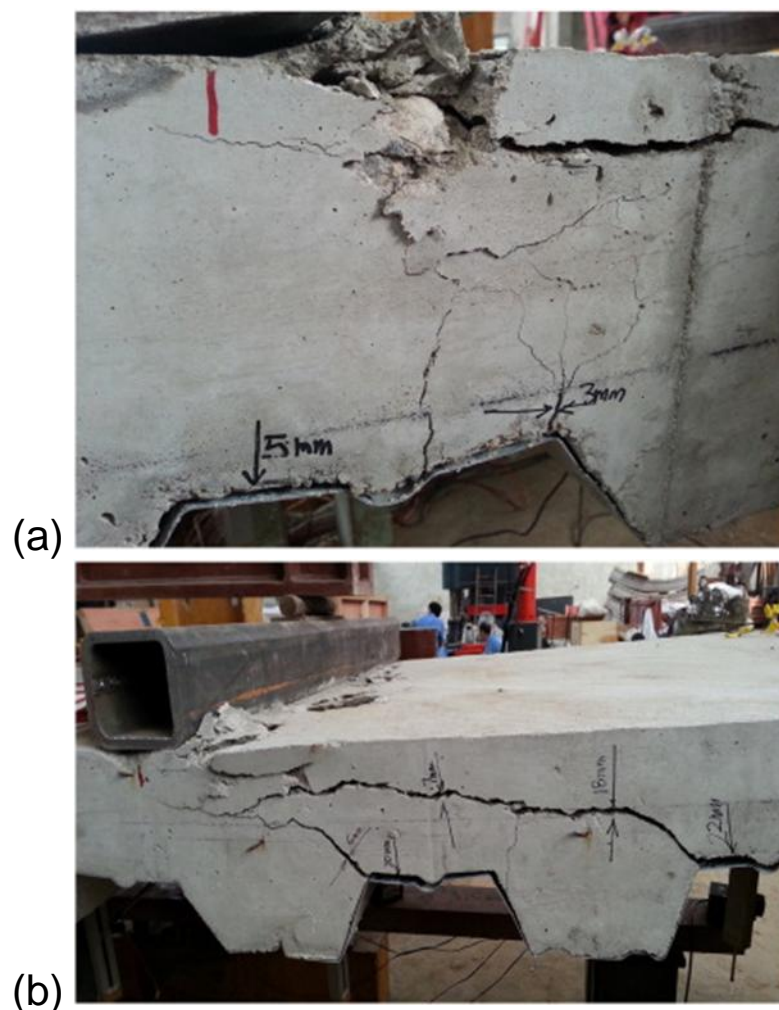


Figure 2-9: (a) Concrete crushing under loading points in specimens had flexural failure, (b) Specimens with shear failure (Chen et al., 2015)

Recent studies have further advanced the understanding of USFB performance. Pereira Júnior et al. (2023) investigated the flexural behaviour of steel–concrete USFBs integrated with precast hollow-core slabs through the development of a finite element model based on experimental tests and perform a parametric study. The findings indicated that the flexural performance and crack control was highly sensitive to factors such as dilation angles and reinforcement ratios in concrete topping. Notably, models lacking steel tie bars through web openings demonstrated reduced bearing capacity. The study emphasised the importance of incorporating tie bars to enhance structural performance and provided insights into the position of the plastic neutral axis under varying loading conditions.

Experimental four-point bending experimental tests on long-span USFBs incorporating lightweight and ultra-lightweight concretes was the subject of research presented by Tsavdaridis et al. (2024). The 7.2-meter span beams demonstrated increased bending resistance due to composite action facilitated by plug shear connections through web openings and additional tie bars. The study concluded that cracked section properties should be considered for accurate deflection analysis, and the failure mode was governed by the crushing of concretes prior to reaching the plastic bending resistance of the composite section.

The extensive body of research on USFBs underscores their effectiveness in achieving robust composite action, structural efficiency, and adaptability in modern construction. Their design facilitates integration with various slab types and building services, making them a preferred choice in shallow floor applications. While much of the recent work has concentrated on structural aspects such as flexural behaviour and shear performance, other important topics like fire resistance have also been addressed, as exemplified by the study of Alam et al. (2021), further broadening the understanding of USFB applications.

2.5.4 Composite Slim Floor Beam (CoSFB)

Composite Slim Floor Beam is one of the most recent slim floor systems. It is composed of a steel I-beam section with circular web openings and a plate welded to the bottom flange of the beam. The steel decking or prefabricated slabs are placed over the bottom plate and concrete is poured in site with placing steel reinforcement passing through the web openings, that creates concrete dowels that transmit the shear between the beam and the slab (Hechler et al., 2013).

Similar to USFB, the shear connection is made at the web and not on the upper flange, and therefore, no increase in the beam height or the floor thickness will be required. This type of systems has been used with different kinds of slabs such as the composite decking systems and hollow core precast slabs (Lawson et al., 2015; ArcelorMittal, 2019). Figure 2-10 shows a schematic drawing of the CoSFB.

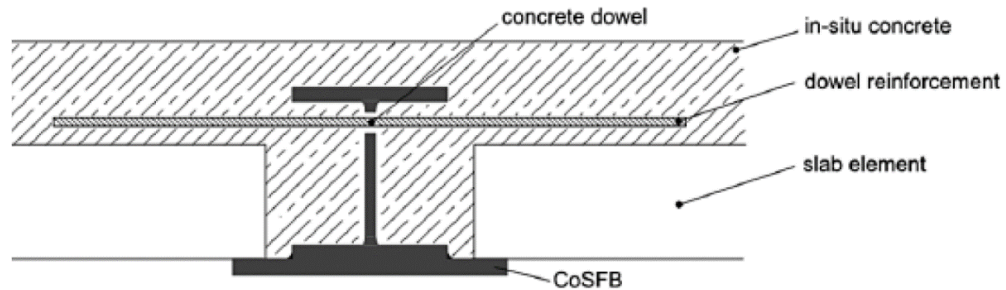


Figure 2-10: Composite slim floor beam (CoSFB) (Lawson et al., 2015)

Hechler et al. (2013) tested the shear capacity of the shear connectors concrete dowels into 6 CoSFBs through push-out tests. The tests investigated the influence of varying the concrete compressive strength, the thickness of the steel beam web, the web hole diameter and the reinforcement bar diameter that passes through the web. It was found that the concrete strength barely influenced the shear capacity of the connectors, while a small effect on the shear capacity has been recognised when changing the web thickness. However, a significant increase in bearing capacity by doubling the diameter of the bar was observed. Therefore, the influence of the reinforcement bar seems to be crucial in design for the bearing capacity and demonstrated that concrete infill around the web hole has a great effect on the bearing capacity of the concrete dowels' shear connectors.

Baldassino et al. (2018) investigated the service and ultimate behaviour of two full-scale composite slim floor beam (CoSFB) specimens using HEB 200 steel sections with welded bottom plates embedded in concrete. First specimen was left unloaded for the entire duration of 10 months, while started loading the second specimen after 3 months under distributed load until the end of the 10 months. The study aimed to monitor the effects of creep and shrinkage on the tested specimens. Afterwards, both specimens were tested to failure using four-point bending tests. Both beams exhibited ductile flexural behaviour by concrete crushing. The shear-lag effects played an important role in the flexural response. At the end of the tests, the shear connector steel reinforcing bars installed through the web holes deformed locally with increased deformation moving away from the

centerline (Figure 2-11). The study validated the effectiveness of CoSFBs in meeting Eurocode requirements for both serviceability and ductility, and highlighted their potential for use in high-performance shallow floor systems.

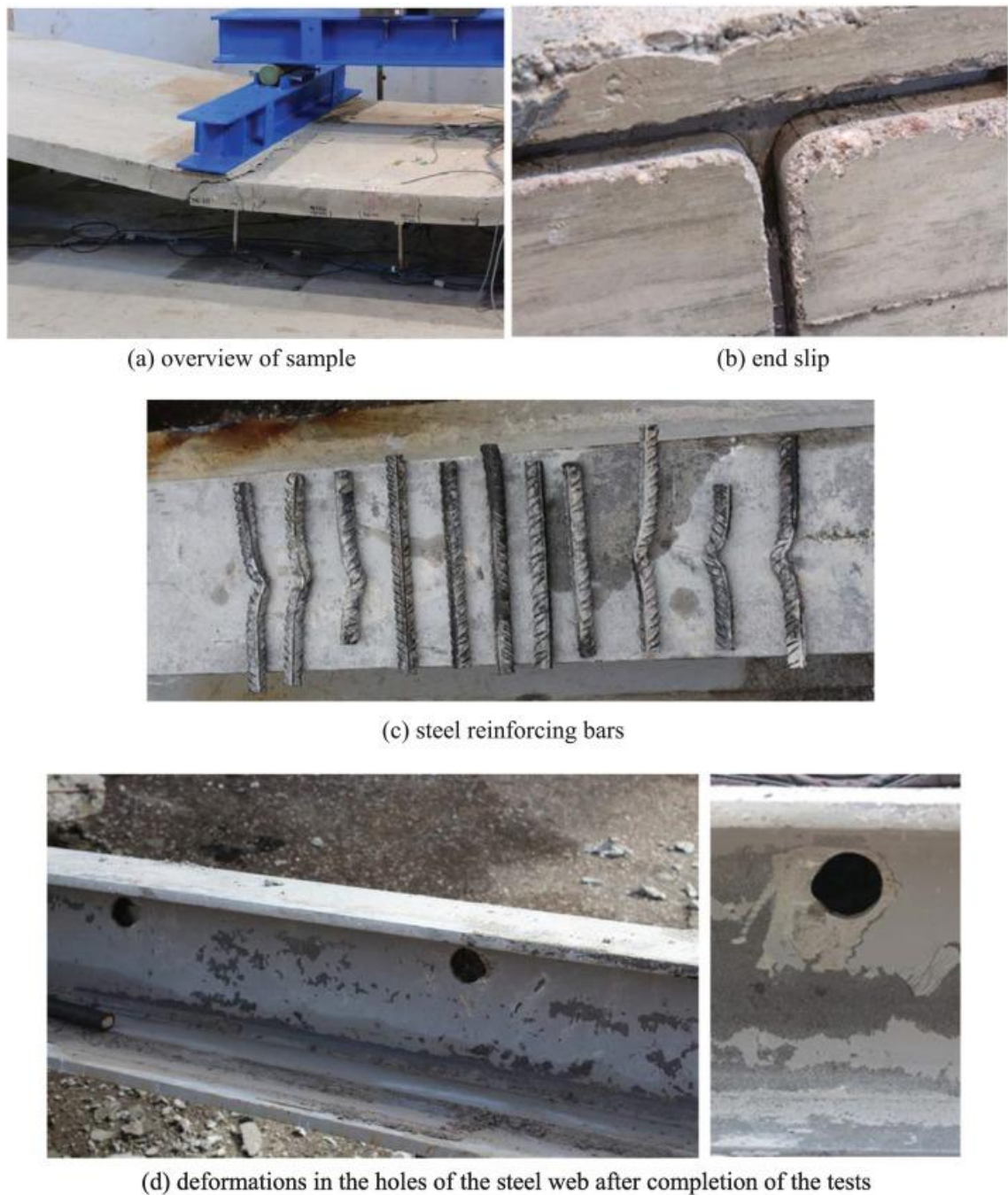


Figure 2-11: Observations of failure condition at the completion of the ultimate tests (Baldassino et al., 2018)

Sheehan et al. (2019) performed a total of nine bending tests (four-point and six-point bending) on nine CoSFBs specimens to study the effect of different parameters on the maximum bending capacity. Parameters included shear connection type and degree of shear connection, the effect of the top concrete cover, the effect of the location of the loadings and the type of the loading. In general, the CoSFBs were made by encasing HEB 200 steel beam section with

web opening in the middle of T-shape concrete slab. Additionally, a 400X15 mm steel plate was welded to the bottom of the steel beam. The total depth of the beam was 240 mm (120 mm is the thickness top slab part), the span of the slabs is 6 m and the width is 2 m. Due to the various parameters under study, each specimen gave different bending capacity that showed the effect of a specific parameter. All the specimens showed flexural failure, however, the mid-span deflection exceeded $L/40$ at failure which is way higher than the serviceability limits and end-slip exceeded 6 mm which indicated ductile behaviour. The main outcome of the research is that the transverse bars passing through holes in the steel beam web proved to be effective shear connectors and that the use of bigger size of web holes (concrete dowels) clearly enhances the performance of CoSFBs. The calculated maximum values of the shear in each specimen showed a good agreement with a previously done test on similar slabs but with 4 m span. The difference is that the specimens of the previous tests failed in shear, while the current specimens failed in flexure.

Dai et al. (2020) continued the investigation into slim-floor composite beams with dowel shear connectors, building on Sheehan et al. (2019)'s findings on transverse bar connectors. Dai et al. employed a numerical model validated against experimental data to study the effect of various parameters on the shear performance, including dowel diameter, reinforcement, and concrete strength. Testing was conducted under both eccentric and concentric loading, with shear connection provided through dowel action of transverse bars of diameters ranging between 12 and 24 mm in web holes with diameters up to 160 mm. Findings indicated that larger dowel holes increased shear strength, however, the larger hole causes more reduction in steel sections web's area, reducing the load-bearing capacity. Therefore, for the tested steel section, the optimum hole diameter was recommended to be from 80 to 120 mm. In addition, dowel action enhanced the overall ductility of slim-floor systems, with specimens achieving mid-span deflection up to $span/50$, showing significant agreement with prior findings on transverse bars as effective shear connectors.

Borghi et al. (2021) presented a parametric numerical investigation comparing CoSFBs to ASBs using ABAQUS software. Finite element models were developed and calibrated against experimental data. The analysis considered load-deflection behaviour of composite beams with variable parameters related

to concrete and steel components. Results showed that CoSFBs offer improved bending resistance and structural efficiency compared to ASBs due to their effective shear connection provided by transverse bars through web openings. The CoSFB specimens exhibited smaller plastic deformations, confirming their advantages over ASBs. The parametric study also revealed that steel related parameters have substantial influence on the slim floors behaviour compared to concrete related parameters.

The extensive and evolving research on CoSFBs underscores their growing significance in modern structural systems. That is mainly because – as in USFBs – it effectively combine shallow profile geometry with enhanced shear connectivity through dowel action at web openings, allowing for robust composite action without increasing floor thickness.

2.5.5 Deltabeam

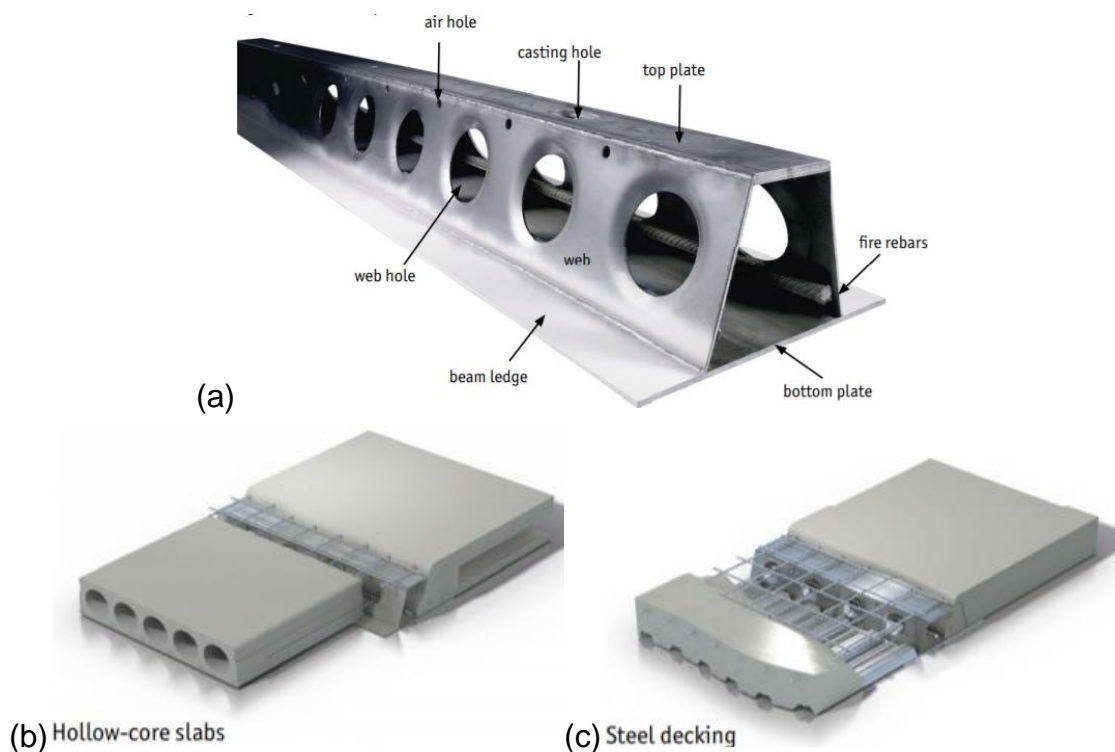


Figure 2-12: (a) Deltabeam parts (b,c) The use of Deltabeam with hollow core and composite steel decking slabs (PEIKKO, 2014)

Deltabeam is another type of slim floor beams having several distinguishing features from the other beams. It is made of cut steel plates that are welded together at factory to form a trapezoidal boxed cross-section with the bottom flange being larger than the top one and equipped with ledges that allows placing various types of floor slabs, such as hollow core slabs and composite slabs with steel decking. The boxed section is not closed and it comes with circular openings

in the two webs which allows it to be filled with concrete cast in-situ with placing steel reinforcement passing through the web openings to form concrete dowels that transmit the shear between the beam and the slab and provide effective composite action of steel Deltabeam body with infill concrete after full hardening. Figure 2-12 presents the components in the cross-section of Deltabeams and the use of Deltabeam with different types of slabs.

Peltonen and Leskelä (2006) conducted 75 push-out tests to investigate the capacity of the concrete dowel in Deltabeam with variable parameters of web hole diameter, the geometry of the lip (mainly the lip depth), and concrete strength. The push-out tests were designed based on the assumption that only the concrete outside of the steel box plus the concrete dowel within the lip depth are effective to the shear resistance mechanism. Therefore, a foil parting the concrete infill was used to simulate the concrete dowel shear connection in the push-out test specimens. The tests demonstrated the ductile load-slip behaviour of the concrete dowel, with average maximum slips of 6-9 mm. The disassembling of the specimens showed that failure of all specimens was due to the shearing off of the concrete dowel. The effect of the depth of the lip, which is the depth of the concrete dowel, had less effect on the resistance of the 75mm diameter web holes. A formula was developed for the shear resistance of the concrete dowel P_{max} (Equation 2-3), where f_{ctm} is the mean tensile strength of the concrete, $k_R(f_{ctm})$ is a resistance factor that depends on the geometry of the hole (depth and diameter), and $A_{\emptyset w}$ is the area of the hole.

Equation 2-3

$$P_{max} = k_R(f_{ctm})f_{ctm}A_{\emptyset w}$$

Further insights were provided by Kyriakopoulos et al. (2021), who undertook an extensive experimental and numerical campaign to investigate the flexural behaviour and robustness of Deltabeams. Seven full-scale specimens were tested under three-point sagging bending to evaluate ductility, composite interaction, and structural resilience under large displacements. Two groups were studied: Type 1 with shear studs on the top flange and limited confinement, and Type 2 with enhanced side confinement and no concrete topping. Results showed that Type 2 specimens exhibited superior ductility and slip performance due to enhanced confinement, achieving high deflections (up to L/16) without strength degradation. Full shear interaction was confirmed by strain

measurements and corroborated via nonlinear finite element simulations in Abaqus, demonstrating good agreement with experimental data. At the end of the tests, type 1 sections could not prevent spalling of top concrete, causing buckling in the web and top plate (Figure 2-13 (a)). On the other hand, the confinement in type 2 sections prevented spalling of concrete and the specimens were in good condition (Figure 2-13 (b)). In a related study, Kyriakopoulos et al. (2022) investigated the behaviour of Deltabeams under extreme deformation conditions, employing both experimental tests and numerical modelling. This study emphasised the robustness of the composite system and highlighted the key structural features that ensure performance during large displacement and progressive collapse scenarios.

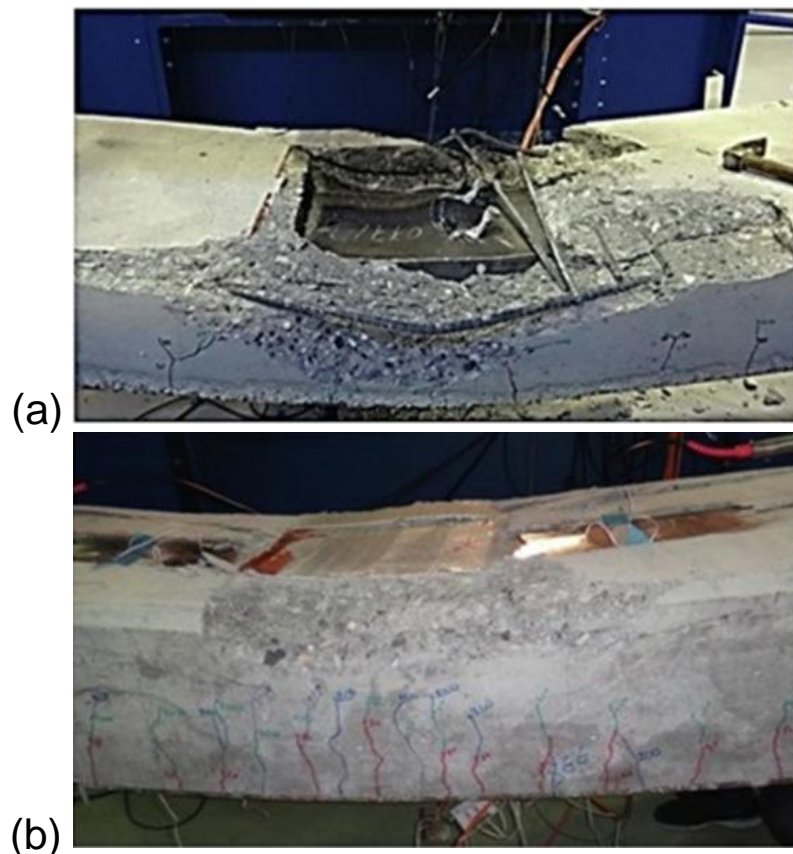


Figure 2-13: Conditions of (a) Type 1 sections and,(b) Type 2 sections at the end of the tests (Kyriakopoulos et al., 2021)

Although introduced only in the late 1990s, Deltabeam systems have been the subject of extensive research due to their structural efficiency and application flexibility. In addition to structural performance, numerous studies have explored other critical aspects, such as fire resistance performed by Maraveas (2017) and Beckmann et al. (2023). These investigations further affirm the comprehensive interest and development of Deltabeam technology in modern structural engineering.

2.5.6 Summary

The comparison table below (Table 2-1) summarises the differences and similarities between the shallow composite flooring systems previously discussed. The comparison incorporates key attributes including structural configuration, shear connection mechanisms, span and depth limitations, as well as practical advantages and disadvantages. This is based on the discussion presented in the previous sections and complemented by data extracted from the study by Ahmed and Tsavdaridis (2019).

Table 2-1: Comparative summary of shallow composite beam systems

System	Slim Floor Beam (SFB)	Asymmetric Slim Floor Beam (ASB)	Ultra-Shallow Floor Beam (USFB)	Composite Slim Floor Beam (CoSFB)	Deltabeam
Steel Section Components	Universal column section + welded bottom plate	Rolled I-section with large bottom flange	Welded asymmetric cellular T-sections	I-section + welded bottom plate	Trapezoidal welded box
Web Holes	No	No	Yes	Yes	Yes
Shear Connection Type	Concrete infill	Concrete infill	Concrete dowel via web holes + tie bars and dowels	Concrete dowel via web holes + tie bars and dowels	Concrete dowel via web holes + tie bars and dowels
Composite Action Efficiency	Moderate	Moderate	High	High	High
Span Limitation (m)	5-10	6-7.5	Up to 10	Up to 12	Up to 13.5
Depth Limitation (mm)	280-320	310-340	300	350	200-500
Advantages	Simple fabrication, low floor height	No need for bottom plate, easy integration with slabs	High composite efficiency, service integration, low depth	High composite efficiency, service integration, low depth	Lightweight, flexible with slab types, long spans
Disadvantages	Limited composite action, low shear connection efficiency	Limited composite action, low shear connection efficiency	Requires precise dowel detailing, more fabrication work	Requires precise dowel detailing, more fabrication work	Complex manufacturing, dependent on detailing for shear

2.6 Prefabricated Slabs

The growing call for sustainable practices has led to the development of innovative integrated floor slabs that enable wide spans and integrated building services. Various flooring systems have been developed, that offer advantages for residential and office buildings, malls and airport structures. Notably, slim floor construction, characterised by the integration of steel beams into slabs, has emerged as a focal point of research and resulted in the development of various products. This construction approach combines the benefits of prefabricated slab elements with steel-framed construction, resulting in an economically viable building solution that effectively meets the demands outlined above (Hechler and Braun, 2010).

Slim composite beam systems have been paired with various types of prefabricated flooring slabs, such as steel-decking composite slabs and hollow core precast slabs (Lawson et al., 2015). The use of prefabricated slabs in such systems has many advantages; one of them is the great performance in time and cost reduction (Hicks, 2003; Mullett, 1992). This section gives an overview of the PUSS flooring system and the previous research done on it, as well as one of the widely used prefabricated slabs that will be used in the comparative LCA of this thesis, which is the hollow core precast slab.

2.6.1 Prefabricated Ultra-Shallow Slabs (PUSS®)

The recently developed prefabricated ultra-shallow slab (PUSS) flooring system represents a flooring solution designed for efficient, sustainable construction. PUSS units are fully fabricated offsite by casting-in-place reinforced ribbed concrete slabs within two parallel flange C-channel steel beams, which are connected with a novel horizontally oriented shear connection system. This system consists of either (1) horizontally-oriented web-welded shear studs (WWSS), (2) horizontal steel dowels welded to the webs, or (3) a combination of both shear connection systems (WWSS with dowels) (Ahmed and Tsavdaridis, 2018). The horizontal steel dowels connections pass through the slab from one edge steel beam to the other, which makes them useful during the process of casting concrete as they hold the two edge beams in place, minimising the need for additional framework. For building installation, the prefabricated slabs are moved as ready-made floor units to the construction site and installed at their intended locations in the building. Figure 2-14 provides schematic drawings of a

segment of a standard 2 m wide PUSS unit featuring a connection system composed of a combination of WWSS and steel dowels.

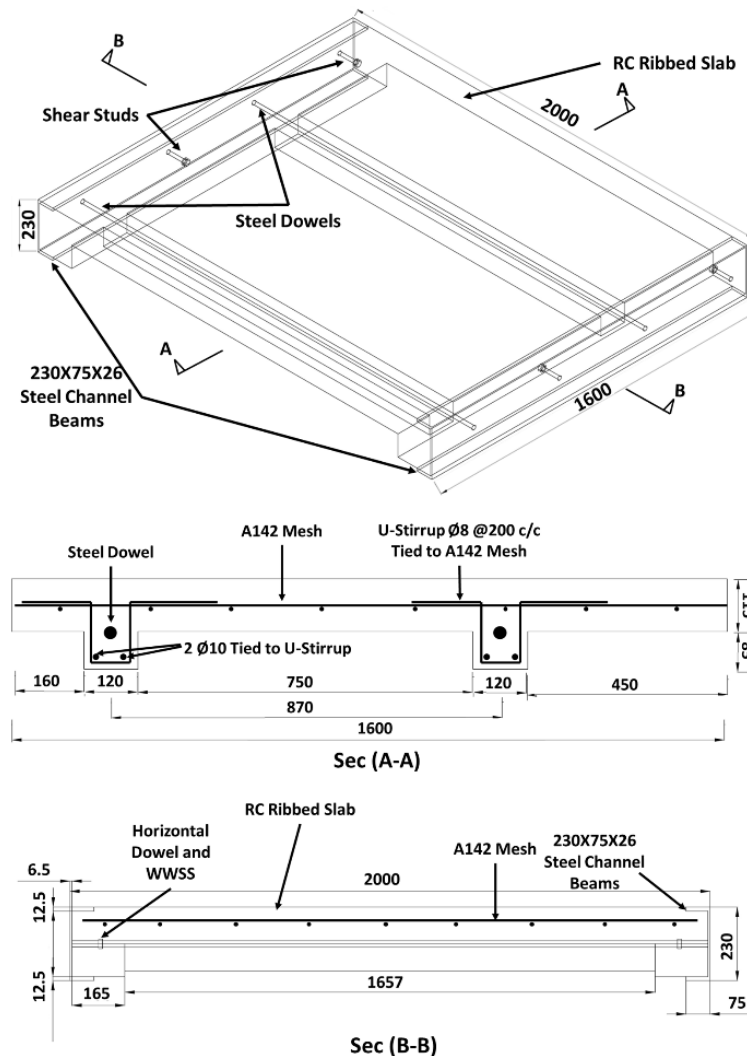


Figure 2-14: Schematic drawing of a 1.6m segment of a standard PUSS flooring unit with steel dowel and WWSS shear connection system (Alali and Tsavdaridis, 2021)

Previous studies of PUSS have emphasised its advantages, highlighting its light weight, which is a result of the use of lightweight concrete along with troughs and ribs running below the thin concrete flange. That facilitates the construction of lightweight buildings, as slabs contribute significantly to the overall weight of the structures. In addition, the slabs' shape, characterised by regular voids underneath the ribbed slab permits the integration of building services and ceiling fixtures, thereby reducing the overall building height. Alternatively, the voids can accommodate the placement of acoustic insulation materials (Ahmed, 2019).

Furthermore, the outcomes of the previous Life Cycle Assessment (LCA) and Life Cycle Cost (LCC) studies conducted on the flooring system demonstrated some advantages of PUSS made of lightweight aggregate concrete (LWC) with Lytag in comparison to precast hollow core and the Cofradal slabs (ArcelorMittal, 2019),

indicating a considerable decrease in the overall Global Warming Potential (GWP), energy consumption, time and cost. Moreover, the implementation of wider units made of lightweight materials reduces the number of necessary lifts during slabs installation, the overall transportation cost, construction time and energy consumption. In addition, the well-monitored and controlled prefabrication offsite significantly reduces the required on-site work, which usually causes construction errors and tends to be more costly compared to offsite work (Ahmed and Tsavdaridis, 2018).

Additionally, the performance of shear connection system employed in PUSS flooring system was previously examined under direct static shear force using the push-out test methodology. The research included experimental tests and numerical finite element parametric study. The investigations incorporated three concrete types: normal weight concrete (NWC), lightweight aggregate concrete with Lytag aggregates (LWC), and ultra-lightweight aggregate concrete with Leca aggregates made of expanded clay (ULWC).

The findings of the research stated that both shear connection systems showed ductile failure behaviour, however, the WWSS with dowels system showed more ductile failure mode and showed an interlocking mechanism and strong tie between the concrete and the horizontal dowels together with the shear studs. That makes the WWSS with dowels system preferred over the WWSS system in regions with high shear. Also, it has been found that there is a great relation between the shear strength of the shear studs and dowels with the ultimate strength of concrete and the diameter of the shear connectors. The results indicate that the shear strength increases as the concrete strength increases, which reduces the feasibility of using ULWC in such a shear connection system unless its compressive strength is enhanced by the used some admixtures and additives. Also, it was found that the shear strength increases as the height of the shear studs and the diameter of the shear studs or dowels increases due to the increase of the shear connection area.

As a result of the push-out tests observations, a formula was developed to predict the shear resistance of the shear connection system (Equation 2-4) (Ahmed and Tsavdaridis, 2020).

Equation 2-4

$$P_{sd} = 1.873(f_{ck}da_r)^{0.835} \leq 0.8f_uA_s$$

Where: P_{sd} is the shear resistance of shear stud or dowel,
 f_{ck} is the cylinder compressive strength of concrete,
 d is the diameter of stud or dowel,
 a_r is the distance from first stud or dowel to the top of concrete,
 f_u is the ultimate tensile strength of the material of the stud or dowel
 which should not be greater than 500 N/mm^2 ,
 and A_s is the cross-sectional area of the shear stud or dowel.

From the final outcomes of the performed research, some recommendations are going to be considered in this research. It was recommended that the WWSS shear connection system should be used only in regions with low shear, while the WWSS with dowels system should be used in regions with high shear. That is because of the more ductile failure and the high shear resistance and tying resistance shown by the WWSS with dowels system. In addition, although that the ultra-lightweight concrete (contains Leca aggregates) significantly reduces the unit weight of concrete, its low compressive strength weakens the shear strength capacity and therefore it is not recommended to use it with this system unless its strength is enhanced by the use of additives and admixtures. It was also recommended to continue the research on the shear connection system by testing the slab units under static flexural tests to develop design methodologies of the PUSS units and that is what is going to be studied in this research (Ahmed, 2019). Figure 2-15 displays a grid of PUSS flooring system composed of five PUSS units, sitting on the bottom flange of the composite beams, and within their depth.

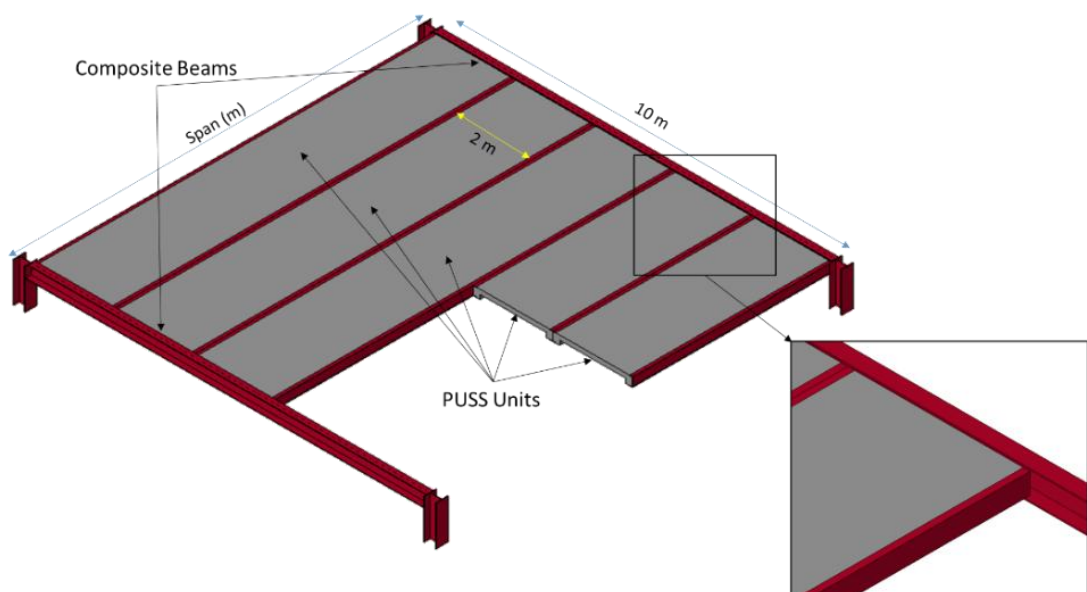


Figure 2-15: Grid of PUSS flooring system

2.6.2 Hollow Core Slabs

Hollow core slabs have been widely used in flooring and roofing applications since the 1950s. They are favoured for their nearly fully automated production process, which optimises material use, saves time, and offers environmental benefits. Compared to solid concrete, hollow core slabs can save up to 50% in concrete usage and 30% in steel consumption (International Federation for Structural Concrete (*fib*), 2000).

Typically produced from reinforced concrete, hollow core slabs feature longitudinal voids that reduce their overall weight and cost. Their depths generally range from 150 to 450 mm, depending on the required span and load-bearing capacity, with spans of up to 20 metres for high-depth, low-load applications (Way et al., 2007). Figure 2-16 shows typical hollow core slab units and their cross-sections.

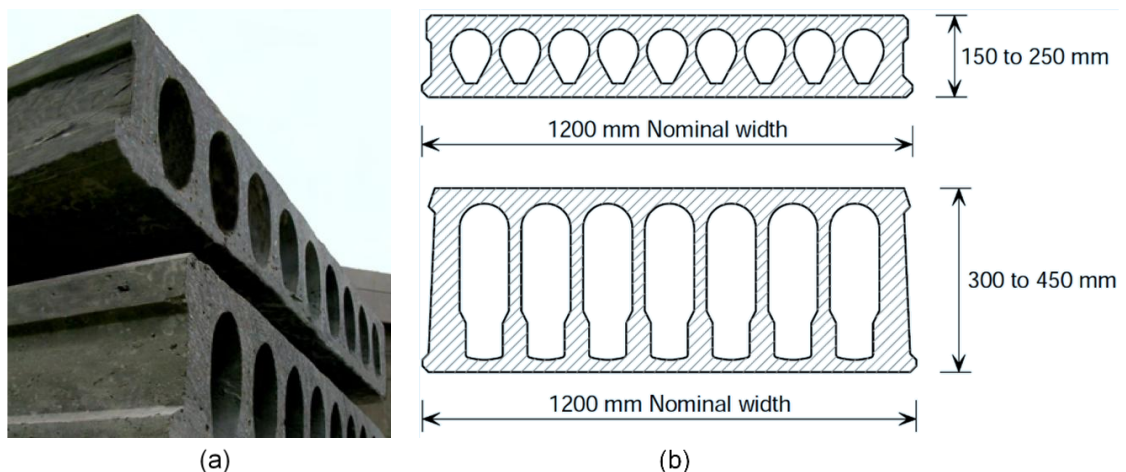


Figure 2-16: (a) Hollow core floor units (b) Typical cross-sections for floor units (Way et al., 2007)

Precast hollow core concrete units have fire resistance of 1 to 2 hours and good in insulating sounds. They come in different shapes of voids and the units can be manufactured in a variety of shapes and sizes to suit the requirements of the construction site. Casting complex shapes to match architectural needs might require difficult preparation of forms on-site with big chances of errors, fabricating and pre-casting such units offsite under factory controlled conditions is more economic and has more accuracy with much less chances of error (Way et al., 2007). After installation, a 50 to 75 mm concrete topping is often applied on-site to create a level surface, which adds weight but can enhance the mechanical properties of the slab (Mones and Breña, 2013). However, the 1200 mm width of

hollow core slabs limits their span to about 10 metres for slabs with a thickness of less than 300 mm under medium service loads (Longley, 2019).

Hollow-core precast slabs have been used widely as a part of composite flooring systems presented in section 2.5. A lot of research and studies have been done to investigate the benefits and the properties of the precast hollow core slabs in all aspects. The following papers represent some of the previously done works that have studied topics like economic and environmental benefits, shear strength, flexural strength, etc.

Yee (2001a) outlined the environmental and social benefits of precast concrete technology, noting that the benefits extend beyond cost and structural efficiency. One key advantage is the reduction in transport needs for materials and workers, leading to lower emissions and reduced strain on transportation networks. Precast units also contribute to tidier and safer construction sites, with reduced noise and air pollution, which can improve conditions for nearby residents and workers. Additionally, precast technology minimises the need for formwork on-site, particularly in congested urban areas, and enables more efficient production under controlled factory conditions. The durable steel or fibreglass moulds used in precast production can be reused multiple times, reducing material waste compared to the timber formwork typically used in on-site construction.

In a follow-up study, Yee (2001b) highlighted the structural and economic advantages of precast concrete, including significant material savings in both steel and concrete for long-span and high-load structures. The mass production of precast units, combined with the reduced need for on-site labour, further contributes to overall cost savings. Additionally, precast units serve as formwork for composite slab and beam connections, streamlining the construction process. Although the initial cost of formwork for precast production may be higher than traditional on-site formwork, the long-term savings from reusing durable moulds offset these initial costs.

Hawkins and Ghosh (2006) investigated the shear strength of hollow core precast slabs, particularly those with depths greater than 320 mm. Since shear reinforcement is not feasible in such slabs, shear strength depends entirely on the concrete's capacity. Their study presented results from shear strength tests conducted by three U.S. companies and a European research program. The findings revealed that the shear strength of deep hollow core slabs was

sometimes lower than predicted by ACI 318-05 equations. The European tests suggested that hollow core slabs up to 410 mm in depth may require adjusted critical section locations to better evaluate web-shear strength, while the American tests indicated that further research is needed before modifying the design code.

Rahman et al. (2012) conducted four-point bending tests on 15 precast hollow core slab specimens, with depths ranging from 200 to 300 mm and spans of either 2.5 m or 5 m. The study aimed to determine the ultimate load capacity and failure modes of the slabs, correlating these findings with the span-to-depth ratio. Three distinct failure modes were identified: pure flexural failure (for span-to-depth ratios >9), flexure-shear failure (span-to-depth ratios between 3.5 and 9), and web shear failure (span-to-depth ratios <3.5). While the ACI equations accurately predicted web shear failure for ratios <3.5 , they underestimated flexure-shear strength for ratios between 3.5 and 8, and predicted flexure-shear failure where pure flexural failure occurred experimentally (ratios >9).

Zhang et al. (2022) investigated the flexural performance of precast hollow-core (PHC) slabs using high-strength tendons. The study aimed to assess a novel spliced connection method that uses U-shaped steel bars, anchorage bars, and post-cast concrete. Three full-scale specimens were tested: one long slab and two specimens where two shorter slabs were connected to replicate the same total length. Load-displacement responses, failure modes, and strain distributions were analysed. The spliced slabs demonstrated comparable flexural strength and ductility to the long slab, confirming the feasibility of the splicing technique. However, the study highlighted discrepancies in predictions by existing design codes, which overestimated the slabs' flexural capacity. This discrepancy suggests the necessity for refining current code provisions to enhance safety and reliability.

These studies underline the importance of hollow core slabs in structural design due to their material efficiency and structural performance, while also highlighting the need for ongoing research to refine design codes, particularly in relation to deep slabs and shear capacity.

2.6.3 Modular Steel Channel–Concrete Composite Flooring System (MSCCF)

A novel prefabricated flooring system, the Modular Steel Channel–Concrete Composite Floor (MSCCF), has recently been developed by a group of researchers in China to enhance structural performance and accelerate construction for modular and long-span floors. The MSCCF system shares conceptual similarities with the PUSS flooring system, particularly in terms of placing concrete slab between parallel C-channel steel beams to form the structural edge of each slab unit. However, MSCCF is distinguished by employing perforated steel plates (PSPs) as shear connectors. Once placed at the intended flooring location on construction site, adjacent slab modules are connected using high-strength bolts passing through the webs of the channels. This interconnection transforms the back-to-back C-channels into a composite beam system termed the Double C-Channel Beam (DCCB). Figure 2-17 provides a visual representation of the mentioned flooring system. The MSCCF system was designed to eliminate the need for in-situ wet work, thereby significantly improving construction speed and reliability, especially in modular buildings. Its design also aims to provide a highly integrated structural system with robust mechanical performance and efficient load transfer. To evaluate its viability, Fang et al. (2023; 2024a; 2024b) conducted extensive experimental and numerical investigations that addressed various aspects of its flexural behaviour, the performance of PSP shear connectors, and the influence of mechanical interconnection.

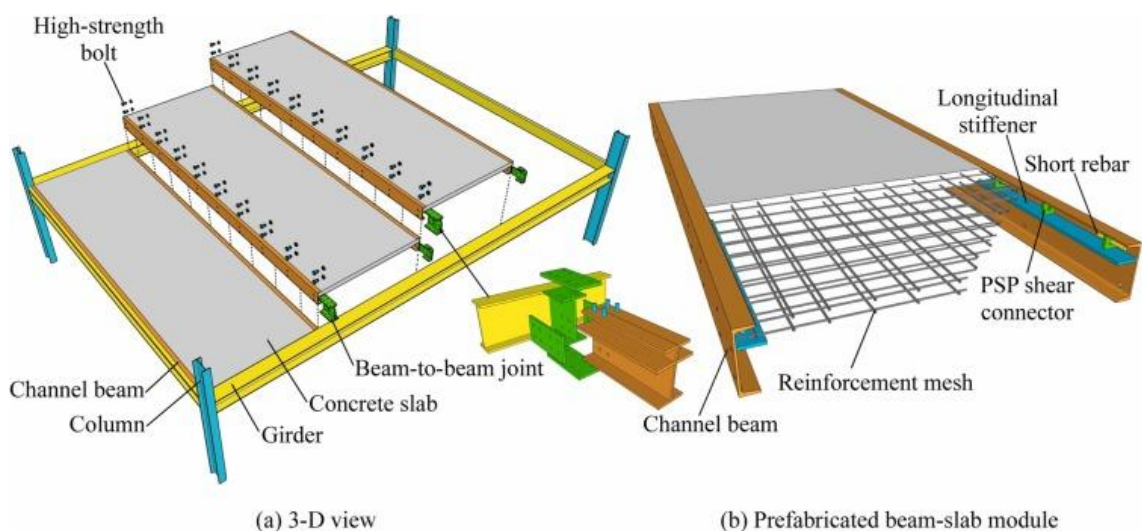


Figure 2-17: Schematic drawings of modular steel channel–concrete composite flooring system (MSCCF) (Fang et al., 2024b)

Fang et al. (2023) tested seven specimens under bending loads to assess the impact of parameters such as slab width, beam depth, and shear connector spacing. Their findings confirmed that the system, when assembled using dry construction methods, offers high efficiency in terms of both structural performance and rapid assembly. The use of high-strength bolts ensured integrity and cooperation between the modules, achieving high flexural stiffness, sufficient ductility, and excellent load-carrying capacity. Notably, the ductility index of the beam was approximately 6.5, with mid-span deflections between $1/444$ and $1/333$ of the span under serviceability loads—well within the acceptable limits defined in AS 2327.1. The PSP connectors were shown to provide robust composite action, with the mechanical behaviour of partially connected beams closely mirroring those of fully connected ones, with less than 10% variation in strength, stiffness, and ductility. However, while increasing slab width marginally improved bending performance, it significantly weakened overall integrity due to increased separation between modules. Increasing beam depth enhanced strength and integrity but reduced ductility.

Further experimental work by Fang et al. (2024b) explored the bending behaviour of complete MSCCF floor systems. Four specimens were tested under different boundary and shear connection conditions. The results demonstrated that bolted connections were instrumental in enhancing both structural integrity and torsional stability. Floors with bolted interconnections resisted lateral-torsional buckling more effectively, with an increase in initial torsional stiffness by up to 144% compared to unbolted floors. Additionally, the bolted systems experienced a change in failure mode—from pure flexural failure in simply supported specimens to punching shear-flexural failure in semi-continuous configurations. The presence of bolts also led to notable gains in overall system stiffness (58%) and ultimate bearing capacity (15%), albeit with a 23% reduction in ductility. While reducing bolt spacing enhanced initial stiffness, it had a minimal effect on strength or ductility. Importantly, PSP connectors remained effective under all tested conditions, even in partially connected configurations.

Complementing these structural investigations, Fang et al. (2024a) conducted a dedicated study on the shear performance of the PSP connectors. A series of 15 push-out tests, combined with validated finite element models, evaluated the influence of variables such as PSP thickness, opening diameter, concrete

strength, and connector spacing. Two main failure modes were observed: PSP failure (typically flexural-shear or fracture at thin sections) and concrete crushing (more prevalent in thicker PSPs or weaker concretes). While all PSP configurations provided high shear stiffness and capacity, only those with thicknesses up to 6 mm showed adequate ductility as defined by Eurocode 4. Increasing PSP thickness improved strength but reduced ductility, with diminishing returns beyond 10 mm. Larger openings in the PSPs enhanced ductility but reduced stiffness and capacity. Similarly, closely spaced PSPs (150 mm) experienced overlapping stress fields that reduced effectiveness compared to single-row configurations. The researchers also derived a shear capacity equation based on both experimental and numerical data, accounting for interaction between concrete and steel. This equation was shown to be accurate and suitable for preliminary design.

In summary, the research on the MSCCF flooring system demonstrated that it is a structurally sound and efficient prefabricated solution for modular buildings, which make it a promising prefabricated flooring solution with potential applications in modular, high-performance, and rapid-construction buildings.

2.6.4 Real-Life Applications of Composite Prefabricated Slabs

The composite prefabricated flooring systems discussed in the preceding sections, including the Prefabricated Ultra-Shallow Slab (PUSS), and the Modular Steel Channel–Concrete Composite Floor (MSCCF), demonstrate a broad range of real-life applications that align with current construction trends, particularly in modular, sustainable, and high-performance building design.

These systems are especially well-suited for use in modular construction due to their offsite fabrication and readiness for immediate installation upon arrival at the construction site. The units are typically transported in a near-finished form and placed directly onto supporting beams without requiring significant on-site adjustment or additional formwork. This minimises construction time and labour demands, reduces disruption in urban environments, and enables faster project delivery schedules. They are also designed to eliminate the need for an in-situ concrete topping altogether, enabling truly dry assembly processes. This is particularly advantageous in reducing construction time and in regions with limited access to wet construction resources. The modular nature of these systems also facilitates integration into volumetric modular buildings, where each

room or unit is fabricated offsite as a complete module. In such applications, the floor system forms an integral part of the volumetric unit and the abovementioned systems can be part of it.

Beyond their role as floor components, the structural detailing and experimental work conducted on the shear connectors used in systems like PUSS and MSCCF carry broader implications. These investigations not only advance the understanding of shear transfer mechanisms in shallow and modular floors but also contribute to the design of shear connectors in composite beam-slab systems used across multi-storey commercial and residential buildings. The findings related to ductility, ultimate strength, and load-slip behaviour of horizontally oriented and perforated shear connectors can be extended to the development of enhanced composite action in steel-concrete hybrid structures.

Additionally, the integration of embedded voids, ducts, or troughs within the slab cross-sections, such as in PUSS and hollow core slabs, allows for the routing of mechanical, electrical, and plumbing services within the floor zone. This functional integration supports more compact and architecturally flexible building designs, reduces floor-to-floor height, and supports the use of prefabricated service modules. Such features are highly valued in modern office buildings, airports, hotels, and high-rise housing.

Lastly, the improved environmental and economic performance of these flooring systems, as evidenced by previous LCA and LCC studies on some of them, makes them appealing options for eco-friendly developments and public infrastructure projects where sustainability, lifecycle cost, and carbon footprint are key concerns. Their potential to reduce construction waste, transport requirements, and operational energy usage further enhances their applicability in environmentally regulated construction sectors.

2.7 Code of Practice

Eurocode 4 (European Committee for Standardization (CEN), 2004b) defines composite beam as "a composite member subjected mainly to bending" while it defines composite slab as "a slab in which profiled steel sheets are used initially as permanent shuttering and subsequently combine structurally with the hardened concrete and act as tensile reinforcement in the finished floor". In this research, although we are examining composite slab units, their way of

construction and load application is more related to the composite beams defined in Eurocode 4 because they are mainly subjected to bending and do not have steel sheets.

Eurocode 4 (CEN, 2004b) serves as the principal design standard adopted throughout this thesis, as it provides a comprehensive and widely recognised framework for the structural design of composite steel–concrete members within the European context. Its provisions for flexural resistance, partial shear connection, and shear connector behaviour are particularly relevant to the PUSS flooring system investigated in this study. In addition to Eurocode 4, equations from ANSI/AISC 360-10 (2010) and AASHTO (2020) are also introduced—specifically for evaluating the shear resistance of headed shear studs. These two codes were selected for their international significance and practical relevance in steel–concrete composite construction, offering alternative approaches for assessing connector behaviour under varying assumptions. Including these standards allows for a broader comparative assessment of shear connector performance when implemented in PUSS slabs. This, in turn, enables identification of the most appropriate predictive model for the system and supports the development of a tailored empirical equation reflecting the actual performance observed in the experimental and numerical studies.

2.7.1 Resistances of Cross-Section of Composite Beams

Bending Resistance: Eurocode 4 (CEN, 2004b) determines the plastic resistance moment of a composite cross-section at ultimate limit states by using stress block method, which assumes that the stresses within the cross-section reach a constant value in both tension and compression. The code specifies some assumptions that should be made in applying the stress block method:

- The structural steel is stressed to its design yield stress f_{yd} in both tension and compression.
- The effective area of the longitudinal steel reinforcements is stressed to their design yield stress f_{sd} in both tension and compression. Otherwise, the reinforcement in compression in concrete slab may be neglected.
- The concrete tensile strength shall be neglected.
- The effective area of concrete in compression for full shear connection is the area between the depth of the plastic neutral axis (PNA) and the most

compressed fibre of concrete. This area resists a constant concrete compressive stress ($\sigma_{c,Rd}$) of $0.85f_{cd}$ where f_{cd} is the design cylinder compressive strength of concrete.

- For partial shear connection, the effective area of concrete in uniform compression stress is the area from most compressed fibre of concrete to the depth where concrete can develop compressive resistance equal to the longitudinal shear resistance of the shear connectors. The ratio of the reduced area of compression for partial shear connection to the whole area of compression for full shear connection is equal to η which is the degree of shear connection and $\eta = \frac{N_c}{N_{c,f}}$, where N_c is the longitudinal shear resistance of the shear connectors and $N_{c,f}$ is the full compressive resistance of the concrete slab.

The plastic stress distribution of a downstand composite beam with full and partial shear connection is shown in Figure 2-18. In the stress block method, the moment capacity of the cross-section is calculated by taking moments about the plastic neutral axis.

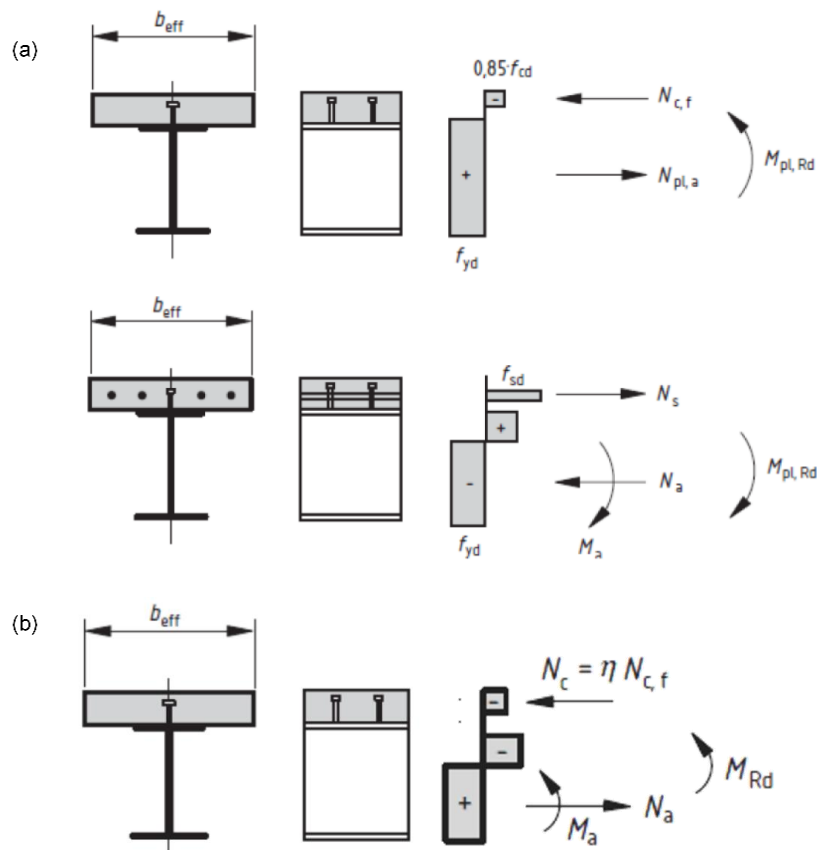


Figure 2-18: (a) Plastic stress distribution of a downstand composite beam with full shear connection in sagging and hogging bending (b) Plastic stress distribution of a downstand composite beam with partial shear connection (CEN, 2004b)

The code also provides a simplified linear interaction method which relates the moment resistance of the cross-section to the degree of shear connection. This simplified linear relationship is expressed in Equation 2-5. Figure 2-19 compares the plots of the increment in the moment resistance as the degree of shear connection increases using the linear interaction and the stress block methods. It is clear from the plots that the linear interactive method gives conservative results.

Equation 2-5

$$M_{Rd} = M_{pl,a,Rd} + (M_{pl,Rd} - M_{pl,a,Rd}) \frac{N_c}{N_{c,f}}$$

Where: M_{Rd} is the design moment resistance of the composite section in partial shear connection,
 $M_{pl,a,Rd}$ is the plastic moment resistance of the steel section,
 $M_{pl,Rd}$ is the design moment resistance of composite section in full shear connection,
 N_c is the longitudinal shear resistance of the shear connectors,
 $N_{c,f}$ is the full compressive resistance of the concrete slab,
and $\frac{N_c}{N_{c,f}} = \eta$ which is the degree of shear connection.

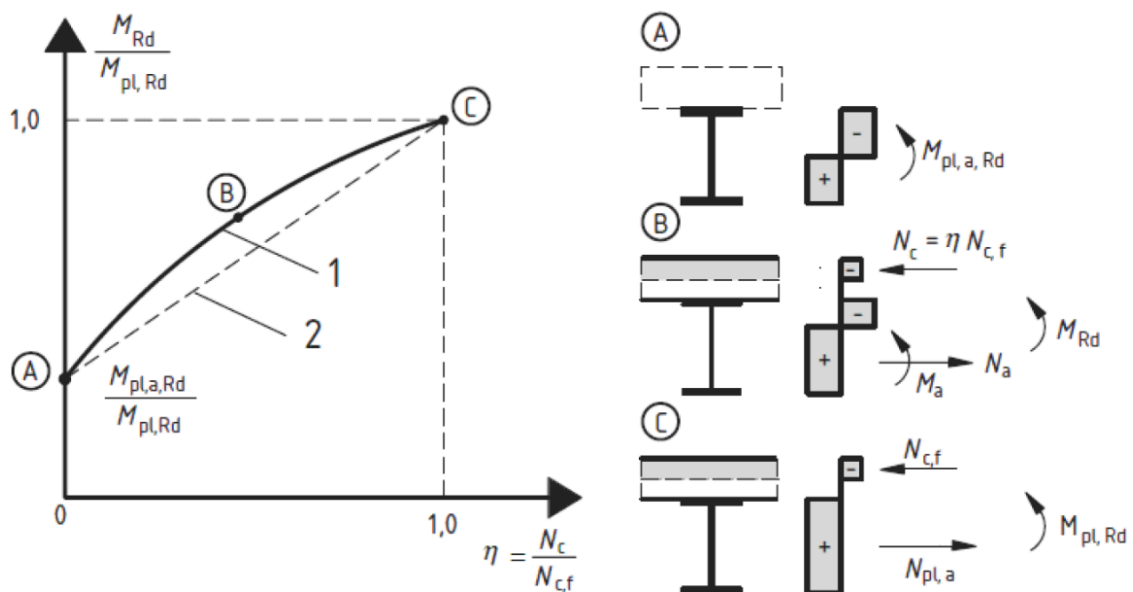


Figure 2-19: Comparison between the plastic stress block method (line 1) and the simplified linear interaction method (line 2) for ductile partial shear connection (CEN, 2004b)

2.7.2 Headed Shear Stud Connection

Eurocode 4 (CEN, 2004b) states that shear connection and transverse shear reinforcement are provided in composite structures to transmit the longitudinal

shear force between structural steel and the concrete, and the effect of natural bond between the two materials is ignored. It also states that the shear connector should be capable of preventing the separation of concrete from structural steel and have sufficient deformation capacity to be ductile connector. A connector is considered ductile if the characteristic slip capacity $\delta_{uk} \geq 6$ mm. Failure and splitting due to longitudinal shear concentrated forces caused by the shear connectors should be prevented. In general, the limitation for the use of partial shear connection for members with span less than 25 m is that the degree of partial shear connection $\eta \geq 0.4$.

The design shear resistance of a welded headed shear stud in solid slab and concrete encasement P_{Rd} should be calculated from Equation 2-6 or Equation 2-7, whichever is smaller.

Equation 2-6

$$P_{Rd} = \frac{0.8f_u\pi d^2/4}{\gamma_V}$$

Equation 2-7

$$P_{Rd} = \frac{0.29\alpha d^2 \sqrt{f_{ck}E_{cm}}}{\gamma_V}$$

Where: γ_V is the partial factor and its recommended value is 1.25,
 f_u is the ultimate tensile strength of the material of the stud, and not larger than 500 N/mm² for studs in solid slab and concrete encasement,
 $\alpha = 0.2 \left(\frac{h_{SC}}{d} + 1 \right)$ for $3 \leq h_{SC}/d \leq 4$ & $\alpha = 1$ for $h_{SC}/d > 4$,
 d is the diameter of the stud,
 h_{SC} is the overall nominal height of the stud,
 f_{ck} is the concrete cylinder compressive strength at the age considered, of density not less than 1750 kg/m³,
and E_{cm} is the secant modulus of concrete.

BS5950-3.1 (British Standards Institution (BSI), 1990) provided specifications for headed shear studs in terms of dimensions and spacing in details. The design shear resistance is also provided with corresponding stud dimensions and normal weight concrete strength, as shown in Table 2-2.

Table 2-2: Characteristic shear resistance of headed shear studs in normal weight concrete (BSI, 1990)

Dimensions of stud shear connectors		Characteristic strength of concrete				
Nominal shank diameter	Nominal height	As-welded height	N/mm ²	N/mm ²	N/mm ²	N/mm ²
			25	30	35	40
mm	mm	mm	kN	kN	kN	kN
25	100	95	146	154	161	168
22	100	95	119	126	132	139
19	100	95	95	100	104	109
19	75	70	82	87	91	96
16	75	70	70	74	78	82
13	65	60	44	47	49	52

NOTE 1 For concrete of characteristic strength greater than 40 N/mm² use the values for 40 N/mm².
NOTE 2 For connectors of heights greater than tabulated use the values for the greatest height tabulated.

The American Institute of Steel Construction (ANSI/AISC 360-10 (2010)) also provides a formula for calculating the nominal shear strength of headed shear studs P_s that is a function of the stud cross-sectional area A_s in mm², the concrete characteristic cylinder compressive strength f_{ck} in MPa and the elastic modulus of concrete E_c in MPa, as given in Equation 2-8. Where f_u is the ultimate strength of the shear stud steel in MPa (but not greater than 500 N/mm²), R_g and R_p are factors depending on the studs and welding arrangement and their multiplication value can be assumed to be 0.75. The shear strength obtained according to AISC is usually higher than that of Eurocode 4.

Equation 2-8

$$P_s = 0.5A_s\sqrt{f_{ck}E_c} \leq R_gR_pA_sf_u$$

The American Association of State Highway and Transportation Officials (AASHTO (2020)) also provides a formula for determining the nominal shear strength of headed shear studs P_s . The formula closely resembles that of ANSI/AISC 360-10, with the inclusion of a resistance factor (ϕ) for shear connectors, typically taken as 0.85. The AASHTO equation is presented in Equation 2-9.

Equation 2-9

$$P_s = \phi 0.5A_s\sqrt{f_{ck}E_c} \leq 0.75f_uA_s$$

Eurocode 4 (CEN, 2005) Annex C provides the equations for designing the shear resistance of horizontal lying headed shear studs that causes splitting in the direction of the slab thickness as shown in Figure 2-20.

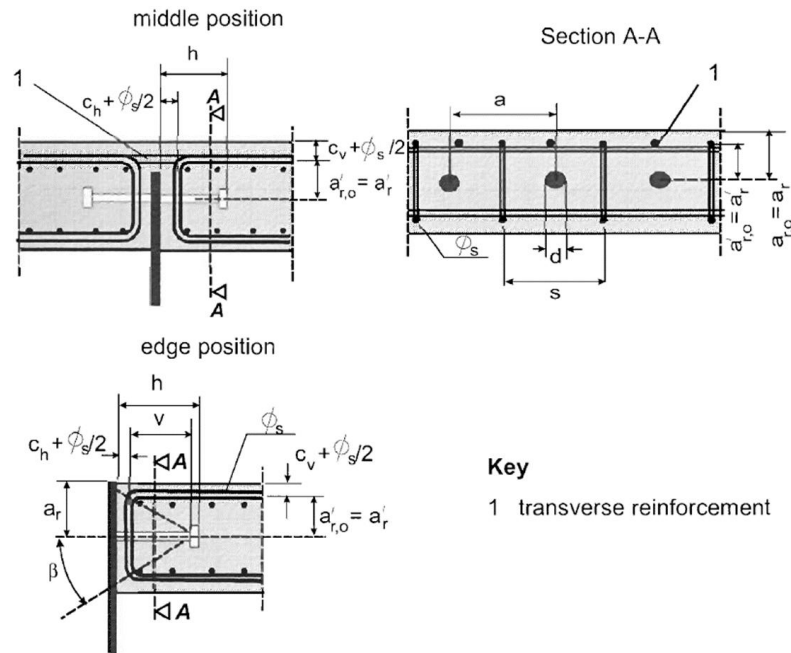


Figure 2-20: Position and geometrical parameters of horizontally lying shear stud connections (CEN, 2005)

That shear resistance should be determined for ultimate limit states other than fatigue by using Equation 2-10.

Equation 2-10

$$P_{RD,L} = \frac{1.4k_V(f_{ck}da'_r)^{0.4}(a/s)^{0.3}}{\gamma_V}$$

Where: $k_V = 1$ for shear connection in edge position and $k_V = 1.14$ for middle position,

f_{ck} is the characteristic concrete cylinder compressive strength at the age considered in N/mm^2 ,

d is the diameter of the shank of the stud within $19 \leq d \leq 25$ mm,

a'_r is the effective edge distance $= a_r - c_v - \phi_s/2 \geq 50$ mm,

a is the horizontal spacing of studs within $110 \leq a \leq 440$ mm,

s is the spacing of stirrups with both $a/2 \leq s \leq a$ and $s/a'_r \leq 3$,

γ_V is a partial factor and its recommended value is 1.25,

a_r is the vertical distance from the edge of the slab to the centre of the stud,

c_v is the vertical concrete cover,

and ϕ_s is the diameter of the stirrups with $\phi_s \geq 8$ mm.

Eurocode 4 (CEN, 2005) Annex C states that to prevent the failure by pull-out of the stud at the edge of the slab, the following conditions should be fulfilled:

For uncracked concrete: $\beta \leq 30^\circ$ or $v \geq \max(110 \text{ mm}; 1.7a'_{r}; 1.7s/2)$

For cracked concrete: $\beta \leq 23^\circ$ or $v \geq \max(160 \text{ mm}; 2.4a'_{r}; 2.4s/2)$

Also, it states that the splitting force in the direction of the slab thickness should be resisted by stirrups, which should be designed for tensile force T_d according to Equation 2-11.

Equation 2-11

$$T_d = 0.3P_{Rd,L}$$

The influence of the vertical shear on the design resistance of stud connectors due to vertical support should also be considered. The interaction may be verified by using Equation 2-12.

Equation 2-12

$$\left(\frac{F_{d,L}}{P_{Rd,L}}\right)^{1.2} + \left(\frac{F_{d,V}}{P_{Rd,V}}\right)^{1.2} \leq 1$$

where $P_{Rd,V}$ is calculated using Equation 2-13.

Equation 2-13

$$P_{Rd,V} = \frac{0.12(f_{ck}\phi_l)^{0.5} \left(d\frac{a}{s}\right)^{0.4} (\phi_s)^{0.3} (a'_{r,o})^{0.7} k_V}{\gamma_V} \text{ [kN]}$$

with the following conditions satisfied:

$$h \geq 100\text{mm}; 110 \leq a \leq 250\text{mm}; \phi_s \leq 12\text{mm}; \phi_l \leq 16\text{mm}.$$

Where: ϕ_l is the diameter of the longitudinal reinforcement with $\phi_l \geq 10\text{mm}$,
 d is the diameter of the shank of the stud within $19 \leq d \leq 25 \text{ mm}$,
 $a'_{r,o}$ is the relative effective edge distance = $a_{r,o} - c_V - \phi_s/2 \geq 50 \text{ mm}$,
 h is the overall height of the headed stud with $h/d \geq 4$,
and $a_{r,o}$ is the relative vertical distance from the slab edge to the centre of the stud.

2.7.3 Testing of Composite Floor Slabs

Eurocode 4 (CEN, 2004b) Annex B gives the detailed test procedure to determine the shear-bond behaviour of composite slabs with profiled steel sheets through

the $m - k$ and the partial shear connection methods. Similar test setup can be applied in testing PUSS units in bending. The standard test set-up for composite slabs is shown in Figure 2-21.

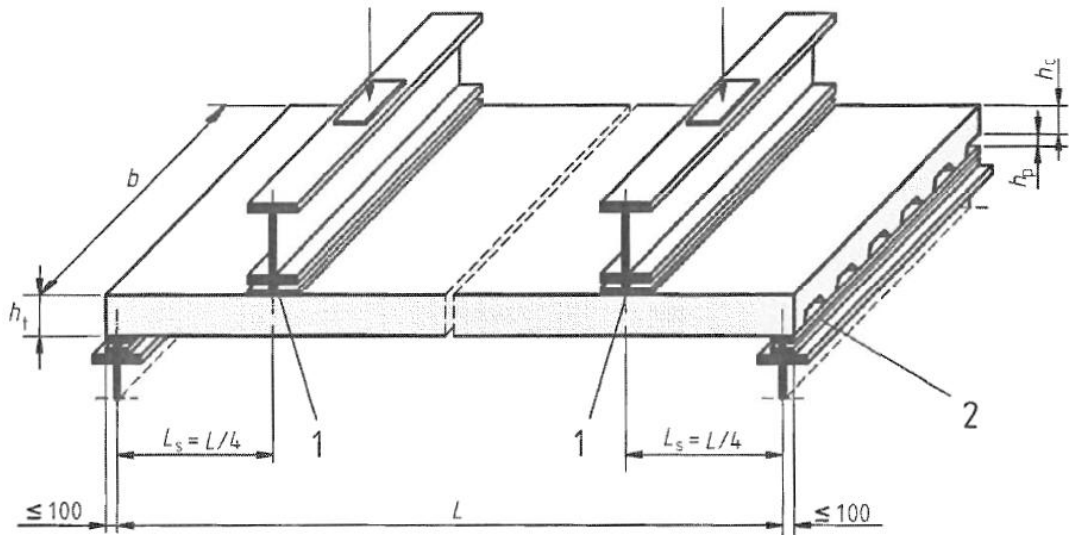


Figure 2-21: Four-point bending test setup (CEN, 2004b)

The $m - k$ method is used to determine m and k factors for the composite slab by full-scale four-point bending tests on a total of six specimens divided into two groups, group A with three maximum possible span specimens and group B with three shortest possible span specimens with assuring longitudinal shear failure for both groups. The m and k parameters are determined by plotting graph of $\frac{V_t}{bd_p}$ versus $\frac{A_p}{bL_s}$. A point is plotted from each specimen and a straight line is drawn to connect these points and a plot similar to the plot in Figure 2-22 will be produced. From that plot, m and k factors are determined and that is given by Equation 2-14

Equation 2-14

$$\frac{V_t}{bd_p} = m \left(\frac{A_p}{bL_s} \right) + k$$

Where: V_t is the support reaction under the ultimate test load which is taken to be 0.5 times the failure load for ductile failure and 0.4 time the failure load for brittle failure,
 b is the width of the slab,
 d_p is the depth of the mid-axis on the profiled sheeting from top of the slab,
 A_p is the cross-sectional area of the profiled sheeting,
and L_s is the shear span.

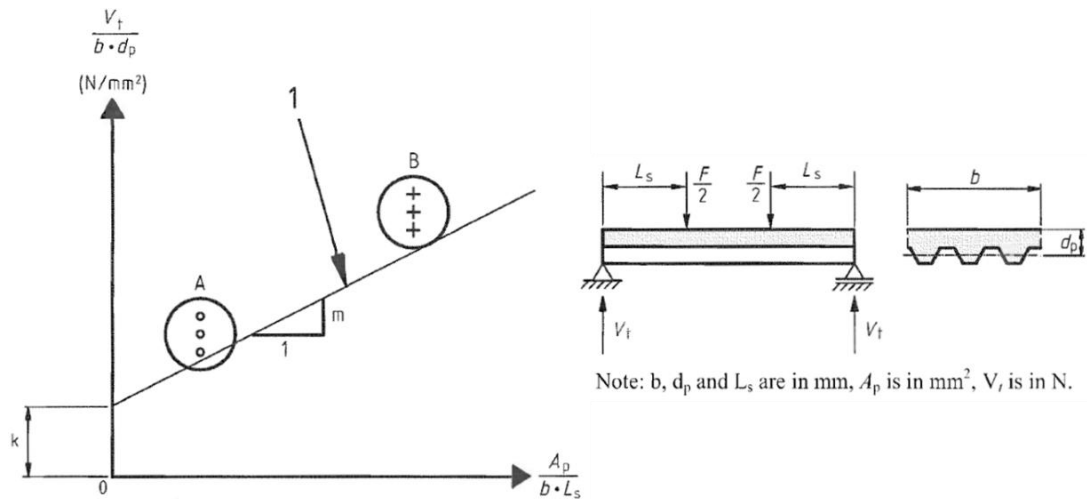


Figure 2-22: Design relationship for longitudinal shear resistance of the composite floor slab (CEN, 2004b)

The partial shear connection method is done by performing four-point bending tests to determine the design value of the longitudinal shear strength of the composite slab $\tau_{u,Rd}$. The partial connection method is more straightforward than the $m-k$ method and it verifies the bending strength of ductile slabs with ductile connections. In this method, the longitudinal shear failure should be assured in 3 slabs with the maximum possible span and 1 slab with the shortest possible span. A graph that relates the bending moment strength with the degree of the shear connection of the slab will be produced at the end of the experimental work as shown in Figure 2-23. From this plot, the degree of shear connection η can be found. The longitudinal shear strength τ_u is related to the ultimate shear stress and can be calculated using Equation 2-15.

Equation 2-15

$$\tau_u = \frac{\eta N_{c,f} - \mu V_t}{b(L_s + L_o)}$$

Where: η is the degree of shear connection from the experiment,
 $N_{c,f}$ is the compressive normal force in concrete,
 μ is the default value of the friction coefficient to be taken as 0,5,
 V_t is the support reaction under the ultimate test load,
 b is the width of the slab,
 L_s is the shear span,
and L_o is the overhang span.

This equation takes into account the additional longitudinal shear resistance produced by the support reaction by the term μV_t . If this resistance is neglected, then this term can be removed.

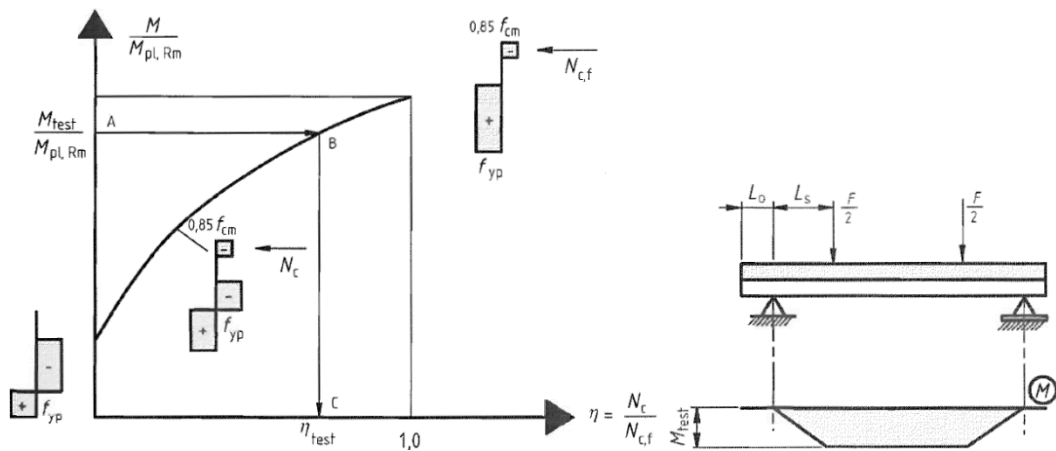


Figure 2-23: Determination of the degree of shear connection from bending moment test (CEN, 2004b)

2.8 Experimental Work on Headed Shear Studs Connections

Various types of shear connectors have been used to transfer the longitudinal shear forces between concrete and steel in SCC beams and slabs, and form the composite action. However, Headed shear studs are the most common type of shear connection used in both bridge and building construction. The current codes of practice provide detailed specifications on their use and design, and that is discussed in section 2.7.2. This section reviews some of the publications that experimentally investigated headed shear studs connectors in solid slabs, profiled decking slabs, the use with lightweight concrete and horizontally lying shear studs. Other experimental tests on other types of shear connectors in different types of composite beams were previously presented in section 2.5.

2.8.1 Headed Studs Used in Solid Slabs

Slutter and Driscoll (1965) carried out nine push-out tests using solid slabs, 12 composite beam tests with 4.5 m span composite beams and one two-span continuous beam test. The conclusions showed that the ultimate flexural strength of the beam is related to the ultimate strength of the stud shear connection, and that the stud's diameter d_s and the concrete cylinder compressive strength f'_c directly govern the ultimate strength of the stud q_u as:

Equation 2-16

$$q_u = 930d_s^2\sqrt{f'_c}$$

Davies (1967) studied the spacing and layout pattern of the studs by conducting 20 small-scale push-out tests using solid slabs. The studs were 10 mm in diameter and 50 mm in height. The results demonstrated that placing two studs per flange perpendicular to the direction of load provides 25% higher failure load than if placed parallel to the direction of load. In addition, it was concluded that the ultimate strength of the studs varies linearly with the longitudinal spacing of the studs.

Johnson et al. (1981) presented statistical analyses of the results of 125 push-out tests from 11 sources with 101 new push-out tests and 4 composite beam tests. The analyses concluded that the strength of studs in push-out tests is strongly influenced by the width of the slabs with little scatter found in the results due to experimental error. One of the parameters studied in the new push-out tests is the height of the weld collar. The results showed that the failure strength of a stud increases continuously as the height of weld collar increases from 0 to $0.35d_s$. The main conclusion is that the stiffness and strength of studs are highest when shank failure occurs. It was also found that it is possible to base the spacing of studs on shank failure loads whenever sufficient breadth of concrete slab can be provided. The minimum breadth is about twice the longitudinal spacing of the studs. The possibility of transferring the maximum shear flow to the slab without splitting the concrete depends on the layout of the studs. They should be spread as uniformly as practicable over the whole available width of the steel flange, and not located in a single straight line above the web.

2.8.2 Headed Studs Used with Profiled Decking

Grant et al. (1977) performed 17 composite beam bending tests using profiled steel decking with 19 mm diameter studs. The considered variables in the study were the yield strengths of the steel beam, geometry of steel decking and degree of partial shear connection. The specimens had spans of 7.3 m or 9.8 m, with a constant slab solid part thickness of 64 mm. Four points loading tests with monotonic load was applied up to the estimated working load, and then cycled 10 times. The results were analysed and compared with 58 additional tests conducted by other researchers that studied variables such as strength and weight of concrete, height and diameter of studs, reinforcements type and loading type. As a conclusion, flexural capacity of a composite beam with profiled steel decking appeared to be more accurately and conservatively estimated if the slab

force is considered to act at the mid-depth of the solid portion above the ribs, rather than at the centroid of the concrete stress block. An equation for the capacity of studs in the ribs of composite beams with profiled steel decking Q_{rib} was developed (Equation 2-17) that is function of the number of studs in the rib N , the heights of the studs and the rib, H and h respectively, and the average rib width W . Where Q_{sol} is the strength of the stud in a flat soffit slab.

Equation 2-17

$$Q_{rib} = \frac{0.85}{\sqrt{N}} \left(\frac{H-h}{h} \right) \left(\frac{W}{h} \right) Q_{sol} \leq Q_{sol}$$

Easterling et al. (1993) indicated that one of the important parameters found from previous studies that controls the shear strength of studs is the position of the studs relative to the stiffener in the bottom flange of the deck. This research project was conducted to evaluate the strong vs. weak stud position issue. Four composite beam tests and eight push-out tests were carried out. All composite beam specimens were with a span of 9.1 m and a width of 2 m with a total of twelve 19 mm diameter studs. The difference between specimens was the position of the studs. The push-out test specimens were constructed using the same deck and studs used in the beam tests. In four specimens, the studs were in the strong position (at the end of the rib in the opposite direction of the force) and in four specimens the studs were placed in the weak position (at the beginning of the rib in the opposite direction of the force). The results showed distinctively different behaviours of the studs in the strong and weak positions. The failure modes of the strong position studs showed developing of concrete shear cones or shearing off the shank, while the weak position studs failed by punching through the deck rib but with more ductile behaviour in terms of load vs. slip. However, the results of both types of tests showed that the values calculated using Equation 2-17 are higher than measured values but no modifications were proposed as further evaluation was required.

2.8.3 Headed Studs Used with Lightweight Concrete

Chinn (1965) tested 10 lightweight composite slabs specimens with headed studs of 13, 16, 19 and 22 mm diameters in push-out tests. The used stud lengths were almost four times of their diameters and the flanges of the steel section were greased. The results demonstrated shear failure mode in all the studs, except for 22 mm, which showed slab cracking. As a finding of the study, it was stated that

the ultimate strength of the studs in push-out tests was 18% to 43% higher than their direct shear strength. The conclusion was that the concrete strength has no effect on the ultimate strength of the studs, as shown in developed formula (Equation 2-18), where d is the stud diameter. However, this was disapproved by the conclusions of the later studies, such as the studies presented below.

Equation 2-18

$$Q_u = 39.22d^{1.766}$$

Ollgaard et al. (1971) carried out 48 push-out tests on headed studs of 16 and 19 mm diameter with normal and lightweight concretes. The research studied seven parameters, which are the stud diameter, the number of studs per slab, the compressive and tensile strengths of concrete, the elastic modulus of concrete, the density of concrete, and the type of aggregate. The results of the study showed that the strength of the studs is highly influenced by the concrete compressive strength and elastic modulus, compared to the minimal effects of the tensile strength and density of the concrete. Similar deformation behaviour of studs in both types of concrete were noticed, and the strength of the studs in lightweight concrete was 15% to 25% lower than that in normal concrete. The observed failure modes were: concrete failure, stud shearing and a combination of both. A formula for the ultimate strength of the stud was developed (Equation 2-19), which its simplified formula was adopted by the AISC specifications afterward (Equation 2-8). In addition, a mathematical relation between load and slip of the stud was presented (Equation 2-20), where Q is the load in kip and Δ is the slip in inch.

Equation 2-19

$$Q_u = 1.106A_s f'_c{}^{0.3} E_c{}^{0.44}$$

Equation 2-20

$$Q = Q_u(1 - e^{-18\Delta})^{2/5}$$

Hawkins (1973) performed 47 push-out tests on solid slabs studying the effects of five parameters: the type of steel stud material (cold or hot formed), stud diameter (19 or 22 mm), concrete type (normal or lightweight), concrete strength and the presence of reinforcement. As a result, it was found that the concrete strength is the main factor governing the capacity of the studs for a given slip value with less effects of the steel stud material. Only the ultimate tensile strength of the steel stud was found to be an important property and not its yielding

strength. The remaining variables had less significant influence on the capacity of studs. Four failure modes were observed in the tests: shearing of studs, punch-out of studs, pull-out of studs and the cracking of the unreinforced slab.

Valente and Cruz (2009) performed a total of 21 push-out tests on shear connectors with lightweight concrete. Twelve on headed studs connectors of 19, 22 and 25 mm diameter and nine on Perfobond rib shear connectors. Four parameters were under study, which are the type of shear connector, stud diameter, the number of studs (single or double) and the reinforcement arrangement of the slab. The results indicated that LWC is suitable choice for composite structures with some loss in the load capacity with normal concrete. It was stated that in order to ensure the stud shear failure, LWC with a compressive strength of at least 55MPa to 60MPa should be used. LWC showed ductile behaviour for the headed studs and the double stud shear connector allowed an increase in the slip deformation but showed a decrease in the load capacity of the connector. For the Perfobond rib shear connector, large cracking and crushing in some zones of the concrete slab failure was observed but the rib connector did not show any failure. A very stiff behaviour was also observed at the beginning of the test with ductile failure and a very high load capacity associated with it. As in shear studs connectors, it was also observed that the connector load capacity tends to decrease when LWC is used compared to normal concrete. In general, the measured maximum loads of Perfobond connectors were much higher than shear studs.

2.8.4 Horizontally Lying Headed Shear Studs

Kuhlmann and Breuninger (2002) investigated subjecting horizontally lying studs to longitudinal shear by conducting 50 push-out tests. The studs in the tested specimens were welded on the web post of a composite girder or slim-floor tee sections. The failure mode associated with this lying arrangement was mainly a splitting of the concrete because the splitting action of the tension force creates cracks. Hence, vertical stirrups are used to prevent the concrete from expanding. The results of the research showed that the concrete compressive strength, studs diameter, distance from the studs to the top surface of concrete slab, and the amount and arrangement of reinforcement are the most important parameters in the shear strength of the lying studs. The measured characteristic slip value of the lying studs at failure was 17.4 mm, which is much higher than the minimum

value of 6 mm specified by Eurocode 4 and therefore it is considered as ductile shear connection. As a continuation of the previous studies, Kuhlmann and Kürschner (2006) further investigated the horizontally lying studs by applying vertical shear, a combination of vertical and longitudinal shear, and cyclic longitudinal shear in a total of 19 cyclic push-out tests. The results showed that a higher peak load close to static resistance causes a decrease of fatigue life, and that a rise of concrete strength leads to a slight increase of fatigue life. However, the significant influence of the stirrup diameter could not be demonstrated.

Ahmed (2019) performed a total of 8 push-out shear tests on PUSS units with two parameters including the type of concrete (NWC, LWC or ULWC) and the arrangements of two innovative shear connection systems which are the horizontal lying WWSS and a combination of WWSS with horizontal steel dowels. The study also included FEA parametric study that studied other parameters including the diameter of the studs and dowels (16, 19, 20 and 22 mm), the height of the shear studs (75 and 100 mm) and the compressive strength of concrete. The research findings and the developed shear strength equation (Equation 2-4) were previously presented in section 2.6.1.

2.9 Summary

This chapter provides a comprehensive literature review covering various aspects relevant to the research on Prefabricated Ultra-Shallow Slabs (PUSS). It begins with exploring the role of construction in addressing sustainability challenges. Additionally, it included an in-depth exploration of composite beams and shallow flooring systems, offering a foundation for understanding the structural behaviour of such systems and their associated shear connectors. The review also examined prior experimental studies that investigate the performance of shear connectors, with a particular focus on headed shear studs, and their relevance to the PUSS flooring system.

Sustainability has become a major concern in construction, and this chapter explored how PUSS addresses these issues. The literature on sustainability practices, material selection, and prefabrication emphasised the importance of using lightweight prefabricated systems like PUSS to reduce CO₂ emissions, energy consumption, and construction waste. Life Cycle Assessment (LCA) studies of similar prefabricated systems, including hollow core slabs, demonstrated the potential for significant environmental benefits when adopting

such systems. The sustainability review informed this thesis by identifying key parameters, such as material choices and manufacturing processes, that influence the environmental performance of flooring systems.

A key challenge identified in this review is the scarcity of literature on shear connection systems used in PUSS, particularly those involving horizontally lying studs and steel dowels. However, insights gained from studies of other shear connection systems provide useful guidelines for developing methodologies to test the behaviour of PUSS shear connectors under direct longitudinal shear forces and flexural loads.

The results of previous push-out tests on PUSS have shown that parameters such as the concrete strength, diameter and length of shear connectors, and the location of the connectors significantly influence the composite action and the overall strength of SCC flooring systems. These findings will be critical for analysing the flexural tests conducted in this research.

The information gathered from prior studies of four-point bending tests and other composite beams influenced the design of experimental and numerical investigations in this thesis. Factors such as the strength of concrete, the geometry of the steel beams, and the arrangements of the shear connectors, which have a direct impact on composite action and bending capacity, were considered when designing the experiments and the finite element analysis (FEA) models.

In summary, this research contributes to the limited literature on the novel shear connectors employed in PUSS, as well as the performance of lightweight composite flooring systems under flexural loads. Additionally, the findings from this study may help refine the design provisions of Eurocode 4, offering potential modifications to improve the design methodologies for shallow composite floor systems. The results will also provide essential data for future sustainability assessments, guiding the development of more environmentally friendly flooring systems.

Chapter 3

Life Cycle Assessment (LCA) Study

3.1 Introduction

To quantify the environmental benefits of using PUSS flooring system and to understand if there are any important trade-offs, this chapter presents a comprehensive comparative Life Cycle Assessment (LCA) study of the ecological impacts associated with PUSS flooring and the widely used hollow core slabs at variable live loads, spans, transportation distances and allocation methods. The study compares a total of four distinct slabs used in buildings internal floorings: hollow core precast slabs and three PUSS slabs with different concrete types.

3.2 Methodology

The adopted method for the LCA study is the Cradle-to-Grave approach, using an attributional methodology, to evaluate the global warming potential and embodied energy of the flooring systems in accordance to BS EN 15978 (British Standards Institution (BSI), 2011b). This include the life cycle stages from acquisition of raw materials (module A1), manufacturing of slabs (module A3), transportation (modules A2, A4, C2) and construction (module A5), as well as end-of-life (EOL) stages of the flooring systems, which covers demolition and disposal or recycling (modules C1, C3, C4, D). The listed modules numbers are in accordance with BS EN 15804:2012+A2:2019 (BSI, 2019a) where A1-A3 are product stage modules, A4-A5 are construction stage modules, B1-B7 are use stage modules, C1-C4 are end of life stage modules and D is recycling module as seen in Figure 3-1.

CONSTRUCTION WORKS LIFE CYCLE INFORMATION													SUPPLEMENTARY INFORMATION BEYOND CONSTRUCTION WORKS LIFE CYCLE			
A1 - A3			A4 - A5		B1 - B7							C1 - C4			D	
PRODUCT STAGE			CONSTRUCTION PROCESS STAGE		USE STAGE							END OF LIFE STAGE			BENEFITS AND LOADS BEYOND THE SYSTEM BOUNDARY	
A1	A2	A3	A4	A5	B1	B2	B3	B4	B5	B6	B7	C1	C2	C3	C4	D
Raw material supply	Transport	Manufacturing	Transport	Construction - Installation process	Use	Maintenance	Repair	Replacement	Refurbishment	Operational energy use	Operational water use	Deconstruction demolition	Transport	Waste processing	Disposal	Reuse, recovery, recycling, potential

Figure 3-1: Life cycle stages modules in accordance with BS EN 15804:2012+A2:2019 (BSI, 2019a)

In addition, Figure 3-2 presents a flowchart of the general system boundaries for the whole life (Cradle-to-Grave) of construction projects with modules numbers. The life cycle stages included in the presented LCA study are delimited in the figure with a dashed line, clearly specifying the boundaries of this study.

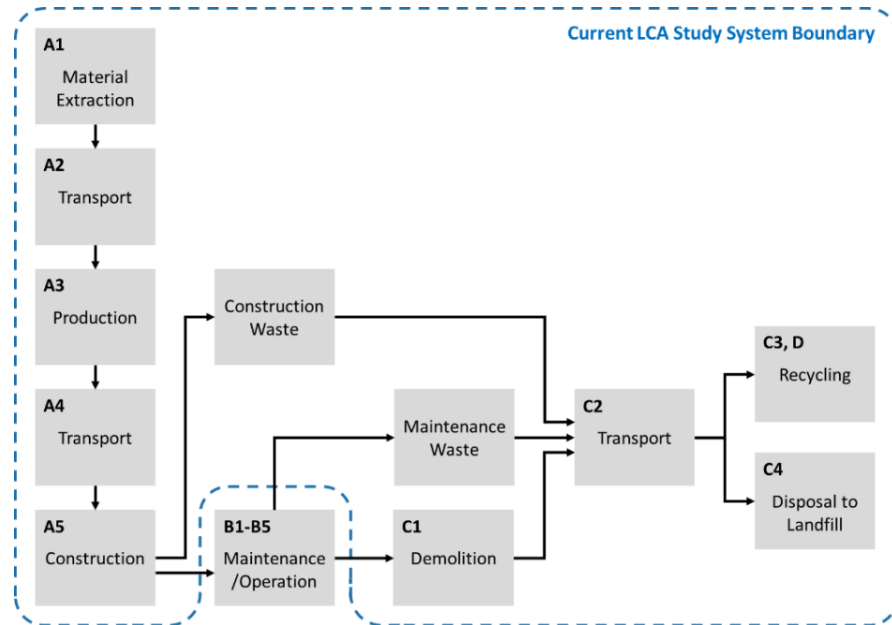


Figure 3-2: LCA general life cycle stages of a structural product with LCA study boundaries

3.3 Comparative Study

The scope of this study is to evaluate the environmental impacts of PUSS flooring system for a selection of live loads/ spans scenarios (total of 16 scenarios, consisting of four slab spans (6, 8, 10 and 12 m) and four live loads (2, 3, 4 and 5 kN/m²), – Table 3-1) and compare the performance with hollow core precast slabs which are the current state-of-art long-span precast flooring system. The selected range of live loads and spans are within practical ranges commonly used for long-span floorings in industry standards for typical applications in residential, office, and commercial buildings. Figure 3-3 presents a flowchart of the LCA model structure applied in this study.

Table 3-1: Live load/ slab span scenarios of the LCA study

		Live Load (kN/m ²)			
		2	3	4	5
Span (m)	6	LL 2 – Span 6	LL 3 – Span 6	LL 4 – Span 6	LL 5 – Span 6
	8	LL 2 – Span 8	LL 3 – Span 8	LL 4 – Span 8	LL 5 – Span 8
	10	LL 2 – Span 10	LL 3 – Span 10	LL 4 – Span 10	LL 5 – Span 10
	12	LL 2 – Span 12	LL 3 – Span 12	LL 4 – Span 12	LL 5 – Span 12

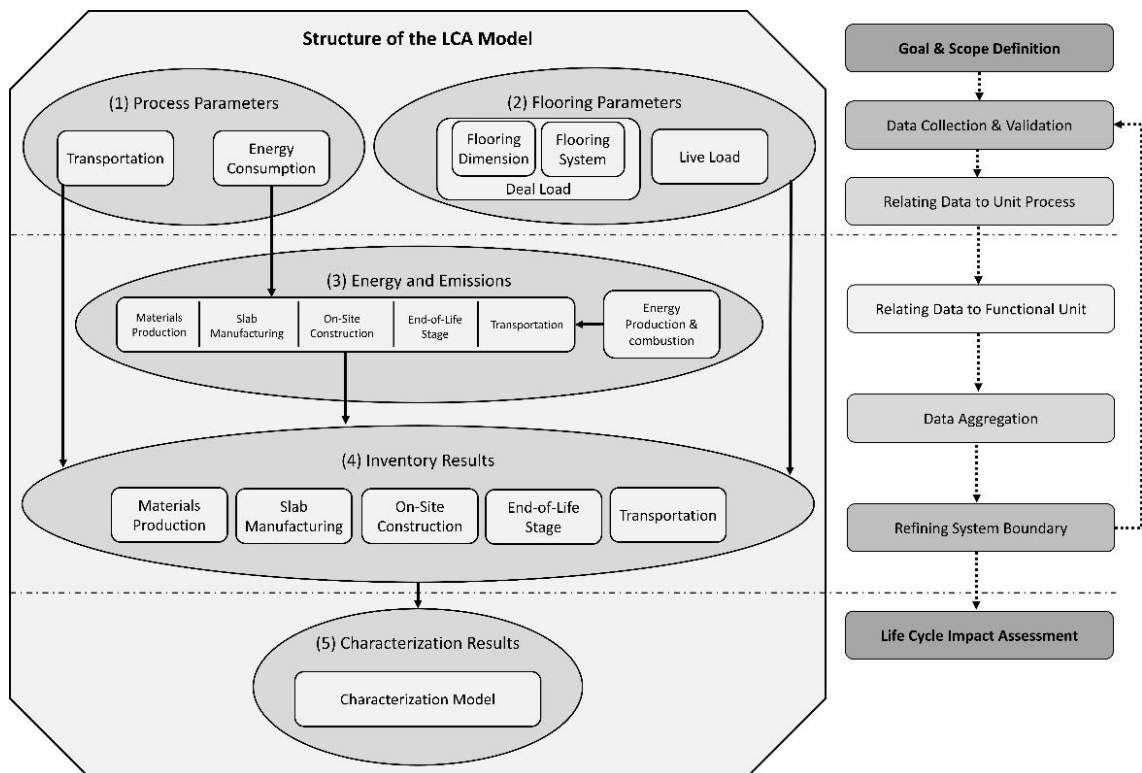


Figure 3-3: Structure of the LCA model for this study

The performance of the PUSS system is assessed using three distinct practical concrete types: normal weight concrete (NWC), lightweight aggregate concrete with Lytag aggregates (LWC) – as recommended by previous LCA studies of PUSS –, and geopolymer concrete (GPC). The comparative study is useful in identifying the most environmental friendly option. Table 3-2 outlines the characteristics of each flooring system included in the study. In addition,

Table 3-3 presents the details of concrete mix designs used in each flooring system.

Table 3-2: Characteristics of the flooring systems

Flooring system	Concrete material	Width of slab (mm)	Span of slab range (m)	Live load range (kN/m ²)	Depth of slab (mm)	Dead load range (kN/m ²)
Hollow core precast slab	NWC	1200	6 to 12	2 to 5	200 to 400	3.23 to 5.84
PUSS	NWC	2000			200 to 430	2.99 to 4.64
PUSS	LWC with Lytag	2000			2.09 to 3.36	
PUSS	GPC	2000			2.78 to 4.35	

Table 3-3: Details of concrete mix designs used in the studied flooring systems

Flooring system	Concrete material	Cement (kg/m ³)	Water (kg/m ³)	Aggregates (kg/m ³)		Fly Ash (kg/m ³)	NaOH (kg/m ³)	Density (kg/m ³)	Concrete Grade
				Fine	Coarse				
Hollow core precast slab	NWC	454	213	660	1073	-	-	2400	C40/50
PUSS	NWC	343	175	621	1261	-	-	2400	C20/25
PUSS	LWC with Lytag Aggregates	250	197.5	625	520	-	-	1592.5	C20/25
PUSS	GPC	-	112	623	935	469	75	2214	C40/50

Although the structural performance of PUSS using GPC has not yet been experimentally examined, GPC is included in this LCA study due to its potential as an environmentally friendly alternative to conventional Portland cement. As discussed previously in the literature review, GPC replaces cement partially or fully by industrial by-products such as fly ash (FA) or ground granulated blast furnace slag (GGBS), substantially reducing environmental impacts (Provis and Van Deventer, 2014; Salas et al., 2018). While GPC encompasses a wide range of concrete mixes, Salas et al. (2018) compiled extensive data on various GPC mixes, evaluating their environmental impacts relative to their compressive strength. For this study, the Alkali Activated GPC with FA mix, as presented by Yang et al. (2013), was chosen because it represents a practical GPC mixes combining satisfactory structural performance and favourable environmental credentials, providing a compressive strength of 40 MPa.

Additional to the environmental potentials of GPC, the worldwide efforts towards the standardisation of alkali-activated materials are moving rapidly over the previous decade and resulted in the production of national specifications and guidelines for alkali-activated materials in many countries such as the UK, Switzerland, Australia and China (Provis, 2018). Additionally, the adoption of geopolymer concrete is gradually increasing across multiple construction sectors, particularly in precast applications (Heath et al., 2013). In the UK, the market for geopolymer concrete was valued at approximately USD 275.3 million in 2024 and is projected to grow to approximately USD 515.7 million by 2030, with a compound annual growth rate (CAGR) of about 11% (Grand View Research, 2024).

Nevertheless, the widespread commercial use of GPC in the UK still faces practical challenges, primarily the declining availability of consistent-quality FA and GGBS. Given that the selected GPC mix in this study relies predominantly on FA, it is critical to acknowledge the reduced availability of high-quality FA in the UK, a consequence of the gradual closure of coal-fired power plants. According to Kwasny et al. (2024), UK production of suitable-quality FA for concrete applications was approximately 4.6 million tonnes in 2014, with around 50% of this quantity utilised in concrete production. Despite the declining fresh FA supply, the UK possesses significant reserves of lagoon and landfill FA, estimated at over 100 million tonnes. Research demonstrates that with proper processing, such as drying, grinding, and screening, these reserves could be effectively made available for use in GPC applications (Kwasny et al., 2024).

3.3.1 Functional Unit

The unit of comparison or the functional unit in this study is chosen to be one square meter (m^2) of flooring area for each live load/ span scenario. Therefore, each of the 16 live loads/ spans scenarios are evaluated separately and then the final outputs of each scenario are combined in a table to explore the pattern of change in environmental impacts with the increase of applied live load or span. All the GHG emissions, energy consumption, and materials are then related to this functional unit, e.g. $kg\ CO_{2,e}/m^2$, MJ/m^2 , kg/m^2 , etc.

3.3.2 System Boundaries

The LCA study assesses the entire life of the flooring systems, from mining (A1) and manufacturing of flooring materials to production of slabs (A3), on-site construction (A5), end-of-life (EOL) demolition (C1) and disposal to landfill (C4) or recycling (C3). It also includes the transportations between each life cycle stage (A2, A4, C2), considering transportation distances relevant to the UK industry. However, the operation (use) and maintenance stage (B1-B5) is not included in the system boundary, as explained in section 3.5.1.2d. This is displayed in Figure 3-2 as well as a detailed flowchart in Figure 3-4. The grid of each flooring system is chosen to be 12 m wide X the span of the slab which is variable for each span scenario ranging between 6 m and 12 m (Figure 3-5). The simplified general life cycle inventory calculation equation for each flooring system per functional unit is presented in Equation 3-1.

Equation 3-1

$$\begin{aligned} LCI_{Total} = & \sum_{i=1}^n (M_{Material(i)} \times LCI_{Material(i)}) + \sum_{i=1}^n (T_{Construction(i)} \times LCI_{Construction(i)}) \\ & + \sum_{i=1}^n (M_{Demolition(i)} \times LCI_{Demolition(i)}) + \sum_{i=1}^n (M_{Recycling(i)} \times LCI_{Recycling(i)}) \\ & + \sum_{j=1}^m \left(\sum_{i=1}^n (M_{Transportation(i)} \times D_{Transportation(i)} \times LCI_{Transportation(i)}) \right) \end{aligned}$$

Where: LCI_{Total} is the total LCI (carbon emissions or embodied carbon) of flooring system per functional unit ($CO_{2,e}/m^2$ of slab or MJ/m² of slab),

$M_{Material(i)}$ is the mass of each material used in production per functional unit (kg/m² of slab),

$LCI_{Material(i)}$ is the LCI of each material per kg of material ($CO_{2,e}$ or MJ per kg of material),

$T_{Construction(i)}$ is the operation time of each construction equipment per functional unit (hr/m² of slab),

$LCI_{Construction(i)}$ is the LCI of each equipment per hr of usage ($CO_{2,e}$ or MJ per hr of usage of equipment),

$M_{Demolition(i)}$ is the mass of each material demolished at EOL per functional unit (kg/m² of slab),

$LCI_{Demolition(i)}$ is the LCI of each demolished material per kg of material ($CO_{2,e}$ or MJ per kg of demolished material),

$M_{Recycling(i)}$ is the mass of each material recycled at EOL per functional unit (kg/m² of slab),

$LCI_{Recycling(i)}$ is the LCI of each recycled material per kg of material ($CO_{2,e}$ or MJ per kg of recycled material),

$M_{Transportation(i)}$ is the mass of each material/ product being transported in each of the transportation stages per functional unit (tonne/m² of slab),

$D_{Transportation(i)}$ is the distance of each transportation stage in (km) and $LCI_{Transportation(i)}$ is the LCI of transportation trucks per tonne of materials per km ($CO_{2,e}$ or MJ per tonne.km).

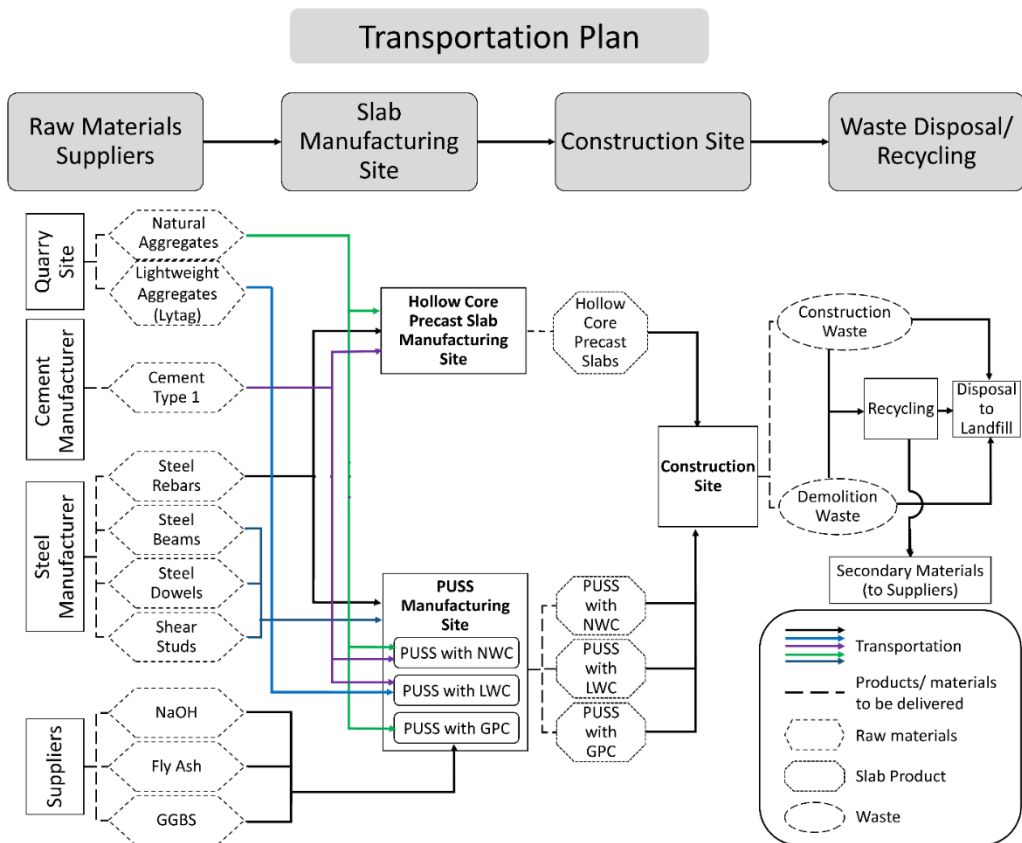


Figure 3-4: System boundaries of the studied flooring systems

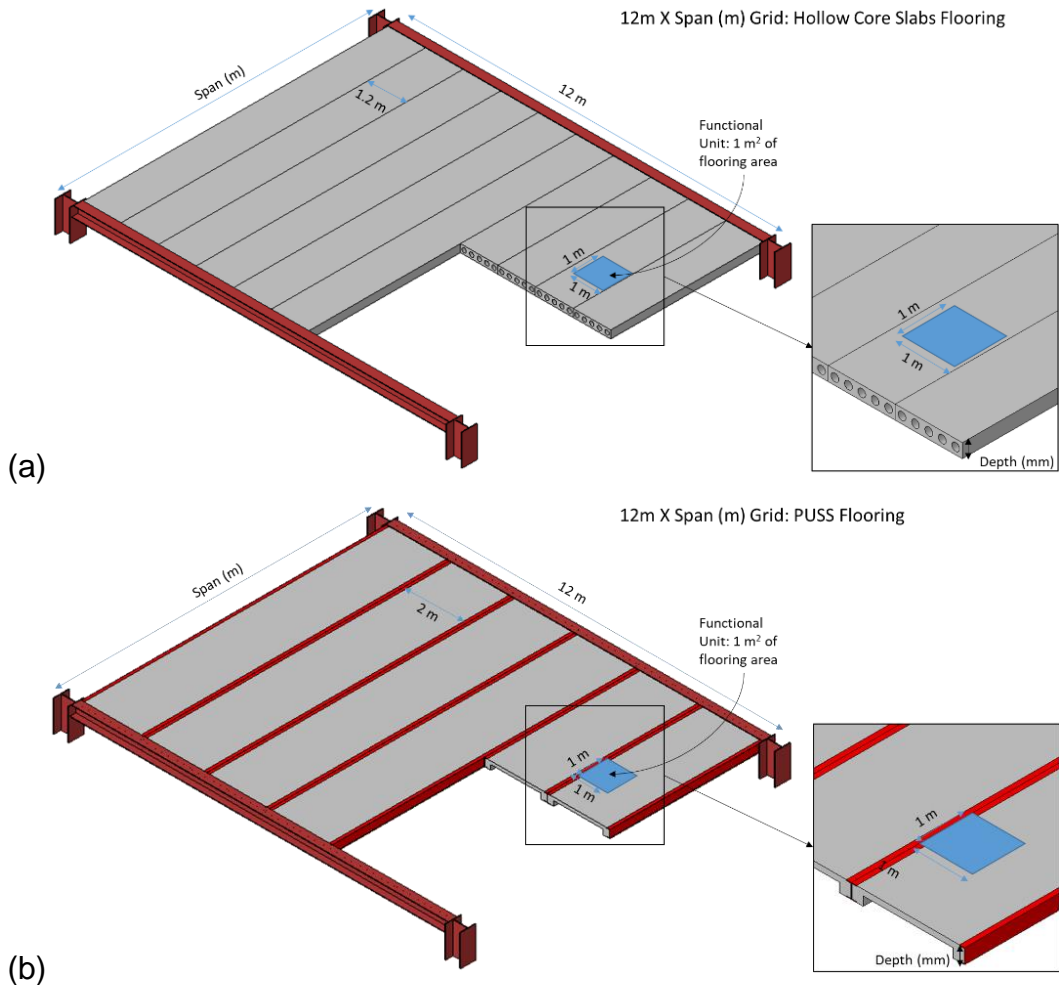


Figure 3-5: Grids of (a) Hollow core flooring (b) PUSS flooring

3.3.3 Impact Categories and Calculation Methodology

The study is focused on the environmental impacts associated with these flooring systems during their entire life. The impact categories compared in the study are:

- Global Warming Potential (GWP), which is an indicator of the extent of global warming caused by GHGs over a period of time (usually 100 years). For CO₂, the characterisation factor is 1 for GWP (Brander et al., 2012). The characterisation factors of other GHGs for GWP as CO_{2,e} over 20, 100 and 500 years are provided in Table 3-4. The LCIA results for GWP are calculated at midpoint level using conversion factors from IPCC guidelines (Masson-Delmotte et al., 2021).
- Embodied Energy (EE), which is an indicator of the total energy consumption during the life cycle of the product. The calculation of EE does not differentiate between renewable from non-renewable energy sources.

Table 3-4: GWP Characterisation factors of GHGs (Masson-Delmotte et al., 2021)

GHG	GWP indicator	GWP-20	GWP-100	GWP-500
CO ₂	CO _{2,e}	1	1	1
CH ₄ -fossil		82.5 ± 25.8	29.8 ± 11	10 ± 3.8
CH ₄ -non fossil		79.7 ± 25.8	27 ± 11	7.2 ± 3.8
N ₂ O		273 ± 118	273 ± 130	130 ± 64

3.4 Life Cycle Inventory (LCI)

The inventories of all the inputs flow such as materials and energy, and outputs flow, for example, air emissions and wastes are quantified for each product system. The gathered coefficients of carbon emissions and embodied energy for all the materials, equipment use, and transportation from a group of references from the UK where possible or nearby countries are given in Table 3-5 & Table 3-6. In addition, the approximated waste factors of each of the production materials and the transportation distances are also gathered and presented in Table 3-7 & Table 3-8. Waste factors are the additional material required to accommodate errors or mistakes, typically estimated as a percentage of material over the needed amounts of raw materials.

Table 3-5: Embodied carbon and energy of the materials for production and EOL processes

	Embodied Carbon Coefficient (kg CO _{2,e} /kg)	Embodied Energy Coefficient (MJ/kg)	Notes	Reference
Materials:				
Concrete mix 40/50 MPa (density: 2400 kg/m ³)	0.151	1	Using UK weighted average cement	(Hammond and Jones, 2011)
Concrete mix 25/30 MPa (density: 2400 kg/m ³)	0.113	0.78		
Precast concrete	0.029	0.45	Added to the coefficient of the concrete mix	
Cement - general (UK weighted average)	0.74	4.5		
Fly ash	0.008	0.1		
GGBS	0.083	1.6		
NaOH	0.6329	3.505		(Thannimalay, 2013)
Water	0.001	0.01		(Hammond and Jones, 2011)
Fine aggregates (sand)	0.0048	0.081		
Coarse aggregates (gravel or crushed rock)	0.0052	0.083		
Steel reinforcement (density: 7850 kg/m ³)	0.077	1.04	For each 100 kg of rebar per m ³ of concrete, added to the coefficient of the concrete mix	
Shear studs & dowels	1.4	17.4	UK Typical - EU 59% Recycled	
Steel sections	1.53	21.5		
Prestressed reinforcement	1.81	20.3		(Hjulsbro, 2020)
End-of-life processes:				
Concrete demolition	0.00054	0.007		(Sjunnesson, 2005)
Recycling steel rebars, shear studs & dowels	-0.33	-3.2	using 50:50 method	(Hammond and Jones, 2011)
Recycling steel sections	-0.39	-4.2	using 50:50 method	

Table 3-6: Embodied carbon and energy for construction equipment and transportation

	Embodied Carbon Coefficient	Unit	Embodied Energy Coefficient	Unit	Reference
Construction equipment:					
Concrete compactor	0.2	kg CO _{2,e} /m ³	1.18	MJ/m ³	(Gorkum, 2010)
Tower crane of 100 ton	53.23	kg CO _{2,e} /hour	720	MJ/hour	
Concrete pump	46.12	kg CO _{2,e} /hour	540	MJ/hour	
Transportation:					
20-ton diesel fuel truck	0.15	kg CO _{2,e} /tonne.km	2.4	MJ/tonne.km	(Hammond and Jones, 2011)

Table 3-7: Approximate waste factors of each of the production materials

Materials Waste	Waste Factor	Reference
Precast Concrete	0.01	(Orr et al., 2020)
In-Situ Concrete	0.053	
Steel Sections	0.01	
Steel Rebars	0.053	
Steel Deck	0.01	
Others	0.01	

Table 3-8: Approximate transportation distances at between different life cycle stages

Transportation	Distance (km)	Reference
Cementitious materials to manufacturing site	100	(Hammond and Jones, 2011)
Aggregates to manufacturing site	38	
Precast units to construction site	155	
Demolition to landfill	50	(Orr et al., 2020)

3.5 Inventory Results

The inventory results for each flooring system over the range of the investigated live load/ slab span scenarios are presented in this section. The calculation of these results for each scenario undertakes a series of steps. The first is the manual design of each flooring system based on the live loads and slab spans inputs, followed by quantifying the total amount of materials per flooring system. From these quantities, the inventory results are calculated at different life cycle stages of each flooring system, which are: manufacturing, transportation, on-site construction and end-of-life (demolition and recycling). A detailed example of these steps for one of the live load/ slab span scenarios is provided in section 3.5.1 followed by overall outcomes for all the scenarios in section 3.5.2. These two sections detail the results using the approximate transportation distances listed in Table 3-8 and the coefficients of the “50:50” allocation approach for EOL

recycling (Table 3-5). In addition, sensitivity analysis covering the transportation distance and EOL recycling allocation approaches is discussed in section 3.5.3.

3.5.1 Example of Inventory Results Calculation Methodology

This section outlines a detailed example of the calculation procedure for the inventory results of one of the analysed live load/ slab span scenarios. Specifically, for slabs span = 8 m undertaking 3 kN/m² live load (LL 3 – Span 8).

3.5.1.1 Design Optimisation of the Flooring Systems

In this step, the flooring systems are designed manually to carry a live load equal to 3 kN/m² for a span equal to 8 m, considering Serviceability Limit State (SLS) and Ultimate Limit State (ULS), including design for deflection, flexure, and longitudinal shear.

- Hollow core precast slab is designed in accordance with Eurocode 2 (CEN, 2004a). Initially, the slab depth is selected from the manufacturers' recommendations for this specific live load and span and designed to have this depth, which is 200 mm (Longley, 2019; Forterra, 2020; FP McCann, 2021). Furthermore, two additional slabs are designed with two larger depths (with 50 mm increment). The production materials for each of the three designs are quantified, and the inventory results are calculated for each design. The design with the lowest values is selected (Table 3-9). Note that an additional 50 mm finishing layer is needed, which adds to the total flooring depth and materials.
- PUSS units (with NWC, LWC or GPC) are designed – as in Chapter 4 – in accordance with Eurocode 4 (CEN, 2004b), taking into consideration the findings of previous laboratory tests performed on PUSS units (Ahmed and Tsavdaridis, 2020; Alali and Tsavdaridis, 2023; Alali and Tsavdaridis, 2024). The depth of the slab depends on the available PFC steel sections in the UK market (British Steel, 2018). The initial steel section is selected to be equal to the designed depth of the one-step lower live load/ slab span scenario. Therefore, the selected initial steel section for this design is 260x90x35 PCF. In addition, two more slabs are designed with the two larger steel sections (300x90x41 PFC and 300x100x46 PFC). As in the design process of hollow core slabs, the design that produces the lowest

values is selected. For consistency, the same depth is selected for all the three PUSS systems (Table 3-9).

After evaluating the total inventory results for each of the three designs of each flooring system, the outcomes are compared to select the design with the lowest GWP and EE per functional unit. As shown in Table 3-9, the second designs (highlighted in green) for each flooring system exhibit the lowest values. Therefore, for this live load/ span scenario, the design with 250 mm depth is selected for the hollow core slabs, while the design with 300 mm depth is selected for PUSS units (using 300x90x41 PFC).

Table 3-9: Comparison of total inventory results for design optimisation

Design		Flooring system			
		Hollow core precast slab	PUSS with NWC	PUSS with LWC	PUSS with GPC
1 st Design	Depth (mm)	200	260 (using 260x90x35 PFC)		
	GWP (kg CO _{2,e} /m ² of slab)	190.06	126.43	101.55	96.25
	EE (kg MJ/m ² of slab)	2075.12	1594.03	1302.04	1383.45
2 nd Design	Depth (mm)	250	300 (using 300x90x41 PFC)		
	GWP (kg CO _{2,e} /m ² of slab)	165.42	120.36	99.83	92.39
	EE (kg MJ/m ² of slab)	1707.77	1527.08	1293.10	1336.98
3 rd Design	Depth (mm)	300	300 (using 300x100x46 PFC)		
	GWP (kg CO _{2,e} /m ² of slab)	171.23	124.74	104.28	96.86
	EE (kg MJ/m ² of slab)	1760.29	1594.52	1361.20	1404.97

The decision to select deeper slabs (the 2nd designs) for minimised environmental impacts contrasts with the expectation that shallower depths (1st designs) would have lower impacts. This can be attributed to the fact that shallower depths require denser reinforced concrete to meet structural requirements, which might potentially increase the overall environmental impact. Furthermore, in the case of PUSS system, shallower slabs may necessitate wider side concrete joists, which could lead to higher concrete usage. For instance, in the presented case, the 260 mm slabs have more concrete compared with the 300 mm slabs, as detailed in Table 3-10, which presents the individual material mass and total mass per square meter for each design of the flooring systems.

Table 3-10: Comparison of material quantities in all design alternatives

Flooring system		Hollow Core Precast Slab	PUSS with NWC	PUSS with LWC	PUSS with GPC
Material (kg per m ² of slab)					
1 st Design	Concrete	292.74	311.01	206.37	286.92
	Steel/prestressed reinforcement	44.04	16.48	16.48	16.48
	Finishing Layer	126.36	0.00	0.00	0.00
	Steel section	0.00	53.08	53.08	53.08
	Shear connectors	0.00	2.43	2.43	2.43
	Total mass (kg per m ² of slab)	463.14	383.01	278.36	358.91
2 nd Design	Concrete	373.02	301.73	200.21	278.35
	Steel/prestressed reinforcement	28.61	9.74	9.74	9.74
	Finishing Layer	126.36	0.00	0.00	0.00
	Steel section	0.00	63.21	63.21	63.21
	Shear connectors	0.00	2.43	2.43	2.43
	Total mass (kg per m ² of slab)	527.98	377.11	275.59	353.74
3 rd Design	Concrete	402.16	300.85	199.63	277.54
	Steel/prestressed reinforcement	28.61	9.71	9.71	9.71
	Finishing Layer	126.36	0.00	0.00	0.00
	Steel section	0.00	69.18	69.18	69.18
	Shear connectors	0.00	2.43	2.43	2.43
	Total mass (kg per m ² of slab)	557.13	382.17	280.95	358.87

3.5.1.2 Detailed Inventory Results

The detailed inventory results for each life cycle stage are outlined in Table 3-11 and Table 3-12 for GWP and EE, respectively. These outputs are also illustrated as bar charts in Figure 3-6 & Figure 3-7. Comparing the total GWP of PUSS flooring systems with hollow core slabs demonstrates that PUSS reduces the associated GWP by 27.24%, 39.65% and 44.15%, respectively, when implementing NWC, LWC and GPC in PUSS. Similarly, PUSS flooring system consumes less total energy compared with hollow core slabs, saving 10.58% when using NWC, 24.28% with LWC and 21.71% with GPC. The detailed life cycle stages inventory results provide a better understanding of the difference in environmental performance between the flooring systems at each life cycle stage.

- a. Manufacturing/ production stage: This stage comprises the inventory results of all materials used in producing the flooring systems (A1, A3) as well as off-site slabs manufacturing process (A5). Material inventories cover all the emissions and embodied energy from the acquisition of raw materials (A1), processing them and transporting them to the slabs

manufacturing sites (A2). The findings demonstrate that for all the flooring systems, this stage produces between 90 to 93% of the total carbon emissions and consumes between 87 to 91% of the total energy. During this stage, when compared with hollow core slabs, PUSS flooring produces 20.90%, 31.63% & 37.72% less carbon emissions when NWC, LWC & GPC are used respectively. In terms of embodied energy, PUSS with NWC consumes only 1.7% less energy than hollow core slabs, while PUSS with both LWC and GPC has about 13% less embodied energy than hollow core slabs.

- b. Transportation stage(s): The inventory results herein combine four main transportation stages, which are the transportation of slabs and construction materials to construction site (A4), transportation of manufacturing waste to landfill, transportation of construction waste to landfill and transportation of EOL demolition to final disposal (C2). The calculated GWP and EE are for fuel combustion from the transportation using 20-tonne payload diesel trucks. The assumed transportation distances are given in Table 3-8. The outputs show that for the studied flooring systems, transportation stage makes an average of around 8% of the total GWP and 10% of the total EE, which makes it the second highest proportion. The inventory results from transportation stages highly depend on the transportation distances. Therefore, a sensitivity analysis of the transportation distance variation is presented in section 3.5.3.1. Additionally, the weight of the flooring system plays an important factor, thus, hollow core slabs have the largest values because they are the heaviest. In comparison to it, PUSS has 18%, 41.5% & 23.4% lower GWP and EE with NWC, LWC & GPC respectively. It is clear that PUSS with LWC has the lowest outcomes in this stage due to its lighter weight.
- c. On-site construction stage: As the analysed flooring systems are prefabricated, on-site construction (A5) inventory results are mainly from the use of power operated tools and equipment such as cranes to install the slabs into their places. In addition, the installation of the finishing layer to hollow core slabs requires the use of concrete pumps, compactors and vibrators (Gorkum, 2010). Off-site production mitigates the percentage of GWP and EE accompanying on-site construction stage and makes it only about 1% or less. Consequently, this stage is marginal, having little effect

on the overall outcomes. Findings also indicate that PUSS flooring reduces the on-site construction GWP and EE by about 44% in comparison to hollow core slabs. This is because the wider 2 m PUSS units decrease the overall required number of slabs when compared with hollow core slabs and thereafter reduce the needed operation time of tower cranes. In addition, PUSS flooring system does not require a finishing layer, which reduces the need of construction equipment on-site.

- d. Operation (use) & maintenance stage (B1-B5): Floorings in buildings, along with structural elements in general, are designed to remain operational throughout the lifetime of the building with little or no maintenance required. In addition, in the event maintenance becomes necessary, impacts are expected to be almost equal across all flooring systems in various load/ span scenarios. Therefore, the inventory results associated with this stage are assumed to have negligible effects on the overall outcomes.
- e. End-of-life (EOL) stage: This stage reflects the impacts related to building demolition (C1) and materials reusability potential (recycling) (C3). The ICE inventory (Hammond and Jones, 2011) provides the necessary information about the recyclability of steel elements, stating that about 95% of steel sections and 75% of the reinforcement bars can be recycled, while the remaining disposed to landfill (C4) (Ahmed and Tsavdaridis, 2018). For concrete, only its demolition and disposal to landfill are considered in this study. The inventory results from the demolition of the flooring systems are extremely insignificant, contributing to less than 0.2% of the total GWP and EE. Conversely, recycling plays a noteworthy role in LCA outcomes, recovering a portion of the total GWP and EE, thereby presented as negative values. The larger amount of steel components used in PUSS flooring, in comparison to hollow core slabs, results in recovery values of GWP and EE that exceed those of hollow core slabs by over 170%. In the recycling calculations of this example, the '50:50 allocation' approach is employed, assigning burdens from recycling processes equally to the flooring system and subsequent products in which the material is used. Using this approach for recycling, hollow core slabs recovers only about 6% of the total GWP and EE, whereas for PUSS units with different concrete materials, the recycling-based recovery

ranges from 12% to 18%. Note that there is a level of uncertainty associated with selecting the best EOL recycling allocation method. The 'substitution method' involves assigning the environmental impacts associated with the recycled materials entirely to the product under assessment, enhancing its environmental advantages, which is expected to be supported by products manufacturers. On the other hand, the 'cutoff method' allocates the benefits of recycling entirely to the subsequent products. These two methods represent the extremes of distributing the benefits, and the selection of other methods such as the '50:50 allocation' approach leads to results between the two extremes (Hammond and Jones, 2011; Huang et al., 2013; Allacker et al., 2014). While the application of different allocation approaches definitely leads to pronounced disparity in the final outcomes (Nicholson et al., 2009), the sensitivity analysis by Cherubini et al. (2018) showed that, in most cases, it has no impact on the relative ranking in comparative LCA studies. A sensitivity analysis of the allocation methods is presented in section 3.5.3.2 and its outcomes agrees with Cherubini et al. (2018).

Table 3-11: GWP results for LL= 3 kN/m² & span= 8 m (GWP - kg CO_{2,e}/m² of slab)

Flooring system Life cycle stage	Hollow core precast slab	PUSS with NWC	PUSS with LWC	PUSS with GPC
Manufacturing	161.96	128.11	110.73	100.87
Transportation	13.18	10.81	7.71	10.10
On-site construction	1.47	0.83	0.83	0.83
Demolition	0.26	0.16	0.11	0.15
Recycling	-11.45	-19.55	-19.55	-19.55
Total	165.42	120.36	99.83	92.39

Table 3-12: EE results for LL= 3 kN/m² & span= 8 m (EE – MJ/m² of slab)

Flooring system Life cycle stage	Hollow core precast slab	PUSS with NWC	PUSS with LWC	PUSS with GPC
Manufacturing	1574.43	1547.47	1363.77	1368.95
Transportation	210.85	172.94	123.37	161.53
On-site construction	19.71	11.25	11.25	11.25
Demolition	3.43	2.09	1.39	1.93
Recycling	-100.64	-206.68	-206.68	-206.68
Total	1707.77	1527.08	1293.10	1336.98

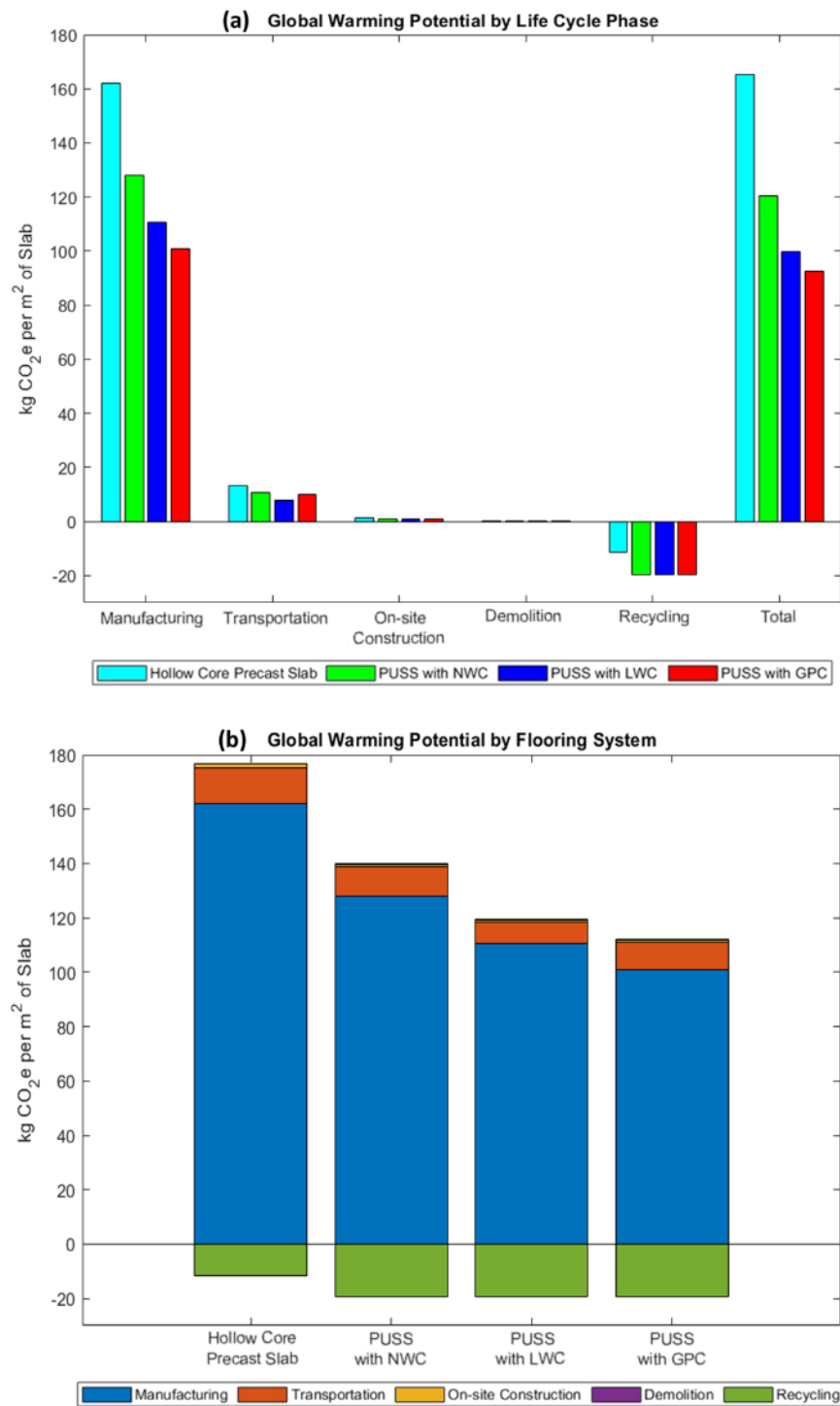


Figure 3-6: GWP results for LL= 3 kN/m² & span= 8 m (a) by life cycle stage (b) by flooring system

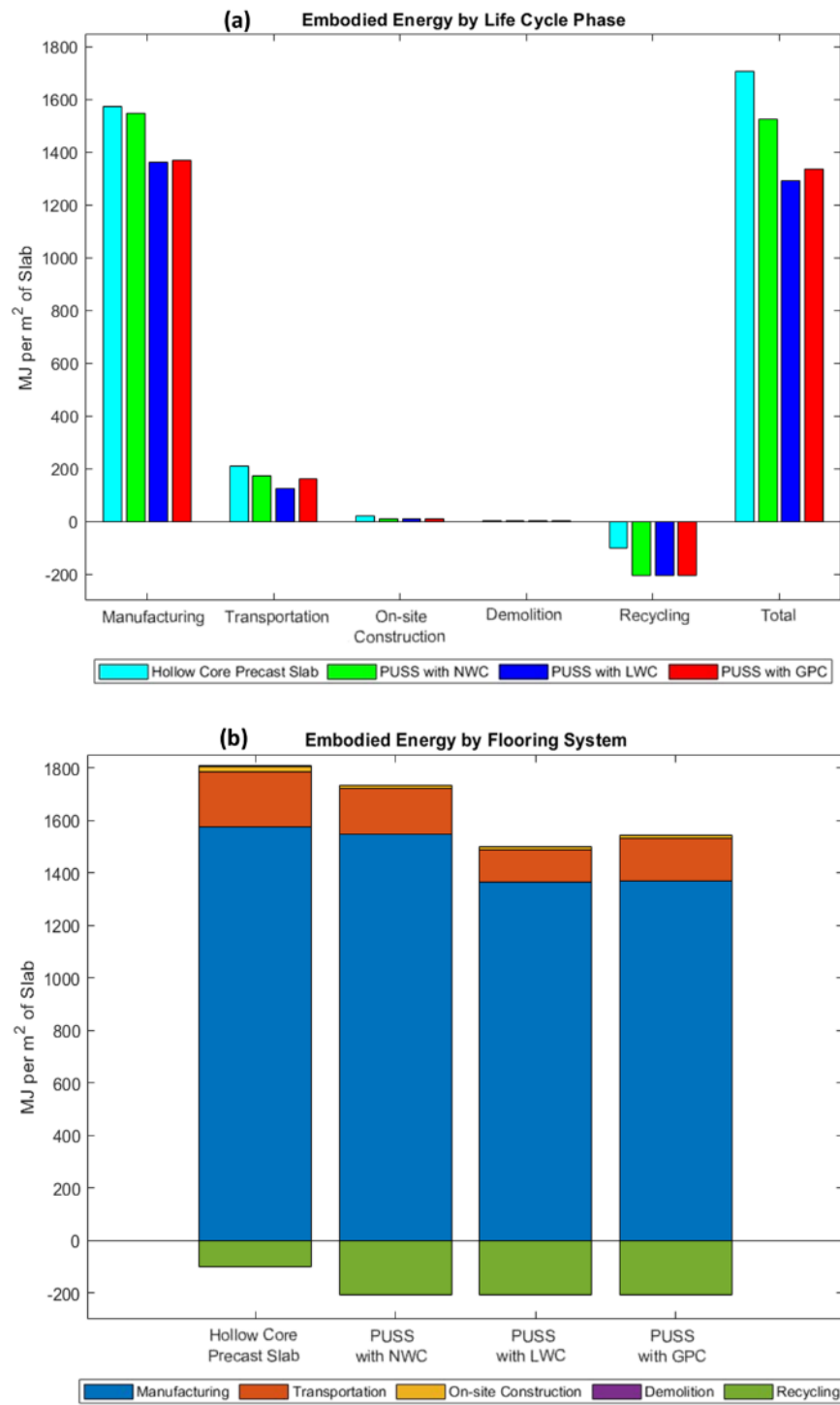


Figure 3-7: EE results for LL= 3 kN/m² & span= 8 m (a) by life cycle stage (b) by flooring system

3.5.2 Assessment of All Live Load/ Slab Span Scenarios

The methodology for calculating inventory results, as outlined in section 3.5.1, is similarly applied for the remaining 15 live load/slab span scenarios. The results for all the scenarios are then compiled and compared, providing a comprehensive perspective to the LCA results associated with varying live loads and spans in flooring systems. The gathered detailed inventory results associated with every load/slab span scenario are presented in Appendix A.

3.5.2.1 Global Warming Potential (GWP)

The cumulative GWP of all the analysed flooring systems across the examined scenarios are gathered and compared in Table 3-13. Each GWP result for the three PUSS floorings is followed by a percentage that indicates the extent to which it deviates from the hollow core slabs (benchmark) with identical spans and live loads. Green shades demonstrate that all calculated GWPs for PUSS floorings are lower than those of hollow core slabs, with darker shades representing higher deviation. Upon a comprehensive analysis, it is evident that PUSS with GPC stands out as the option with lowest GWP, followed by PUSS with LWC, and then PUSS with NWC. Moreover, it is noteworthy that PUSS flooring exhibits slightly greater benefits at lower spans, with the percentage difference from hollow core slabs decreasing a little as spans increase, though still yielding favourable results. These results are visually presented as 3D surfaces in Figure 3-8 (a) which illustrates distinct variations in results across the investigated live loads and spans without any overlap. The same results are also depicted in a 2D plot for GWP versus span in Figure 3-8 (b). Both figures reveal a clear linear relationship between the total GWP and the live load and span. To precisely capture this relationship, the results for each flooring system are fitted into linear equations of the form presented in Equation 3-2. The derived linear equations are evaluated using the coefficient of determination (R-squared) which is most appropriate to examine how linear equations fit to the data (Figueiredo et al., 2011; Chicco et al., 2021). All the derived equations for GWP agreed with the analysis outcomes, yielding R^2 values higher than 0.977. The high R^2 values (close to 1) indicate that the model explains a large proportion of the variance in the data, confirming the suitability of using R-squared for this analysis. The flooring system-dependent coefficients and corresponding R^2 values for each flooring system are provided in Table 3-14.

Equation 3-2

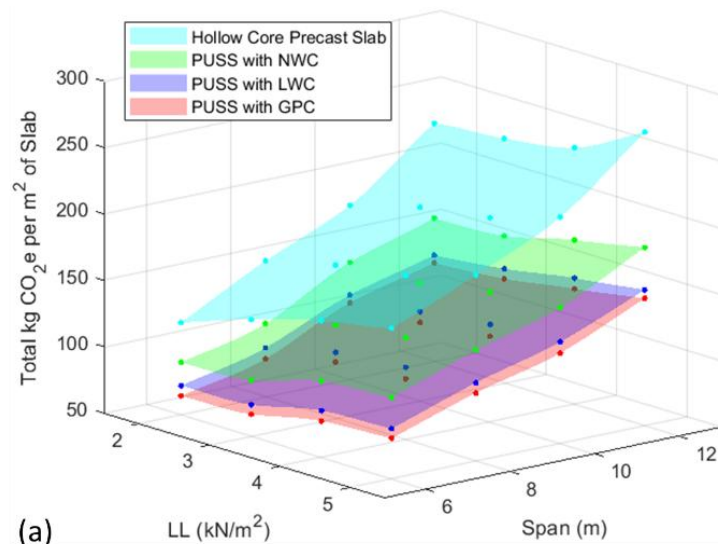
$$GWP \text{ (kg CO}_{2,e}\text{/m}^2 \text{ of slab)} = a_1S + b_1LL$$

Where: a_1 & b_1 are flooring system-dependent coefficient
 S & LL are the slab span and live load variables respectively

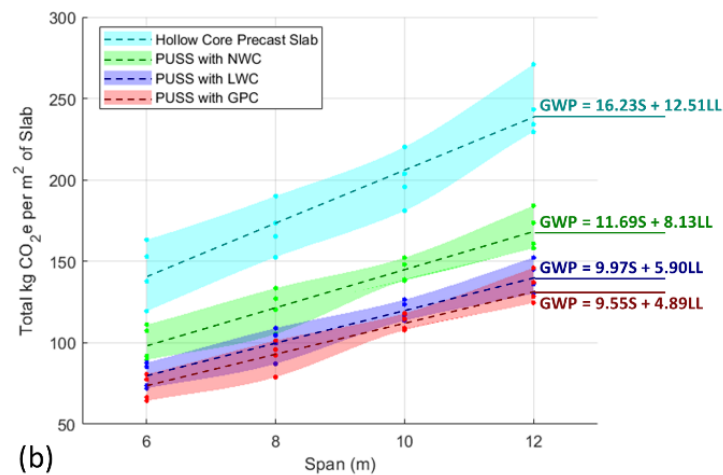
Table 3-13: Comparison of GWP results for all live load/ slab span scenarios (kg CO_{2,e}/m² of slab)

Span (m)	LL (kN/m ²)	Hollow core precast slab	PUSS with NWC	% of HC	PUSS with LWC	% of HC	PUSS with GPC	% of HC
6	2	119.5	89.5	74.9%	72.1	60.3%	64.4	53.9%
6	3	137.8	92.0	66.7%	73.7	53.5%	66.6	48.3%
6	4	153.0	107.4	70.2%	85.3	55.7%	77.5	50.6%
6	5	163.3	111.1	68.0%	87.8	53.8%	80.6	49.4%
8	2	152.6	105.4	69.1%	87.1	57.1%	78.9	51.7%
8	3	165.4	120.4	72.8%	99.8	60.3%	92.4	55.9%
8	4	173.6	127.1	73.2%	104.6	60.3%	95.8	55.2%
8	5	190.0	133.5	70.3%	109.0	57.3%	101.3	53.3%
10	2	181.1	138.2	76.3%	113.6	62.7%	107.7	59.5%
10	3	195.7	138.9	70.9%	117.1	59.8%	109.0	55.7%
10	4	203.8	148.0	72.6%	123.5	60.6%	114.6	56.3%
10	5	220.3	152.3	69.1%	126.5	57.4%	118.1	53.6%
12	2	229.5	158.1	68.9%	130.3	56.8%	124.5	54.3%
12	3	234.1	160.8	68.7%	136.0	58.1%	128.5	54.9%
12	4	243.3	173.7	71.4%	145.0	59.6%	137.1	56.3%
12	5	271.1	184.1	67.9%	152.2	56.2%	146.0	53.9%

* Green shades indicate that GWPs for PUSS floorings are lower than those of hollow core slabs, darker shades represents higher deviation



(a)



(b)

Figure 3-8: (a) 3D plot of GWP results (b) 2D plot of GWP results with curve fitting equations

Table 3-14: Constants of curve fitting equations for GWP and EE

Flooring system	GWP (kg CO _{2,e} /m ² of slab)			EE (MJ/m ² of slab)		
	a ₁	b ₁	R ²	a ₂	b ₂	R ²
Hollow Core Precast Slab	16.23	12.51	0.9773	172.14	125.39	0.9578
PUSS with NWC	11.69	8.13	0.9873	154.56	88.64	0.9852
PUSS with LWC	9.97	5.90	0.9913	134.42	63.70	0.9815
PUSS with GPC	9.55	4.89	0.9793	139.92	65.96	0.9717
GWP = a ₁ * S + b ₁ * LL			EE = a ₂ * S + b ₂ * LL			
S = span (m) & LL = live load (kN/m ²)						

3.5.2.2 Embodied Energy (EE)

The cumulative EE of flooring systems are outlined in Table 3-15. As with the GWP analysis previously discussed, each EE outcome is accompanied by a color-coded percentage, indicating its deviation from the hollow core slabs (benchmark) with comparable spans and live loads. Following an inclusive evaluation, the analysis reveals that PUSS with LWC stands out as option with the lowest associated EE, succeeded by PUSS with GPC, and then PUSS with NWC. This order differs from the observed GWP outcomes. Furthermore, as indicated by the GWP results, a noticeable trend emerges, in which the difference in EE between PUSS and hollow core slabs is more pronounced at lower spans and live loads, but diminishes as these variables increase. The visual representation of the results is illustrated as 3D surfaces in Figure 3-9 (a). Also, Figure 3-9 (b) presents a 2D plot depicting EE versus span, offering a graphical representation. Similar to GWP graphs, a clear linear relationship between the total EE and the live load and span is noticed from the figures. Employing curve fitting, the results for each flooring system are expressed through linear equations, as outlined in Equation 3-3, which closely align with the results of the LCA, achieving R² values surpassing 0.957. The flooring system-dependent coefficients as well as R² values for each flooring system are presented in Table 3-14. The impact of the slab span on the total inventory results (GWP and EE) appears more pronounced than that of the live load, signified by its higher coefficients within Equation 3-2 & Equation 3-3.

Equation 3-3

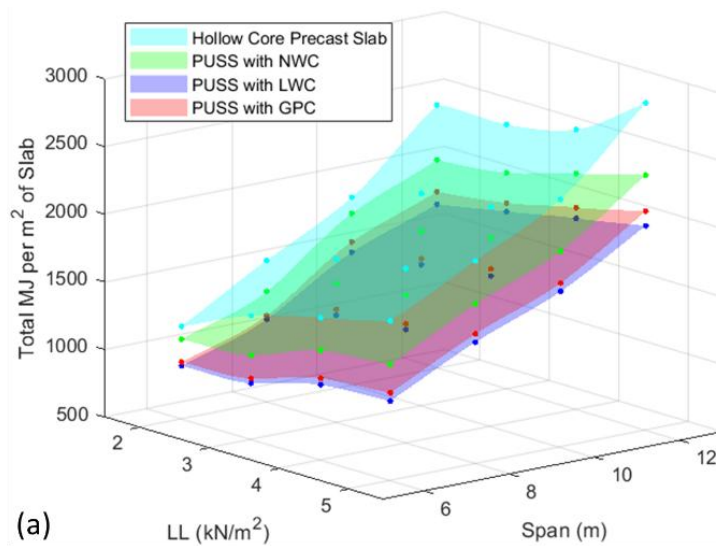
$$EE \text{ (MJ/m}^2 \text{ of slab)} = a_2 S + b_2 LL$$

Where: a_2 & b_2 are flooring system-dependent coefficient,
and S & LL are the slab span and live load variables respectively.

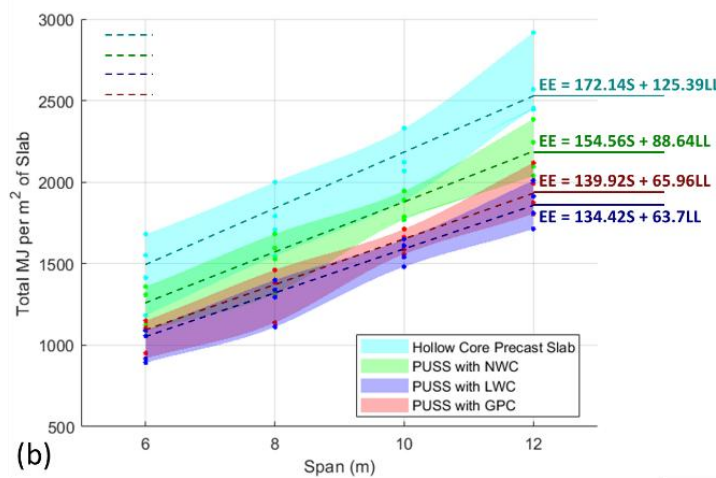
Table 3-15: Comparison of EE results for all live load/ slab span scenarios (MJ/m² of slab)

Span (m)	LL (kN/m ²)	Hollow core precast slab	PUSS with NWC	% of HC	PUSS with LWC	% of HC	PUSS with GPC	% of HC
6	2	1182.8	1088.3	92.0%	892.6	75.5%	919.4	77.7%
6	3	1414.1	1122.5	79.4%	915.7	64.8%	950.6	67.2%
6	4	1551.9	1309.3	84.4%	1056.6	68.1%	1105.6	71.2%
6	5	1681.3	1358.9	80.8%	1090.5	64.9%	1150.0	68.4%
8	2	1545.7	1316.0	85.1%	1111.8	71.9%	1138.5	73.7%
8	3	1707.8	1527.1	89.4%	1293.1	75.7%	1337.0	78.3%
8	4	1792.3	1594.8	89.0%	1340.0	74.8%	1383.4	77.2%
8	5	1999.8	1681.9	84.1%	1399.4	70.0%	1461.3	73.1%
10	2	1887.4	1768.8	93.7%	1481.3	78.5%	1558.2	82.6%
10	3	2068.6	1788.4	86.5%	1541.1	74.5%	1585.7	76.7%
10	4	2122.2	1890.4	89.1%	1611.3	75.9%	1663.6	78.4%
10	5	2330.5	1946.1	83.5%	1649.4	70.8%	1712.1	73.5%
12	2	2445.7	2039.2	83.4%	1712.7	70.0%	1804.8	73.8%
12	3	2453.6	2095.2	85.4%	1810.1	73.8%	1873.7	76.4%
12	4	2568.7	2244.9	87.4%	1913.0	74.5%	1992.5	77.6%
12	5	2917.7	2385.7	81.8%	2010.1	68.9%	2118.4	72.6%

* Green shades indicate that EEs for PUSS floorings are lower than those of hollow core slabs, darker shades represents higher deviation



(a)



(b)

Figure 3-9: (a) 3D plot of EE results (b) 2D plot of EE results with curve fitting equations

3.5.2.3 Floor Weight and Depth

The inventory results previously outlined do not solely assess the environmental performance of the flooring system. Additional measures contribute to reduced environmental impacts by enabling the downsizing of other structural elements, leading to a reduction in overall material consumption within a building. Utilising lighter floorings, for instance, reduces the dead loads imposed on other structural elements like beams, columns, and foundations. Furthermore, a shallower slab depth diminishes the necessary beam size, subsequently lowering the overall building height and reducing material usage.

The densities of the flooring systems, expressed as mass per square meter of the flooring area, are compared side by side in Figure 3-10 for direct assessment. The figure notably displays PUSS with LWC as the lightest option among the studied systems, followed by PUSS with GPC. In contrast, hollow core slabs exhibit significantly greater weight, nearly doubling that of PUSS with LWC. Furthermore, all three PUSS flooring options demonstrate nearly identical slope increments with increasing spans, however, the slope associated with hollow core slabs is steeper, indicating a more substantial disparity, especially at higher spans. It is also evident from the figure that changes in live load have a relatively minor impact on the flooring weight compared with the changes in span which have more significant influence.

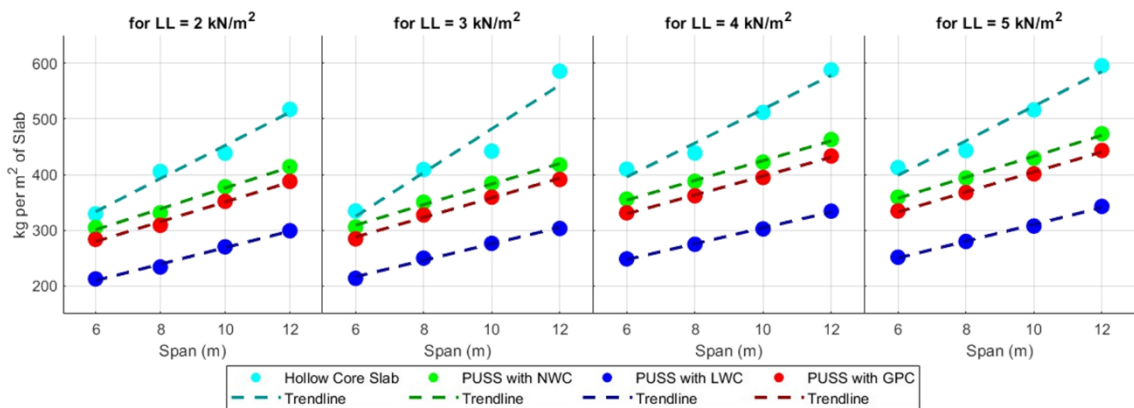


Figure 3-10: Floor weight change pattern with increasing spans and live loads

As illustrated in Figure 3-11, the depths of hollow core slabs and PUSS units closely align at smaller spans. However, as spans increase, hollow core slabs exhibit smaller depths compared with PUSS. While this might initially appear as an advantage to hollow core slabs, they require an additional 50 mm finishing layer, a requirement not needed for PUSS flooring. Consequently, it can be

concluded that the depth is of less significance in comparing the environmental performance of the two flooring systems.

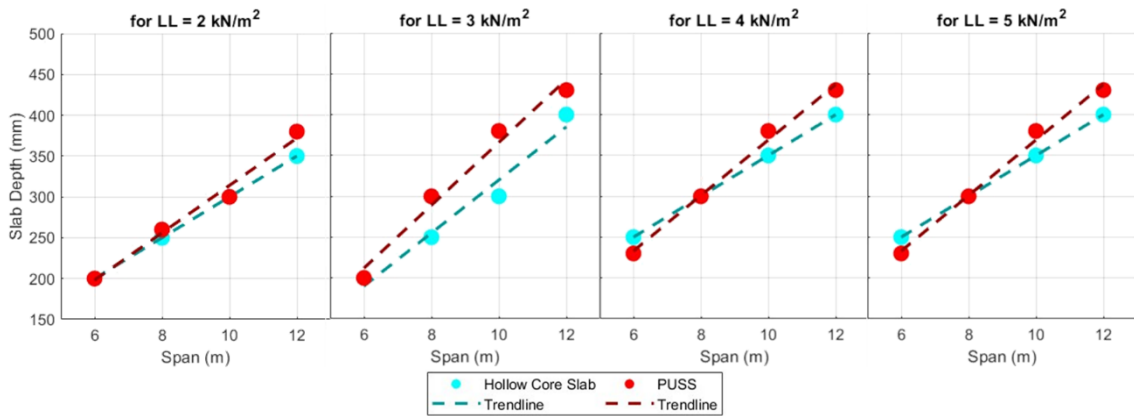


Figure 3-11: Floor depth change pattern with increasing spans and live loads

Based on the densities and depths of the slabs under examination, linear equations were derived through curve fitting. The derived equations are useful to roughly estimate the densities (Equation 3-4) and depths (Equation 3-5) of the slabs by substituting the magnitude of the live loads and spans. The flooring system-dependent coefficients for these equations as well as R² values for each flooring system are presented in Table 3-16.

Equation 3-4

$$\text{Density (kg per m}^2 \text{ of slab)} = a_3S + b_3LL$$

Equation 3-5

$$\text{Depth (mm)} = a_4S + b_4LL$$

Where: a_3, a_4, b_3 & b_4 are flooring system-dependent coefficient
 S & LL are the slab span and live load variables respectively

Table 3-16: Constants of curve fitting equations for densities and depths of slabs

Flooring System	Density (kg per m ² of slab)			Mass (mm)		
	a ₃	b ₃	R ²	a ₄	b ₄	R ²
Hollow Core Precast Slab	37.90	33.40	0.9273	31.25	11.67	0.9376
PUSS with NWC	28.11	36.38	0.8483			
PUSS with LWC	20.64	24.58	0.8873			
PUSS with GPC	26.35	33.73	0.8562			
Density = a ₃ * S + b ₃ * LL				Depth = a ₄ * S + b ₄ * LL		
S = span (m) & LL = live load (kN/m ²)						

3.5.3 Sensitivity Analysis

A sensitivity analysis is applied to explore the impacts of uncertainties in transportation distance and EOL recycling allocation methods on the LCA outputs. These parameters are selected due to their significant influence on the results, ranking second and third after the off-site construction phase, and the

level of uncertainty associated with them. The analysis aims to assess the effects of varying transportation distances and the recycling allocation methods on the final GWP and EE outcomes of the LCA study.

In addition to transportation distance and EOL recycling allocation methods, there are several other parameters that can influence LCA results and could be considered in sensitivity analyses within construction-related studies. These include variations in material production processes (such as different cement manufacturing routes, clinker ratios, or energy mixes), assumptions related to the service life of the structural system, maintenance and repair schedules, and alternative transportation modes (such as rail, road and sea). Furthermore, the use of renewable energy during manufacturing may significantly affect embodied carbon results. While these parameters are acknowledged as potentially impactful, their inclusion is beyond the scope of this study. Nevertheless, their influence is recognised and has been noted in the recommendations for future research.

3.5.3.1 Transportation Distance

The previously presented LCA results utilise the approximate transportation distances listed in Table 3-8. For the sensitivity analysis, these distances are adjusted by factors of 1/3, 2/3, 2, and 3 times the original values to account for uncertainty. The results of this analysis are illustrated in Figure 3-12 (GWP) and Figure 3-13 (EE).

The general conclusion from this sensitivity analysis is that varying the transportation distance does not alter the ranking of the environmental performance of the studied flooring systems. PUSS with GPC consistently remains the best performer in terms of GWP, while PUSS with LWC is the best in terms of EE. Hollow core slabs, on the other hand, consistently exhibit the worst performance across all 16 scenarios analysed.

However, the sensitivity analysis reveals that the impact of transportation distance on the final GWP and EE outcomes (as a percentage compared with the previously presented results) varies between the flooring systems. For GWP, the transportation distance has the least effect on hollow core slabs and the greatest effect on PUSS with GPC. Specifically, reducing the distances to 1/3 of the original values decreases the total GWP of hollow core slabs by an average of

approximately 5%, and by 6% for both PUSS with NWC and PUSS with LWC, while it reduces the GWP of PUSS with GPC by an average of 9%. Conversely, increasing the distances to three times the original values raises the total GWP by about 16% for hollow core slabs, 18% for both PUSS with NWC and PUSS with LWC, and 27% for PUSS with GPC.

In terms of EE, the transportation distance affects PUSS with both NWC and LWC the least, while PUSS with GPC is the most affected. Calculations with 1/3 distances reduce the total EE by around 8% for hollow core slabs, 7.7% for both PUSS with NWC and PUSS with LWC, and 10% for PUSS with GPC. Conversely, using three times the original distances increases the total EE by approximately 24% for hollow core slabs, 23% for both PUSS with NWC and PUSS with LWC, and 30% for PUSS with GPC. These findings underscore that while transportation contributes 5.75% to 11.5% of the total GWP and 7% to 14.5% of the total EE in the initial LCA, these contributions can vary significantly with actual transportation distances.

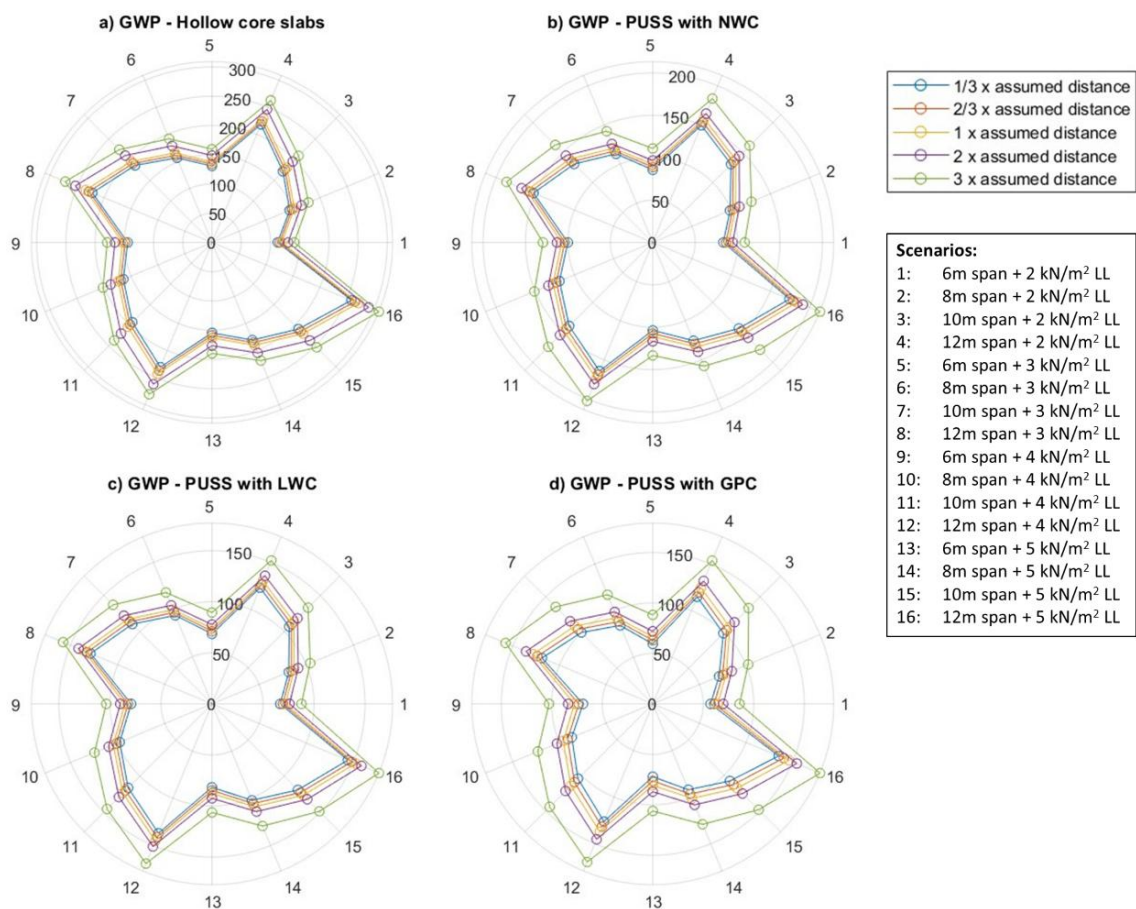


Figure 3-12: Sensitivity analysis of transportation distance effect on GWP outcomes

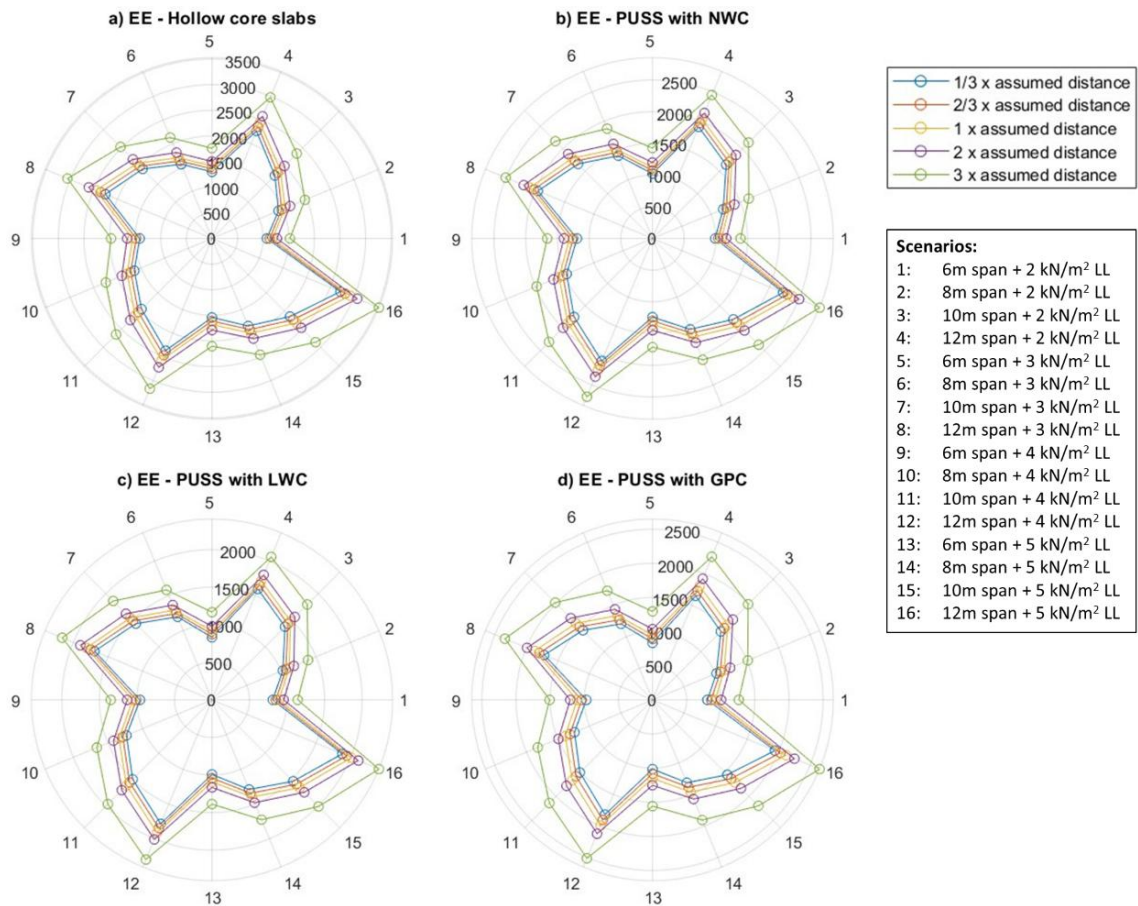


Figure 3-13: Sensitivity analysis of transportation distance effect on EE outcomes

3.5.3.2 EOL Recycling Allocation Approach

The LCA study in sections 3.5.1 and 3.5.2 employs the “50:50” allocation approach for EOL recycling as outlined in section 3.5.1.2.e, wherein 50% of the recycling benefits are attributed to the studied flooring systems. To evaluate the sensitivity of this assumption, two additional approaches are considered: the “cutoff” approach, which excludes any recycling benefits from the studied floorings, and the “substitution” approach, which allocates 100% of the recycling benefits to the studied floorings (Hammond and Jones, 2011; Huang et al., 2013; Allacker et al., 2014). The results of this analysis are presented in Figure 3-14.

Similar to the transportation distance, the sensitivity analysis for recycling allocation methods indicates that altering the allocation approach does not change the ranking of the environmental performance of the studied flooring systems across all the 16 scenarios analysed. However, the impact of changing allocation approaches is most pronounced for both PUSS with GPC and PUSS with LWC. Adopting the cutoff approach increases the GWP and EE associated with these floorings by an average of approximately 20% and 15%, respectively, compared with the 50:50 approach. Conversely, utilising the substitution

approach decreases the GWP and EE by similar percentages. For hollow core slabs, the changes are the least significant, having an average of about 7% in GWP and 6% in EE. For PUSS with NWC, the average percentages are about 15% and 13%, respectively.

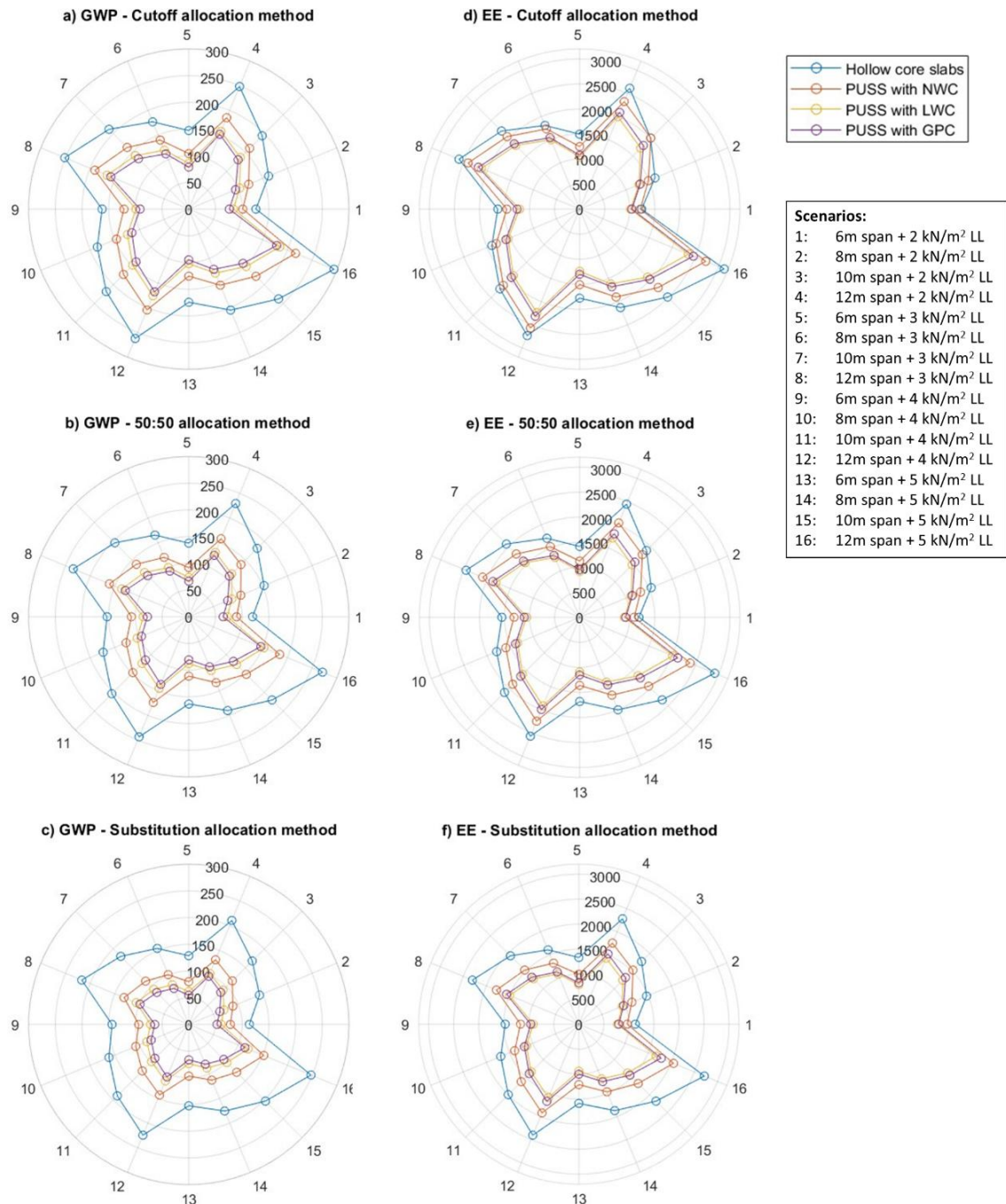


Figure 3-14: Sensitivity analysis of recycling allocation method effect on GWP and EE outcomes

Overall, using the substitution approach decreases the GWP and EE outcomes for all flooring systems, but as a percentage, the difference between PUSS flooring and hollow core slabs increases, further favouring PUSS flooring. Conversely, the cutoff approach increases the GWP and EE outcomes for all

flooring systems, but as a percentage, the difference between PUSS flooring and hollow core slabs decreases, though PUSS flooring still has less associated environmental impacts.

3.6 Results Discussion

Building upon the detailed analysis of the results, this section explores the broader implications of the study findings by having an overall look at the life cycle stages of all the explored scenarios, and discussing the key factors influencing the environmental impacts of the studied flooring systems in the context of UK geographical conditions. The following key points highlight the main takeaways from the analysis:

- a. The manufacturing phase of the analysed flooring systems constitutes a significant portion, ranging from 86% to 94%, of the total calculated GWP for all flooring systems and between 83% and 93% of the total EE. These high proportions are consistent with findings from previous research on precast floorings, where the manufacturing phase often accounts for up to over 90% of the total environmental impacts (Balasbaneh et al., 2022). These percentages are lower for smaller live loads and slabs' spans and gradually increase as these variables increase. This is primarily attributed to the inclusion of materials inventories in this phase. Moreover, a substantial portion of the impacts comes from the construction process, leaving minimal share from on-site construction work.
- b. The inventory results from all transportation phases throughout the life cycle of the flooring systems accounts for a relatively small but significant share of the environmental impacts. For the investigated live load/ slab span scenarios, when using the approximate average transportation distances within UK (Table 3-8), transportation contributes to between 5.75% and 11.5% of the total GWP and 7% to 14.5% of the total EE, which is consistent with previous research stating that transportation on average contributes to between 7% and 10% of total GWP and EE (Balasbaneh et al., 2022; Vukotic et al., 2010). These percentages can vary significantly due to the uncertainties in transportation distances or transportation modes, as highlighted in the sensitivity analysis. Although the transportation-related impacts increase with larger live loads and spans - due to the heavier slabs requiring more transportation trips- it is found that

their proportional contribution to the total inventory results decreases. This inverse relationship is a result of the transportation phase's relatively lower impact compared to the manufacturing phase.

- c. The on-site construction phase contributes only between 0.25% and 1.25%, respectively, of the total GWP and EE for the PUSS flooring system with the three concrete alternatives, whereas it is responsible for a range of 0.35% to 2.2% of the total GWP and EE for the hollow core slabs flooring system, in agreement with the case study presented by Balasbaneh et al., (2022) stating that on-site construction is responsible for around 2% of the total GWP and EE of hollow core slabs. These percentages are inversely proportional to the live load and span. The elevated results and percentages accompanying hollow core slabs is attributed to the necessity of adding a finishing layer.
- d. The end-of-life (EOL) phase comprises two sections: demolition to landfill, mainly considered for demolished concrete, and the recycling of steel elements in the flooring system. The demolition of concrete in the flooring systems appears negligible, responsible for less than 0.25% of the total inventory results for all floorings across all live load/ span scenarios. Conversely, recycling is a major contributor to the difference between the two flooring systems in the final results. Under the "50:50" allocation approach, steel recycling recovers between 4% and 7% of the total inventory results for hollow core slabs and between 10% and 18% for PUSS floorings. These percentages are directly proportional to the live load and span. However, the sensitivity analysis in section 3.5.3.2 demonstrates that the recovery percentage can vary significantly depending on the selected EOL recycling allocation approach.
- e. The inventory results across all live load/ span scenarios reveal an overall better environmental performance of the PUSS flooring system with all three concrete alternatives compared with hollow core slabs, considering both GWP and EE. PUSS with GPC emerges as the option with the lowest overall GWP, reducing it by 40% to 50% in comparison to hollow core slabs. It is followed by PUSS with LWC, which achieves savings between 37% and 46% of the total GWP generated by hollow core slabs, and finally, PUSS with NWC, which demonstrates reductions between 24% and 33% of the total GWP generated by hollow core slabs. Regarding EE, PUSS

with LWC is identified as the option with the lowest overall EE, conserving between 21% and 35% of the total EE generated by hollow core slabs. It is followed by PUSS with GPC, achieving savings between 17% and 32% of the total EE generated by hollow core slabs, and finally, PUSS with NWC, which shows reductions of only between 6% and 20% of the total EE generated by hollow core slabs.

The reduction in the total inventory results for PUSS flooring compared with hollow core slabs is a cumulative effect derived from all life cycle phases. For the manufacturing phase, the reduction results from the use of less materials and the incorporation of concretes with less environmental impacts in PUSS with LWC and PUSS with GPC floorings. In transportation phase, savings are attributed to the lighter weights of PUSS slabs, enabling the transportation of larger number of slabs per truck loading. For the on-site construction phase, the wider PUSS units reduce the required number of slabs, subsequently minimising the number of lifts needed by tower cranes for slab placement. Hollow core slabs necessitate the use of additional on-site equipment, such as concrete pumps and compactors, for finishing layer placement. For concrete demolishing phase, there is negligible difference; however, the higher steel content in PUSS flooring allows for a greater recovery percentage during recycling.

3.7 LCA Study Limitations

While the LCA conducted in this chapter offers valuable insights into the environmental performance of different flooring systems, a number of limitations should be acknowledged. Firstly, the analysis excludes the maintenance and operational phase due to the limited availability of reliable and standardised inventory data for these stages. This omission may slightly underestimate the total environmental impacts, although previous studies suggest the contribution of this phase is often minimal for passive structural components.

Secondly, the study employs the ICE (2011) inventory database to quantify embodied energy (EE) and embodied carbon (EC), as it provides a more comprehensive dataset covering both indicators. While this version is slightly dated, it remains the most suitable for dual-indicator assessments. A verification exercise was carried out using the newer ICE v3.0 (2019) and ICE v4.0 (2024) databases, which include EC data only. The updated values resulted in an average increase of around 5% in EC figures across all flooring systems, without

altering the relative ranking or final conclusions. Therefore, retaining ICE (2011) inventory ensures consistency with both the embodied energy analysis and the peer-reviewed publication produced from this chapter.

Finally, the LCA results are specific to UK-based conditions, including transportation distances, material availability, and construction practices. While this enhances regional relevance, it may limit the direct applicability of the results to other geographical contexts with different infrastructure or material sourcing profiles.

3.8 Conclusions and Recommendations

Construction sector stands as a major contributor to environmental degradation, responsible for significant GHGs emissions and consuming considerable amounts of energy. Addressing the worldwide demand and in the meantime reducing these harmful effects can be achieved only by restricting the impacts of construction, given the economic growth and the escalating demand for new buildings to accommodate a growing population. A more viable approach involves the widespread adoption of sustainable and environmentally friendly construction practices. Several construction techniques are recognised as environmentally friendly alternatives to traditional construction methods. Notably, opting for prefabrication instead of on-site concrete casting, substituting cement in concrete with more sustainable materials, the use of lighter construction materials, and deploying optimised composite structural elements contribute significantly in reducing the environmental impacts and resource consumption.

This chapter evaluates the environmental performance of two flooring systems—PUSS and hollow core slabs—through a comparative LCA study. Both flooring systems demonstrate comparable functional behaviours in terms of fire resistance, thermal insulation, and the presence of voids for the passage of building services. To ensure similar structural performance, both systems were designed to withstand equivalent loads and compared across 16 live load/ slab span scenarios. The PUSS flooring system is assessed utilising three concrete alternatives: NWC, LWC, and GPC. The LCA includes evaluating the EE and GWP of the flooring systems from cradle-to-grave. The study highlights the environmental advantages of the fully prefabricated composite flooring systems (PUSS) and its benefits over the widely used hollow core precast flooring system.

The assessment outcomes reveal that, regardless of the flooring span and applied live loads, PUSS with GPC exhibits the most favourable performance in terms of GWP, closely followed by PUSS with LWC. However, in terms of EE, PUSS with LWC emerges as the top performer, with PUSS with GPC closely trailing. The marginal difference in the two impacts makes selecting the best option challenging. Nevertheless, the lighter weight of PUSS with LWC implies additional savings in inventory results through design modifications to the underlying structure, from beams to foundations. This characteristic makes it the flooring option with the best environmental performance in this study. Following these two floorings, PUSS with NWC ranks third, while hollow core slabs exhibits the least favourable environmental performance. Furthermore, the sensitivity analysis results confirm that variations in transportation distance and recycling allocation methods do not alter the relative ranking of the flooring systems. This robustness in ranking underscores the reliability of the findings despite potential uncertainties in these parameters.

The findings of this chapter indicate that various manufacturing approaches significantly influence the GHGs emissions and EE, ranked from most to least impactful, these approaches are: reduction of material consumption, off-site production, optimisation of the transportation distance and increasing slab unit width.

It is essential to note that the design of the analysed PUSS and hollow core units is in accordance with EC2 and EC4. The use of alternative design codes may yield different designs, consequently affecting the total inventory results and accordingly the derived curve-fitting equations. Nevertheless, the difference should remain within the acceptable limits and follow the same overall trend. In addition, while this study has yielded valuable outcomes, there is room for enhancement in future research to provide even more comprehensive outcomes. Two areas recommended for further research are discussed below:

1. The design of PUSS units is constrained by the utilisation of existing British steel parallel flange channel (PFC) sections. Incorporating custom-made sections into consideration has the potential to yield even more versatile designs. This expansion would facilitate the investigation of the impact of larger slab spans, given that the currently available sections can achieve a maximum span of 12 m in PUSS units. Future studies could also involve

exploring new calculation methodologies or generating new materials and equipment inventories instead of relying on published databases.

2. Moreover, for enhanced precision, future studies are encouraged to expand the sensitivity analysis by including other influential parameters, such as variations in material production processes, energy sources, or transportation modes, as briefly discussed in Section 3.5.3. In addition, detailed inventory results from operation and maintenance stage of the flooring systems can be considered, as well as end-of-life (EOL) concrete recycling. While these factors might not lead to significant changes in outcomes or substantial differences between flooring systems, their inclusion would contribute to the overall accuracy of the outputs. Lastly, examining the impact of flooring systems on underlying structural elements and quantifying the resultant material savings, when added to the total inventory results of the floorings, has the potential to significantly enhance the environmental performance of lighter flooring systems.

Chapter 4

Experimental Four-Point Bending Tests

4.1 Introduction

Literature review identified the need for investigating the flexural behaviour of the prefabricated ultra-shallow flooring system (PUSS) experimentally. This chapter presents the four-point bending tests performed on a total of four PUSS units. The test specimens were designed to study the effects of concrete type, shear connection system and the depth of the slabs on the flexural behaviour of the slab. All test specimens were tested under displacement controlled monotonic loading. This chapter outlines the specimens design, details and preparation, test setup details, instrumentation, test observations and the results.

4.2 Experimental Program

The experimental work of this research investigates the flexural behaviour and failure mechanism of the prefabricated ultra-shallow flooring system (PUSS) under bending by performing four-point bending test. In this test, the shear resistance of the shear connectors and the degree of composite action caused by the shear connections between steel and concrete under bending are also examined. The details of four 4-point bending test specimens and test procedures conducted in this study are presented in the following sections.

4.2.1 Details of Test Specimens

In the construction practices, PUSS slabs are designed to have a fixed width of 2 m. This dimension is selected taking into consideration the possibility to fit in transportation means (Ahmed, 2019). The test specimens were initially designed to represent the actual construction practice 2 m width. In addition, more slabs with larger spans were initially planned to be tested. Due to the limited availability of allocated space and time for conducting the tests at George Earle laboratory (GEL), the number of test specimens was reduced, and specimens were scaled down while maintaining practical dimensions of 4 m clear span and 1.1 m width, representing scaled-down models of true slabs with 7.3 m spans. Two shear connectors systems were used in the experiments and were selected based on the recommendations from literature, which are (a) web-welded shear studs with

horizontally lying steel dowels (WWSS with dowels) and (2) horizontally lying dowels only (Ahmed, 2019). The tests investigated the effects of:

- 1) Two shear connection systems:
 - a) WWSS with dowels
 - b) Dowels only
- 2) Two types of concrete:
 - a) Normal weight concrete
 - b) Lightweight aggregates concrete using Lytag aggregate
- 3) Two steel sections (with different depths):
 - a) 230 mm depth (steel section 230x75x26 PFC)
 - b) 300 mm depth (steel section 300x100x46 PFC)

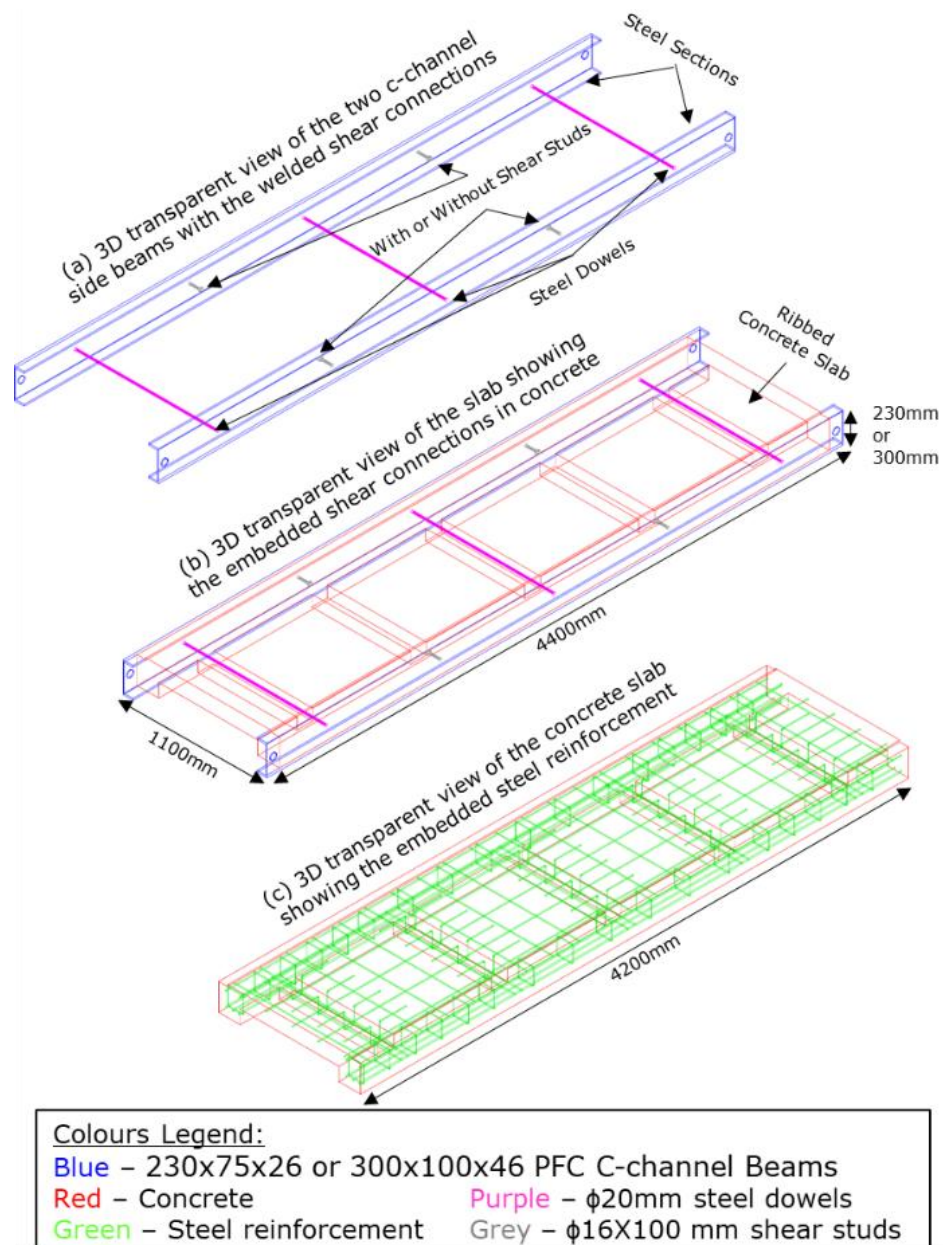


Figure 4-1: 3D view of the details of test specimens

Two 230x75x26 PFC channel steel sections are used as edge beams for three specimens, while two 300x100x46 PFC channel steel sections are used for specimen NWC-300-SD. For the three of the specimens, the shear connection system is composed of three steel dowels of Ø20 mm (spanning across the width) welded to the web posts of each PFC steel beam passing through the slabs ribs. In addition, two shear studs with Ø16 mm are welded horizontally to the web posts of each beam at the remaining two rib locations, as shown in Figure 4-1. For LWC-230-D specimen, only three steel dowels with Ø20 mm are used. Note that for all the tested specimens, shear connectors are welded at the midpoint of the slab depth, at a depth of 115 mm for specimens with 230 mm depth, and at a depth of 150 mm for the fourth specimen, which has 300 mm depth. Finally, two of the specimens are cast with normal weight concrete and the other two with lightweight concrete – with Lytag aggregates. The dimensions and differences between the test specimens are presented in Table 4-1. In addition, detailed drawings of all the four specimens are illustrated in Appendix B.

Table 4-1: Specimen test matrix

Specimen	Specimen name	Width (mm)	Length (mm)	Depth (mm)	Steel Beam size	Concrete type	Shear connectors	Degree of shear connection (η)
1	NWC-230-SD	1.1	4.4 (4 m clear span)	230	230x75x26 PFC	NWC*	3 x Ø20 mm steel dowels with	100%
2	LWC-230-SD					LWC*	4 x Ø16 mm WWSS	100%
3	LWC-230-D					LWC	3 x Ø20 mm steel dowels only	67%
4	NWC-300-SD			300	300x100x46 PFC	NWC	3 x Ø20 mm steel dowels with 4 x Ø16 mm WWSS	57%
*NWC and LWC stand for normal weight concrete and lightweight concrete with Lytag, respectively.								

The implemented shear connectors, which are a combination of WWSS and steel dowels or steel dowels only, compose the longitudinal shear connection system. However, the longitudinal shear connection system also affects the bending resistance of PUSS units due the composite action between steel beams and the concrete slab. Using the principle of equilibrium between tension and compression, the depth of plastic neutral axis (PNA) in PUSS units can be calculated at different degrees of shear connection, where the degree of shear

connection η ($\eta = R_q/R_c$) is the ratio of the longitudinal shear resistance of the shear connectors, R_q to the compressive resistance of the slab in full shear connection, R_c .

In order to estimate the required type, spacing and size of shear connectors to achieve full shear connection in the first two specimens, and to evaluate the degree of shear connection (η) in the remaining specimens, the shear resistance of the employed shear connectors and the longitudinal shear between steel beams and concrete slab need to be evaluated. Equation 4-1 is utilised in this study to assess the shear resistance of the shear connectors. However, it is important to note that the procedure outlined in Eurocode 4 (CEN, 2005) for calculating longitudinal shear between steel and concrete is not directly applicable to the studied flooring system. This procedure is primarily designed for vertical headed shear studs connecting top concrete slabs to bottom steel beams. In the case of PUSS units, horizontal shear connectors welded to the sides of the steel beams connect them to the concrete slab. Therefore, an alternative approach is adopted in this study to evaluate the longitudinal shear between steel and concrete, which is based on the concept of shear flow in built-up members (q).

Equation 4-1

$$q = VQ / I$$

Where: q is the shear flow between the composite members (steel section and concrete) in unit of shear force per unit of length,
 V is the value of the shear force at the section,
 Q is the first moment of area of steel section in relation to the neutral axis,
and I is the moment of inertia of the entire cross-section about the neutral axis.

The calculation of shear flow of each specimen involves substituting the shear force related to the section's bending moment capacity. Then, the total longitudinal shear force between steel and concrete is determined by multiplying the shear flow (q) by the shear span. Finally, the necessary spacing and size of shear connectors to achieve full shear connection are estimated using their shear resistance capacities derived from Equation 2-4 ($P_{sd} = 1.873(f_{ck}da_r)^{0.835} \leq 0.8f_uA_s$). It is worth noting that the calculated total longitudinal shear forces

between steel side beams and concrete slab are relatively small and the utilisation of only 5 shear connectors with 870 mm spacing on each side of the slabs of 230 mm depth is sufficient to achieve full degree of shear connection. This is primarily due to the relatively low magnitude of first moment of area associated with steel sections (Q) as they are small in area and their neutral axes are close to the neutral axes of the composite sections.

4.2.2 Specimens Preparation

The fabrication of formwork and shuttering for the concrete ribbed slabs and steelwork (from welding of shear connectors to shaping of reinforcements) were conducted by SC4 Ltd. (a British steel fabricator) (Figure 4-2). to provide lifting anchors for the slabs, holes with 50 mm diameter were drilled at the two ends of the side C-channel steel beams.

Ready-mix concretes conforming to BS EN 197-1 (BSI, 2011a) were cast in the prepared formworks at the worksite of SC4 on two separate days, the first day for casting NWC and the second day for LWC. A vibrator was used to ensure appropriate compaction (Figure 4-3). Concrete sample cubes and cylinders specimens were prepared from the same ready-mix concrete used for the specimens (Figure 4-4 (a)). NWC and LWC used in the four specimens were both of concrete class 20/25, with a maximum aggregate size of 14 mm. Slump tests on both types of concrete gave an average of around 100 mm slump (Figure 4-4 (b)). Afterwards, slabs were kept at the worksite for 30-50 days for curing at an average temperature of about 15°C before moving them to the University of Leeds to prepare for testing.

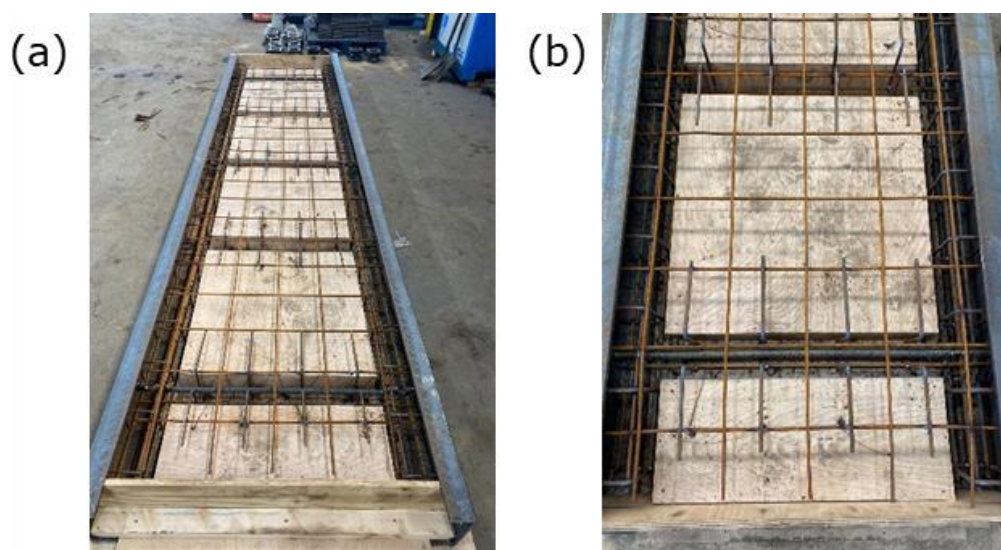


Figure 4-2: Prepared specimens before casting concrete



Figure 4-3: Cast specimen

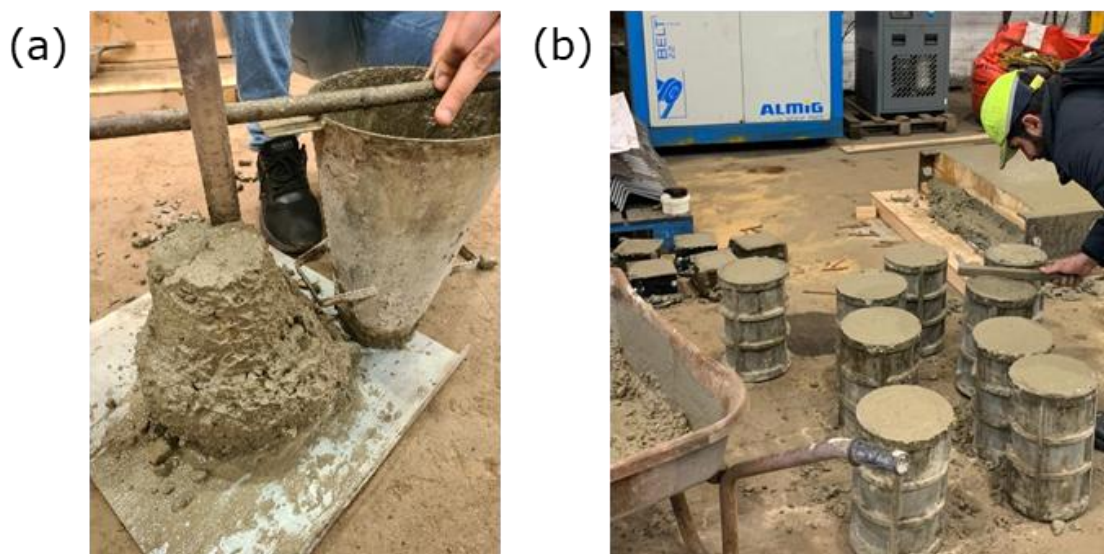


Figure 4-4: (a) Slump test (b) Prepared concrete cylinders and cubes

4.2.3 Materials Properties

4.2.3.1 Concrete Properties

From the concrete cubes and cylinders samples taken from the cast concrete, the density of NWC and LWC were measured to be 2230 kg/m^3 and 1560 kg/m^3 respectively. Standard tests were carried out to determine the properties of all materials (concrete and steel). The material properties of concrete obtained from compression and splitting tensile tests performed on the concrete cubes (at day 7, day 14, day 28 and on-the-day of the tests – 3 cubes each day) and 3 concrete cylinders (on the day of experiments) in accordance with BS EN 12390-3 (BSI, 2019b) and BS EN 12390-6 (BSI, 2009) are presented in Table 4-2. Figure 4-5 shows the average stress-strain curves for the cylinder compressive strength of NWC and LWC on tests days. In addition, Figure 4-6 presents pictures taken during and after the concrete samples testing process.

Table 4-2: Concrete properties

Specimen	Concrete type	Average cube compressive strength, (MPa) – Day 7, 14, 28			Average strength, (MPa) – Day of the Experiment			E_c (GPa)
		Day 7	Day 14	Day 28	Cube - compressive	Cylinder - compressive	Split tensile	
NWC-230-SD	NWC	11.7	17.5	20.6	26.9	22.4	2.15	28.5
LWC-230-SD	LWC	11.4	16.5	19.7	26.2	21.56	1.86	11.05
LWC-230-D	LWC	11.4	16.5	19.7	26.4	22.46	1.97	11.7
NWC-300-SD	NWC	11.7	17.5	20.6	27.1	22.5	2.2	26.9

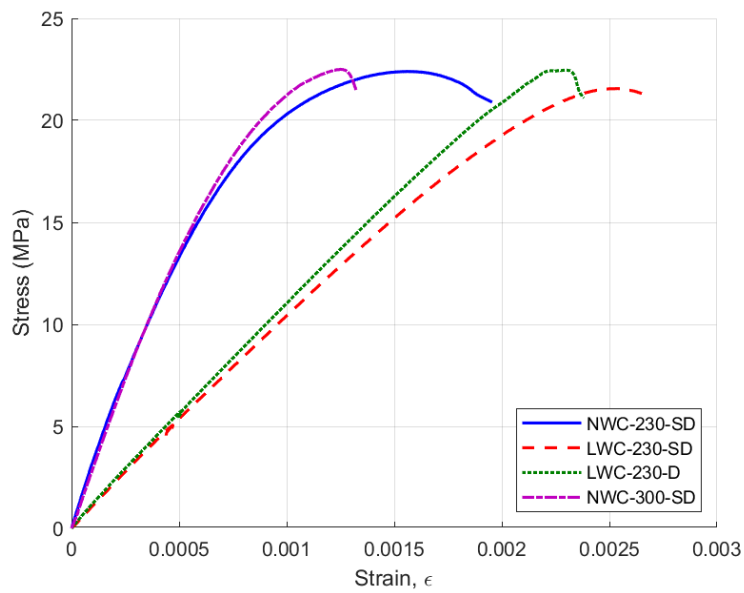


Figure 4-5: Average stress-strain curves of cylinder compressive tests for NWC and LWC on the day of the experiments

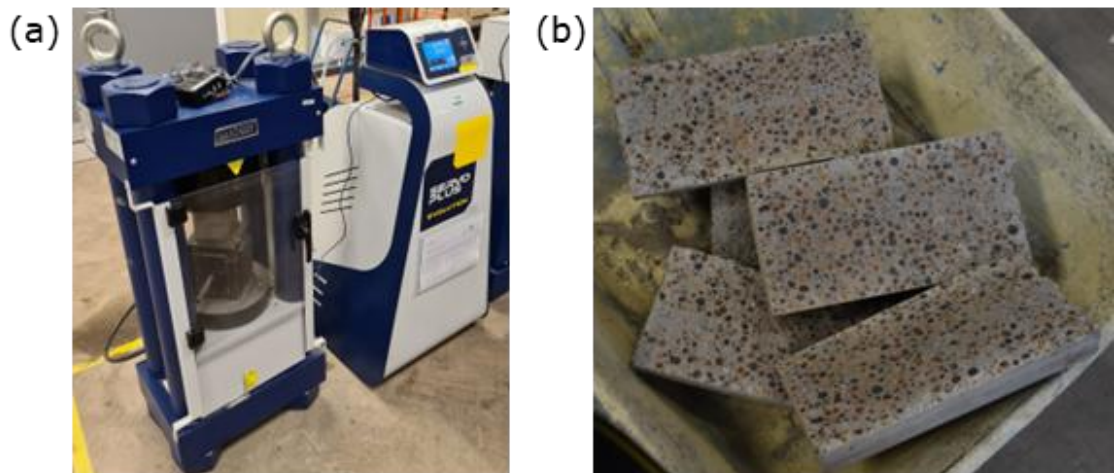


Figure 4-6: (a) NWC concrete cube under compression test; (b) LWC concrete cylinders after splitting tensile test

4.2.3.2 Steel Properties

A total of 10 coupons were machined from the steel section of the test specimens. Six of the coupons were cut from the 230x75 steel sections (3 from webs & 3 from flanges) and the remaining four were cut from the 300x100 steel sections (2 from webs & 2 from flanges). The steel coupons were tested under uniaxial tension according to ISO 6892-1 (ISO, 2019). Figure 4-7 (a) shows a picture of steel coupons after testing and Figure 4-8 displays the stress-strain curve of the steel section coupons. Similar tests were also carried out on coupons from the steel rebars and shear connectors (steel dowels and shear studs) as presented in Figure 4-7 (b) and their associated stress-strain curves are provided in Figure 4-9. The average tensile strength of steel coupons obtained from steel beam section, rebars and shear connectors are presented in Table 4-3.



Figure 4-7: (a) Steel rebar during tensile test; (b) Steel section coupons after tensile test

Table 4-3: Average mechanical properties of steel sections, rebars and shear connectors

Coupons from	f_y (MPa) (Average)	f_u (MPa) (Average)	E_s (GPa) (Average)
Flanges of 230x75x26 PFC	405	528	200
Webs of 230x75x26 PFC	434	545	200
Flanges of 300x100x46 PFC	448	543	200
Webs of 300x100x46 PFC	455	547	200
Ø20 mm steel dowels	484	657	210
Ø16 mm shear studs	600	700	210
Ø8 mm - Ø12 mm steel rebars	571	677	210

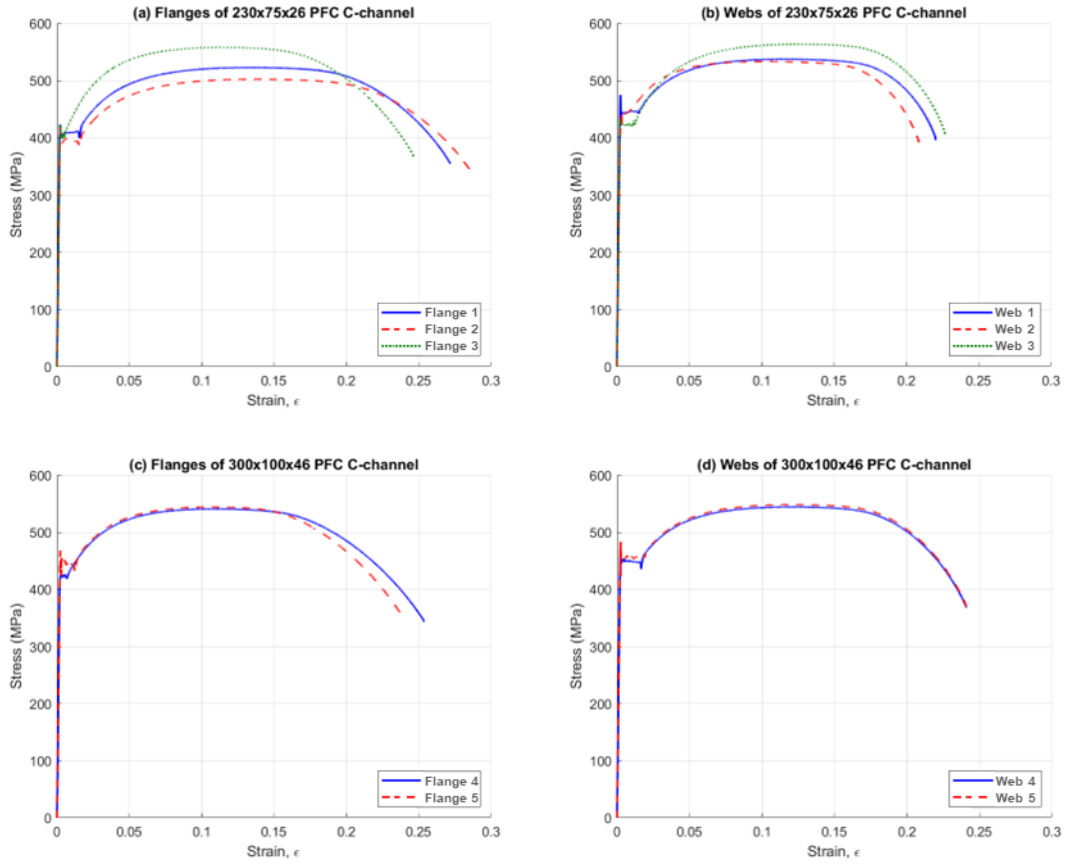


Figure 4-8: Stress-strain curves of steel section coupons

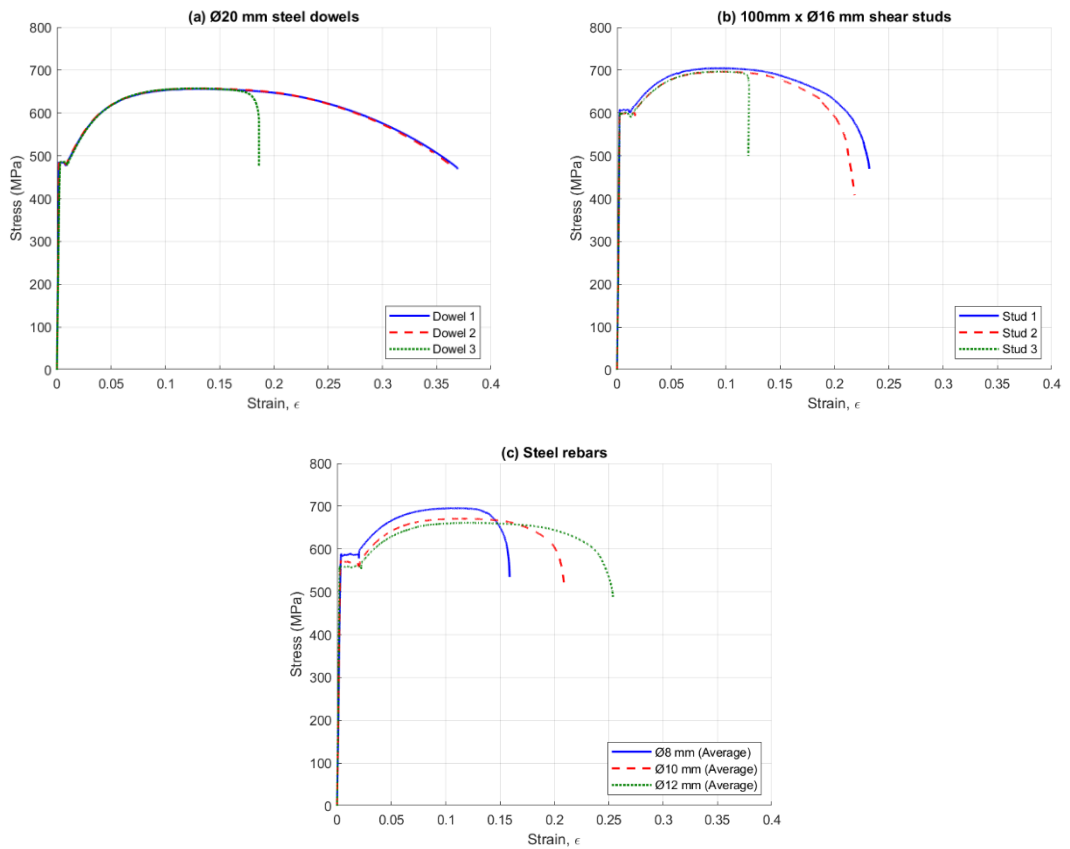


Figure 4-9: Stress-strain curves of shear connectors and steel rebars

4.2.4 Test Setup and Loading Protocol

The four-point bending tests are carried out in accordance with the specifications of Eurocode 4 (CEN, 2004b). Test specimens are simply supported near the two ends of their lengths with an overhang of 100 mm at both ends. Two concentrated line loads of equal magnitudes are applied symmetrically on the middle part of the specimens using a 1000 kN hydraulic jack and spreader beams to translate the load from the hydraulic jack to the specimens. The distance between the centreline of the line loads is 1000 mm and it is the same for all the tests. A load cell is connected to the hydraulic jack to record the loading readings and the whole loading apparatus is attached to the reaction frame as shown in Figure 4-10 to Figure 4-12.

The static displacement controlled monotonic loading is applied in cycles, starting by applying three pre-loading incremental loading cycles in the elastic loading range to break local bonds between concrete and steel as well as to establish the residual deflections and slips within the elastic region. Each of these cycles is followed by a release. Then, a fourth cycle is applied on specimens up to the ultimate capacity (maximum expansion of the hydraulic jack) as presented in Table 4-4. To properly evaluate the flexural behaviour of PUSS in the post-elastic range, the four-point bending tests are displacement controlled, with a sufficiently small displacement rate (1 mm/minute) to avoid dynamic impacts and to be able to track every damage in the specimens. Each test takes at least 3 hours to conduct which is more than the minimum duration for the test specified by Eurocode 4 (CEN, 2004b) stating that similar four-point bending tests on composite slabs should take at least 1 hour before reaching failure.

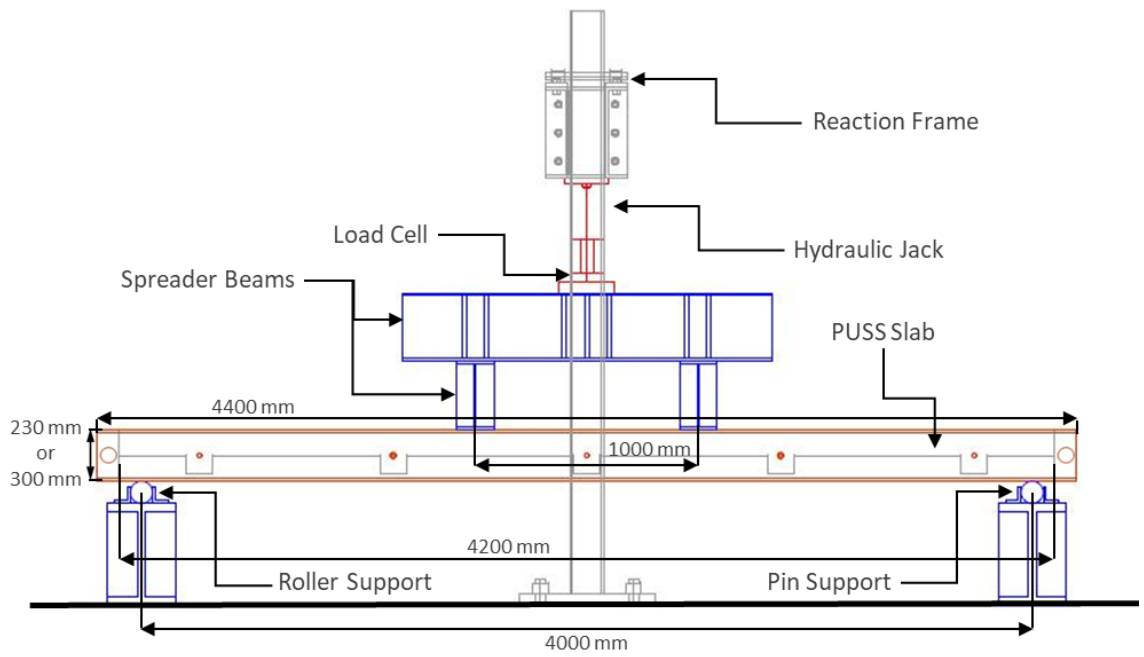


Figure 4-10: Side view sketch of the test setup for 4 m span PUSS slab

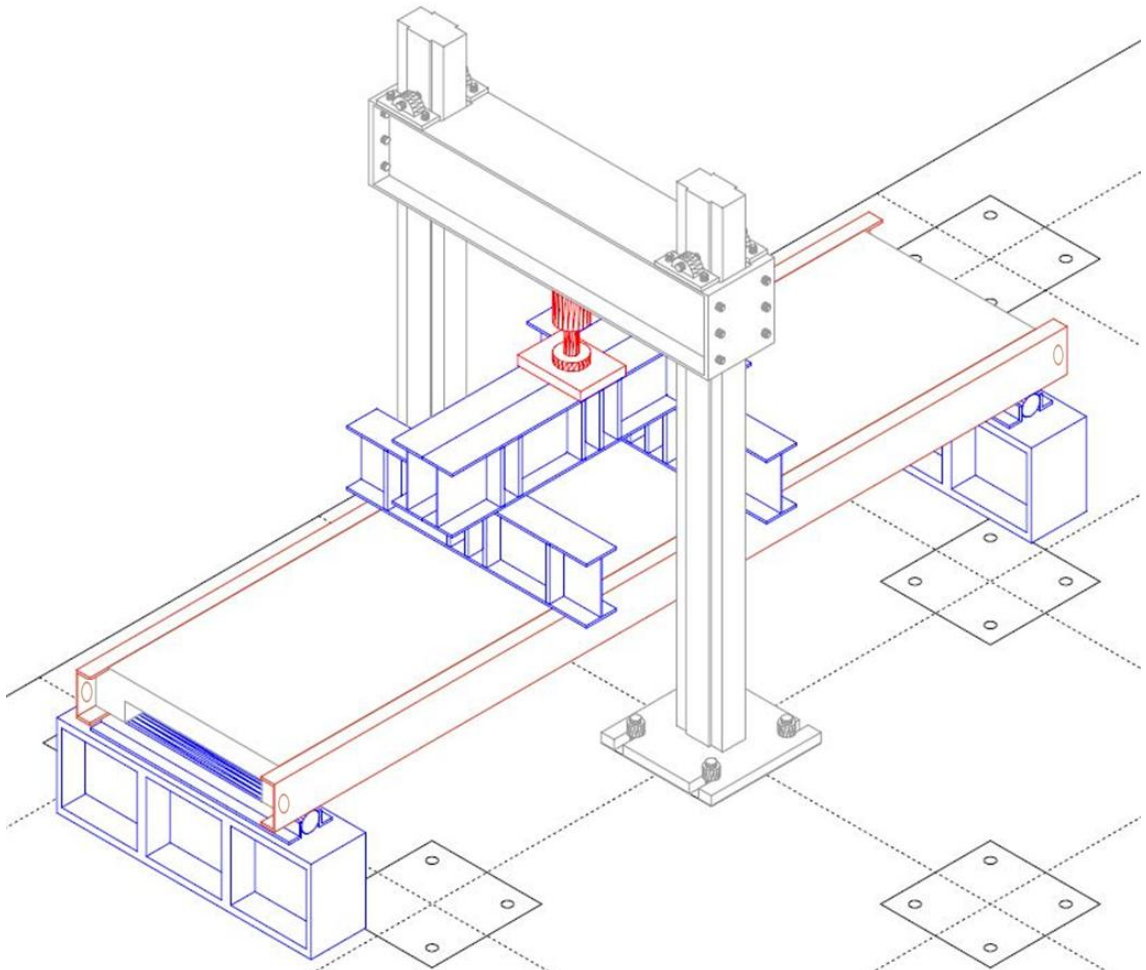


Figure 4-11: 3D view sketch of the test setup for 4 m span PUSS slab on the GEL floor

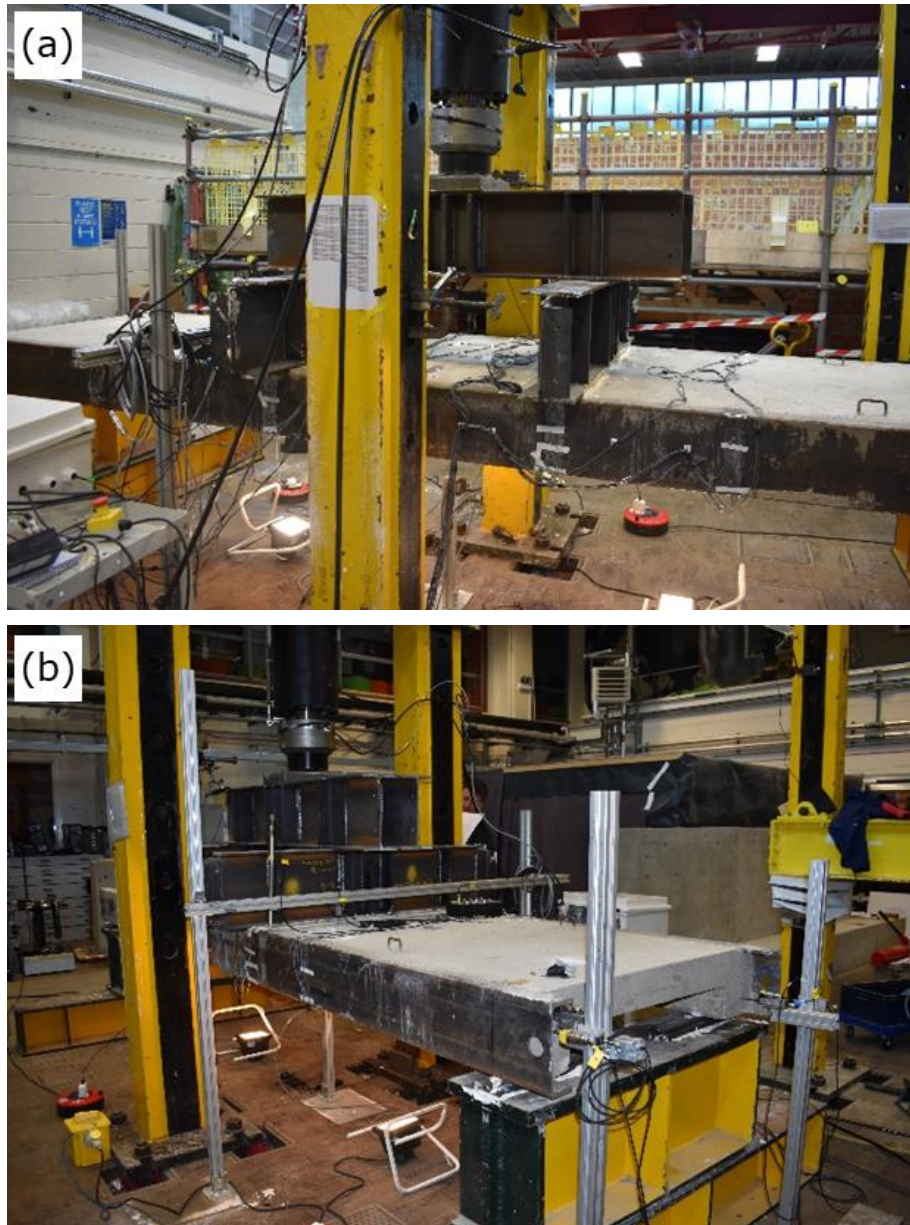


Figure 4-12: Test setup

Table 4-4: Loading cycles

Loading cycles	Aimed displacement	Displacement in mm
First cycle	1/3 x SLS max allowed deflection	≈ 4 mm
Second cycle	2/3 x SLS max allowed deflection	≈ 8 mm
Third cycle	1 x SLS max allowed deflection	≈ 12 mm
Final cycle	Maximum expansion of the hydraulic jack	≈ 170 mm
<ul style="list-style-type: none"> Maximum allowable SLS deflection = $\text{span}/360 = 4000/360 = 11.11 \text{ mm}$ 		

4.2.5 Instrumentation

A 1,000 kN hydraulic jack is used to apply the load (with a maximum extension of around 170 mm). A calibrated load cell is placed under the jack to measure the applied load, as shown in Figure 4-10 to Figure 4-12. To monitor the development

of cracks with the increasing load-deflection, a total of 8 cameras are distributed around the test setup to capture the cracks propagation on videos/ photos since it was dangerous to be near slab while testing to visually monitor the cracks.

In addition, each specimen is calibrated to measure the strain, displacement and end-slip at various locations. Instruments such as strain gauges (singles and rosettes) as well as linear variable differential transformers (LVDT) are installed at multiple regions above the slabs. These regions are classified into 3 groups based on their distance from the mid-span of the slab, where region (I) stands for the strain gauges fixed at mid-span, while regions (II) and (III) are for strain gauges fixed at 0.5 m and 1 m distances from mid-span, respectively. The instruments are linked to a data logger (DAQ) system, which is connected to a computer to record all the readings at different load levels at once. The general instrumentation layout for the test setup is shown in Figure 4-13. A total of twenty-three 5 mm strain gauges, seven 60 mm single strain gauges, four 5 mm rosettes and ten LVDTs are placed over each slab, taking into consideration the symmetry of the slab and loading frame.

The details of the attached strain gauges and LVDTs are as follows:

- 23 of 5 mm strain gauges were placed on the two steel side beams to measure strain-stress development in the slabs. They were distributed along 5 main lines: (a) CL of the slab, (b) 2 lines directly below the spreader beams and (c) 2 lines 1 m from the slab CL. Part of them were placed on the top and bottom flanges and the most were placed on the web at 1/4, 1/2 and 3/4 of the slabs depths.
- In addition to these strain gauges, 4 of 5 mm tri-axial Rosettes strain gauges were placed on the steel side beams on the lines below the spreader beams where the maximum stresses are expected to develop.
- 7 of 60 mm strain gauges were placed on the top surface of the concrete slab at various locations to monitor the stress development in concrete.
- 4 LVDTs were placed horizontally at one end of the slab, two on the concrete slab and the other two on the steel side beams to measure the slip between steel and concrete.
- 1 vertical LVDT was attached to the hydraulic jack to measure its expansion, and 5 additional vertical LVDTs were also placed on the top

and the bottom of the slab to measure the deflection variation at different locations.

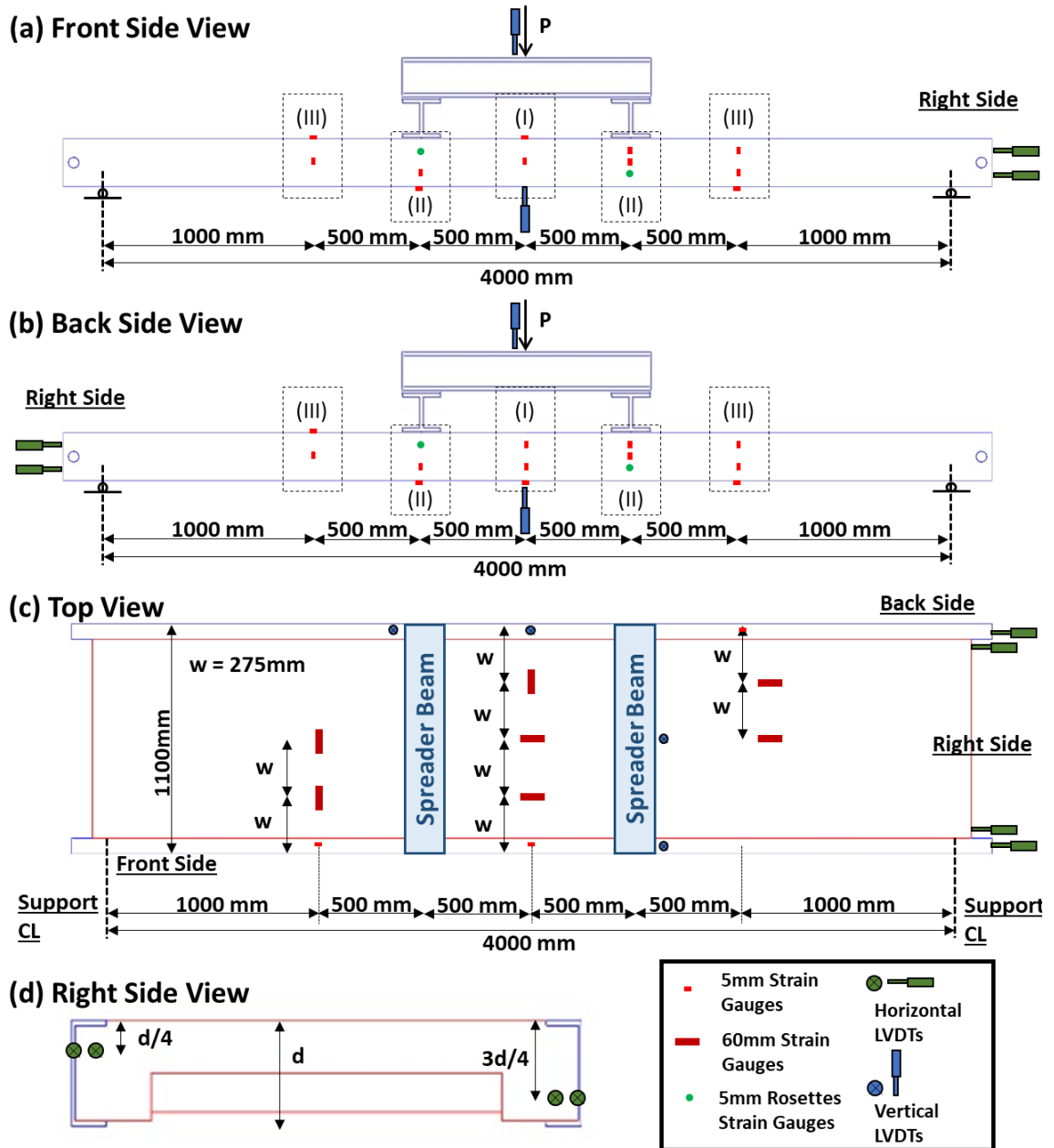


Figure 4-13: Strain gauges, rosettes strain gauges and LVDTs layout

4.3 Test Results

The summary of the results obtained from the four 4-point bending tests on PUSS units is presented in the following sections.

4.3.1 Maximum Moment vs. Mid-span Deflection

The four experiments are ended upon the hydraulic jack extending to its maximum expansion (around 170 mm), while load plateauing is reached. At this point, none of the specimens shows complete collapse but multiple of the strain

measurements in the steel exceeds the yielding point. In addition, several long deep cracks are detected at the bottom surface of the concrete slabs. At tests termination, all specimens' mid-span deflections exceed 160 mm (L/25 or higher), surpassing significantly the serviceability (SLS) limits. Consequently, specimens are considered to have failed in all practical purposes. From the data collected from the LVDT attached to the hydraulic jack and the load cell, the "Maximum Moment vs. Mid-span Deflection" curves are derived for each test specimen and presented in Figure 4-14. In addition, Table 4-5 gives a comparison of the value of the load reached at specific deflections during the experiments.

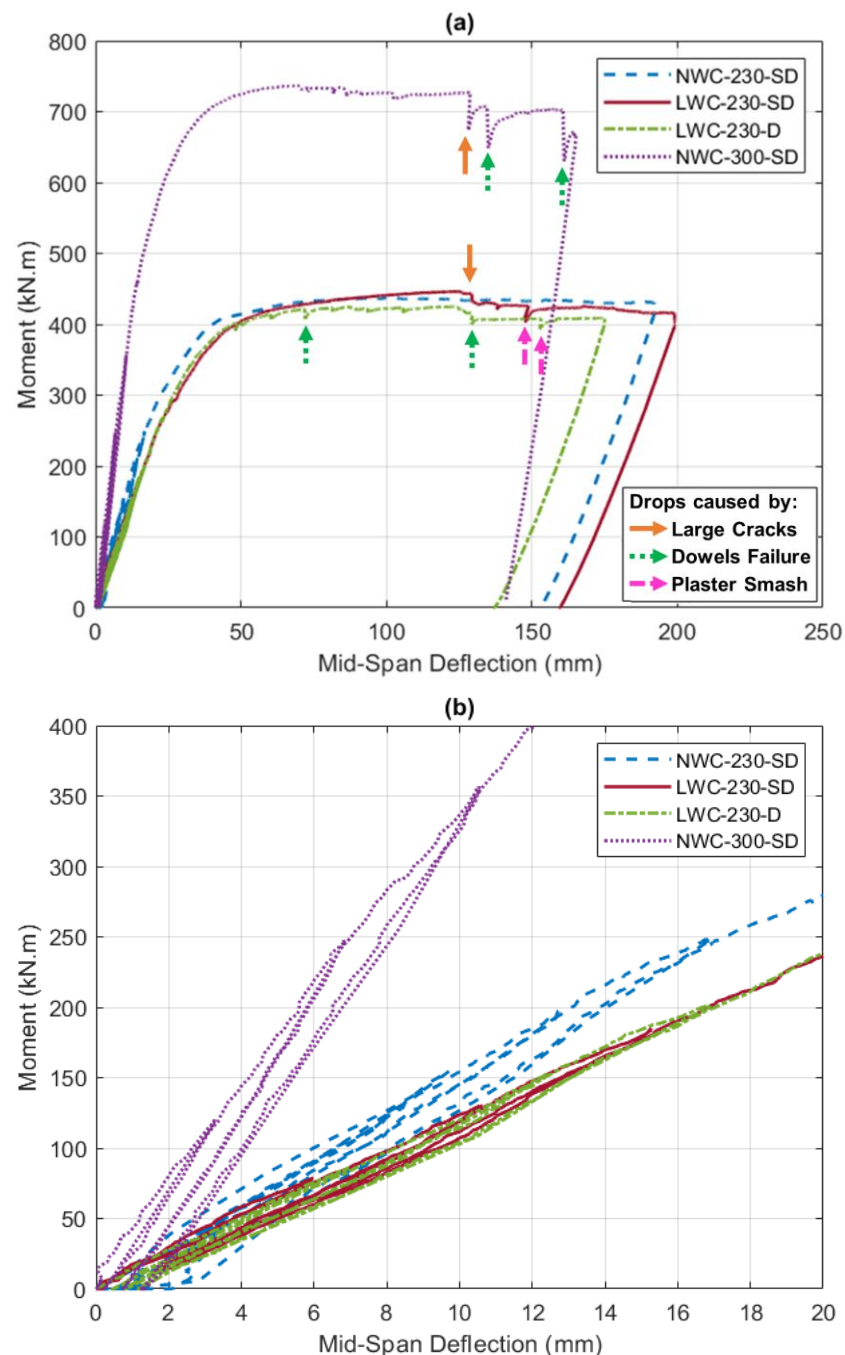


Figure 4-14: Relationship between moment and mid-span deflections (a) for the whole tests (b) for the first three pre-loading cycles

Taking a close look at the first 3 loading cycles in (Figure 4-14 (b)), three different initial stiffnesses are obtained as anticipated, with NWC-300-SD being the largest due to the larger steel section, NWC-230-SD in the middle, and both LWC-230-SD and LWC-230-D having the lowest because of lower modulus of elasticity of LWC in comparison to NWC. It is worth noting that the latter two specimens have the same initial stiffness as they are made of the same steel C-channel section and concrete material, even though that different shear connectors are employed. This shows that the initial stiffness of PUSS specimens is not influenced by the type and amount of shear connectors employed in the slabs, however, it is a function of the size of the steel section as well as the concrete strength and material. The figure also displays the effectiveness of the first three preloading cycles of all four tests in maintaining the same stiffness after each cycle and breaking the local bonds between steel and concrete. By having an overall view of the whole tests (Figure 4-14 (a)), it is noticed that other than the initial stiffness, all four specimens show similar behaviours during the tests except NWC-300-SD reaching much higher capacity due to its deeper PFC sections. Furthermore, it is observed that the transition from the elastic region to yielding for both NWC specimens is steeper in comparison to LWC specimens. After yielding, all specimens start to gain a small additional capacity up to reaching the plateau. At the early plateau stage, they behave in an identical manner with NWC specimens having smoother lines until larger cracks and shear connectors failure start to appear causing some drops in the curves, which is discussed in more detail in sections 4.3.4 and 4.3.5.

Table 4-5: Comparison of load values at specific stages of the tests

Mid-span displacement (mm)	Load (kN) in specimen			
	NWC-230-SD	LWC-230-SD	LWC-230-D	NWC-300-SD
4 mm of first loading cycle	119.4	77.7	67.4	192.1
8 mm of second loading cycle	216.5	130.3	129.2	377.8
12 mm of third loading cycle	296.5	196.7	192.1	531.3
20 mm of the final cycle	414.0	315.0	318.2	735.0
40 mm of the final cycle	551.0	495.0	504.0	941.6
Maximum load (kN)	582.9	594.9	566.4	982.2
Moment at maximum load, i.e. moment capacity (kN.m)	437.2	446.2	424.8	736.6

By comparing the maximum loads reached in each specimen from Figure 4-14 (a) and Table 4-5, it is clear that the LWC-230-SD specimen gained a slightly higher maximum load in comparison to the NWC-230-SD specimen, although both have concretes of similar strengths. However, the use of lighter concrete in LWC-230-SD specimen reduces the dead load of the slab and allows it to gain capacity for higher live loads. On the other hand, LWC-230-D specimen showed lower capacity in comparison to the aforementioned specimens as the shear connectors used, which are composed of 3 steel dowels only, provide a lower degree of shear connection.

Table 4-6: Evaluation of test results in comparison to calculated capacities using stress block method

	NWC-230-SD	LWC-230-SD	LWC-230-D	NWC-300-SD
Calculated moment capacity of steel section, M_s (kN.m)	304.9	304.9	304.9	678.4
Calculated moment capacity of composite section at full degree of shear connection, $M_{c,Full}$ (kN.m)	409.3	408.7	408.7	837.5
Calculated degree of shear connection (η)	100%	100%	67%	57%
Calculated moment capacity of composite section at the degree of shear connection, M_c (kN.m)	409.3	408.7	399.7	814.0
Test moment capacity, M_{Test} (kN.m)	437.2	446.2	424.8	736.6
M_{Test}/M_c	1.068	1.092	1.063	0.905
Modified moment capacity of composite section at full degree of shear connection based on test results, $M_{c,Test,Full}$ (kN.m)			446.2	-
Re-calculated degree of shear connection (η)			63%	-
Re-calculated moment capacity of composite section at the degree of shear connection, M_{c2} (kN.m)			432.2	-
M_{Test}/M_{c2}			0.983	-

Finally, comparing the maximum moment capacities (M_{Test}) obtained from the tests to the calculated maximum moment capacities using the stress block method (M_c), a difference between 6.3% and 9.5% is recorded (Table 4-6). This can be attributed to workmanship issues during the casting of the specimens outside controlled laboratory conditions. This indicates that the stress block

method is accurate enough (<10% difference) to be used in predicting the moment capacity of PUSS units. For a more precise prediction of the degree of shear connection in the LWC-230-D specimen, LWC-230-SD specimen is taken as a reference and its test moment capacity is considered in Table 4-6 to be equal to the calculated moment capacity of LWC-230-D at full degree of shear connection. This makes the difference between the test's maximum moment capacity (M_{Test}) and the calculated maximum moment capacity (M_{c2}) for LWC-230-D equal to 1.7% which is fairly low. It is worth mentioning that when ANSI/AISC 360-10 (Equation 2-8 - $P_s = 0.5A_s\sqrt{f_{ck}E_c} \leq 0.75f_uA_s$), AASHTO (Equation 2-9 - $P_s = \emptyset 0.5A_s\sqrt{f_{ck}E_c} \leq 0.75f_uA_s$) and EC4 – Annex C (Equation 2-10 - $P_{Rd,L} = \frac{1.4k_v(f_{ck}da'_r)^{0.4}\left(\frac{a}{s}\right)^{0.3}}{\gamma_v} \leq \frac{0.8f_u\pi d^2}{\gamma_v}$) equations are employed to evaluate the degree of shear connection for LWC-230-D and NWC-300-SD, the calculated results did not match well the experimental results. The calculated values show that the LWC-230-D specimen exhibits degree of shear connection between 90% and 100% while the NWC-300-D specimen exhibits degree of shear connection of 100%. The moment capacities obtained from the tests (M_{Test}) as shown in Table 4-6 for the two specimens, demonstrated that the moment capacities reached in the tests are closer to the calculated values of moment capacities (M_c) at the degree of shear connections obtained from Equation 2-4 (Ahmed & Tsavdaridis, 2020), which proves that for the tested specimens, this equation is more accurate than the aforementioned equations (Equation 2-8, Equation 2-9 and Equation 2-10) in estimating the shear resistance of the shear connectors P_{sd} in PUSS. However, as this equation is derived barely on direct shear push-out tests results, it can be improved by taking into consideration the results from this research which studies the performance of the shear connectors under flexural loading.

4.3.2 Stress Distribution in Steel Sections

Figure 4-15 displays the recorded strains measured in the PFC steel sections at various stages of the tests and at multiple distances from slabs' mid-spans (locations I, II and III in Figure 4-13 (a)). The strain gauges at these locations are placed at the top and bottom flanges as well as three strain gauges along the height of the webs to capture the stress distribution along the height of the steel sections. The presented strain readings are from the stages of (1) the mid-elastic

region, (2) the beginning of the plateau, and (3) the mid-plateau of each specimen. Note that each specimen has strain gauges placed at multiple symmetric spots to account for the unlikely event of having some damaged gauges; hence, some of the readings presented in the figure are averaged from more than one reading and some are for one reading only. In addition, as it was not possible to attach strain gauges on the top flanges at location II (directly below the load spreader beams), the provided strains in the figure at these locations are estimated by assuming a linear variation of strains through the steel section.

By taking an overall look at the figure, it is observed that the steel sections of all specimens have similar strain development during the test. General similarities and differences that can be derived from the figures are summarised below:

- 1) In all the locations of all specimens, the strains in the top flanges (which are in compression) are always lower than the strains in the bottom flanges (in tension), meaning the PNA of the sections is above the mid-height of the sections. Therefore, more focus is on the bottom strains in the following points. In addition, near linear variation of stresses over the cross-section can be captured.
- 2) Location III (1 m from the mid-span) has the lowest strains development at different stages of the tests as it is far from the maximum moment area (between the loading points), where the maximum strain in the bottom flanges at the mid-plateau stage barely reaches the yield strain (about $2100 \mu\epsilon$) with the exception for LWC-230-SD where the yield strain is not reached.
- 3) At location I (at mid-span), for the full shear connection specimens, i.e., NWC-230-SD and LWC-230-SD, the strains in the bottom flanges at the mid-elastic region are very close to the yield strain and this strain is exceeded in the start of the plateau region. On the other hand, for the other two specimens which have a lower degree of shear connection, lower strains are measured at the bottom flanges at these stages, just crossing the yield strain lines at the start of the plateau region.
- 4) For location II (below the point loads), the case is a slightly different as all the specimens have almost similar values of strains at mid-span and at the start of the plateau regions; being around the yield strain at the first stage and almost doubling this value of strain at the second stage.

- 5) At the third stage (mid-plateau), strains significantly increase in all the specimens, especially at the bottom flanges achieving over 10,000 $\mu\epsilon$ at locations I and II, which indicates reaching maximum capacities at these locations and leaving permanent deformations in the steel beams. The measured strains at these two locations are close to each other, which is mainly due to the constant moment between the two loading points. It can also be captured that at this stage and these locations, the stress variation along the depth of the steel sections is less linear. This is due to the high compression and tension stresses developed at the top and bottom flanges respectively because of bending after reaching the maximum capacities.
- 6) In all specimens, it is evident from the figures that the depth of the neutral axis exhibits slight variations across different locations within the same specimen. This phenomenon can be attributed to the upward shifting of the neutral axis positions as the tension steel begins to yield and concrete initiates cracking. Consequently, it is observed that, typically, locations closer to the mid-span where bending moments are higher, demonstrate elevated neutral axes compared to locations farther from mid-span (location III).

As one might expect, at the final stages of loading, where ultimate capacities are reached, the PFC steel sections should undergo web crippling under the high concentrated loads. However, this was not the case when testing the PUSS units, as the concrete partial encasement within the steel sections along the flanges and with shear connectors that prevent the steel sections from moving away from concrete, no obvious web crippling is noticed at any location along the steel sections.

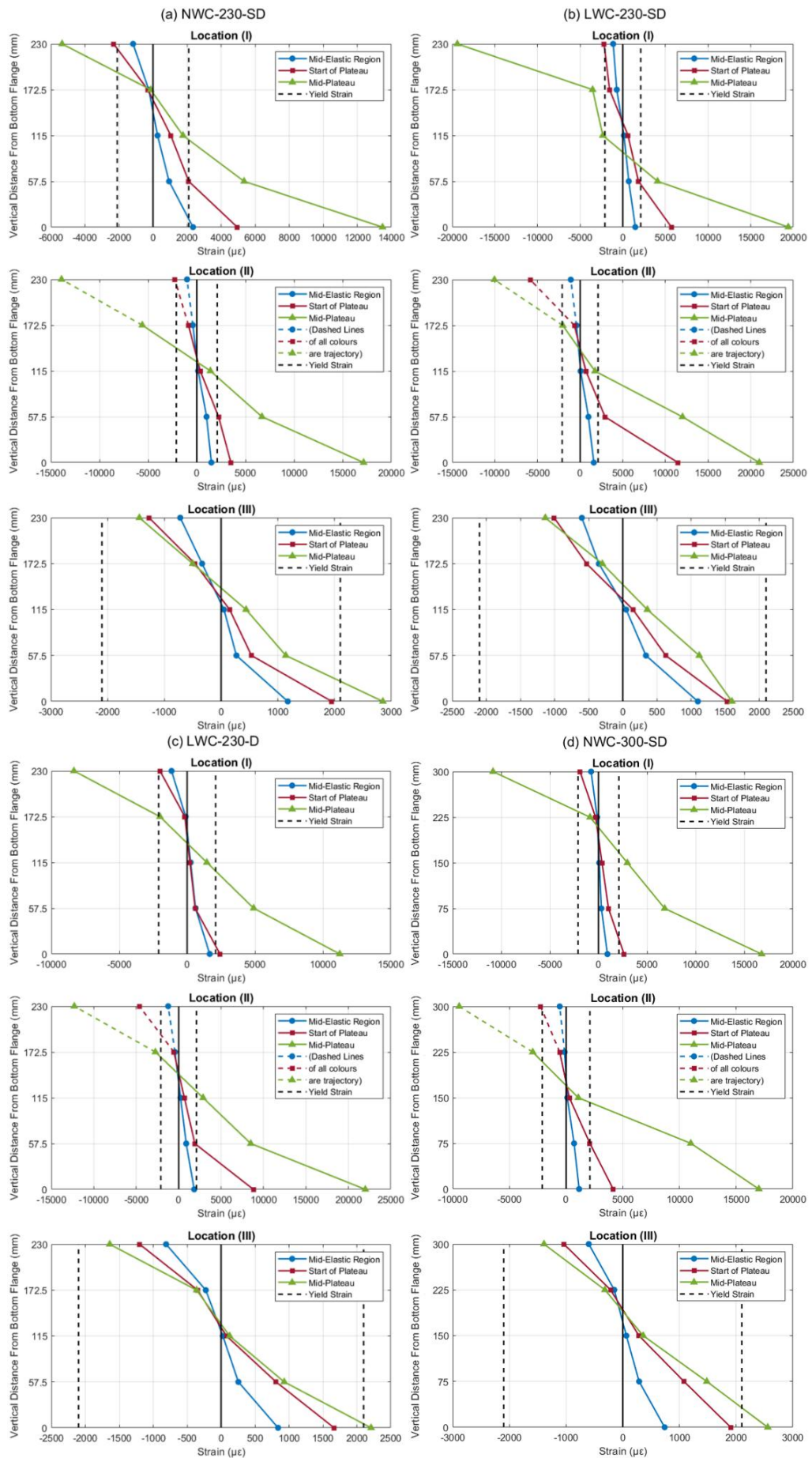


Figure 4-15: Strains measured in steel section at different locations and different stages of tests

4.3.3 Stress in Concrete Top Surface

Capturing stress development in concrete is more challenging in comparison to steel sections, as cracks developing right underneath the attached strain gauges can ruin the readings, making it difficult to record strains at the bottom surface of concrete. To obtain a general picture of the strain/stress development at the top surface of concrete, the relationship between the hydraulic jack opening and the longitudinal strains measured at the top surface of concrete along the centreline of the slabs is captured herein and presented in Figure 4-16. Figure 4-16 (a) depicts strains recorded at the mid-span of the slab and Figure 4-16 (b) depicts strains recorded at 1 m from the mid-span of the slab. Note that the strain gauge readings for the second location of LWC-230-SD are lost during the test and therefore not included in the figure.

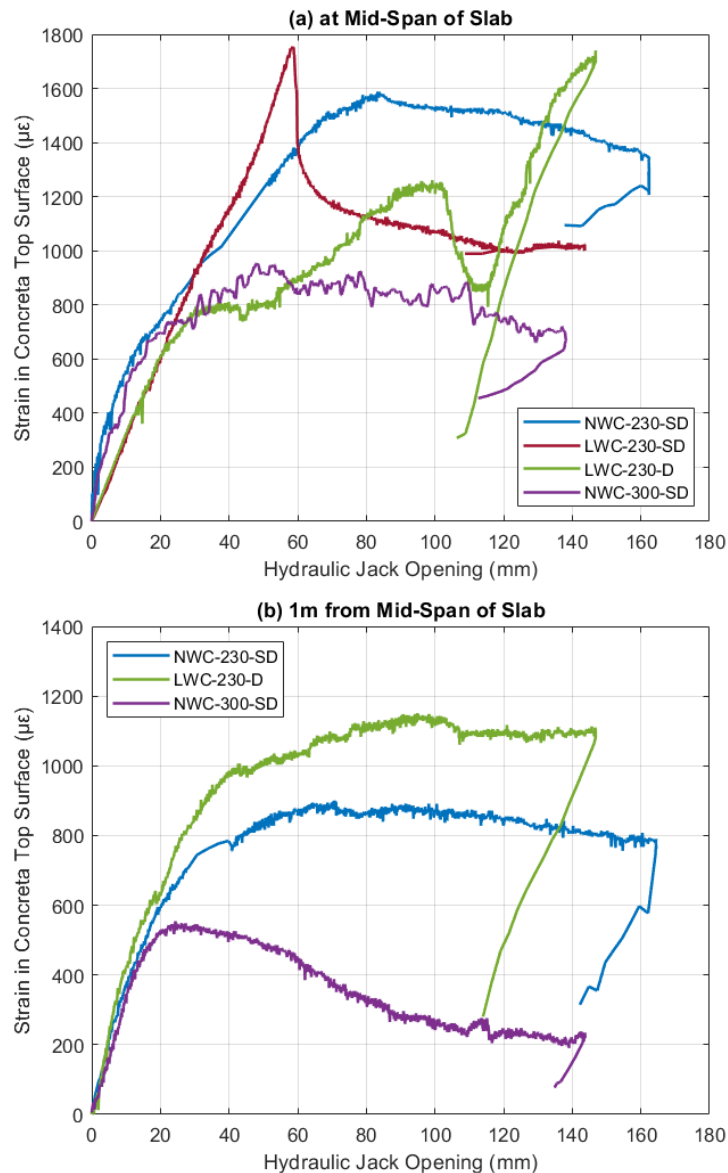


Figure 4-16: Strains measured along the CL of the top surface of concrete at (a) mid-span (b) 1 m from mid-span

From the two figures, some general outcomes can be concluded, as follows:

- 1) Moving farther from the mid-span reduces the measured strains (i.e. stresses) at the top surface of concrete because the applied moment becomes lower.
- 2) Test specimens with NWC have slightly higher stiffness at mid-span in comparison to specimens with LWC. This difference in stiffness is not very clear at 1 m distance from mid-span, which can be attributed to lower stress development at this location.
- 3) Because of the lower modulus of elasticity of LWC, similar stresses in LWC and NWC specimens result in higher strains in LWC in comparison to NWC. Therefore, the recorded strains in LWC specimens reach higher values during the tests in comparison to specimens with NWC. For example, specimens NWC-230-SD and LWC-230-SD are of comparable capacities and similar values of stresses are expected to be achieved at the concrete's top surface, which translates to higher strains in the LWC specimen.
- 4) By comparing the specimens of similar concrete materials (i.e., NWC-230-SD with NWC-300-SD and LWC-230-SD with LWC-230-D), it is observed that specimens with a lower degree of shear connection (LWC-230-D and NWC-300-SD) experience lower maximum strains developed in the concrete surface. This proves that the full capacity of concrete is not being utilised, as the shear connectors are not fully engaged and do not provide a full degree of shear connection. Moreover, it is noticed that at NWC-300-SD specimen (the one with the lowest degree of shear connection), at 1 m from the mid-span, the strains in the concrete started to decrease gradually after a 20 mm hydraulic jack opening, which is around the mid-elastic region. This shows that for specimens with lower degree of shear connection, at low moments locations, loads are mainly carried by steel sections with minimal contribution of the concrete.
- 5) The strain readings in LWC-230-SD at mid-span were expected to be larger, but a sudden reduction in strain was recorded at 60 mm hydraulic jack opening, which can be related to the occurrence of a crack beneath the strain gauge. Similarly, there is a drop in the strain for LWC-230-D at around 100 mm hydraulic jack opening due to the failure of one of the shear connectors at this point. Afterwards, the strains gradually resume increasing, showing redistribution of the loads after the failure of the shear connector.

4.3.4 Crack Development and Failure Mechanism

The video cameras placed beneath the test specimens allowed tracking of the crack development at the bottom ribbed surface of the concrete slab. The point at which cracks started to appear varies from specimen to specimen, but the main similarity is that they start with a horizontal hairline crack directly below the two loading points. The videos captured earlier development of visible cracks connected to the two sides of the slabs at lower loads in LWC specimens. For specimen NWC-230-SD, the horizontal hairline crack appeared during the final cycle at hydraulic jack opening equal to 6 mm and load to 138.3 kN. This crack continued to grow until becoming more visible and connected to the two opposite steel sections at 25.7 mm hydraulic jack opening and load equal to 449.1 kN. For specimen LWC-230-SD, the hairline crack onset appeared during the 2nd pre-loading cycle at hydraulic jack opening equal to 4 mm and load to 73.5 kN. This crack continued to grow until becoming more visible and connected to the two opposite steel sections during the final cycle at 13.6 mm hydraulic jack opening and load equal to 253.8 kN. For specimen LWC-230-D, the hairline crack started developing during the 3rd pre-loading cycle at hydraulic jack opening equal to 11.1 mm and load to 249.2 kN. The crack continued to grow until becoming more visible and connected to the two opposite steel sections during the final cycle at 23.9 mm hydraulic jack opening and load equal to 413 kN. For specimen NWC-300-SD, the hairline crack onset appeared during the 3rd pre-loading cycle at hydraulic jack opening equal to 10.2 mm and load to 396.7 kN. This crack continued to grow until becoming more visible and connected to the two opposite steel sections during the final cycle at 16 mm hydraulic jack opening and load equal to 593.3 kN. The order of load values at which cracks start to appear or spread between the opposite steel beams does not necessarily represent the order of strength of the specimens as several reasons cause some cracks to appear before others.

As the deflections increase, hairline cracks start to widen and grow gradually in depth. In addition, similar smaller cracks start to appear in the region around the previously developed cracks, having similar horizontal directions. At the end of the tests, a single clear deep horizontal crack surrounded by some smaller cracks is noticed below the loading points in NWC specimens. On the other hand, LWC specimens show more cracks forming a nest of deep horizontal cracks below the loading points. Figure 4-17 captures the cracks below the loading points at the

end of each test. Having a close look, it is observed that the cracks below the two loading points of each specimen are not of equal sizes as they differ in thickness by 2 to 4 mm. However, this difference is not of high significance as it is mainly caused by the smashing of the plaster below the spreader beams at some stage of the experiment causing a little movement of the beams and therefore, unsymmetrical load distribution. The horizontal cracks at the end of the tests indicate flexural failure of all specimens without signs of diagonal cracks that point out the presence of shear failure.

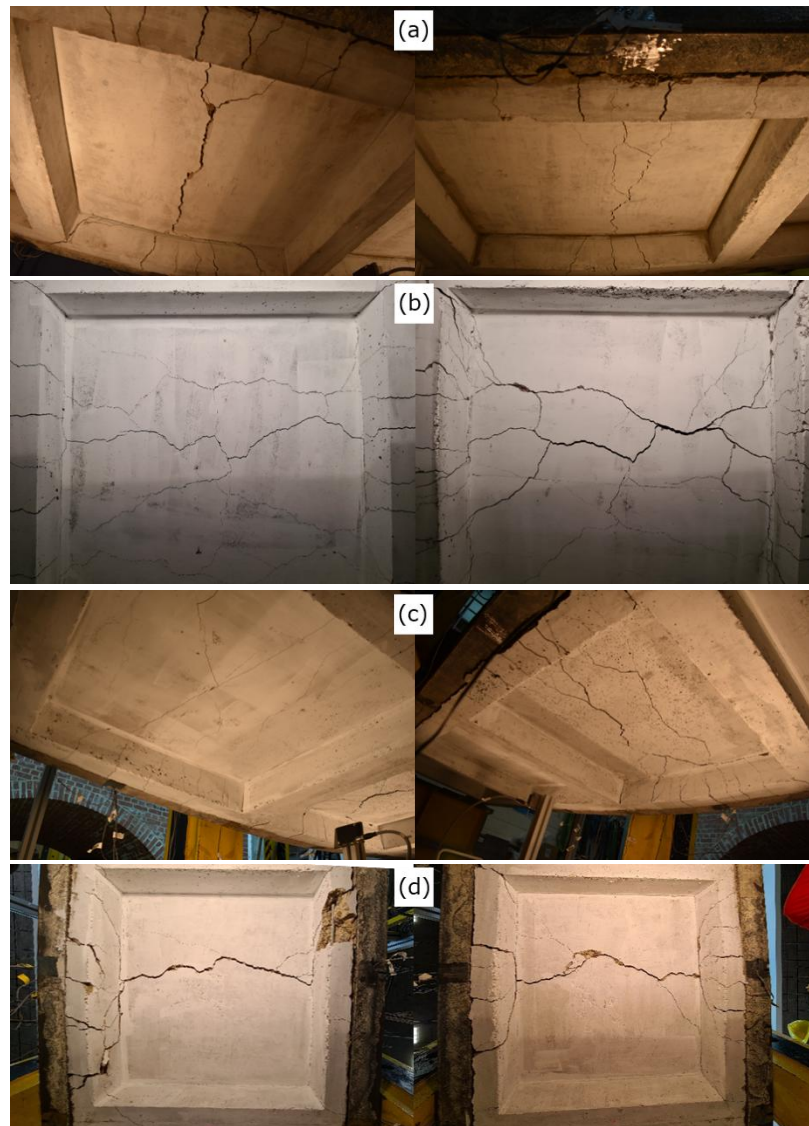


Figure 4-17: Horizontal cracks at the end of the tests below loading points in (a) NWC-230-SD, (b) LWC-230-SD, (c) LWC-230-D and (d) NWC-300-SD

The larger development of cracks in the LWC specimens is expected because of the lower stiffness of LWC in comparison to NWC specimens. However, this appears to have no effect on the capacity of the LWC specimens. The fact that they have similar strengths resulted in LWC-230-SD achieving even higher load capacity than NWC-230-SD. However, the larger number of cracks in the LWC

specimens explains the greater number of drops for the LWC specimens in the mid-span deflection versus moment curves, in the plateau region as shown in (Figure 4-14 (a)). For every specimen, each new deep crack that started to appear caused a small drop in the curve followed by load redistribution causing the load to go back to its previous values. However, some large cracks resulted in loss of capacity, and thus permanent drop – such as the ones caused by large cracks developing in LWC-230-SD and NWC-300-SD at mid-span deflection \approx 125 mm (Figure 4-14 (a)). In addition, there are drops caused by the failure of some of the shear connectors, as discussed in section 4.3.5.

4.3.5 Shear Connectors Failure

A low degree of shear connection is applied in some specimens to study the failure of the shear connectors in PUSS under flexural loading. As anticipated, failure of shear connectors was recorded for the specimens LWC-230-D and NWC-300-SD as they are designed with η values of 67% and 57%, respectively. The longitudinal shear causing failure of the shear connectors is larger near the supports and therefore, the failure of shear connectors in both specimens occurred at the shear connectors near the supports, which are the horizontal steel dowels. Every steel dowel is welded to the two opposite PFC steel sections, so when the bond (weld) on one side fails, it is considered that the steel dowel failed in shear. Another failure can possibly occur afterwards when the other side fails too.

For the LWC-230-D specimen, the first failure of one side of a steel dowel near the support occurred at mid-span deflection equal to 72 mm. A second failure also occurred at mid-span deflection around 125 mm but this time in the steel dowel near the other support. Both failures occurred in the connectors at the same side steel section. From Figure 4-14 (a) in section 4.3.1, it is noticed that the first failure caused a little drop in the mid-span deflection versus moment curve, but the specimen regained its capacity after that, which indicates that the steel dowel is still active as it is still connected to the opposite steel section. On the other hand, the drop associated with the second failure caused a permanent loss of capacity as one of the steel sections is no longer connected to the concrete slab (apart from one shear connector at mid-span which kept the steel section connected to the concrete but it does not contribute to the composite action), causing a reduction in the remaining degree of shear connection.

Specimen NWC-300-SD also experienced two shear failures in its shear connectors. The first failure occurred at the steel dowel near one of the supports at mid-span deflection equal to 135 mm. The second failure occurred at the same steel dowel but on the opposite side connected to the PFC section at mid-span deflection equal to 160 mm. Figure 4-14 (a) shows that the specimen recovered its capacity after the first failure, which indicates that the steel dowel is still active as it is still connected to the other side steel section. On the other hand, the drop associated with the second failure caused a permanent loss of capacity as the steel dowel is no longer engaged, causing a reduction in the remaining degree of shear connection.

To visually examine the deformed shape of the shear connectors after being tested, the concrete around the locations of the shear connectors was removed to expose the connectors as presented in Figure 4-18. Figure 4-19 shows the condition of the undamaged shear connectors from specimens NWC-230-SD and LWC-230-SD. The condition of both damaged and undamaged shear connectors for specimens LWC-230-D and NWC-300-SD are captured in Figure 4-20 and Figure 4-21, respectively. It is observed that none of the shear connectors show any permanent deformation at the end of the tests, even for those that failed. It appears that the failed shear connectors have broken welds without having shown any bending in the steel dowels. In addition, exposing the sides of concrete slabs near the failed shear connectors by cutting steel edge beams in specimens LWC-230-D and NWC-300-SD revealed that some diagonal cracks started to develop near the shear connectors prior to their failure due to longitudinal and vertical shears as can be seen in Figure 4-22.

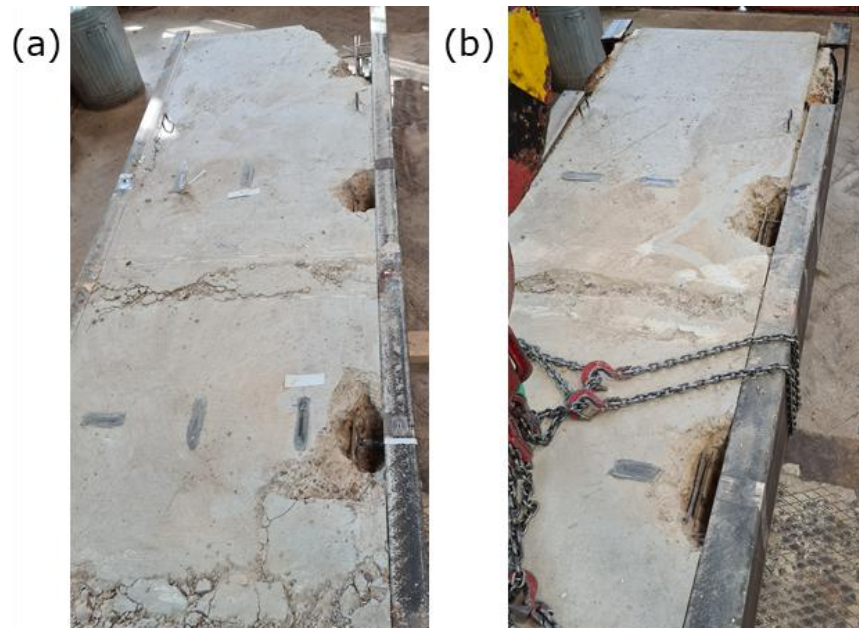


Figure 4-18: Holes broken around shear connectors in specimens (a) NWC-230-SD and (b) NWC-300-SD



Figure 4-19: Condition of shear connectors after the tests for (a) NWC-230-SD and (b) LWC-230-SD

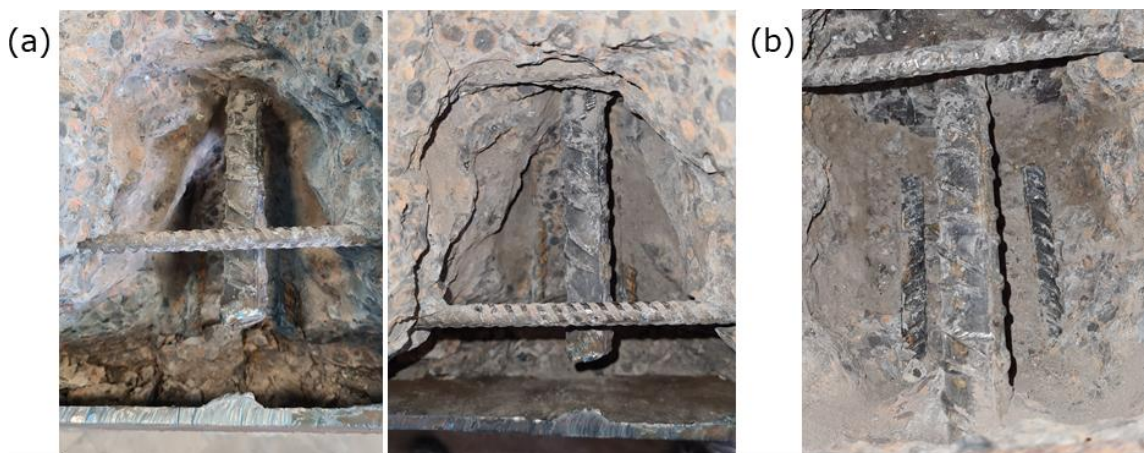


Figure 4-20: Condition of (a) failed and (b) undamaged shear connectors after the test for LWC-230-D

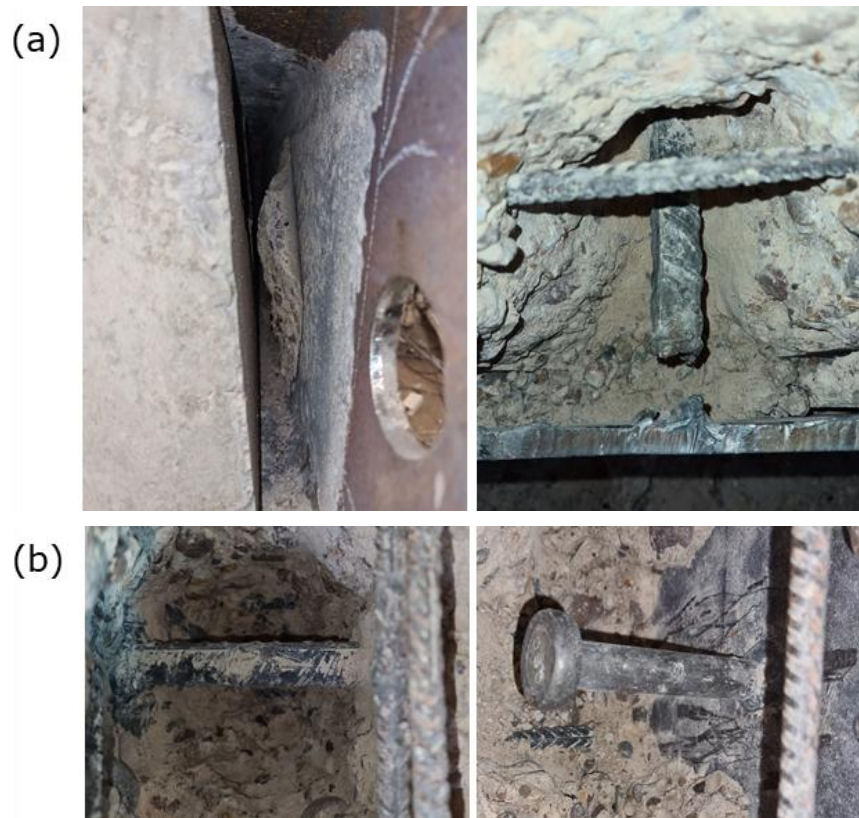


Figure 4-21: Condition of (a) failed and (b) undamaged shear connectors after the test for NWC-300-SD



Figure 4-22: Cracks in concrete near the failed shear connectors in NWC-300-SD

4.3.6 End-Slip

Figure 4-23 displays the relationship between the mid-span moment and end-slip between concrete and steel sections at the top and bottom flanges for each of the test specimens measured by the horizontal LVDTs placed at the ends of the slabs. It is shown that in the elastic region, none of the test specimens reached end-slips larger than 2 mm in the top or the bottom flanges. Thereafter, the end-slips increase rapidly during the plateau phase. The maximum end-slip at each flange of NWC-230-SD and LWC-230-SD specimens is between 3 mm to 5 mm. For specimens LWC-230-D and NWC-300-SD, similar end-slip behaviour as the aforementioned specimens is noticed before the failure of the first shear

connector, reaching average end-slips of 2 mm and 6 mm, respectively. However, following the failure of the shear connectors, end-slips values exhibited a precipitous escalation, reaching maximum end-slips of 8 mm and 25 mm at the end of the tests, respectively. The much higher end-slip at the end of the test on NWC-300-SD is due to the higher depth as well as the failure of the steel dowel near the support where measurements are taken from both of its sides making complete separation between the concrete and steel sections.

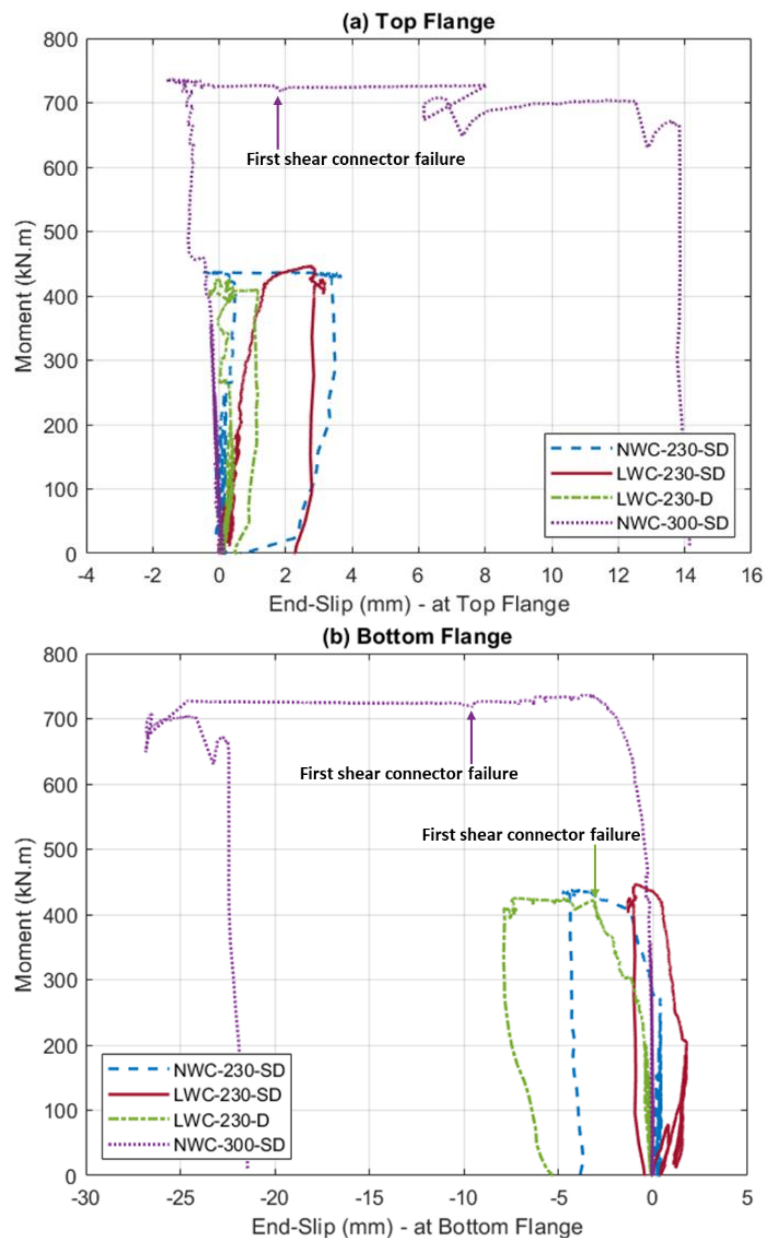


Figure 4-23: Relationship between moment and end-slip at (a) top flange and (b) bottom flange

The shear connection system employed in PUSS was tested previously to be ductile by Ahmed and Tsavdaridis (2020) under direct shear tests, reaching end-slips at the failure of the shear connectors higher than the 6 mm which is the minimum value specified by Eurocode 4 (CEN, 2004b) for ductile shear connector

behaviour. Nevertheless, the distinct loading nature caused by bending on the shear connectors resulted in a different behaviour of the shear connectors, since the failed shear connectors did not experience any permanent deformation before their failure. In addition, end-slips higher than 6 mm is only reached after the failure of some of the shear connectors. These findings may not conclusively categorise the shear connectors of PUSS as brittle in bending. It is important to note that the limits outlined in Eurocode 4 (CEN, 2004b) for ductile behaviour of shear connectors mainly applicable for headed shear studs welded to the upper flange of composite beams. Consequently, there is a need for enhancements to account for horizontal shear connectors positioned at the mid-depth of composite sections.

More importantly, the results of bending tests demonstrate that PUSS composite system as a whole behave in a ductile manner since the shear connection system in PUSS units enable them to maintain structural integrity as unified rigid bodies without exhibiting any failure in the shear connectors until reaching ultimate load capacities of the slabs and high deflections exceeding at least four times of the SLS deflections. Furthermore, test results also evident that higher degree of shear connection result in achieving higher deflections before any shear connector failures occur.

Additional to end-slips, a horizontal separation between steel sections and concrete develops during the tests, especially at the end of the slabs. This separation was not monitored during the tests, but measured manually after the end of the tests. Figure 4-24, Figure 4-25 and Figure 4-26 depict the separation at the end of the tests for all four specimens. The specimens that exhibited shear failure have much larger separation at locations near the failed shear connectors reaching values of 20 mm for the LWC-230-D specimen and 40-60 mm for the NWC-300-SD specimen. However, the maximum measured separation at the supports near the undamaged shear connectors in these two specimens as well as NWC-230-SD and LWC-230-SD is 5 mm.

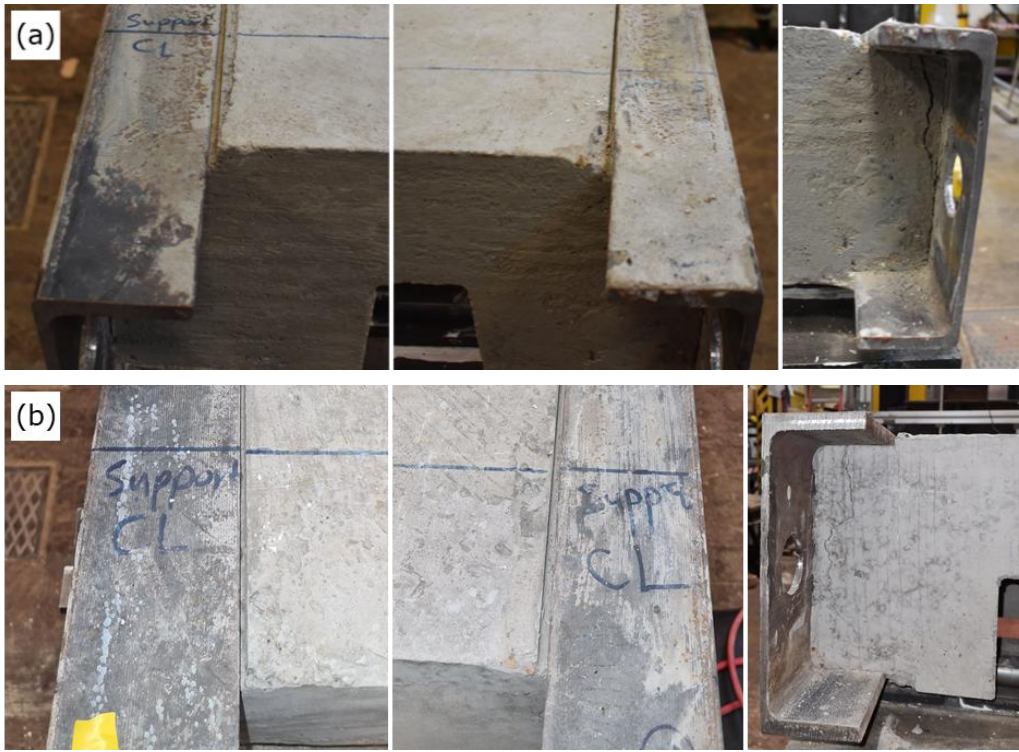


Figure 4-24: Separation between steel and concrete at the end of the tests for (a) NWC-230-SD and (b) LWC-230-SD

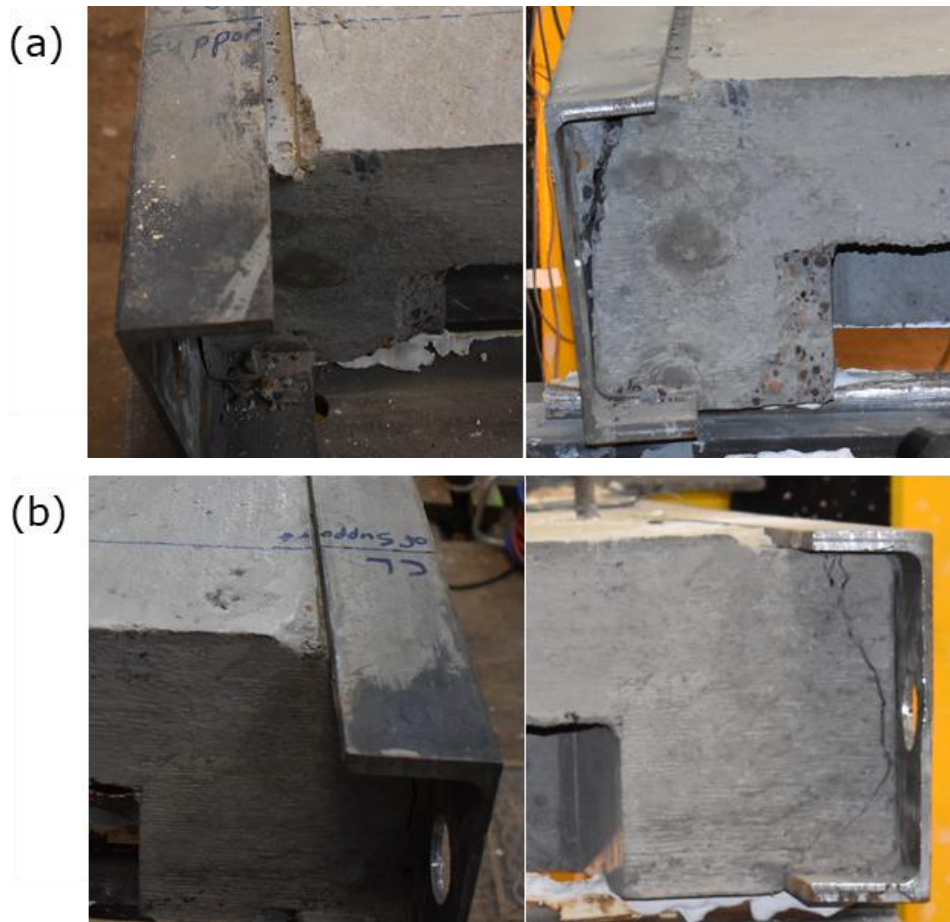


Figure 4-25: Separation between steel and concrete at the end of the test for LWC-230-D at the sides (a) near and (b) far from the failed shear connector

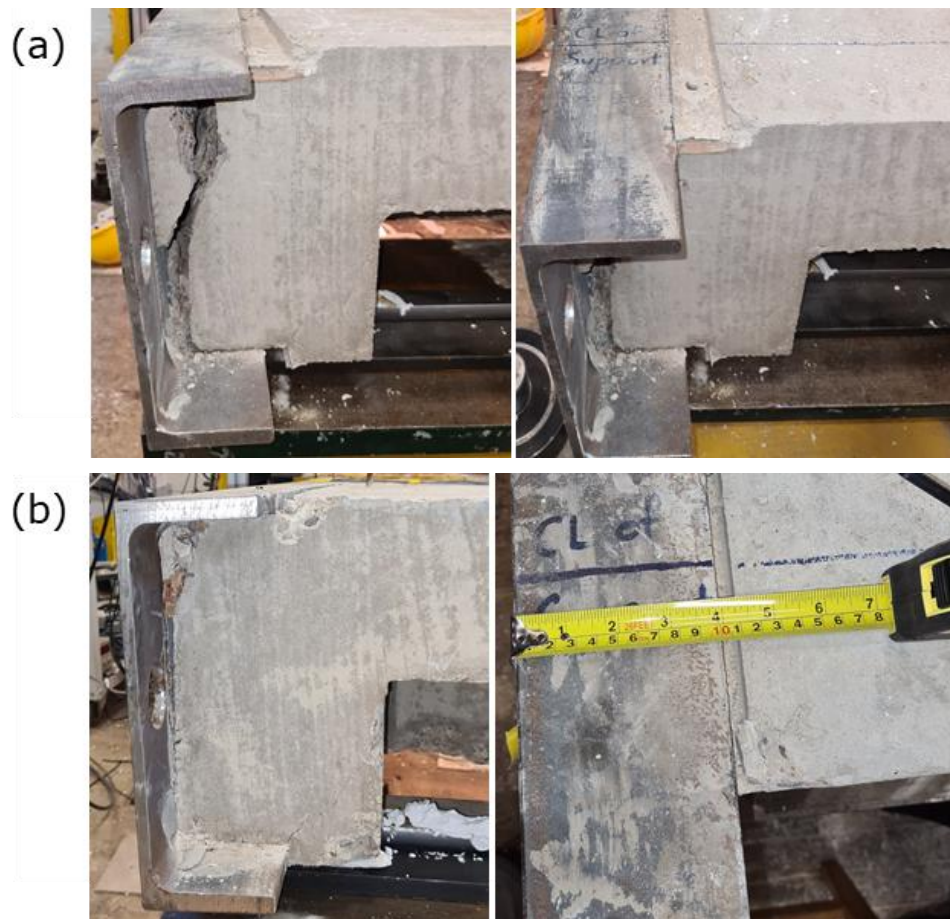


Figure 4-26: Separation between steel and concrete at the end of the test for NWC-300-SD at the sides (a) near and (b) far from the failed shear connector

4.4 Concluding Remarks

This experimental work investigates the flexural behaviour of prefabricated steel-concrete composite ultra-shallow flooring units, aka PUSS[®], by performing four full-scale four-point bending tests, following push-out tests on the same system. Based on the results presented herein, the following points are concluded:

- PUSS specimens made with LWC and NWC have similar performances in bending, and both can achieve similar moment capacities when NWC and LWC are made of similar concrete strengths. However, larger cracks develop during the tests on LWC specimens because of their lower modulus of elasticity. Tests results showed that the development of these cracks causes an average of 7% loss of strength at later stages of the tests.
- PUSS specimens with LWC demonstrate lower initial stiffness in bending in comparison to PUSS specimens with NWC. However, those with LWC can also accommodate a bit higher live loads in comparison to those with NWC because of lower weight, which reduces the dead load on slabs.

- Lowering the degree of shear connection reduces the moment capacities of PUSS units and causes failure to some of the shear connectors at higher displacements. The failure of the shear connectors results in further loss of moment capacity and causes separation between the concrete and the side steel sections.
- PUSS with full degree of shear connection reaches end-slips lower than 6 mm at the end of the tests. On the other hand, the use of a lower degree of shear connection increases the end-slips to values higher than 6 mm but only after the failure of some shear connectors. The 6 mm limit specified by EC4 for ductile behaviour of shear connectors is not necessarily relevant to the welded horizontal shear connectors employed in PUSS. Therefore, further experimental tests/ FEA models with various degrees of shear connections are required to evaluate the ductility of the shear connection system and the associated end-slips as well as making the required enhancements to EC4.
- The shear connection system employed in PUSS allows the whole composite system to behave in a ductile manner as a single rigid body and enables it to achieve deflections extremely greater than SLS deflections before any failure in the shear connectors occur, which proves the effectiveness of the applied novel shear connection system.
- The use of this type of shear connection system composed of web-welded shear studs and horizontal steel dowels proved to be very effective in bending and have high resistance to the longitudinal shear between the steel sections and concrete. None of the shear connectors exhibited any permanent deformation at the end of the tests (even the ones that failed). Furthermore, calculations and test results showed that only a small number of shear connectors is required in PUSS to reach the full degree of shear connection in comparison to other shear connection systems with vertical studs. However, even a smaller number of shear connectors need to be employed in PUSS to lower the degree of shear connection and achieve ductile behaviour.
- The formula for calculating the shear resistance of shear connections that was previously introduced by Ahmed and Tsavdaridis (2020) (Equation 2-4), was employed by the authors to produce a new formula for calculating the degree of the shear resistance and to evaluate the moment

capacities of PUSS with the stress block method. The newly developed formula proved to give satisfactory results within a 10% difference in comparison to tests results. Hence, it is quite accurate to be used in designing PUSS units of similar dimensions to the examined specimens. However, there is room for updating this equation by including more parameters in the study, either experimentally or by performing a parametric FEA study.

4.5 Limitations

The experimental test plan was subject to a number of limitations that affected its scale and scope. Due to the extended closure of laboratories during the COVID-19 pandemic and subsequent restrictions on access and high demand on university labs, the availability of testing space and time at the George Earle Laboratory (GEL) became highly constrained. As a result, the originally planned experimental scope, including longer and wider specimens, larger number of specimens and additional concrete types such as geopolymer concrete (GPC), had to be revised.

Specifically, the full-scale PUSS units, which are typically designed with a 2 m width in actual construction practice, were scaled down to a width of 1.1 m and a clear span of 4 m which is also within practical usage dimensions. This decision was made to enable the feasibility of testing within the available laboratory space. Nevertheless, steel beam dimensions, shear connectors, reinforcement detailing, and concrete mixes were maintained using standard, commercially available profiles to ensure realistic constructability and material behaviour. This approach preserved the practical relevance of the results, and the reduced specimens remained representative of real-world PUSS applications.

The primary objective of the physical testing was to generate a reliable dataset for calibrating and validating finite element (FE) models. These models were subsequently used to simulate the performance of full-scale units, thereby ensuring the applicability of the conclusions. Moreover, the reduced span allowed the specimens to reach their full flexural capacity under relatively higher applied loads than would typically be expected for longer-span units, which provided valuable insight into performance of the flooring system. Therefore, while minor scale effects may exist, such as altered deflection profiles or load-to-span ratios,

their influence is considered limited and does not undermine the validity of the findings.

In addition to the specimen scale, there were other technical limitations during testing. Monitoring concrete cracks propagation during loading was particularly challenging due to safety concerns that restricted close visual inspection of the specimens in real-time. Similarly, stress development in embedded shear connectors could not be directly measured during testing; their condition was only assessed post-failure through destructive inspection, which proved difficult and time-consuming.

These constraints are acknowledged as part of the study's limitations and have been carefully considered when interpreting the results and conclusions.

Chapter 5

Finite Element Analysis

5.1 Introduction

Physical experimental testing of the flexural behaviour of PUSS units provides accurate, reliable and valuable results. However, it is a time-consuming investigation procedure and is associated with high costs and resources consumption. In addition, monitoring the stresses, strains, and cracks developments over the test specimens is difficult. Alternatively, utilising finite element analysis (FEA) is a common practice and much more economical in terms of time and resources compared to the experimental work. The accuracy of the FE model is highly dependent on precise geometrical drawings, appropriate material models selection, mesh size, correct load application and solution derivation techniques. Physical tests, however, remain essential for FEA to validate the established models before implementing them in further parametric investigations. Therefore, accurate FE models are developed to simulate the flexural behaviour of the PUSS units in four-point bending tests presented in Chapter 4.

This chapter presents the results of a FE parametric study that investigates the flexural behaviour of PUSS units and the employed shear connection system under bending. To enhance the understanding of the performance of the employed shear connectors and predict their shear strength, a high-fidelity FE model is elaborated, exploring the effects of various parameters. Specifically, parameters under study are the depth of slabs, span of slabs, concrete type, concrete strength, and the size of the employed shear connectors. The study includes a total of 324 FE models and aims to quantify the shear strength of the shear connectors employed in PUSS flooring, and their effects on the composite action of PUSS units under bending.

Numerical modelling techniques utilising the ABAQUS 2022 (Dassault Systèmes, 2022) software are applied to simulate the flexural behaviour observed in the experimental findings as closely as possible. These techniques are also directed to optimise computer storage usage and minimise the analysis runtime while maintaining results accuracy. Modelling techniques include the proper definition of material properties, geometry, partitioning, meshing, selection of element

types, modelling contact interactions, as well as boundary and loading conditions. A concise overview of the modelling procedure is presented in this chapter.

5.2 Modelling Procedure

The general-purpose ABAQUS 2022 finite element analysis software is selected to model the structural response of the PUSS flooring system under flexural loads. The ABAQUS interactive computer-aided engineering (CAE) interface has a simple input language that simplifies its use for analysing complex problems while still providing highly accurate solutions. This makes it an ideal tool for analysing countless types of engineering problems including the structural response to static and dynamic loads.

The modelling process in ABAQUS can be divided into nine main steps (modules), and they are typically performed in the following order:

- e) Parts Geometry Modelling: This step involves sketching detailed geometrical shapes of the model parts which is done in “Part” module.
- f) Materials Modelling: In “Property” module, materials properties are defined and assigned to the individual parts.
- g) Analysis Method and Outputs: The appropriate analysis method is specified in the “Step” module. Several methods can be selected, such as Static/General, Static/RIKS and the Dynamic/Explicit. In addition, the time period of the step and the analysis increments are specified in this module, along with the requested analysis outputs.
- h) Model Assembly: Assembly of the previously created parts to create the full model geometry is performed in the “Assembly” module. Additionally, the required partitioning of the assembly is done which helps later on in making appropriate meshes.
- i) Definition of Interactions and Constraints: In this step, all constraints, contacts, and surface interactions in the model are established in the “Interaction” module.
- j) Definition of Loads and Boundary Conditions: In “Load” module, all loads applied on the model. Reactions and boundary conditions are also defined.
- k) Model Meshing: The final step before running the analysis is to mesh the model to the proper element size in the “Mesh” module. Suitable mesh controls and elements types are also assigned.

- l) Run Analysis: Following the previous steps, the model becomes ready for analysis. A job is created in the “Job” module and submitted for analysis.
- m) Results Visualisation and Processing: Once the analysis is complete, the results are processed into graphical outputs, tables, plots, etc. in the “Visualisation” module.

The details of the modelling procedures of all aspects related to the FE validation and the parametric study models are discussed in the following sections.

5.3 Material Properties

The precision of analysis outcomes is highly dependent on the accurate definition of the mechanical properties for the materials that make up the model’s parts. This enables the derivation of precise predictions of the model’s behaviour. This section presents the development procedure of reliable materials properties, including defining the materials’ stress-strain relationships, damage development, and other related characteristics. PUSS units are composed of two main materials: concrete and steel, which is used for the steel beam sections, shear connectors and steel reinforcement.

5.3.1 Concrete

ABAQUS provides two main options to model concrete plasticity properties and damage development: the concrete smeared cracking model and the concrete damaged plasticity model. Both models are appropriate for modelling the inelastic behaviour of concrete, each with its own limitations and suitability for certain loading conditions. In this study, the concrete damaged plasticity model is selected as it showed its excellence over the other option in representing concrete’s inelastic behaviour and tracking the progression of individual cracks. This model assumes that the primary concrete failure mechanisms are the compressive crushing and tensile cracking. The definition of the compressive and tensile stress-strain behaviour outside the elastic range in ABAQUS is accomplished using the concrete compression hardening and concrete tension stiffening options, respectively. Additionally, the concrete compression damage and concrete tension damage options are used to model the compressive and tensile damage of concrete, respectively (Dassault Systèmes, 2022).

The damaged plasticity model assumes that for concrete subjected to uniaxial tensile loading, the stress-strain response exhibits a linear elastic relationship up

to the tensile failure stress σ_{t0} . Beyond that point, concrete follows a softening stress-strain behaviour. Figure 5-1 (a) plots the response of concrete subjected to uniaxial tensile loading based on the damaged plasticity model, where σ_t is the tensile stress, E_0 is the initial elastic stiffness of concrete, ε_t is the total tensile strain, $\varepsilon_t^{\sim pl}$ is the tensile plastic strain and ε_t^{el} is the tensile elastic strain. For compression, the model assumes that under uniaxial loading, concrete initially behaves in a linear elastic manner up to the initial yield stress σ_{c0} , followed by a plastic region, which initiates with stress hardening until reaching the ultimate compression stress σ_{cu} and then enters a strain softening region. Figure 5-1 (b) illustrates the response of concrete subjected to uniaxial compression loading based on the damaged plasticity model, where σ_c is the compressive stress, E_0 is the initial elastic stiffness of concrete, ε_c is the total compressive strain, $\varepsilon_c^{\sim pl}$ is the compressive plastic strain and ε_c^{el} is the compressive elastic strain. Unloading concrete at a point within the softening portion weakens the unloading response and degrades the elastic stiffness of concrete. This degradation is defined by the tension damage parameter d_t and compression damage parameter d_c , ranging from zero for undamaged condition to one for the condition when the material has lost its total strength.

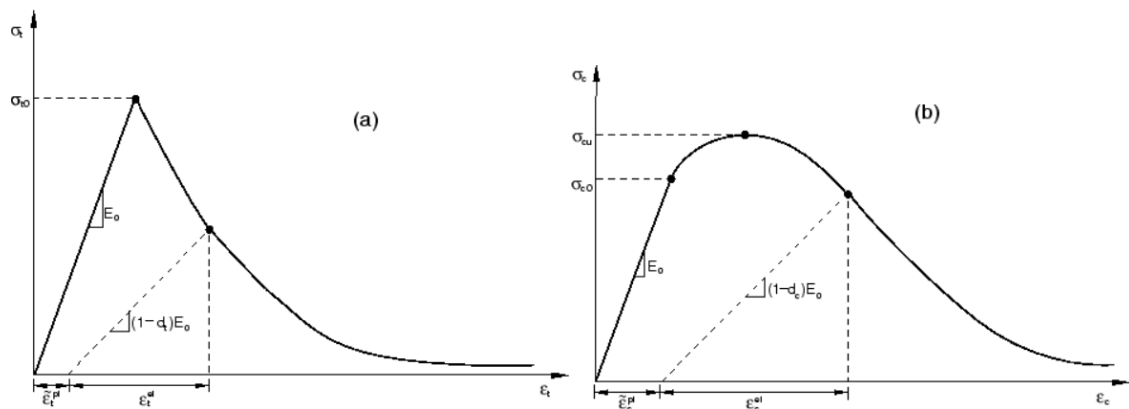


Figure 5-1: Response of concrete to uniaxial loading in (a) Tension and (b) Compression (Dassault Systèmes, 2022)

To simulate precise plastic behaviour of concrete, the concrete damaged plasticity model implements some non-associated potential plastic flow, yield, and viscoplastic regularization functions that are dependent on a set of parameters. These include the dilation angle (ψ) which is taken as 38° (Ahmed and Tsavdaridis, 2022), the flow potential eccentricity (ε), the ratio of the second stress invariant on the tensile meridian to that on the compressive meridian at initial yield (K_c), viscosity (μ) and the ratio of initial equibiaxial compressive yield

stress to initial uniaxial compressive yield stress (σ_{b0}/σ_{c0}) which are taken in analysis as the default values from ABAQUS documentation: 0.1, 2/3, 0 and 1.16, respectively (Dassault Systèmes, 2022).

5.3.1.1 Tension Softening

In concrete damaged plasticity model, the tensile stress in concrete increases linearly with respect to strain until cracking begins. Following the crack, tension softening behaviour occurs, and the tensile stress gradually decreases to zero. This behaviour can be presented by various approaches that defines the post-failure stress-strain relationship or the fracture energy cracking criterion, which demonstrates the brittle behaviour of concrete by a stress-displacement response instead of a stress-strain response. Linear (Dassault Systèmes, 2022) and bilinear (Hillerborg, 1985) functions are available in the literature to define the brittle behaviour. However, this study used the most accurate method, which is the exponential expression established by Cornelissen et al. (1986) based on experimental results. Figure 5-2 compares the differences between the three models.

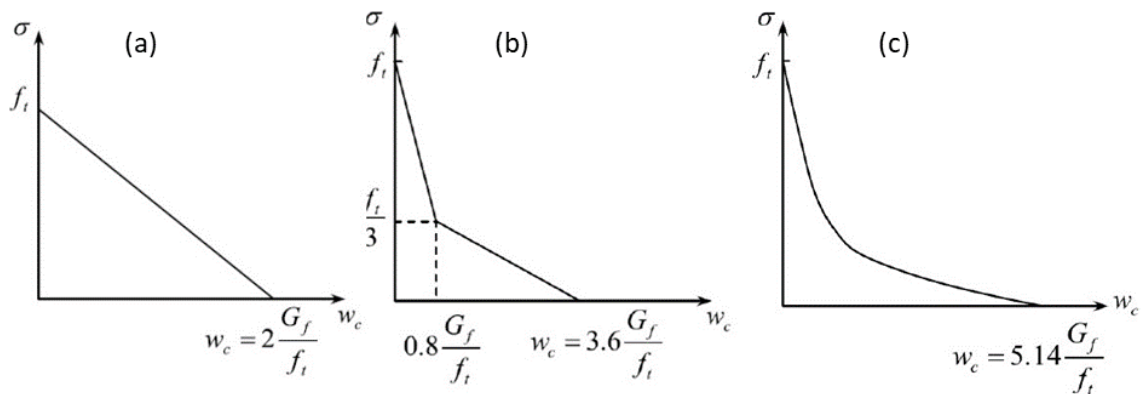


Figure 5-2: Comparison between (a) Linear (Dassault Systèmes, 2022) (b) Bilinear (Hillerborg, 1985) and (c) Exponential (Cornelissen et al., 1986) tension softening models

For the exponential model, the tensile stress σ_t , the crack opening displacement w , and the tensile damage parameter d_t for concretes with normal and lightweight aggregates can be calculated from Equation 5-1, Equation 5-2 and Equation 5-3.

Equation 5-1

$$\frac{\sigma_t}{f_t} = f(w) - \frac{w}{w_c} f(w_c)$$

Equation 5-2

$$f(w) = \left[1 + \left(\frac{c_1 w}{w_c} \right)^3 \right] \exp \left(- \frac{c_2 w}{w_c} \right)$$

Equation 5-3

$$d_t = 1 - \frac{\sigma_t}{f_t}$$

Where: w is the crack opening displacement,
 w_c is the crack opening displacement at which stress can no longer be transferred and it is equal to $5.14G_f/f_t$ for NWC (Cornelissen et al., 1986),
 f_t is the tensile strength of concrete,
 G_f is the fracture energy in N/m and $G_f = 73f_{cm}^{0.18}$ for NWC, $G_f = 24 + 16f_t$ for LWC with normal weight sand and $G_f = 16f_t$ for LWC with lightweight sand (*fib*, 2013),
 c_1 is a material constant. $c_1 = 3$ for NWC and $c_1 = 1$ for LWC, and c_2 is a material constant. $c_2 = 6.93$ for NWC and $c_2 = 5.64$ for LWC (Qureshi and Lam, 2012).

5.3.1.2 Compression Behaviour

Modelling the compressive behaviour of concrete in this study uses different approaches depending on the concrete type implemented in PUSS unit. For normal weight concrete (NWC), the compressive stress-strain behaviour is determined based on the constitutive law from Eurocode 2 (Equation 5-4) (CEN, 2004a). The schematic diagram of the stress-strain relationship from this equation is depicted in Figure 5-3.

Equation 5-4

$$\frac{\sigma_c}{f_{cm}} = \frac{k\eta - \eta^2}{1 + (k - 2)\eta}$$

Where: σ_c is the compressive stress of the normal concrete,
 f_{cm} is the Mean value of concrete cylinder compressive strength,
 $\eta = \varepsilon_c/\varepsilon_{c1}$
 ε_c is the compressive strain of concrete,
 ε_{c1} is the compressive strain of concrete at the peak stress f_{cm} ,
 $\varepsilon_{c1}(\text{‰}) = 0.7f_{cm}^{0.31} \leq 2.8$
 $k = \frac{1.05E_{cm} \times |\varepsilon_{c1}|}{f_{cm}}$
and E_{cm} is the secant modulus of elasticity $E_{cm} = 22 \times \left(\frac{f_{cm}}{10}\right)^{0.3}$

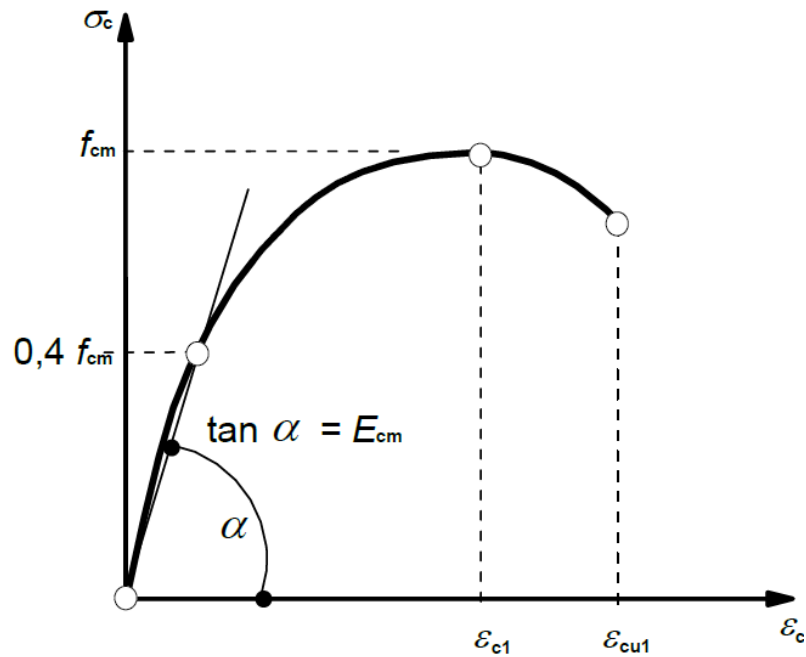


Figure 5-3: Schematic representation of the stress-strain relationship for Concrete in compression ($0,4f_{cm}$ is used for the definition of E_{cm}) (CEN, 2004a)

This equation is valid for $0 < |\varepsilon_c| < |\varepsilon_{cu1}|$, where ε_{cu1} is the nominal ultimate strain which can be taken as 0.0035 for concrete characteristic compressive cylinder strength of 12–50 MPa as stated in Eurocode 2 (CEN, 2004a). For a characteristic compressive strength greater than 50 MPa, ε_{cu1} can be calculated from Equation 5-5.

Equation 5-5

$$\varepsilon_{cu1} = 2.8 + 27 \left[\frac{98 - f_{cm}}{100} \right]^4$$

For lightweight concrete (LWC), Eurocode 2 uses similar representation for the stress-strain relationship in compression as for NWC, with some modifications. For LWC, the term f_{cm} is referred to as f_{lcm} . Similarly, the secant modulus of elasticity E_{cm} is replaced with $E_{lcm} = E_{cm} \cdot \eta_E$ where $\eta_E = (\rho/2200)^2$ and ρ is the oven-dry density of LWC. In addition, the strain values ε_{c1} and ε_{cu1} are substituted by ε_{lc1} and ε_{lcu1} calculated by $\varepsilon_{lc1}(\%) = kf_{lcm}/E_{lcm}$, $\varepsilon_{lcu1} = \varepsilon_{lc1}$ where $k = 1.1$ or 1 for LWC with normal weight sand or LWC with lightweight sand, respectively (CEN, 2004a).

In this research, the compressive stress-strain behaviour for LWC is defined by a combination of the stress-strain relationship presented in Eurocode 2 and the mathematical model established by Almusallam and Alsayed (1995) which is given in Equation 5-6. The schematic diagram of this stress-strain relationship model with its parameters is plotted in Figure 5-4.

Equation 5-6

$$f_c = \frac{(k - k_p)\varepsilon_c}{\left[1 + \left(\frac{(k - k_p)\varepsilon_c}{f_0}\right)^n\right]^{1/n}} + k_p\varepsilon_c$$

Where: f_c is the compressive stress of concrete corresponding to the strain ε_c ,

$n = -\frac{\ln 2}{\ln\left(\frac{f_1 - k_p}{f_0 - k_p}\right)}$ and it is the curve-shape factor,

$$f_1 = f_{cm} \left[2 \frac{\varepsilon_1}{\varepsilon_0} - \left(\frac{\varepsilon_1}{\varepsilon_0} \right)^2 \right],$$

$$\varepsilon_1 = \frac{0.65f_0}{k - k_p} \text{ for LWC,}$$

$f_0 = 19.1 + 1.3f_{cm} - k_p\varepsilon_0$ for LWC and it is a reference stress,

$$\varepsilon_0 = (0.398f_{cm} + 18.147) \times 10^{-4} \text{ for LWC,}$$

$k = 180.9f_{cm} + 7770.7$ for LWC and it is the initial slope of the curve which is equal to the modulus of elasticity E_c ,

and $k_p = 1374.5 - 871.1f_{cm}$ for LWC and $f_{cm} \geq 15 \text{ MPa}$, and it is the final slope of the curve.

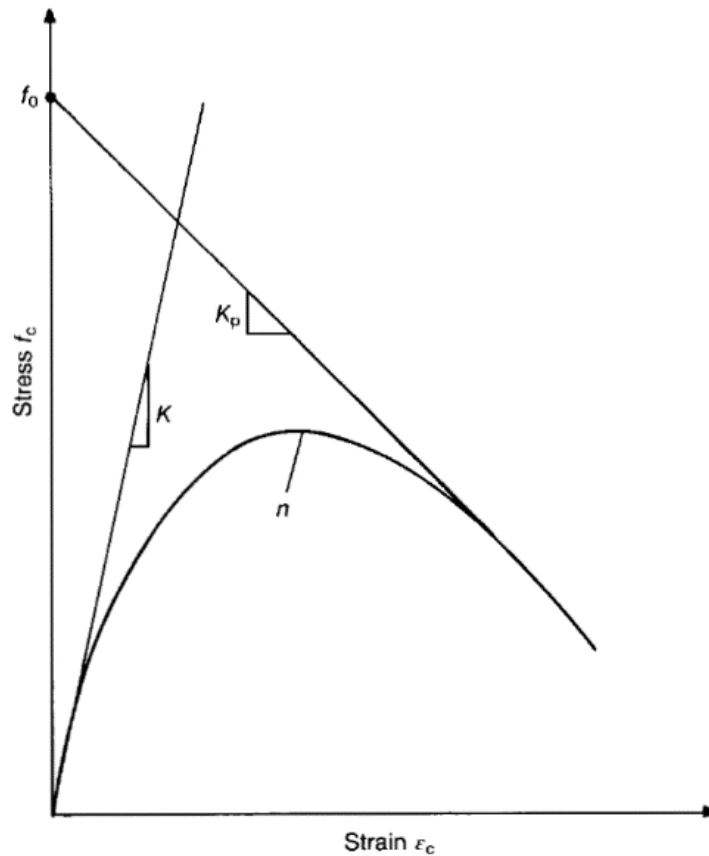


Figure 5-4: Schematic diagram of stress-strain relationship model established by Almusallam and Alsayed (1995) with its parameters

The third concrete type implemented in the parametric study is geopolymer concrete (GPC). Since this covers a wide range of concrete mixes that vary in their mechanical properties, the generalised model for stress-strain behaviour of unconfined GPC in compression presented by Ganesan et al. (2014) is selected to model the compressive stress-strain behaviour for GPC (Equation 5-7). Additionally, modulus of elasticity (E_c) is calculated from Equation 5-8.

Equation 5-7

$$f_c = \frac{f_{cc} \left(\frac{\varepsilon_c}{\varepsilon_{cc}} \right)^{1.62}}{0.62 + \left(\frac{\varepsilon_c}{\varepsilon_{cc}} \right)^{1.62}}$$

Where: f_c is the compressive stress of concrete corresponding to the strain ε_c ,
 f_{cc} is the peak compressive stress,
and ε_{cc} is the strain corresponding to peak stress.

Equation 5-8

$$E_c = 6965 \sqrt{f_{ck}}$$

Where: f_{ck} is the characteristic compressive strength of GPC.

From the concrete properties obtained from experimental tests on concrete samples (section 4.2.3.1), the concrete properties curves for FE validation models are derived. Figure 5-5 depicts the concrete properties curves used for NWC in specimen NWC-230-SD and LWC in specimen LWC-230-D.

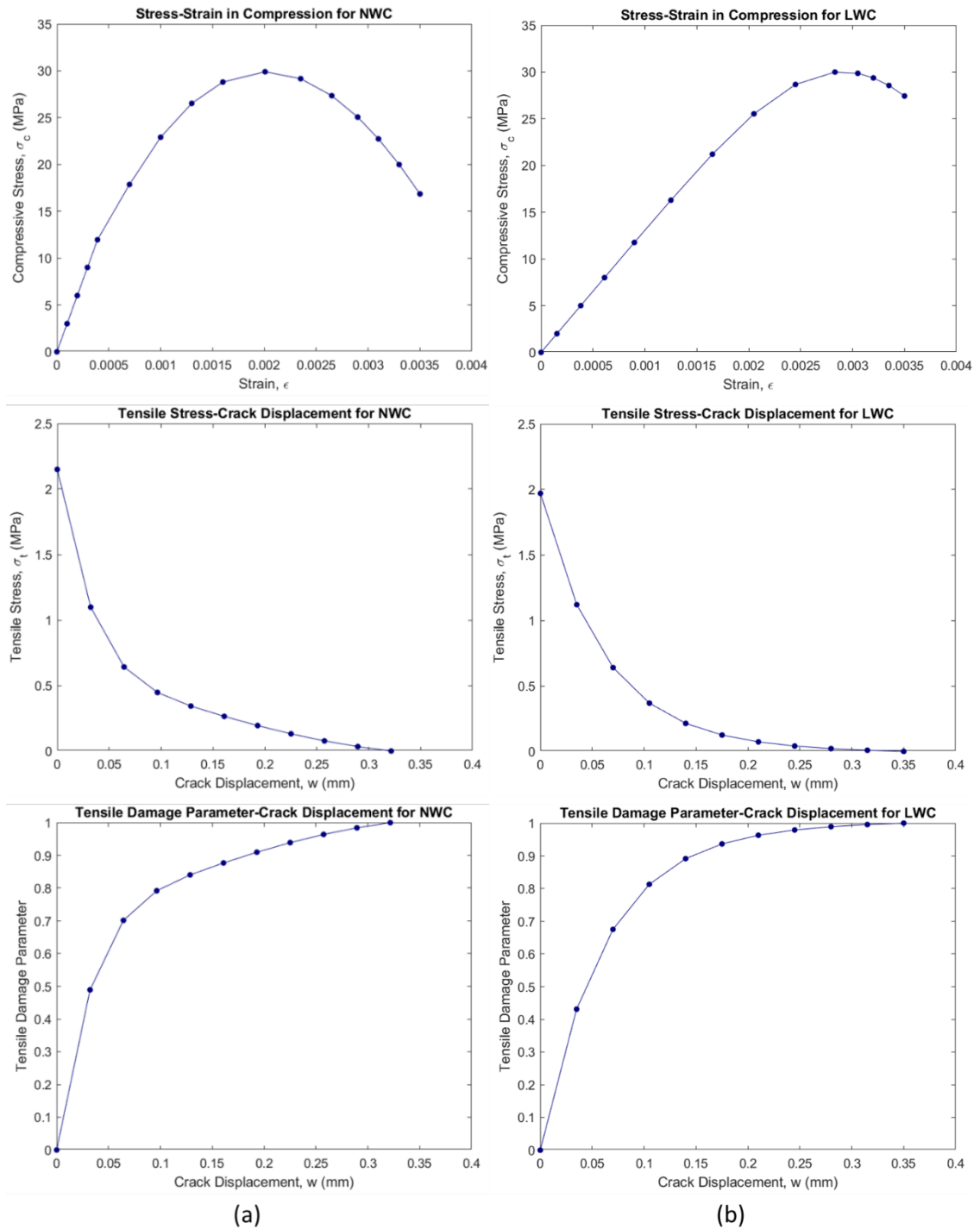


Figure 5-5: Curves of concrete properties used in modelling FE validation models for (a) Specimen NWC-230-SD & (b) Specimen LWC-230-D

5.3.2 Steel Elements

PUSS units encompass three main types of steel elements: steel reinforcement, steel C-channel beam sections and shear connectors (studs and dowels). Steel is modelled in accordance with ABAQUS formulation as a combined isotropic/kinematic hardening material. For steel reinforcement elements, steel is modelled as an elastic perfectly plastic material, where the elastic behaviour is followed by yielding, in a bi-linear stress-strain relationship (Figure 5-6 (a)).

However, steel beams and shear connectors are modelled considering a tri-linear stress-strain relationship due to their significant influence on the results. In this approach, the elastic behaviour is followed by strain softening before yielding occurs, as shown in Figure 5-6 (b). The ultimate strain (ϵ_u) corresponding to the peak stress (f_u) is defined to be 15 times the yield strain (ϵ_y), while the fracture strain (ϵ_r) is set to be 10 times ϵ_u , in compliance with Díaz et al. (2018).

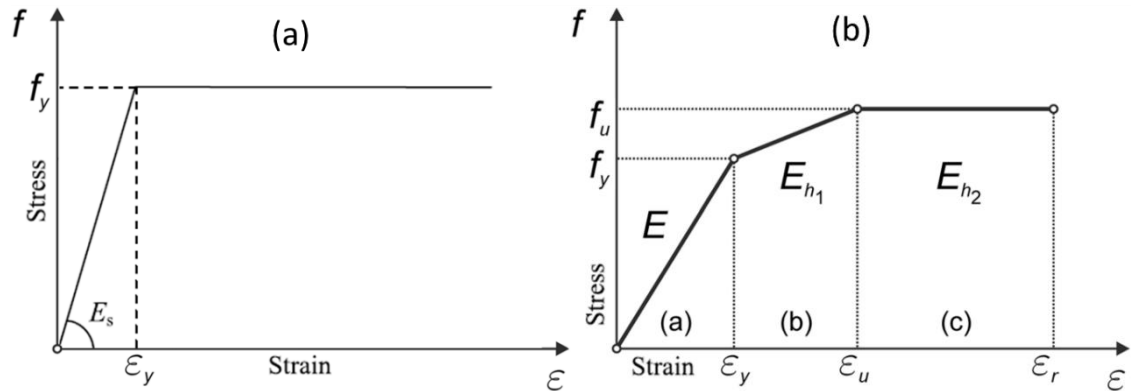


Figure 5-6: (a) Bi-linear elastic perfectly plastic and (b) Tri-linear stress Strain Curves (Díaz et al., 2018)

The ductile damage modelling option is also used to model the behaviour of the shear connectors in order to simulate their load-slip behaviour. Stress triaxiality is considered the primary factor for damage since the loading rate is slow, eliminating the influence of the strain rate. In addition, with no temperature change, the influence of the thermal effects can be ignored. To model the stress triaxiality effects, the stress triaxiality equation proposed by Xu et al. (2012) is used to produce the graph presented in Figure 5-7.

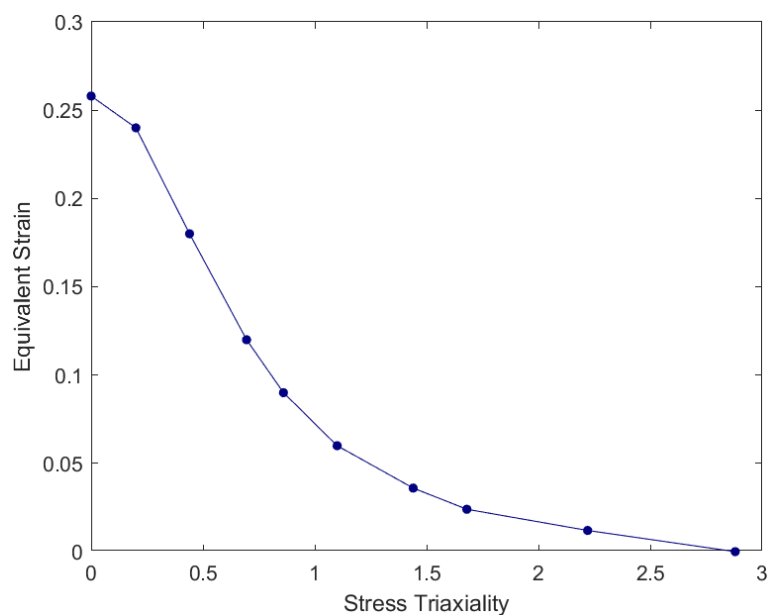


Figure 5-7: Stress triaxiality damage initiation model for shear connectors

From the yield and ultimate stresses for steel elements obtained from experimental tests on steel samples (section 4.2.3.2), the stress-strain curves for FE validation models are derived. Figure 5-8 illustrates these curves for steel reinforcement, shear connectors and steel beams.

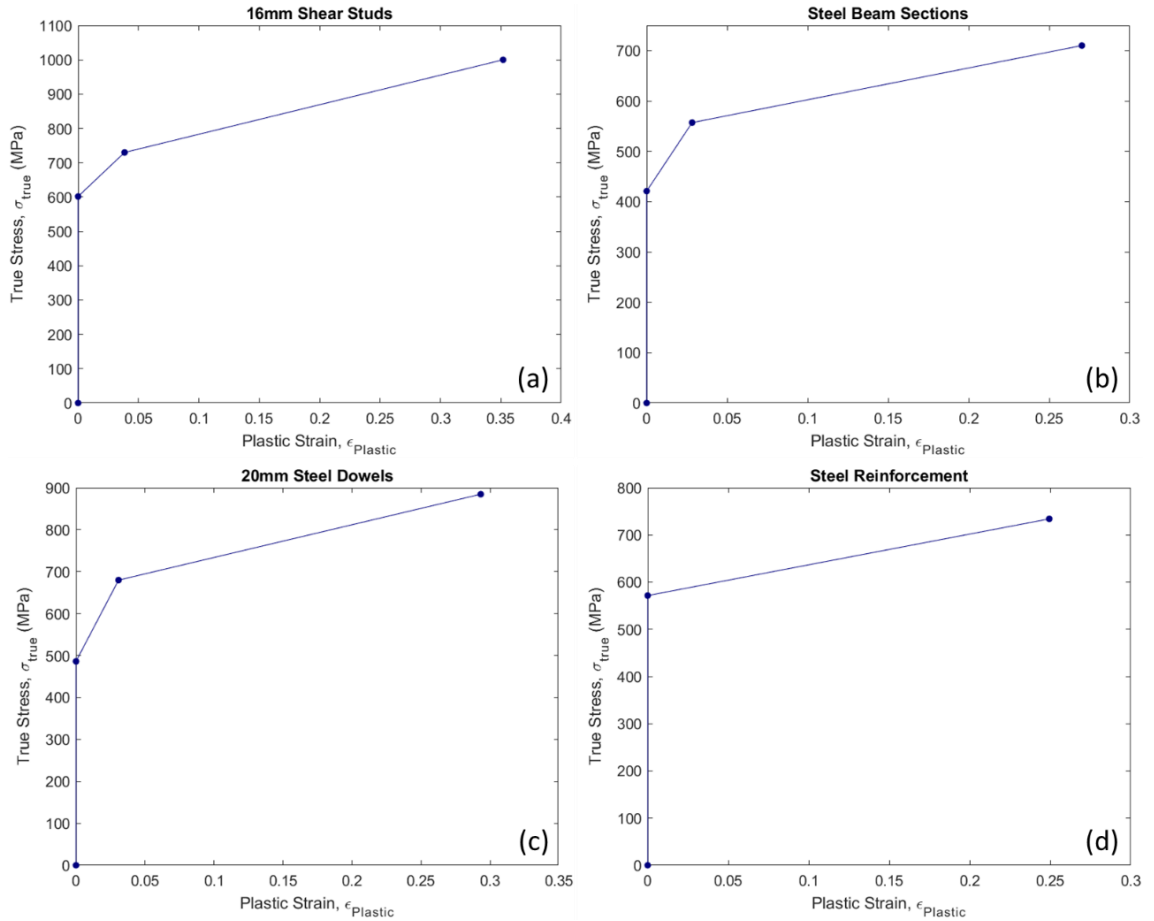


Figure 5-8: True stress-plastic strain curves of (a) Shear Studs (b) Steel beams (c) Steel dowels & (d) Steel reinforcement

5.4 Model Description

The established FE models resemble the arrangement of the flexural tests reported in Chapter 4. For model validation, the geometrical details and material properties of the four experimentally tested PUSS specimens are defined. The symmetrical arrangement of the experiments and load application are considered in creating the models, and only one quarter of the tested specimens is modelled to reduce the computational time and storage requirements. The main components of the FE models are: concrete slab, steel beam, web-welded shear studs, steel dowels, steel reinforcement (including mesh reinforcement, stirrups and reinforcement of side concrete beams), support, and loading beam. These parts are modelled and then assembled to form one quarter of the four-point bending test, as presented in Figure 5-9.

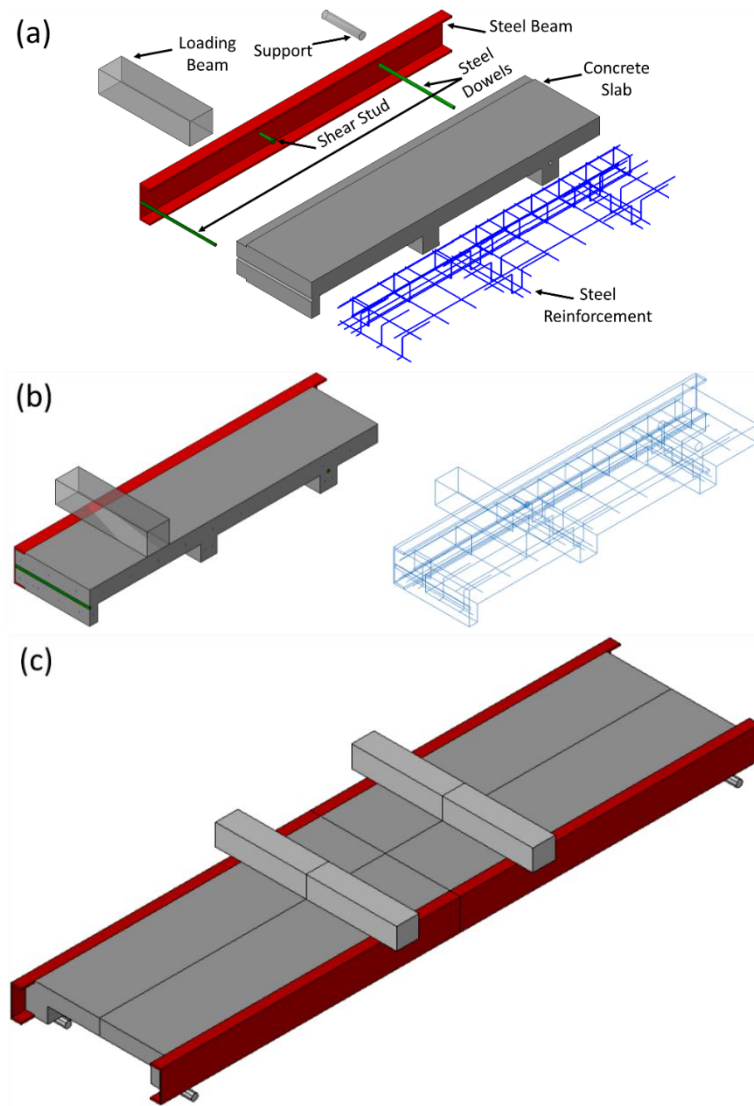


Figure 5-9: (a) Parts involved in FE Models (b) Assembled view of FE Models (one quarter) (c) Assembled view of full model

5.4.1 Interactions and Constraints

After model assembly, appropriate contact properties are defined between surfaces in contact, which is of great importance to achieve reliable results. In this model, there are five main types of surface-to-surface contact pairs: the contact between the steel beam section and shear connectors, the concrete slab and shear connectors, the concrete slab and the steel beam section, the slab and the loading beam, and finally, the slab and the support below it.

In the experimental work, shear connectors are welded to the steel beams. Therefore, for the interaction between the steel beam and the shear connectors, the shear connectors are merged with the steel beam sections to form one part and remain tied to each other with no slip. This was validated as realistic based on the results of push-out test experimental and numerical analysis (Ahmed, 2019).

The remaining contact pairs are modelled as surface-to-surface contact interactions, defined by normal and tangential behaviours properties. Since all surfaces in contact are hard, “hard” contact normal behaviour is assumed, allowing only small penetration of the slave surfaces into the master surfaces. For the tangential behaviour, the “penalty” method is used and a friction coefficient of 0.5 is adopted for contact between the concrete slab and the shear connectors. Otherwise, a frictionless contact is defined for the remaining contact pairs (Ahmed and Tsavdaridis, 2022; Qureshi and Lam, 2012).

In addition to the above contact pairs, there is an interaction between the concrete slab and the steel reinforcement within it. This contact and the slip between the two elements are of less importance and therefore, it is modelled using the “embedded” constraint in ABAQUS. This technique shortens the analysis time required by the software since it assumes no slip between the two elements. Snapshots of the contact pairs and embedded reinforcement in the models are captured in Figure 5-10.

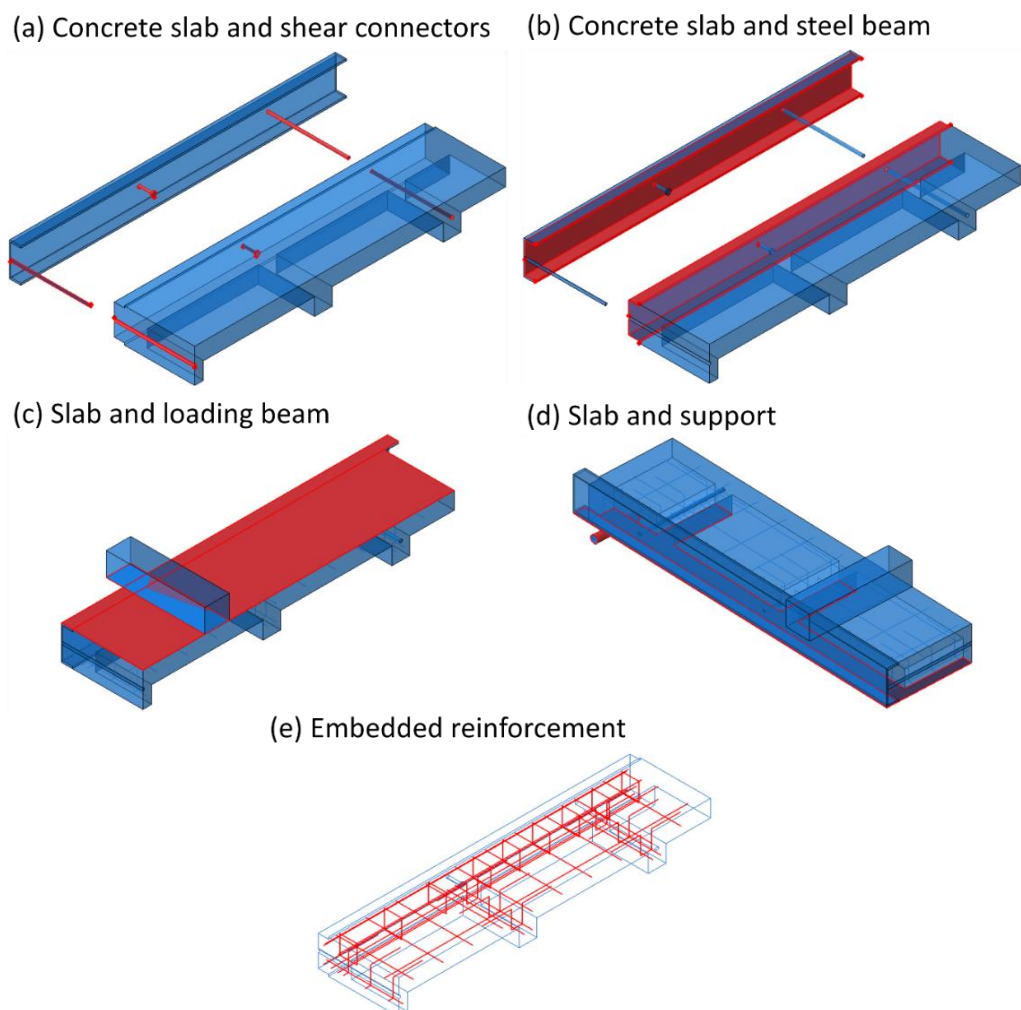


Figure 5-10: Surface contact pairs and embedded reinforcement

5.4.2 Boundary Conditions and Load Application

In ABAQUS, the definition of symmetrical constraints and supports' degrees of freedom (DOFs) is accomplished through applying boundary conditions (BC) to the model. Moreover, since the load application in the proposed FE models is displacement-controlled, it is also assigned as a BC.

Due to symmetry, only one quarter of the four-point bending test is modelled, and the symmetric BC is applied to the two surfaces at the symmetric planes of the specimens. The X-axis symmetric BC is applied to surface 1 (Figure 5-11(a)), which restrains the translational displacement in X-direction (U1) and rotations around Y and Z axes (UR2 and UR3). In a similar approach, Z-axis symmetric BC is applied to surface 2 (Figure 5-11 (a)). Additionally, the support is assumed to be fixed, and “encastre” BC is assigned to a reference point (RP) attached to it, restricting all DOFs of the support (Figure 5-11 (b)). For load application, a downward displacement boundary condition is applied to another RP located at the centre of the loading beam (Figure 5-11 (c)).

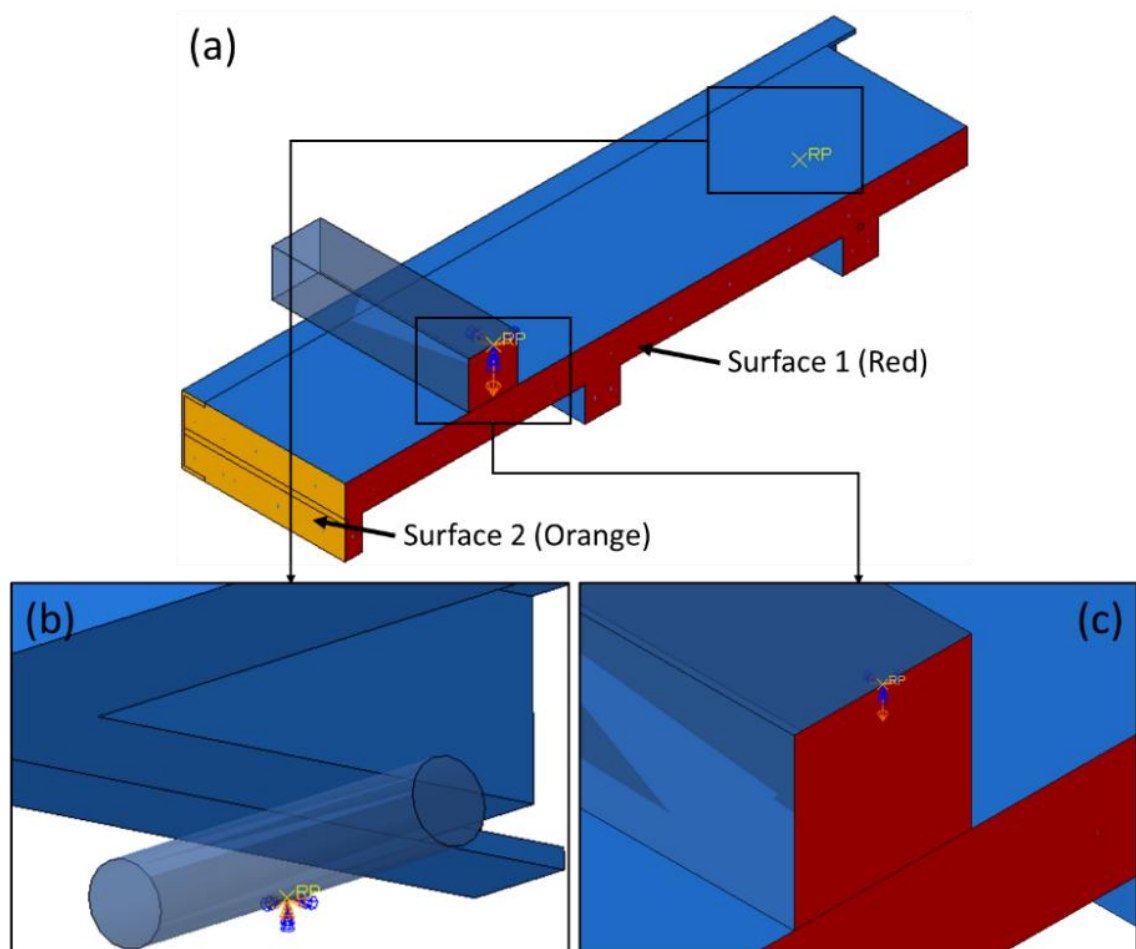


Figure 5-11: FE model boundary conditions

5.4.3 Analysis Method

ABAQUS offers a wide range of analysis methods, each suitable for specific applications. In the established FE models, displacement should be applied slowly to the loading beam to simulate the experimental work and avoid the inertial effects associated with load application. This is essential to obtain accurate solutions for quasi-static problems. Typically, the “static, general” analysis approach with non-linear material properties and geometry is suitable for predicting results of quasi-static problems. This approach was implemented in a preliminary FE parametric study of the flexural behaviour of PUSS (Alali and Tsavdaridis, 2021), and it provided reliable results.

However, this approach consumes a significant amount of time, computer power and storage for the relatively large models under investigation. Moreover, convergence problems are often encountered when running some models, which terminates the analysis before reaching ultimate loads. Therefore, the “dynamic/ explicit” analysis method is used in the validation and parametric study models. Although it is an approach mainly implemented in analysing dynamic problems, it has proven effective in the analysis of quasi-static problems and showed great results, especially when dealing with shear studs and shear connectors (Abdullah, 2004; Ahmed and Tsavdaridis, 2022; Genikomsou and Polak, 2015; Qureshi and Lam, 2012; Ríos et al., 2017; Xu et al., 2012;). The analysis of quasi-static problems requires ensuring that inertial effects are minimal by using smooth amplitude for displacement application (Figure 5-12). In addition, a mass scaling factor of 1.0×10^6 was implemented to increase the stable time increment. The “dynamic/ explicit” analysis method was preferred in this study because it is capable of reducing computational time (through applying mass scaling factor) and storage requirements without compromising the accuracy of the results. It is also efficient in modelling non-linear impact as well as solving contact and discontinuous problems.

In both the validation and parametric study models, a total step time ranging between 200 and 500 seconds is assigned depending on the specimen length and the corresponding maximum displacement (typically set to reach at least $L/40$), enabling sufficient solution resolution. While these durations are significantly shorter than actual experimental testing time, they are consistent with best practices in quasi-static simulation. The validity of the quasi-static

assumption was verified by monitoring the ratio of kinetic energy (ALLKE) to internal energy (ALLIE), which remained well below the commonly accepted threshold of 5-10%, confirming that inertial effects are negligible throughout the analyses.

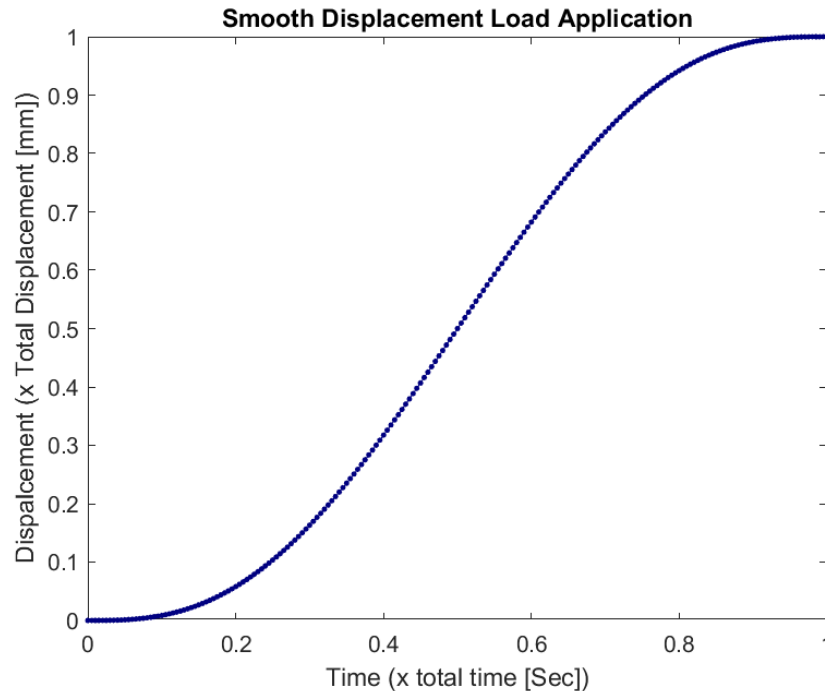


Figure 5-12: Smooth amplitude for load application

5.4.4 Meshing and Element Types

Appropriate meshing shapes, sizes and elements types play a major role in performing precise FEA. This is usually done after proper partitioning of model assembly or parts, as a final step before running the analysis. Finer meshes provide better end results and improved visualisation of stress, strain and crack distribution but require longer computation time and more storage. Therefore, the focus was first on obtaining well-shaped mesh elements, and a mesh sensitivity study was conducted to choose a reasonable mesh size that gives accurate results in the shortest possible time. Based on the outcomes of the sensitivity analysis (section 5.5.1), the selected element size for the model is 20 mm with smaller 7 mm meshing for shear connectors and areas near them in order to achieve accurate results at the shear connection locations. For the support and loading beam, larger 50 mm meshes are applied where discrete rigid elements are used. Figure 5-13 captures multiple views of the meshed FE model with a detailed view of the smaller mesh size on and around shear connectors.

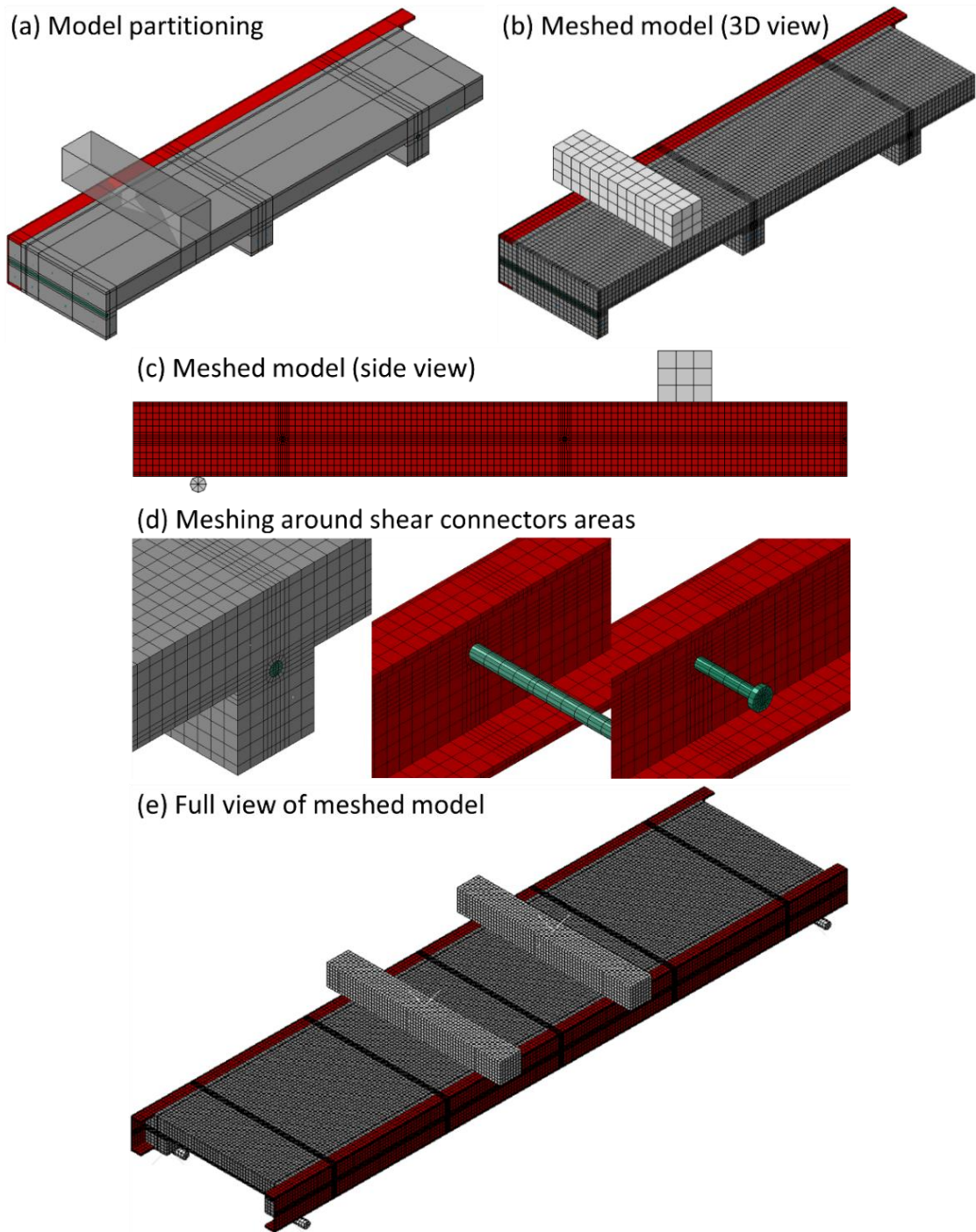


Figure 5-13: FE model meshing

For element types selection, ABAQUS offers a wide range of standard and explicit mesh element library. In the developed models, three main element types are implemented. The first type of elements is the three-dimensional eight-node solid explicit elements with reduced integration (C3D8R), which are used for solid components including the concrete slab, steel beam section and shear connectors. In this type, each node has three translational degrees of freedom (3DOF). The second type of element is used for all the steel reinforcement in the models, which is the three-dimensional two-node truss elements (T3D2). This

type of element represents a slender structural element subjected to axial forces only without bending. Finally, since deformations of the loading beam and support are negligible compared to the test specimen, discrete rigid elements are applied to them using three-dimensional four-node bilinear quadrilateral elements (R3D4). Figure 5-14 illustrates the elements types used in each part of the FE models.

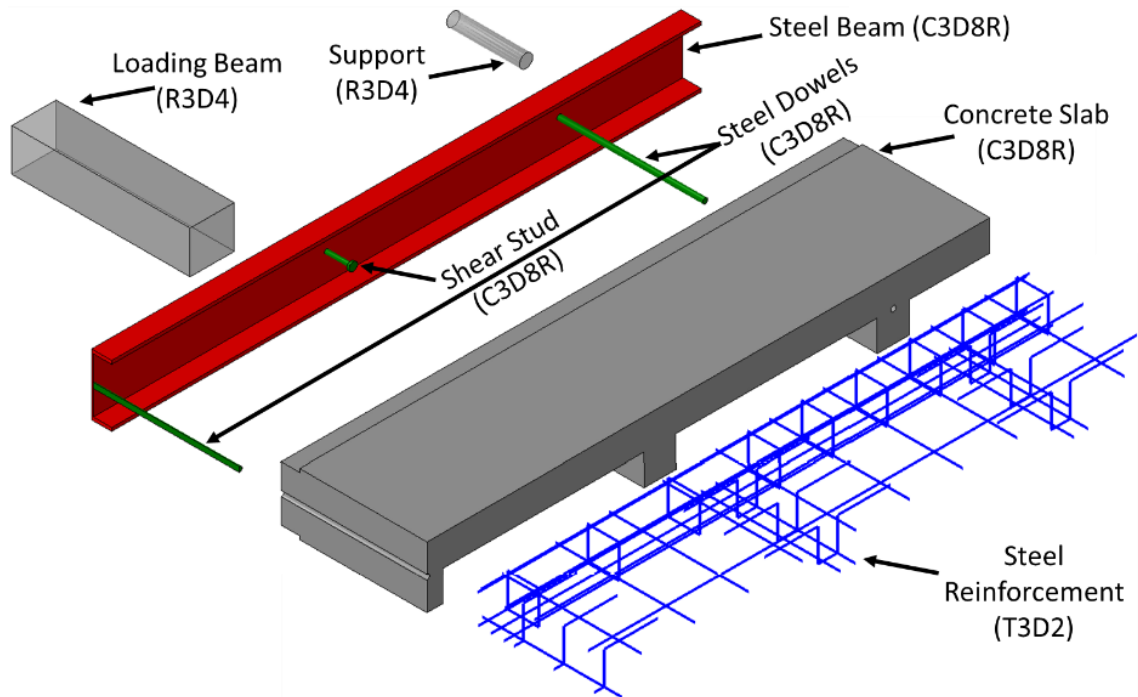


Figure 5-14: FE model element types

5.5 FE Model Validation

To verify the reliability of the results of the FE models implementing the assumptions outlined in the previous sections, the modelling approach was first validated against the experimental four-point bending tests observations presented in Chapter 4. This included extracting results from models with various mesh sizes to perform a mesh sensitivity study and select the optimum overall mesh size for the FE parametric study.

5.5.1 Mesh Sensitivity Analysis

The four models resembling the experimentally tested PUSS units were evaluated in a mesh sensitivity analysis using various global mesh sizes ranging between 10 to 50 mm, with local mesh sizes ranging between 5 to 20 mm for shear connectors and areas around them. The outcomes of the conducted comparison concluded that a 20 mm global mesh size with 7 mm mesh size for shear connectors is the most appropriate size to carry out the FE parametric study. The results associated with this size provided close agreement with

experimental results (more details in section 5.5.2) and captured the crack development observed in the experimental testing. Although the smaller 10 mm global mesh size with 5 mm mesh size for shear connectors provided better visualisation in monitoring crack progression and stress distribution, the numerical results were nearly identical to the results derived from models with a 20 mm size. Figure 5-15 clarifies the influence of mesh refinement on the accuracy of the simulation. Mid-span moment vs displacement curves are extracted from models with each mesh size and are presented in the figure. These curves demonstrate clear convergence behaviour. While finer meshes (20 mm and 10 mm) produced nearly identical responses in all specimens, coarser meshes (50 mm and 35 mm) consistently produce lower moment capacities. Additionally, the calculation time and storage requirement increased dramatically using mesh sizes smaller than 20 mm, as illustrated in Figure 5-16. Take into consideration that the FE parametric study investigated wider 2 m PUSS units with spans reaching 12 m, which would require longer calculation times and higher storage compared to the smaller validation models.

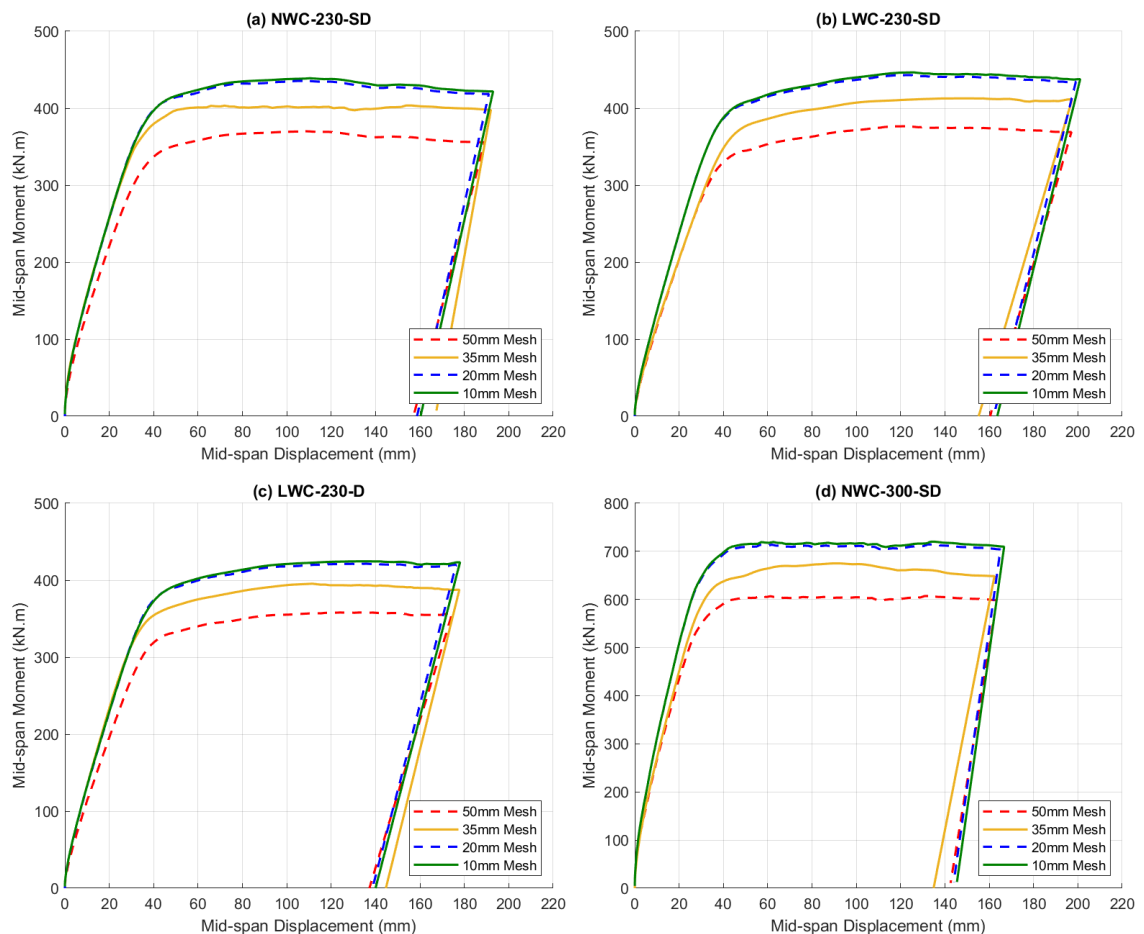


Figure 5-15: Mesh convergence study of mid-span moment vs displacement curves of FE validation models

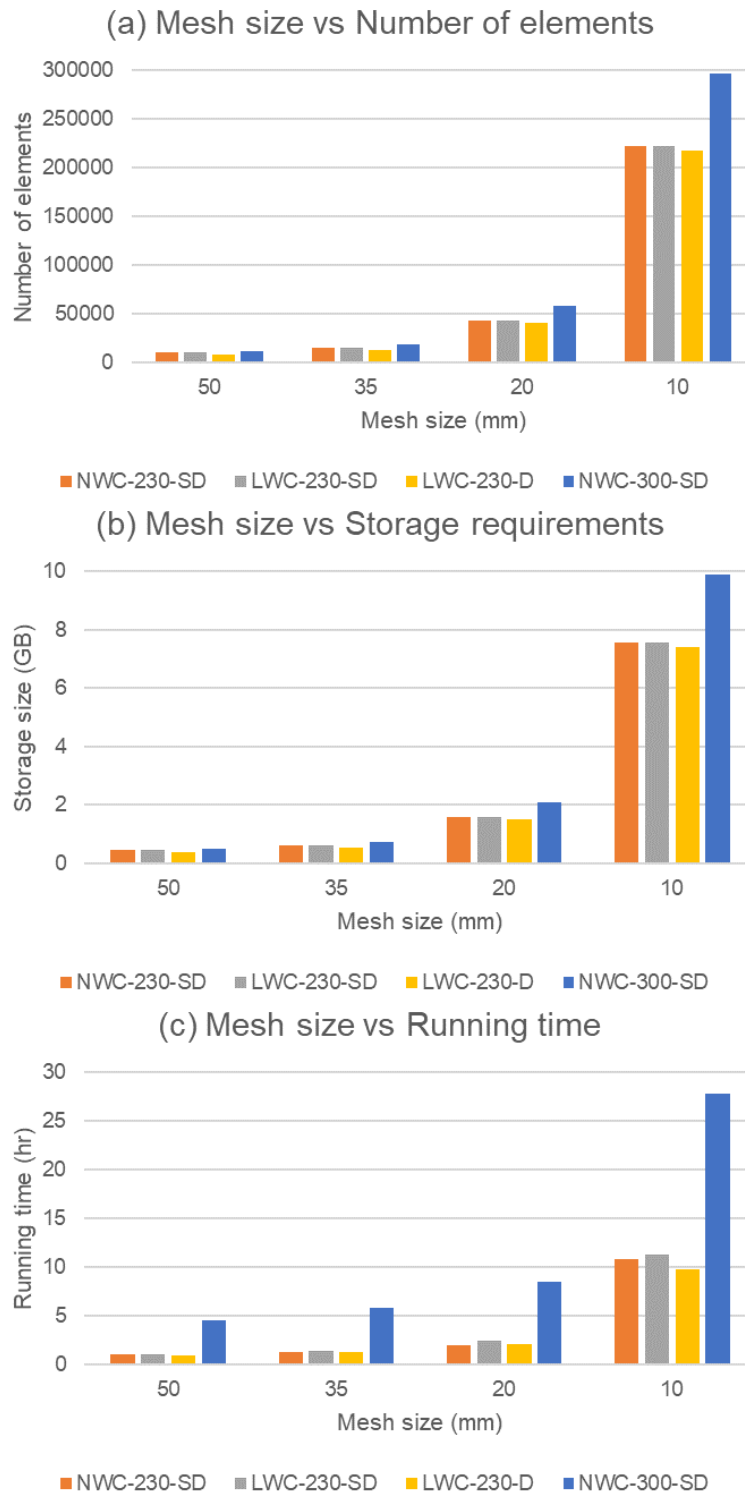


Figure 5-16: Mesh sensitivity analysis of FE validation models

5.5.2 Results Comparison

The results of the FE models simulating the experimentally tested PUSS units were compared with the laboratory tests outcomes. The comparison included multiple aspects, such as load-deflection curves, slips, deflection shapes, crack progression, crack distribution, and separation between the steel beam and concrete slab. The numerical models were capable of capturing the load-

displacement curves of the experiments, reflecting similar overall curve shape, initial stiffness, transition from elastic to plastic regions, and maximum loads. Figure 5-17 illustrates the agreement of the mid-span moments vs mid-span displacements curves of the four experiments. Although, the models accurately predicted the ultimate loads reached by each specimen, one limitation was their inability to reflect the strength drop in PUSS units associated with large cracks and failure of shear connectors since they are tied to the steel beams. A comparison of the maximum moments and initial stiffness slopes between the experimental tests and FE models is summarised in Table 5-1. The presented results are close for all specimens, with maximum difference being around 7% for initial stiffness and just over 1% for maximum mid-span moments.

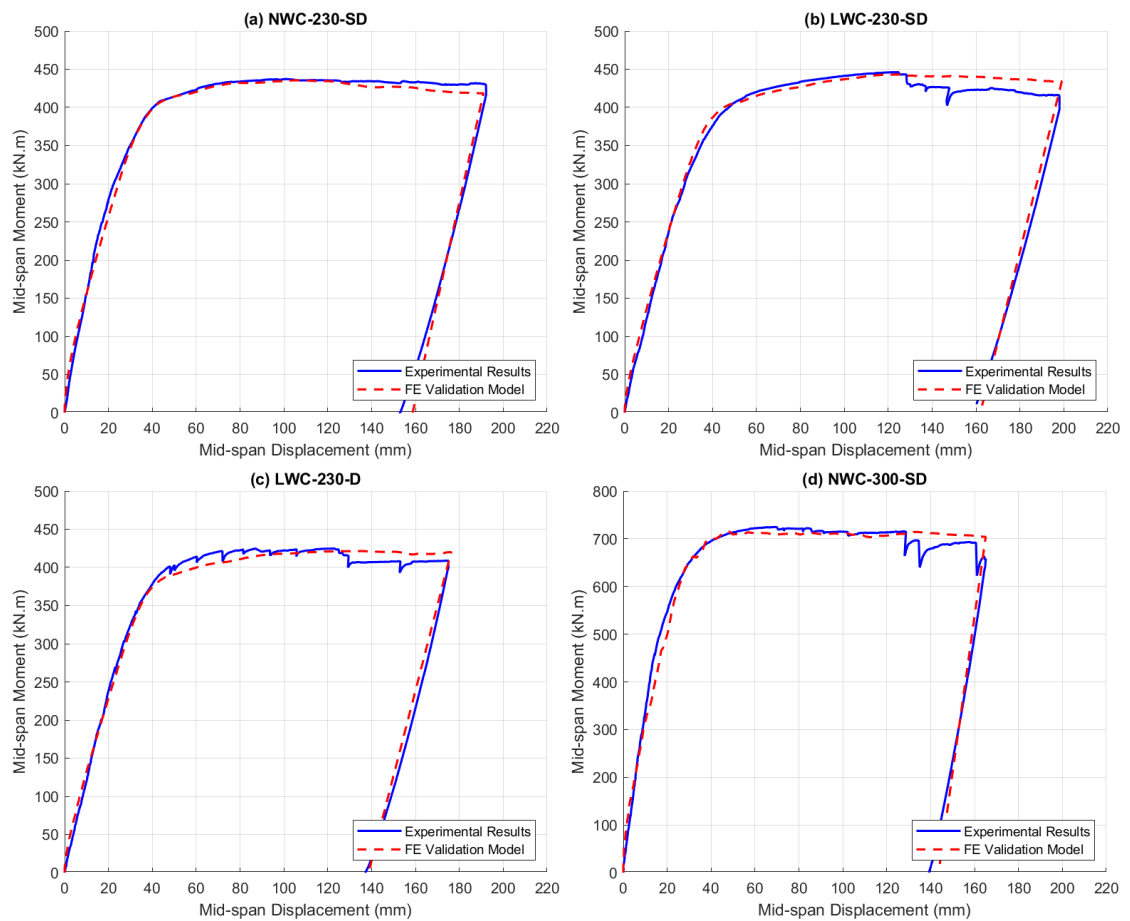


Figure 5-17: Comparison of mid-span moment vs displacement curves of FE models and experimental four-point bending tests

Table 5-1: Comparison of FE models results and experimental four-point bending tests

#	Specimen	Maximum Mid-span Moment (kN.m)			Initial Stiffness Slope		
		Test	FEA	Ratio (Test/FEA)	Test	FEA	Ratio (Test/FEA)
1	NWC-230-SD	437.19	435.51	1.0039	15.384	14.769	1.0416
2	LWC-230-SD	446.2	443.05	1.0071	11.953	12.740	0.9382
3	LWC-230-D	424.8	421.44	1.0080	12.296	12.295	1.0001
4	NWC-300-SD	724.79	715.11	1.0135	35.163	32.843	1.0706
		Mean		1.0081	Mean		1.0126
		CV		0.35%	CV		4.91%

Visual evaluation of the numerical models' outcomes showed that the validation models well-captured the deflected shapes, crack progression and distribution, bending of shear connectors, slips and separation between the steel beam and concrete slab. Figure 5-18 to Figure 5-22 provide visual comparison of the FE outcomes with the experimental tests at end of tests. In addition, Figure 5-23 to Figure 5-26 depict the contour plots of stress distributions over steel beam section and shear connectors in test specimens at 100 mm displacement.

The validation models showed good agreement between FEA outcomes and the four-point bending laboratory tests, demonstrating the reliability of the proposed modelling approach for use in the FE parametric study.

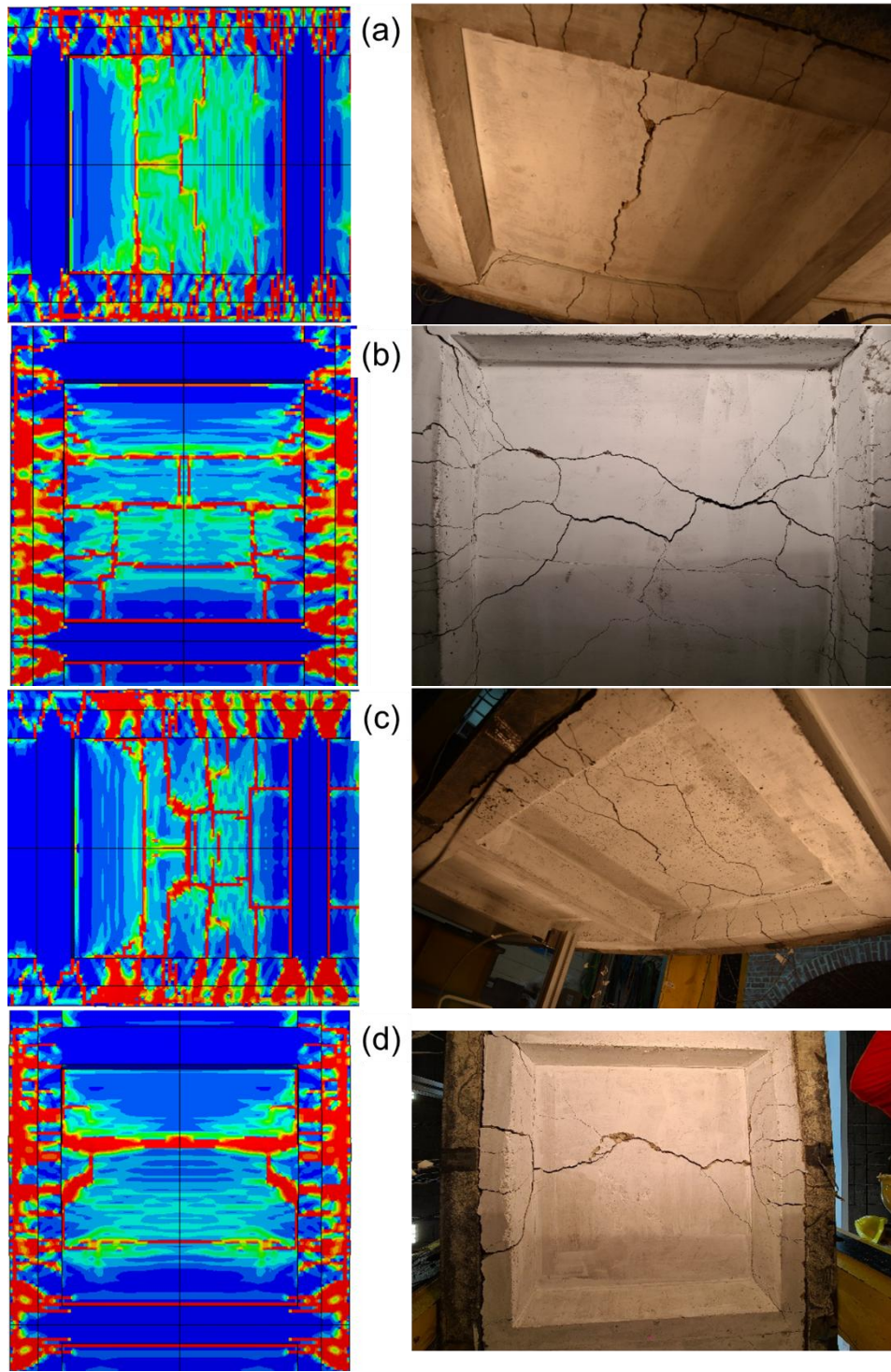


Figure 5-18: Comparison of cracks at the end of tests beneath specimens in FE models and experiments of (a) NWC-230-SD (b) LWC-230-SD (c) LWC-230-D & (d) NWC-300-SD

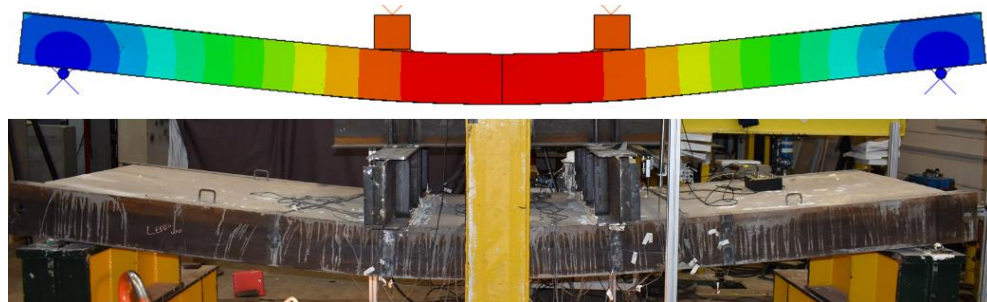


Figure 5-19: Comparison of deflected shape at the end of the test in FE model and experiment of specimen LWC-230-D

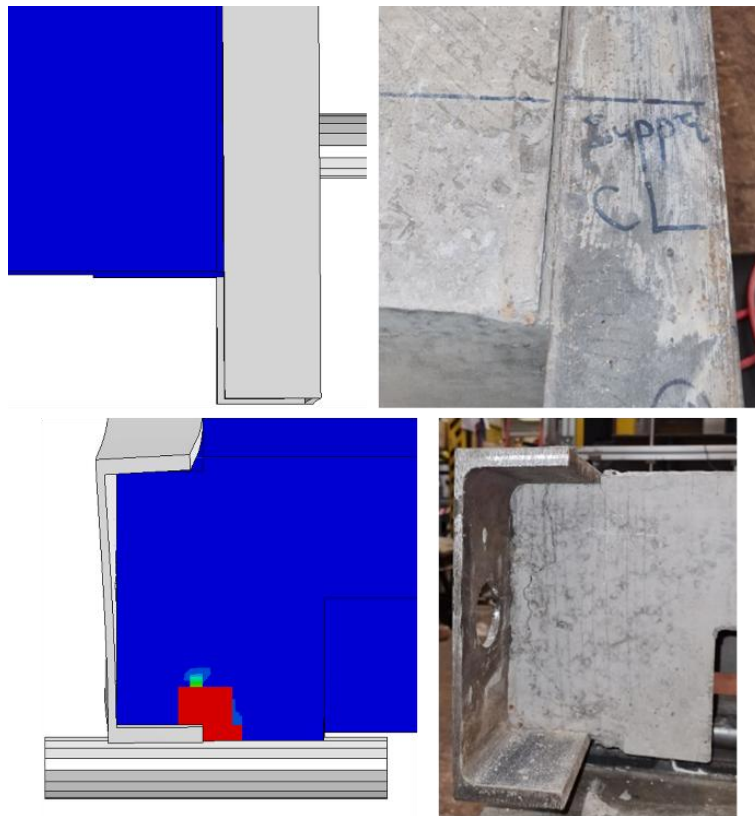


Figure 5-20: Comparison of separation between steel beam and concrete slab at the end of the test in FE model and experiment of specimen LWC-230-SD

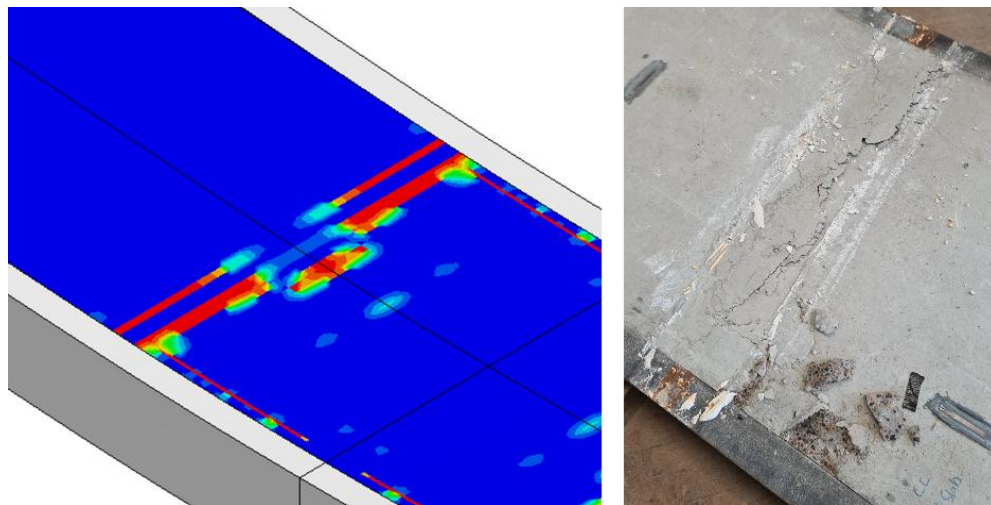


Figure 5-21: Comparison of compression cracks below loading beams at the end of the test in FE model and experiment of specimen LWC-230-SD

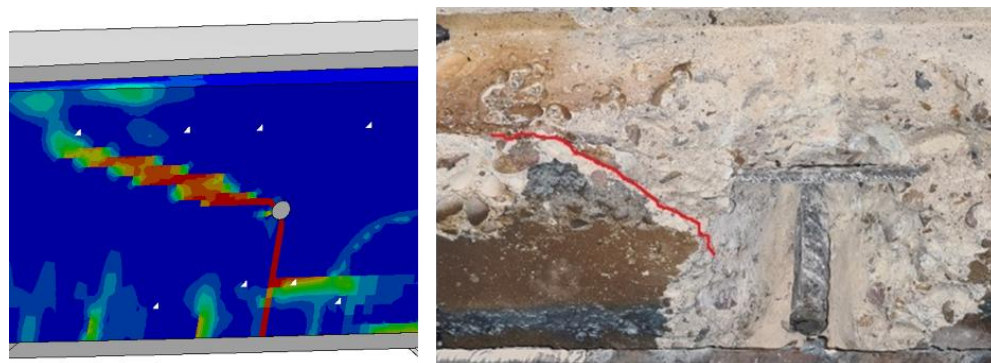


Figure 5-22: Comparison of internal diagonal crack near steel dowel at the end of the test in FE model and experiment of specimen NWC-300-SD

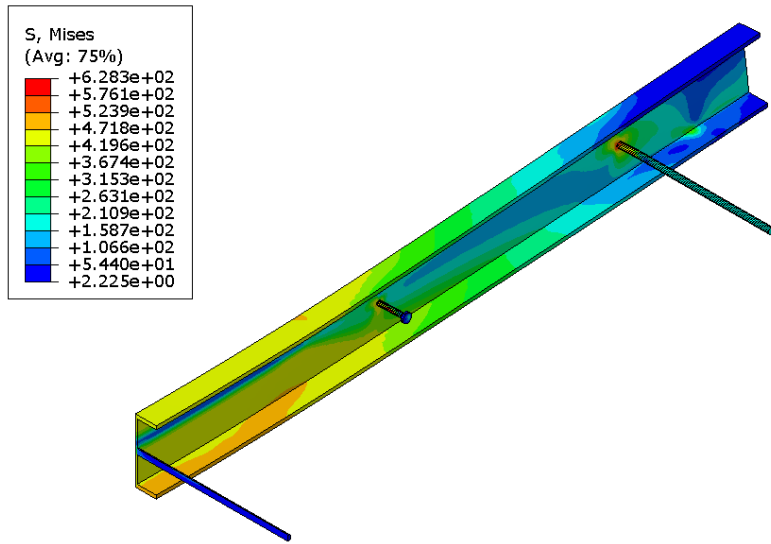


Figure 5-23: Stress contour plots on steel beam and shear connectors of NWC-230-SD at 100 mm displacement

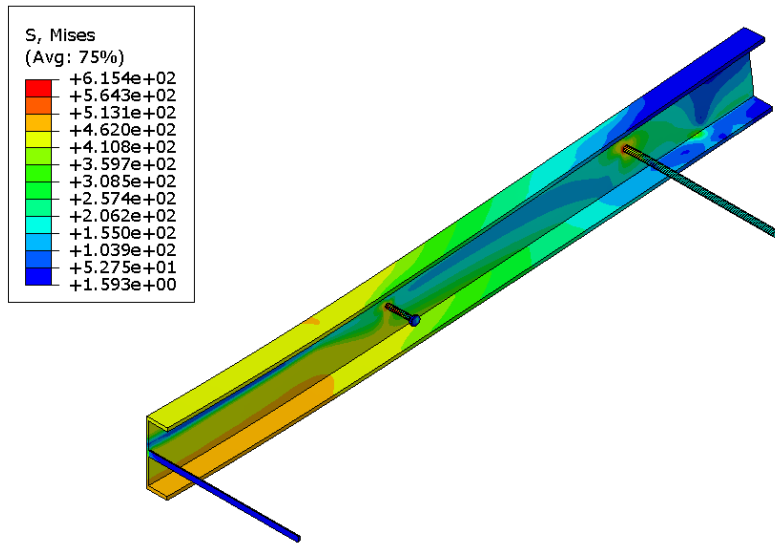


Figure 5-24: Stress contour plots on steel beam and shear connectors of LWC-230-SD at 100 mm displacement

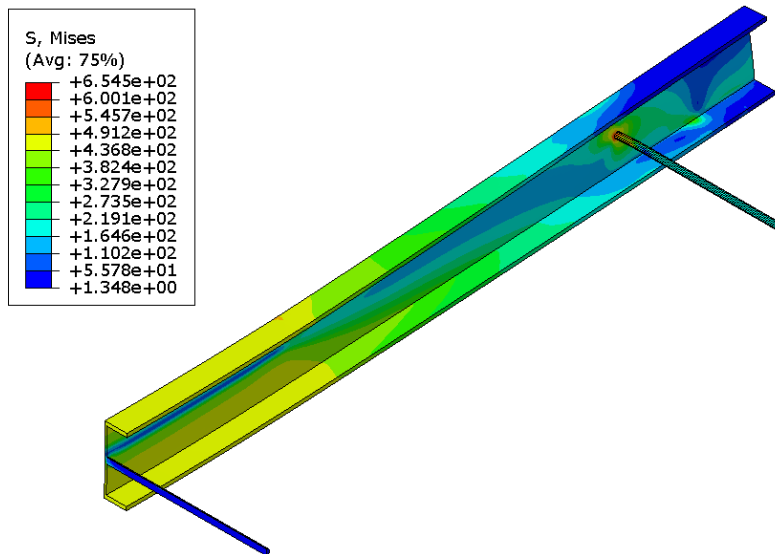


Figure 5-25: Stress contour plots on steel beam and shear connectors of LWC-230-D at 100 mm displacement

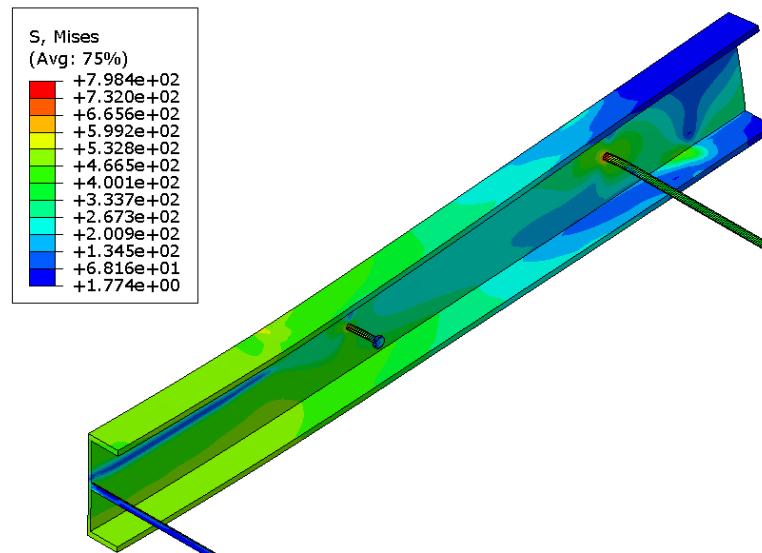


Figure 5-26: Stress contour plots on steel beam and shear connectors of NWC-300-SD at 100 mm displacement

5.6 Parametric Investigation

The elaborated FE modelling procedure is applied to conduct a parametric study, investigating the effects of variable parameters on the flexural behaviour of PUSS units and the performance of the employed shear connection system in bending. The parameters considered in the parametric study are the type of concrete, strength of concrete, depth of the slab, span of the slab and the degree of shear connection. The three types of concrete included in the investigation are NWC, LWC and GPC, each with variable strengths of 20, 30 and 40 MPa. The depths of the slabs ranges between 200 to 300 mm, with spans ranging from 3 to 12 m. Three spans are chosen for each depth, which differ from depth to depth, selecting practical spans for each depth based on design requirements. Finally, each model formed from the previous parameters is tested at three variable degrees of shear connection ranging between 40% to 100%. Different degrees of shear connection are achieved through employing different combinations of WWSS with diameter between 10 mm and 19 mm, and dowels with diameters between 8 mm to 25 mm. The degree of shear connection for each model is calculated based on the shear resistance of the employed shear connectors calculated using Equation 2-4 ($P_{sd} = 1.873(f_{ck}da_r)^{0.835} \leq 0.8f_uA_s$).

From the aforementioned parameters, a total of 324 parametric FE models are created for PUSS units with various configurations. Table 5-2 presents the parameters matrix of the study.

Table 5-2: FE parametric study matrix

#	Parameters	Variable 1	Variable 2	Variable 3	Variable 4	# of Variables
1	Concrete material	NWC	LWC	GPC		3
2	Concrete strength (MPa)	20	30	40		3
3	Slab depth (mm) Steel section	200 PFC 200x75x23	230 PFC 230x75x26	260 PFC 260x90x35	300 PFC 300x100x46	4
4	Slab span (m)	3 4 6	4 6 8	6 8 10	8 10 12	3
5	Degree of shear connection (η)	$\approx 100\%$	$\approx 75\%$	$\approx 50\%$		3
Total number of models						324

The established models simulate four-point bending tests on PUSS units with different parameters arrangements. For consistency, the distance between the centreline of the loading beams is fixed at 1000 mm in all the models, regardless of the span of the slab, as shown in Figure 5-27. Slabs are loaded in displacement-controlled manner using smooth amplitude (Figure 5-12) with appropriate step time to minimise the inertial effects. Tests are terminated only after loading beam displacement reaches at least $L/40$ or higher, significantly exceeding the serviceability (SLS) limits. At this point, specimens are considered to have failed for all practical purposes.

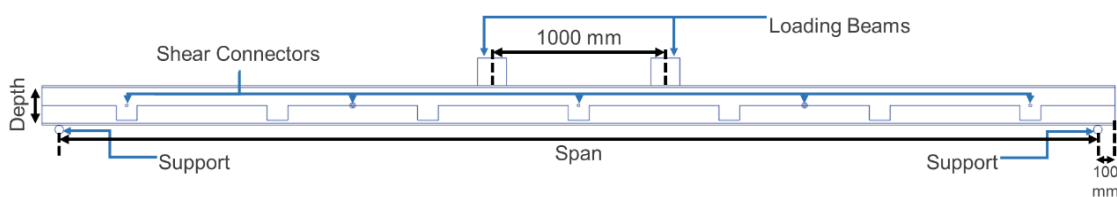


Figure 5-27: General FEA model arrangement

5.6.1 Parametric Study Results

A summary of the FE parametric study results is presented in Table 5-3 to Table 5-14. These tables provide a comparison between the values of maximum moments and degrees of shear connection derived from the FE models and those calculated from stress block method. They also tabulate the values of the initial stiffness and yield moment for each model, obtained from midspan moment vs displacement curves. The naming convention for each model in the tables reflects the values of each parameter included in the study, the general format of

the model names is “Depth”-“Span”-“Concrete type”-“Concrete strength”-“Degree of shear connection variable”.

For example, model “200-4-NWC-30-1” represents a PUSS unit with a depth of 200 mm, a span of 4 m, made of 30 MPa NWC. For every model created from the first four parameters (without the degree of shear connection), three different degrees of shear connection are applied by employing different combinations of shear connectors. This is represented by 1, 2 or 3, where 1 indicates the higher end degree of shear connection (usually represents full degree of shear connection) and 3 indicates the lowest end (around 50%).

To ensure the validity of the quasi-static assumptions in the explicit dynamic analyses, energy monitoring was carried out for all parametric models. Figure 5-28 illustrates representative plots showing the internal energy (ALLIE) and kinetic energy (ALLKE) of selected models over time. It can be seen that the kinetic energy remains below 5-10% of the internal energy throughout the analyses, indicating that inertial effects are negligible and that the simulations closely replicate quasi-static behaviour. This approach aligns with best practices in quasi-static explicit modelling and further supports the reliability of the presented results.

The following sections briefly discuss the effects of each parameter under investigation on the flexural behaviour of PUSS slabs and the performance of the employed shear connectors through an analysis of the FEA results.

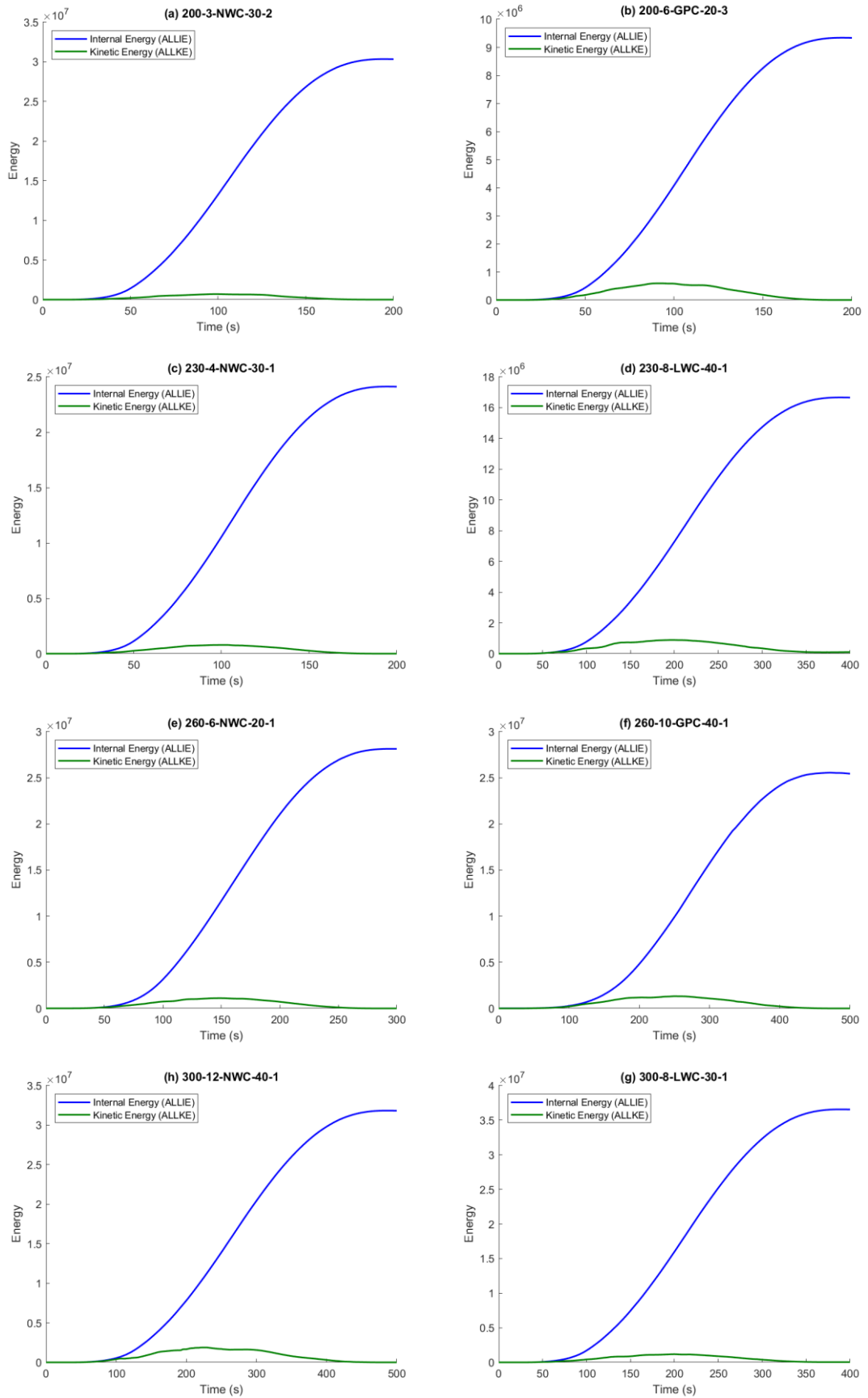


Figure 5-28: Comparison between internal energy (ALLIE) and kinetic energy (ALLKE) over analysis time for selected FE models,

Table 5-3: Summary of FE parametric study results for models with depth = 200 mm and span = 3 m

#	Model	Shear connectors	Initial stiffness	Yield Moment (kN.m)	Maximum Moment (kN.m)			Degree of shear connection		
					FEA	Calculated*	Ratio (FEA/Calculated)	FEA	Calculated*	Ratio (FEA/Calculated)
1	200-3-NWC-20-1	25mm Dowels + 19mm WWSS	17.9	262.6	348.7	347.8	1.003	100.0	100.0	1.000
2	200-3-LWC-20-1	25mm Dowels + 19mm WWSS	17.9	255.6	339.3	340.8	0.996	62.4	66.6	0.937
3	200-3-GPC-20-1	25mm Dowels + 19mm WWSS	17.8	253.8	336.9	337.1	0.999	56.8	57.2	0.993
4	200-3-NWC-20-2	12mm Dowels + 13mm WWSS	18.4	272.2	361.5	361.4	1.000	100.0	100.0	1.000
5	200-3-LWC-20-2	12mm Dowels + 13mm WWSS	17.0	269.8	358.3	358.3	1.000	85.0	85.1	0.998
6	200-3-GPC-20-2	12mm Dowels + 13mm WWSS	19.1	260.1	345.4	345.6	0.999	58.7	59.1	0.993
7	200-3-NWC-20-3	10mm Dowels + 10mm WWSS	20.0	278.2	369.5	369.4	1.000	100.0	100.0	1.000
8	200-3-LWC-20-3	10mm Dowels + 10mm WWSS	19.0	273.0	362.6	365.1	0.993	78.5	83.3	0.943
9	200-3-GPC-20-3	10mm Dowels + 10mm WWSS	20.0	266.4	353.8	349.5	1.012	64.6	57.8	1.117
10	200-3-NWC-30-1	25mm Dowels + 19mm WWSS	15.3	258.8	345.7	347.8	0.994	83.8	100.0	0.838
11	200-3-LWC-30-1	25mm Dowels + 19mm WWSS	14.1	257.1	343.4	340.8	1.008	75.5	66.6	1.133
12	200-3-GPC-30-1	25mm Dowels + 19mm WWSS	16.2	254.5	339.9	337.1	1.008	64.1	57.2	1.121
13	200-3-NWC-30-2	12mm Dowels + 13mm WWSS	16.6	260.6	348.2	361.4	0.963	63.8	100.0	0.638
14	200-3-LWC-30-2	12mm Dowels + 13mm WWSS	16.6	260.0	347.4	358.3	0.969	62.3	85.1	0.732
15	200-3-GPC-30-2	12mm Dowels + 13mm WWSS	16.3	257.3	343.7	345.6	0.994	55.8	59.1	0.945
16	200-3-NWC-30-3	10mm Dowels + 10mm WWSS	16.8	275.3	367.8	369.4	0.996	90.0	100.0	0.900
17	200-3-LWC-30-3	10mm Dowels + 10mm WWSS	17.1	268.0	358.1	365.1	0.981	71.0	83.3	0.853
18	200-3-GPC-30-3	10mm Dowels + 10mm WWSS	17.3	262.4	350.5	349.5	1.003	59.4	57.8	1.027
19	200-3-NWC-40-1	25mm Dowels + 19mm WWSS	17.0	280.1	357.2	347.8	1.027	100.0	100.0	1.000
20	200-3-LWC-40-1	25mm Dowels + 19mm WWSS	16.6	274.9	350.5	340.8	1.028	100.0	66.6	1.502
21	200-3-GPC-40-1	25mm Dowels + 19mm WWSS	16.6	271.5	346.1	337.1	1.027	85.8	57.2	1.500
22	200-3-NWC-40-2	12mm Dowels + 13mm WWSS	18.9	287.8	367.0	361.4	1.015	100.0	100.0	1.000
23	200-3-LWC-40-2	12mm Dowels + 13mm WWSS	18.3	279.3	356.2	358.3	0.994	79.9	85.1	0.938
24	200-3-GPC-40-2	12mm Dowels + 13mm WWSS	18.2	275.0	350.6	345.6	1.015	68.8	59.1	1.164
25	200-3-NWC-40-3	10mm Dowels + 10mm WWSS	19.4	281.0	371.9	369.4	1.007	100.0	100.0	1.000
26	200-3-LWC-40-3	10mm Dowels + 10mm WWSS	18.8	273.0	361.2	365.1	0.989	76.1	83.3	0.914
27	200-3-GPC-40-3	10mm Dowels + 10mm WWSS	18.6	270.5	357.8	349.5	1.024	70.6	57.8	1.221
					Average		1.002	Average		1.015
					CV		1.55%	CV		17.99%

* Calculated using Equation 2-4 ($P_{sd} = 1.873(f_{ck}da_r)^{0.835} \leq 0.8f_uA_s$)

Table 5-4: Summary of FE parametric study results for models with depth = 200 mm and span = 4 m

#	Model	Shear connectors	Initial stiffness	Yield Moment (kN.m)	Maximum Moment (kN.m)			Degree of shear connection		
					FEA	Calculated*	Ratio (FEA/Calculated)	FEA	Calculated*	Ratio (FEA/Calculated)
28	200-4-NWC-20-1	16mm Dowels + 16mm WWSS	17.6	248.2	349.6	347.4	1.006	100.0	93.8	1.066
29	200-4-LWC-20-1	16mm Dowels + 16mm WWSS	16.3	245.9	346.4	339.7	1.020	86.9	63.4	1.371
30	200-4-GPC-20-1	16mm Dowels + 16mm WWSS	16.8	243.7	343.3	337.5	1.017	75.1	58.0	1.295
31	200-4-NWC-20-2	10mm Dowels + 10mm WWSS	16.5	256.8	362.0	361.4	1.001	100.0	100.0	1.000
32	200-4-LWC-20-2	10mm Dowels + 10mm WWSS	16.6	254.1	358.2	358.5	0.999	84.7	85.6	0.990
33	200-4-GPC-20-2	10mm Dowels + 10mm WWSS	18.1	251.4	354.3	355.5	0.997	75.8	78.3	0.968
34	200-4-NWC-20-3	8mm Dowels + 10mm WWSS	17.9	261.8	369.1	369.4	0.999	96.0	100.0	0.960
35	200-4-LWC-20-3	8mm Dowels + 10mm WWSS	18.0	258.6	364.5	369.4	0.987	82.2	100.0	0.822
36	200-4-GPC-20-3	8mm Dowels + 10mm WWSS	19.0	255.2	359.6	367.9	0.977	73.5	90.2	0.815
37	200-4-NWC-30-1	16mm Dowels + 16mm WWSS	16.0	240.3	340.0	347.4	0.979	64.2	93.8	0.684
38	200-4-LWC-30-1	16mm Dowels + 16mm WWSS	12.0	239.5	338.8	339.7	0.998	61.3	63.4	0.967
39	200-4-GPC-30-1	16mm Dowels + 16mm WWSS	11.8	237.4	335.8	337.5	0.995	54.3	58.0	0.937
40	200-4-NWC-30-2	10mm Dowels + 10mm WWSS	13.5	245.9	348.0	361.4	0.963	63.5	100.0	0.635
41	200-4-LWC-30-2	10mm Dowels + 10mm WWSS	13.1	242.9	343.7	358.5	0.959	55.8	85.6	0.652
42	200-4-GPC-30-2	10mm Dowels + 10mm WWSS	14.4	238.9	338.0	355.5	0.951	47.2	78.3	0.603
43	200-4-NWC-30-3	8mm Dowels + 10mm WWSS	13.0	247.9	350.8	369.4	0.950	59.8	100.0	0.598
44	200-4-LWC-30-3	8mm Dowels + 10mm WWSS	14.9	245.0	346.7	369.4	0.939	53.9	100.0	0.539
45	200-4-GPC-30-3	8mm Dowels + 10mm WWSS	15.1	242.8	343.5	367.9	0.934	49.5	90.2	0.549
46	200-4-NWC-40-1	16mm Dowels + 16mm WWSS	14.5	261.3	356.5	347.4	1.026	100.0	93.8	1.066
47	200-4-LWC-40-1	16mm Dowels + 16mm WWSS	14.2	257.3	350.9	339.7	1.033	100.0	63.4	1.578
48	200-4-GPC-40-1	16mm Dowels + 16mm WWSS	14.9	257.7	349.9	337.5	1.037	100.0	58.0	1.724
49	200-4-NWC-40-2	10mm Dowels + 10mm WWSS	15.8	265.3	362.0	361.4	1.002	100.0	100.0	1.000
50	200-4-LWC-40-2	10mm Dowels + 10mm WWSS	15.6	261.7	357.1	358.5	0.996	82.0	85.6	0.958
51	200-4-GPC-40-2	10mm Dowels + 10mm WWSS	16.0	261.1	354.6	355.5	0.997	76.4	78.3	0.975
52	200-4-NWC-40-3	8mm Dowels + 10mm WWSS	16.1	269.7	368.1	369.4	0.997	90.9	100.0	0.909
53	200-4-LWC-40-3	8mm Dowels + 10mm WWSS	17.1	267.3	363.1	369.4	0.983	79.6	100.0	0.796
54	200-4-GPC-40-3	8mm Dowels + 10mm WWSS	16.6	266.2	361.6	367.9	0.983	76.8	90.2	0.851
					Average		0.990	Average		0.937
					CV		2.68%	CV		30.61%

* Calculated using Equation 2-4 ($P_{sd} = 1.873(f_{ck}da_r)^{0.835} \leq 0.8f_uA_s$)

Table 5-5: Summary of FE parametric study results for models with depth = 200 mm and span = 6 m

#	Model	Shear connectors	Initial stiffness	Yield Moment (kN.m)	Maximum Moment (kN.m)			Degree of shear connection		
					FEA	Calculated*	Ratio (FEA/Calculated)	FEA	Calculated*	Ratio (FEA/Calculated)
55	200-6-NWC-20-1	16mm Dowels + 16mm WWSS	17.2	204.8	347.2	347.8	0.998	92.1	100.0	0.921
56	200-6-LWC-20-1	16mm Dowels + 16mm WWSS	13.8	204.0	345.7	345.3	1.001	83.7	82.0	1.021
57	200-6-GPC-20-1	16mm Dowels + 16mm WWSS	16.2	200.3	339.0	343.3	0.987	61.6	75.0	0.821
58	200-6-NWC-20-2	10mm Dowels + 10mm WWSS	17.7	213.4	362.9	361.4	1.004	100.0	100.0	1.000
59	200-6-LWC-20-2	10mm Dowels + 10mm WWSS	16.7	207.6	352.3	361.4	0.975	71.9	100.0	0.719
60	200-6-GPC-20-2	10mm Dowels + 10mm WWSS	15.2	203.4	344.6	360.8	0.955	57.4	93.2	0.616
61	200-6-NWC-20-3	8mm Dowels + 10mm WWSS	16.6	215.1	366.0	369.4	0.991	85.2	100.0	0.852
62	200-6-LWC-20-3	8mm Dowels + 10mm WWSS	16.6	208.1	353.2	369.4	0.956	63.6	100.0	0.636
63	200-6-GPC-20-3	8mm Dowels + 10mm WWSS	16.8	206.0	349.4	369.4	0.946	57.7	98.6	0.585
64	200-6-NWC-30-1	16mm Dowels + 16mm WWSS	11.6	201.2	347.5	347.8	0.999	94.2	100.0	0.942
65	200-6-LWC-30-1	16mm Dowels + 16mm WWSS	11.0	197.9	341.4	345.3	0.989	68.3	82.0	0.833
66	200-6-GPC-30-1	16mm Dowels + 16mm WWSS	11.6	195.9	337.8	343.3	0.984	58.7	75.0	0.783
67	200-6-NWC-30-2	10mm Dowels + 10mm WWSS	13.3	202.7	350.2	361.4	0.969	67.8	100.0	0.678
68	200-6-LWC-30-2	10mm Dowels + 10mm WWSS	13.6	198.8	343.2	361.4	0.949	55.0	100.0	0.550
69	200-6-GPC-30-2	10mm Dowels + 10mm WWSS	11.6	196.8	339.5	360.8	0.941	49.4	93.2	0.530
70	200-6-NWC-30-3	8mm Dowels + 10mm WWSS	12.2	204.7	353.8	369.4	0.958	64.6	100.0	0.646
71	200-6-LWC-30-3	8mm Dowels + 10mm WWSS	13.2	201.7	348.4	369.4	0.943	56.3	100.0	0.563
72	200-6-GPC-30-3	8mm Dowels + 10mm WWSS	14.0	198.1	341.9	369.4	0.926	47.5	98.6	0.481
73	200-6-NWC-40-1	16mm Dowels + 16mm WWSS	13.2	211.6	359.7	347.8	1.034	100.0	100.0	1.000
74	200-6-LWC-40-1	16mm Dowels + 16mm WWSS	11.6	204.8	347.2	345.3	1.006	92.0	82.0	1.122
75	200-6-GPC-40-1	16mm Dowels + 16mm WWSS	14.3	202.1	342.3	343.3	0.997	71.2	75.0	0.949
76	200-6-NWC-40-2	10mm Dowels + 10mm WWSS	13.2	215.6	366.9	361.4	1.015	100.0	100.0	1.000
77	200-6-LWC-40-2	10mm Dowels + 10mm WWSS	13.3	213.1	362.4	361.4	1.003	100.0	100.0	1.000
78	200-6-GPC-40-2	10mm Dowels + 10mm WWSS	16.8	204.2	346.1	360.8	0.959	60.0	93.2	0.644
79	200-6-NWC-40-3	8mm Dowels + 10mm WWSS	14.8	219.0	373.0	369.4	1.010	100.0	100.0	1.000
80	200-6-LWC-40-3	8mm Dowels + 10mm WWSS	17.4	214.4	364.7	369.4	0.987	82.5	100.0	0.825
81	200-6-GPC-40-3	8mm Dowels + 10mm WWSS	14.6	210.2	357.0	369.4	0.967	69.4	98.6	0.703
					Average		0.980	Average		0.793
					CV		2.70%	CV		22.91%

* Calculated using Equation 2-4 ($P_{sd} = 1.873(f_{ck}da_r)^{0.835} \leq 0.8f_uA_s$)

Table 5-6: Summary of FE parametric study results for models with depth = 230 mm and span = 4 m

#	Model	Shear connectors	Initial stiffness	Yield Moment (kN.m)	Maximum Moment (kN.m)			Degree of shear connection		
					FEA	Calculated*	Ratio (FEA/Calculated)	FEA	Calculated*	Ratio (FEA/Calculated)
82	230-4-NWC-20-1	16mm Dowels + 16mm WWSS	19.1	284.6	425.6	425.8	0.999	74.1	75.0	0.989
83	230-4-LWC-20-1	16mm Dowels + 16mm WWSS	20.3	281.6	419.2	414.1	1.012	58.1	50.6	1.148
84	230-4-GPC-20-1	16mm Dowels + 16mm WWSS	19.8	279.3	417.6	410.7	1.017	55.7	46.3	1.201
85	230-4-NWC-20-2	10mm Dowels + 10mm WWSS	20.4	295.4	440.1	446.6	0.985	77.8	100.0	0.778
86	230-4-LWC-20-2	10mm Dowels + 10mm WWSS	21.9	293.0	436.4	435.5	1.002	70.2	68.3	1.028
87	230-4-GPC-20-2	10mm Dowels + 10mm WWSS	17.2	284.2	425.0	432.3	0.983	51.8	62.5	0.829
88	230-4-NWC-20-3	8mm Dowels + 10mm WWSS	22.1	298.1	446.2	456.7	0.977	74.0	100.0	0.740
89	230-4-LWC-20-3	8mm Dowels + 10mm WWSS	20.2	294.5	440.7	452.6	0.974	65.7	84.9	0.773
90	230-4-GPC-20-3	8mm Dowels + 10mm WWSS	19.9	289.6	431.2	444.8	0.969	52.9	72.0	0.735
91	230-4-NWC-30-1	16mm Dowels + 16mm WWSS	17.2	290.2	417.8	425.8	0.981	55.9	75.0	0.746
92	230-4-LWC-30-1	16mm Dowels + 16mm WWSS	16.3	289.3	416.5	414.1	1.006	53.9	50.6	1.065
93	230-4-GPC-30-1	16mm Dowels + 16mm WWSS	16.9	287.4	413.7	410.7	1.007	50.0	46.3	1.080
94	230-4-NWC-30-2	10mm Dowels + 10mm WWSS	18.8	299.2	428.8	446.6	0.960	56.9	100.0	0.569
95	230-4-LWC-30-2	10mm Dowels + 10mm WWSS	16.2	296.1	424.4	435.5	0.974	51.1	68.3	0.747
96	230-4-GPC-30-2	10mm Dowels + 10mm WWSS	16.7	290.8	418.6	432.3	0.968	44.9	62.5	0.719
97	230-4-NWC-30-3	8mm Dowels + 10mm WWSS	16.4	303.4	434.8	456.7	0.952	57.4	100.0	0.574
98	230-4-LWC-30-3	8mm Dowels + 10mm WWSS	19.9	298.0	427.0	452.6	0.944	48.4	84.9	0.569
99	230-4-GPC-30-3	8mm Dowels + 10mm WWSS	18.8	292.9	421.6	444.8	0.948	43.3	72.0	0.602
100	230-4-NWC-40-1	16mm Dowels + 16mm WWSS	20.6	277.0	433.9	425.8	1.019	100.0	75.0	1.334
101	230-4-LWC-40-1	16mm Dowels + 16mm WWSS	18.3	276.3	432.7	414.1	1.045	100.0	50.6	1.975
102	230-4-GPC-40-1	16mm Dowels + 16mm WWSS	21.3	269.5	424.4	410.7	1.033	70.1	46.3	1.514
103	230-4-NWC-40-2	10mm Dowels + 10mm WWSS	19.5	283.4	444.1	446.6	0.995	87.7	100.0	0.877
104	230-4-LWC-40-2	10mm Dowels + 10mm WWSS	23.8	278.1	438.2	435.5	1.006	74.1	68.3	1.084
105	230-4-GPC-40-2	10mm Dowels + 10mm WWSS	19.6	275.3	433.7	432.3	1.003	64.9	62.5	1.038
106	230-4-NWC-40-3	8mm Dowels + 10mm WWSS	24.9	286.2	451.1	456.7	0.988	82.2	100.0	0.822
107	230-4-LWC-40-3	8mm Dowels + 10mm WWSS	21.0	285.2	446.9	452.6	0.988	75.2	84.9	0.886
108	230-4-GPC-40-3	8mm Dowels + 10mm WWSS	22.4	281.6	441.3	444.8	0.992	66.6	72.0	0.925
					Average		0.990	Average		0.939
					CV		2.47%	CV		32.8%

* Calculated using Equation 2-4 ($P_{sd} = 1.873(f_{ck}da_r)^{0.835} \leq 0.8f_uA_s$)

Table 5-7: Summary of FE parametric study results for models with depth = 230 mm and span = 6 m

#	Model	Shear connectors	Initial stiffness	Yield Moment (kN.m)	Maximum Moment (kN.m)			Degree of shear connection		
					FEA	Calculated*	Ratio (FEA/Calculated)	FEA	Calculated*	Ratio (FEA/Calculated)
109	230-6-NWC-20-1	16mm Dowels + 16mm WWSS	20.2	284.8	431.5	429.4	1.005	100.0	97.0	1.031
110	230-6-LWC-20-1	16mm Dowels + 16mm WWSS	19.1	280.6	425.9	422.7	1.008	75.4	65.5	1.150
111	230-6-GPC-20-1	16mm Dowels + 16mm WWSS	19.4	278.1	421.9	420.2	1.004	63.6	59.9	1.061
112	230-6-NWC-20-2	10mm Dowels + 10mm WWSS	19.6	289.4	439.8	446.6	0.985	77.3	100.0	0.773
113	230-6-LWC-20-2	10mm Dowels + 10mm WWSS	20.0	284.2	430.5	444.4	0.969	59.6	88.4	0.675
114	230-6-GPC-20-2	10mm Dowels + 10mm WWSS	19.9	280.8	426.2	438.3	0.972	53.3	74.4	0.717
115	230-6-NWC-20-3	8mm Dowels + 10mm WWSS	20.3	296.2	450.7	456.7	0.987	81.4	100.0	0.814
116	230-6-LWC-20-3	8mm Dowels + 10mm WWSS	20.6	291.5	443.2	456.3	0.971	69.6	95.3	0.731
117	230-6-GPC-20-3	8mm Dowels + 10mm WWSS	20.7	285.4	433.6	449.1	0.965	55.9	78.7	0.710
118	230-6-NWC-30-1	16mm Dowels + 16mm WWSS	11.8	278.5	422.3	429.4	0.984	64.5	97.0	0.665
119	230-6-LWC-30-1	16mm Dowels + 16mm WWSS	17.8	271.0	410.5	422.7	0.971	46.0	65.5	0.702
120	230-6-GPC-30-1	16mm Dowels + 16mm WWSS	15.6	265.0	401.2	420.2	0.955	35.0	59.9	0.583
121	230-6-NWC-30-2	10mm Dowels + 10mm WWSS	15.2	283.5	430.1	446.6	0.963	58.9	100.0	0.589
122	230-6-LWC-30-2	10mm Dowels + 10mm WWSS	15.2	280.4	425.3	444.4	0.957	52.2	88.4	0.591
123	230-6-GPC-30-2	10mm Dowels + 10mm WWSS	15.2	277.3	420.4	438.3	0.959	46.7	74.4	0.628
124	230-6-NWC-30-3	8mm Dowels + 10mm WWSS	15.2	288.1	437.3	456.7	0.958	60.8	100.0	0.608
125	230-6-LWC-30-3	8mm Dowels + 10mm WWSS	14.4	284.2	431.1	456.3	0.945	52.9	95.3	0.555
126	230-6-GPC-30-3	8mm Dowels + 10mm WWSS	16.5	280.8	425.9	449.1	0.948	47.3	78.7	0.600
127	230-6-NWC-40-1	16mm Dowels + 16mm WWSS	20.1	285.2	442.1	429.4	1.030	100.0	97.0	1.031
128	230-6-LWC-40-1	16mm Dowels + 16mm WWSS	20.0	273.6	421.9	422.7	0.998	63.4	65.5	0.968
129	230-6-GPC-40-1	16mm Dowels + 16mm WWSS	18.8	270.1	417.6	420.2	0.994	55.7	59.9	0.929
130	230-6-NWC-40-2	10mm Dowels + 10mm WWSS	20.9	290.2	448.7	446.6	1.005	100.0	100.0	1.000
131	230-6-LWC-40-2	10mm Dowels + 10mm WWSS	19.5	281.4	434.5	444.4	0.978	66.5	88.4	0.752
132	230-6-GPC-40-2	10mm Dowels + 10mm WWSS	19.7	277.4	429.4	438.3	0.980	57.9	74.4	0.778
133	230-6-NWC-40-3	8mm Dowels + 10mm WWSS	20.3	291.7	451.2	456.7	0.988	82.3	100.0	0.823
134	230-6-LWC-40-3	8mm Dowels + 10mm WWSS	21.4	285.2	442.2	456.3	0.969	68.0	95.3	0.714
135	230-6-GPC-40-3	8mm Dowels + 10mm WWSS	21.0	283.4	437.7	449.1	0.975	61.3	78.7	0.779
					Average		0.979	Average		0.776
					CV		2.06%	CV		21.39%

* Calculated using Equation 2-4 ($P_{sd} = 1.873(f_{ck}da_r)^{0.835} \leq 0.8f_uA_s$)

Table 5-8: Summary of FE parametric study results for models with depth = 230 mm and span = 8 m

#	Model	Shear connectors	Initial stiffness	Yield Moment (kN.m)	Maximum Moment (kN.m)			Degree of shear connection		
					FEA	Calculated*	Ratio (FEA/Calculated)	FEA	Calculated*	Ratio (FEA/Calculated)
136	230-8-NWC-20-1	16mm Dowels + 16mm WWSS	11.0	297.2	429.5	429.5	1.000	100.0	100.0	1.000
137	230-8-LWC-20-1	16mm Dowels + 16mm WWSS	11.6	295.1	427.4	426.9	1.001	82.5	79.7	1.035
138	230-8-GPC-20-1	16mm Dowels + 16mm WWSS	12.9	292.8	423.8	424.7	0.998	68.5	71.3	0.962
139	230-8-NWC-20-2	10mm Dowels + 10mm WWSS	12.2	300.9	435.2	446.6	0.975	67.8	100.0	0.678
140	230-8-LWC-20-2	10mm Dowels + 10mm WWSS	12.3	298.7	431.9	446.5	0.967	61.8	97.5	0.634
141	230-8-GPC-20-2	10mm Dowels + 10mm WWSS	12.0	293.6	425.1	441.3	0.963	51.9	80.5	0.645
142	230-8-NWC-20-3	8mm Dowels + 10mm WWSS	13.2	302.2	438.5	456.7	0.960	62.4	100.0	0.624
143	230-8-LWC-20-3	8mm Dowels + 10mm WWSS	14.0	300.7	436.1	456.3	0.956	59.1	95.3	0.620
144	230-8-GPC-20-3	8mm Dowels + 10mm WWSS	12.8	297.0	429.2	449.1	0.956	50.7	78.7	0.644
145	230-8-NWC-30-1	16mm Dowels + 16mm WWSS	7.2	279.1	424.2	429.5	0.988	69.7	100.0	0.697
146	230-8-LWC-30-1	16mm Dowels + 16mm WWSS	7.3	273.9	415.8	426.9	0.974	53.0	79.7	0.664
147	230-8-GPC-30-1	16mm Dowels + 16mm WWSS	7.2	268.4	406.9	424.7	0.958	41.5	71.3	0.582
148	230-8-NWC-30-2	10mm Dowels + 10mm WWSS	7.9	281.1	427.4	446.6	0.957	54.9	100.0	0.549
149	230-8-LWC-30-2	10mm Dowels + 10mm WWSS	7.7	276.9	420.7	446.5	0.942	47.1	97.5	0.483
150	230-8-GPC-30-2	10mm Dowels + 10mm WWSS	7.9	272.2	413.2	441.3	0.936	39.7	80.5	0.494
151	230-8-NWC-30-3	8mm Dowels + 10mm WWSS	8.0	284.3	432.6	456.7	0.947	54.6	100.0	0.546
152	230-8-LWC-30-3	8mm Dowels + 10mm WWSS	9.1	278.5	423.3	456.3	0.928	44.9	95.3	0.471
153	230-8-GPC-30-3	8mm Dowels + 10mm WWSS	7.6	275.1	417.7	449.1	0.930	40.1	78.7	0.509
154	230-8-NWC-40-1	16mm Dowels + 16mm WWSS	9.6	291.0	432.4	429.5	1.007	100.0	100.0	1.000
155	230-8-LWC-40-1	16mm Dowels + 16mm WWSS	12.4	289.9	429.3	426.9	1.006	95.9	79.7	1.203
156	230-8-GPC-40-1	16mm Dowels + 16mm WWSS	9.4	286.1	423.3	424.7	0.997	67.1	71.3	0.941
157	230-8-NWC-40-2	10mm Dowels + 10mm WWSS	13.3	302.9	450.1	446.6	1.008	100.0	100.0	1.000
158	230-8-LWC-40-2	10mm Dowels + 10mm WWSS	10.8	300.4	447.5	446.5	1.002	100.0	97.5	1.026
159	230-8-GPC-40-2	10mm Dowels + 10mm WWSS	11.2	298.5	443.1	441.3	1.004	84.8	80.5	1.054
160	230-8-NWC-40-3	8mm Dowels + 10mm WWSS	14.8	305.1	454.9	456.7	0.996	90.1	100.0	0.901
161	230-8-LWC-40-3	8mm Dowels + 10mm WWSS	11.0	302.9	450.2	456.3	0.987	80.6	95.3	0.845
162	230-8-GPC-40-3	8mm Dowels + 10mm WWSS	15.4	300.1	445.8	449.1	0.993	73.5	78.7	0.934
					Average		0.975		Average	0.768
					CV		2.60%		CV	27.97%

* Calculated using Equation 2-4 ($P_{sd} = 1.873(f_{ck} da_r)^{0.835} \leq 0.8f_u A_s$)

Table 5-9: Summary of FE parametric study results for models with depth = 260 mm and span = 6 m

#	Model	Shear connectors	Initial stiffness	Yield Moment (kN.m)	Maximum Moment (kN.m)			Degree of shear connection		
					FEA	Calculated*	Ratio (FEA/Calculated)	FEA	Calculated*	Ratio (FEA/Calculated)
163	260-6-NWC-20-1	16mm Dowels + 16mm WWSS	20.2	404.1	613.7	612.3	1.002	66.4	64.2	1.035
164	260-6-LWC-20-1	16mm Dowels + 16mm WWSS	20.7	394.6	598.7	600.6	0.997	46.8	48.7	0.961
165	260-6-GPC-20-1	16mm Dowels + 16mm WWSS	19.9	390.6	592.5	590.9	1.003	41.0	39.7	1.034
166	260-6-NWC-20-2	10mm Dowels + 13mm WWSS	20.8	413.9	627.2	642.6	0.976	57.8	87.0	0.664
167	260-6-LWC-20-2	10mm Dowels + 13mm WWSS	19.3	409.8	620.7	633.6	0.980	51.4	66.0	0.780
168	260-6-GPC-20-2	10mm Dowels + 13mm WWSS	20.9	403.4	612.7	618.7	0.990	44.1	49.5	0.891
169	260-6-NWC-20-3	8mm Dowels + 10mm WWSS	21.0	416.7	633.5	659.4	0.961	55.6	100.0	0.556
170	260-6-LWC-20-3	8mm Dowels + 10mm WWSS	20.5	412.9	625.7	649.5	0.963	49.2	76.2	0.645
171	260-6-GPC-20-3	8mm Dowels + 10mm WWSS	20.9	408.1	618.2	629.7	0.982	43.3	52.3	0.827
172	260-6-NWC-30-1	16mm Dowels + 16mm WWSS	14.6	404.9	599.3	612.3	0.979	47.4	64.2	0.738
173	260-6-LWC-30-1	16mm Dowels + 16mm WWSS	13.8	401.9	596.5	600.6	0.993	44.6	48.7	0.917
174	260-6-GPC-30-1	16mm Dowels + 16mm WWSS	14.6	401.2	593.7	590.9	1.005	42.1	39.7	1.060
175	260-6-NWC-30-2	10mm Dowels + 13mm WWSS	14.0	408.6	604.8	642.6	0.941	38.0	87.0	0.437
176	260-6-LWC-30-2	10mm Dowels + 13mm WWSS	15.6	403.6	599.1	633.6	0.946	34.2	66.0	0.519
177	260-6-GPC-30-2	10mm Dowels + 13mm WWSS	14.4	402.8	596.1	618.7	0.964	32.4	49.5	0.654
178	260-6-NWC-30-3	8mm Dowels + 10mm WWSS	14.0	410.4	609.4	659.4	0.924	37.2	100.0	0.372
179	260-6-LWC-30-3	8mm Dowels + 10mm WWSS	15.0	405.8	602.4	649.5	0.927	32.9	76.2	0.432
180	260-6-GPC-30-3	8mm Dowels + 10mm WWSS	16.2	402.9	598.0	629.7	0.950	30.5	52.3	0.583
181	260-6-NWC-40-1	16mm Dowels + 16mm WWSS	18.5	415.8	621.9	612.3	1.016	85.5	64.2	1.332
182	260-6-LWC-40-1	16mm Dowels + 16mm WWSS	19.9	413.9	619.0	600.6	1.031	76.2	48.7	1.565
183	260-6-GPC-40-1	16mm Dowels + 16mm WWSS	18.9	410.2	613.2	590.9	1.038	65.7	39.7	1.656
184	260-6-NWC-40-2	10mm Dowels + 13mm WWSS	19.2	419.1	626.9	642.6	0.976	57.5	87.0	0.660
185	260-6-LWC-40-2	10mm Dowels + 13mm WWSS	19.7	418.0	625.2	633.6	0.987	55.7	66.0	0.844
186	260-6-GPC-40-2	10mm Dowels + 13mm WWSS	19.7	411.0	614.5	618.7	0.993	45.6	49.5	0.922
187	260-6-NWC-40-3	8mm Dowels + 10mm WWSS	19.4	419.5	627.6	659.4	0.952	50.6	100.0	0.506
188	260-6-LWC-40-3	8mm Dowels + 10mm WWSS	19.3	418.7	626.4	649.5	0.964	49.6	76.2	0.652
189	260-6-GPC-40-3	8mm Dowels + 10mm WWSS	22.4	414.2	619.4	629.7	0.984	44.2	52.3	0.845
					Average		0.979	Average		0.818
					CV		2.85%	CV		38.43%

* Calculated using Equation 2-4 ($P_{sd} = 1.873(f_{ck}da_r)^{0.835} \leq 0.8f_uA_s$)

Table 5-10: Summary of FE parametric study results for models with depth = 260 mm and span = 8 m

#	Model	Shear connectors	Initial stiffness	Yield Moment (kN.m)	Maximum Moment (kN.m)			Degree of shear connection		
					FEA	Calculated*	Ratio (FEA/Calculated)	FEA	Calculated*	Ratio (FEA/Calculated)
190	260-8-NWC-20-1	16mm Dowels + 16mm WWSS	13.6	422.8	626.4	619.8	1.011	100.0	78.1	1.280
191	260-8-LWC-20-1	16mm Dowels + 16mm WWSS	12.4	423.0	624.6	609.2	1.025	100.0	59.2	1.688
192	260-8-GPC-20-1	16mm Dowels + 16mm WWSS	12.8	420.7	623.0	599.1	1.040	100.0	47.2	2.120
193	260-8-NWC-20-2	10mm Dowels + 13mm WWSS	12.4	429.3	636.5	644.9	0.987	71.3	100.0	0.713
194	260-8-LWC-20-2	10mm Dowels + 13mm WWSS	13.6	423.9	626.1	638.6	0.980	56.6	75.9	0.746
195	260-8-GPC-20-2	10mm Dowels + 13mm WWSS	14.0	423.0	624.7	623.0	1.003	55.2	53.5	1.031
196	260-8-NWC-20-3	8mm Dowels + 10mm WWSS	13.9	430.5	638.4	659.4	0.968	60.4	100.0	0.604
197	260-8-LWC-20-3	8mm Dowels + 10mm WWSS	13.5	426.0	631.3	655.3	0.963	53.7	85.9	0.625
198	260-8-GPC-20-3	8mm Dowels + 10mm WWSS	14.3	425.0	627.8	629.7	0.997	50.8	52.3	0.971
199	260-8-NWC-30-1	16mm Dowels + 16mm WWSS	8.8	416.6	593.2	619.8	0.957	41.7	78.1	0.533
200	260-8-LWC-30-1	16mm Dowels + 16mm WWSS	9.8	412.4	587.1	609.2	0.964	36.7	59.2	0.619
201	260-8-GPC-30-1	16mm Dowels + 16mm WWSS	8.7	410.4	584.2	599.1	0.975	34.5	47.2	0.731
202	260-8-NWC-30-2	10mm Dowels + 13mm WWSS	9.7	429.1	611.8	644.9	0.949	43.3	100.0	0.433
203	260-8-LWC-30-2	10mm Dowels + 13mm WWSS	9.1	418.2	595.7	638.6	0.933	32.1	75.9	0.423
204	260-8-GPC-30-2	10mm Dowels + 13mm WWSS	10.0	415.3	591.4	623.0	0.949	29.6	53.5	0.553
205	260-8-NWC-30-3	8mm Dowels + 10mm WWSS	9.1	430.7	614.2	659.4	0.932	40.4	100.0	0.404
206	260-8-LWC-30-3	8mm Dowels + 10mm WWSS	9.9	419.2	597.2	655.3	0.911	30.1	85.9	0.350
207	260-8-GPC-30-3	8mm Dowels + 10mm WWSS	10.9	416.0	592.4	629.7	0.941	27.6	52.3	0.527
208	260-8-NWC-40-1	16mm Dowels + 16mm WWSS	9.5	434.5	622.0	619.8	1.003	85.8	78.1	1.098
209	260-8-LWC-40-1	16mm Dowels + 16mm WWSS	16.7	428.9	613.4	609.2	1.007	66.0	59.2	1.115
210	260-8-GPC-40-1	16mm Dowels + 16mm WWSS	10.2	424.8	607.3	599.1	1.014	56.6	47.2	1.200
211	260-8-NWC-40-2	10mm Dowels + 13mm WWSS	12.1	438.6	629.5	644.9	0.976	60.4	100.0	0.604
212	260-8-LWC-40-2	10mm Dowels + 13mm WWSS	12.6	432.9	620.9	638.6	0.972	51.6	75.9	0.679
213	260-8-GPC-40-2	10mm Dowels + 13mm WWSS	12.3	429.1	615.1	623.0	0.987	46.2	53.5	0.863
214	260-8-NWC-40-3	8mm Dowels + 10mm WWSS	13.0	447.0	640.7	659.4	0.972	63.2	100.0	0.632
215	260-8-LWC-40-3	8mm Dowels + 10mm WWSS	13.5	436.6	626.5	655.3	0.956	49.8	85.9	0.579
216	260-8-GPC-40-3	8mm Dowels + 10mm WWSS	14.3	432.2	619.9	629.7	0.984	44.6	52.3	0.852
					Average		0.976	Average		0.814
					CV		3.07%	CV		48.94%

* Calculated using Equation 2-4 ($P_{sd} = 1.873(f_{ck}da_r)^{0.835} \leq 0.8f_uA_s$)

Table 5-11: Summary of FE parametric study results for models with depth = 260 mm and span = 10 m

#	Model	Shear connectors	Initial stiffness	Yield Moment (kN.m)	Maximum Moment (kN.m)			Degree of shear connection		
					FEA	Calculated*	Ratio (FEA/Calculated)	FEA	Calculated*	Ratio (FEA/Calculated)
217	260-10-NWC-20-1	16mm Dowels + 16mm WWSS	12.3	431.9	638.9	622.8	1.026	100.0	91.6	1.092
218	260-10-LWC-20-1	16mm Dowels + 16mm WWSS	10.6	420.0	619.5	615.5	1.006	77.4	69.4	1.115
219	260-10-GPC-20-1	16mm Dowels + 16mm WWSS	11.4	418.4	615.1	603.4	1.019	68.7	51.7	1.329
220	260-10-NWC-20-2	10mm Dowels + 13mm WWSS	11.0	433.6	641.6	644.9	0.995	84.3	100.0	0.843
221	260-10-LWC-20-2	10mm Dowels + 13mm WWSS	12.8	427.1	631.2	641.4	0.984	62.5	83.6	0.748
222	260-10-GPC-20-2	10mm Dowels + 13mm WWSS	11.9	419.5	618.8	623.0	0.993	49.6	53.5	0.927
223	260-10-NWC-20-3	8mm Dowels + 10mm WWSS	12.0	439.9	652.0	659.4	0.989	80.0	100.0	0.800
224	260-10-LWC-20-3	8mm Dowels + 10mm WWSS	13.0	431.7	638.6	655.3	0.975	60.7	85.9	0.706
225	260-10-GPC-20-3	8mm Dowels + 10mm WWSS	11.1	423.2	624.8	629.7	0.992	48.5	52.3	0.926
226	260-10-NWC-30-1	16mm Dowels + 16mm WWSS	7.2	394.5	598.2	622.8	0.961	46.3	91.6	0.505
227	260-10-LWC-30-1	16mm Dowels + 16mm WWSS	7.4	392.6	595.1	615.5	0.967	43.4	69.4	0.624
228	260-10-GPC-30-1	16mm Dowels + 16mm WWSS	6.9	392.2	594.6	603.4	0.985	42.9	51.7	0.829
229	260-10-NWC-30-2	10mm Dowels + 13mm WWSS	9.1	399.8	606.9	644.9	0.941	39.5	100.0	0.395
230	260-10-LWC-30-2	10mm Dowels + 13mm WWSS	9.6	396.5	601.5	641.4	0.938	35.8	83.6	0.428
231	260-10-GPC-30-2	10mm Dowels + 13mm WWSS	7.4	394.3	598.0	623.0	0.960	33.5	53.5	0.626
232	260-10-NWC-30-3	8mm Dowels + 10mm WWSS	9.1	403.5	613.0	659.4	0.930	39.5	100.0	0.395
233	260-10-LWC-30-3	8mm Dowels + 10mm WWSS	9.3	400.9	608.8	655.3	0.929	36.8	85.9	0.428
234	260-10-GPC-30-3	8mm Dowels + 10mm WWSS	9.1	397.9	603.9	629.7	0.959	33.8	52.3	0.645
235	260-10-NWC-40-1	16mm Dowels + 16mm WWSS	10.6	443.1	632.7	622.8	1.016	100.0	91.6	1.092
236	260-10-LWC-40-1	16mm Dowels + 16mm WWSS	10.4	439.0	626.4	615.5	1.018	100.0	69.4	1.440
237	260-10-GPC-40-1	16mm Dowels + 16mm WWSS	11.2	430.4	613.0	603.4	1.016	65.3	51.7	1.263
238	260-10-NWC-40-2	10mm Dowels + 13mm WWSS	12.7	457.4	654.9	644.9	1.015	100.0	100.0	1.000
239	260-10-LWC-40-2	10mm Dowels + 13mm WWSS	11.0	440.6	628.9	641.4	0.981	59.6	83.6	0.713
240	260-10-GPC-40-2	10mm Dowels + 13mm WWSS	10.7	433.6	618.0	623.0	0.992	48.8	53.5	0.912
241	260-10-NWC-40-3	8mm Dowels + 10mm WWSS	13.3	465.2	667.1	659.4	1.012	100.0	100.0	1.000
242	260-10-LWC-40-3	8mm Dowels + 10mm WWSS	11.0	449.7	643.0	655.3	0.981	66.2	85.9	0.770
243	260-10-GPC-40-3	8mm Dowels + 10mm WWSS	11.9	444.2	634.4	629.7	1.007	56.4	52.3	1.078
					Average		0.985	Average		0.838
					CV		2.86%	CV		33.55%

* Calculated using Equation 2-4 ($P_{sd} = 1.873(f_{ck}da_r)^{0.835} \leq 0.8f_uA_s$)

Table 5-12: Summary of FE parametric study results for models with depth = 300 mm and span = 8 m

#	Model	Shear connectors	Initial stiffness	Yield Moment (kN.m)	Maximum Moment (kN.m)			Degree of shear connection		
					FEA	Calculated*	Ratio (FEA/Calculated)	FEA	Calculated*	Ratio (FEA/Calculated)
244	300-8-NWC-20-1	20mm Dowels + 19mm WWSS	18.5	614.8	890.8	891.2	1.000	65.3	65.7	0.993
245	300-8-LWC-20-1	20mm Dowels + 19mm WWSS	17.3	604.1	874.6	875.5	0.999	50.6	51.3	0.986
246	300-8-GPC-20-1	20mm Dowels + 19mm WWSS	20.5	596.4	862.9	859.8	1.004	42.6	40.7	1.047
247	300-8-NWC-20-2	16mm Dowels + 13mm WWSS	19.9	626.4	908.2	929.1	0.978	57.4	89.7	0.640
248	300-8-LWC-20-2	16mm Dowels + 13mm WWSS	20.0	614.4	890.1	920.2	0.967	44.7	70.0	0.639
249	300-8-GPC-20-2	16mm Dowels + 13mm WWSS	19.5	598.2	867.8	904.0	0.960	33.6	53.9	0.623
250	300-8-NWC-20-3	12mm Dowels + 10mm WWSS	20.1	633.8	921.8	949.9	0.970	56.5	100.0	0.565
251	300-8-LWC-20-3	12mm Dowels + 10mm WWSS	20.4	624.3	905.2	946.4	0.956	45.4	87.1	0.521
252	300-8-GPC-20-3	12mm Dowels + 10mm WWSS	20.6	607.7	880.0	920.3	0.956	33.6	55.3	0.607
253	300-8-NWC-30-1	20mm Dowels + 19mm WWSS	12.7	616.2	883.7	891.2	0.992	58.1	65.7	0.883
254	300-8-LWC-30-1	20mm Dowels + 19mm WWSS	12.8	598.6	859.9	875.5	0.982	40.8	51.3	0.795
255	300-8-GPC-30-1	20mm Dowels + 19mm WWSS	12.7	592.2	850.5	859.8	0.989	35.4	40.7	0.870
256	300-8-NWC-30-2	16mm Dowels + 13mm WWSS	13.1	618.2	886.7	929.1	0.954	42.8	89.7	0.477
257	300-8-LWC-30-2	16mm Dowels + 13mm WWSS	12.7	600.9	863.2	920.2	0.938	31.6	70.0	0.451
258	300-8-GPC-30-2	16mm Dowels + 13mm WWSS	13.3	594.2	853.4	904.0	0.944	27.6	53.9	0.511
259	300-8-NWC-30-3	12mm Dowels + 10mm WWSS	13.9	619.7	891.2	949.9	0.938	38.4	100.0	0.384
260	300-8-LWC-30-3	12mm Dowels + 10mm WWSS	12.8	604.6	868.8	946.4	0.918	29.2	87.1	0.336
261	300-8-GPC-30-3	12mm Dowels + 10mm WWSS	12.8	604.1	865.9	920.3	0.941	28.2	55.3	0.510
262	300-8-NWC-40-1	20mm Dowels + 19mm WWSS	16.3	636.8	897.9	891.2	1.008	75.5	65.7	1.149
263	300-8-LWC-40-1	20mm Dowels + 19mm WWSS	14.6	632.2	891.3	875.5	1.018	65.8	51.3	1.283
264	300-8-GPC-40-1	20mm Dowels + 19mm WWSS	14.6	626.4	882.8	859.8	1.027	57.2	40.7	1.404
265	300-8-NWC-40-2	16mm Dowels + 13mm WWSS	17.5	649.7	914.5	929.1	0.984	63.7	89.7	0.709
266	300-8-LWC-40-2	16mm Dowels + 13mm WWSS	11.8	627.5	895.6	920.2	0.973	48.1	70.0	0.686
267	300-8-GPC-40-2	16mm Dowels + 13mm WWSS	16.9	630.3	886.3	904.0	0.980	42.6	53.9	0.790
268	300-8-NWC-40-3	12mm Dowels + 10mm WWSS	18.8	653.6	920.2	949.9	0.969	55.2	100.0	0.552
269	300-8-LWC-40-3	12mm Dowels + 10mm WWSS	16.1	637.7	899.2	946.4	0.950	42.2	87.1	0.485
270	300-8-GPC-40-3	12mm Dowels + 10mm WWSS	14.7	635.3	893.5	920.3	0.971	39.5	55.3	0.713
					Average		0.973	Average		0.726
					CV		2.68%	CV		36.94%

* Calculated using Equation 2-4 ($P_{sd} = 1.873(f_{ck}da_r)^{0.835} \leq 0.8f_uA_s$)

Table 5-13: Summary of FE parametric study results for models with depth = 300 mm and span = 10 m

#	Model	Shear connectors	Initial stiffness	Yield Moment (kN.m)	Maximum Moment (kN.m)			Degree of shear connection		
					FEA	Calculated*	Ratio (FEA/Calculated)	FEA	Calculated*	Ratio (FEA/Calculated)
271	300-10-NWC-20-1	20mm Dowels + 19mm WWSS	16.2	588.7	927.2	898.7	1.032	100.0	77.1	1.298
272	300-10-LWC-20-1	20mm Dowels + 19mm WWSS	18.2	580.9	914.0	885.9	1.032	100.0	60.1	1.663
273	300-10-GPC-20-1	20mm Dowels + 19mm WWSS	17.0	577.5	908.0	870.7	1.043	100.0	47.7	2.094
274	300-10-NWC-20-2	16mm Dowels + 13mm WWSS	17.6	594.2	936.8	930.1	1.007	100.0	100.0	1.000
275	300-10-LWC-20-2	16mm Dowels + 13mm WWSS	17.9	588.1	926.3	927.2	0.999	79.7	82.1	0.970
276	300-10-GPC-20-2	16mm Dowels + 13mm WWSS	18.2	582.4	916.5	907.1	1.010	65.9	56.5	1.166
277	300-10-NWC-20-3	12mm Dowels + 10mm WWSS	19.1	605.2	955.8	949.9	1.006	100.0	100.0	1.000
278	300-10-LWC-20-3	12mm Dowels + 10mm WWSS	18.8	588.9	927.7	949.3	0.977	61.1	95.3	0.642
279	300-10-GPC-20-3	12mm Dowels + 10mm WWSS	18.2	584.8	920.7	920.3	1.000	55.6	55.3	1.006
280	300-10-NWC-30-1	20mm Dowels + 19mm WWSS	8.6	590.6	865.8	898.7	0.963	44.5	77.1	0.578
281	300-10-LWC-30-1	20mm Dowels + 19mm WWSS	8.2	587.3	860.7	885.9	0.972	41.3	60.1	0.687
282	300-10-GPC-30-1	20mm Dowels + 19mm WWSS	9.1	584.4	856.3	870.7	0.984	38.7	47.7	0.811
283	300-10-NWC-30-2	16mm Dowels + 13mm WWSS	8.9	606.6	890.6	930.1	0.958	45.0	100.0	0.450
284	300-10-LWC-30-2	16mm Dowels + 13mm WWSS	8.2	590.3	865.4	927.2	0.933	32.5	82.1	0.396
285	300-10-GPC-30-2	16mm Dowels + 13mm WWSS	9.0	578.6	847.4	907.1	0.934	25.3	56.5	0.448
286	300-10-NWC-30-3	12mm Dowels + 10mm WWSS	8.2	616.9	906.6	949.9	0.954	46.2	100.0	0.462
287	300-10-LWC-30-3	12mm Dowels + 10mm WWSS	9.5	605.4	888.8	949.3	0.936	37.3	95.3	0.391
288	300-10-GPC-30-3	12mm Dowels + 10mm WWSS	9.7	582.5	853.4	920.3	0.927	23.9	55.3	0.432
289	300-10-NWC-40-1	20mm Dowels + 19mm WWSS	12.2	641.9	917.9	898.7	1.021	100.0	77.1	1.298
290	300-10-LWC-40-1	20mm Dowels + 19mm WWSS	14.5	635.3	907.9	885.9	1.025	100.0	60.1	1.663
291	300-10-GPC-40-1	20mm Dowels + 19mm WWSS	15.7	619.0	883.0	870.7	1.014	57.4	47.7	1.202
292	300-10-NWC-40-2	16mm Dowels + 13mm WWSS	12.9	648.8	928.4	930.1	0.998	86.3	100.0	0.863
293	300-10-LWC-40-2	16mm Dowels + 13mm WWSS	14.8	646.5	924.9	927.2	0.997	76.7	82.1	0.934
294	300-10-GPC-40-2	16mm Dowels + 13mm WWSS	14.8	635.6	908.4	907.1	1.001	57.6	56.5	1.019
295	300-10-NWC-40-3	12mm Dowels + 10mm WWSS	14.9	662.2	948.8	949.9	0.999	93.7	100.0	0.937
296	300-10-LWC-40-3	12mm Dowels + 10mm WWSS	15.6	658.4	943.0	949.3	0.993	79.9	95.3	0.839
297	300-10-GPC-40-3	12mm Dowels + 10mm WWSS	14.8	643.5	920.4	920.3	1.000	55.4	55.3	1.002
					Average		0.990	Average		0.935
					CV		3.22%	CV		44.41%

* Calculated using Equation 2-4 ($P_{sd} = 1.873(f_{ck}da_r)^{0.835} \leq 0.8f_uA_s$)

Table 5-14: Summary of FE parametric study results for models with depth = 300 mm and span = 12 m

#	Model	Shear connectors	Initial stiffness	Yield Moment (kN.m)	Maximum Moment (kN.m)			Degree of shear connection		
					FEA	Calculated*	Ratio (FEA/Calculated)	FEA	Calculated*	Ratio (FEA/Calculated)
298	300-12-NWC-20-1	20mm Dowels + 19mm WWSS	15.3	588.8	905.3	903.0	1.003	100.0	88.1	1.136
299	300-12-LWC-20-1	20mm Dowels + 19mm WWSS	14.3	579.3	888.7	893.6	0.995	63.0	68.7	0.916
300	300-12-GPC-20-1	20mm Dowels + 19mm WWSS	15.7	569.4	869.1	879.0	0.989	46.7	54.0	0.864
301	300-12-NWC-20-2	16mm Dowels + 13mm WWSS	15.2	596.1	918.0	930.1	0.987	67.6	100.0	0.676
302	300-12-LWC-20-2	16mm Dowels + 13mm WWSS	16.2	590.8	906.4	929.3	0.975	55.9	91.5	0.611
303	300-12-GPC-20-2	16mm Dowels + 13mm WWSS	15.0	579.9	887.3	907.1	0.978	43.2	56.5	0.764
304	300-12-NWC-20-3	12mm Dowels + 10mm WWSS	15.0	611.3	944.9	949.9	0.995	84.0	100.0	0.840
305	300-12-LWC-20-3	12mm Dowels + 10mm WWSS	17.7	605.1	931.4	949.5	0.981	64.3	96.2	0.668
306	300-12-GPC-20-3	12mm Dowels + 10mm WWSS	15.7	598.5	920.0	920.3	1.000	55.1	55.3	0.996
307	300-12-NWC-30-1	20mm Dowels + 19mm WWSS	8.9	597.6	879.7	903.0	0.974	54.6	88.1	0.620
308	300-12-LWC-30-1	20mm Dowels + 19mm WWSS	7.1	577.7	850.1	893.6	0.951	35.2	68.7	0.513
309	300-12-GPC-30-1	20mm Dowels + 19mm WWSS	8.6	575.4	844.2	879.0	0.960	32.1	54.0	0.595
310	300-12-NWC-30-2	16mm Dowels + 13mm WWSS	7.7	598.7	883.8	930.1	0.950	41.3	100.0	0.413
311	300-12-LWC-30-2	16mm Dowels + 13mm WWSS	9.1	580.8	855.1	929.3	0.920	28.3	91.5	0.309
312	300-12-GPC-30-2	16mm Dowels + 13mm WWSS	8.8	575.6	846.8	907.1	0.934	25.1	56.5	0.444
313	300-12-NWC-30-3	12mm Dowels + 10mm WWSS	8.7	602.6	890.0	949.9	0.937	37.8	100.0	0.378
314	300-12-LWC-30-3	12mm Dowels + 10mm WWSS	8.3	592.1	873.3	949.5	0.920	30.9	96.2	0.321
315	300-12-GPC-30-3	12mm Dowels + 10mm WWSS	10.0	576.7	848.5	920.3	0.922	22.3	55.3	0.403
316	300-12-NWC-40-1	20mm Dowels + 19mm WWSS	13.8	579.6	904.1	903.0	1.001	92.0	88.1	1.045
317	300-12-LWC-40-1	20mm Dowels + 19mm WWSS	13.9	572.7	891.8	893.6	0.998	66.4	68.7	0.967
318	300-12-GPC-40-1	20mm Dowels + 19mm WWSS	14.8	564.4	877.0	879.0	0.998	52.4	54.0	0.970
319	300-12-NWC-40-2	16mm Dowels + 13mm WWSS	14.0	597.2	935.7	930.1	1.006	100.0	100.0	1.000
320	300-12-LWC-40-2	16mm Dowels + 13mm WWSS	13.9	595.3	932.3	929.3	1.003	100.0	91.5	1.092
321	300-12-GPC-40-2	16mm Dowels + 13mm WWSS	14.5	582.5	909.5	907.1	1.003	58.6	56.5	1.037
322	300-12-NWC-40-3	12mm Dowels + 10mm WWSS	16.8	605.3	950.3	949.9	1.000	100.0	100.0	1.000
323	300-12-LWC-40-3	12mm Dowels + 10mm WWSS	14.0	601.2	943.0	949.5	0.993	79.8	96.2	0.829
324	300-12-GPC-40-3	12mm Dowels + 10mm WWSS	13.8	588.8	920.7	920.3	1.000	55.6	55.3	1.006
					Average		0.977	Average		0.756
					CV		2.90%	CV		34.24%

* Calculated using Equation 2-4 ($P_{sd} = 1.873(f_{ck}da_r)^{0.835} \leq 0.8f_uA_s$)

5.6.2 Effect of Slab Depth

The parametric investigation examines four distinct depths of PUSS units through the application of different PFC steel sections. Figure 5-29 demonstrates the implication of varying depths on the flexural behaviour of the slabs. Each of the six graphs depicts midspan moment versus displacement curves derived from a range of FE models, each varying in depth while being consistent in the remaining parameters.

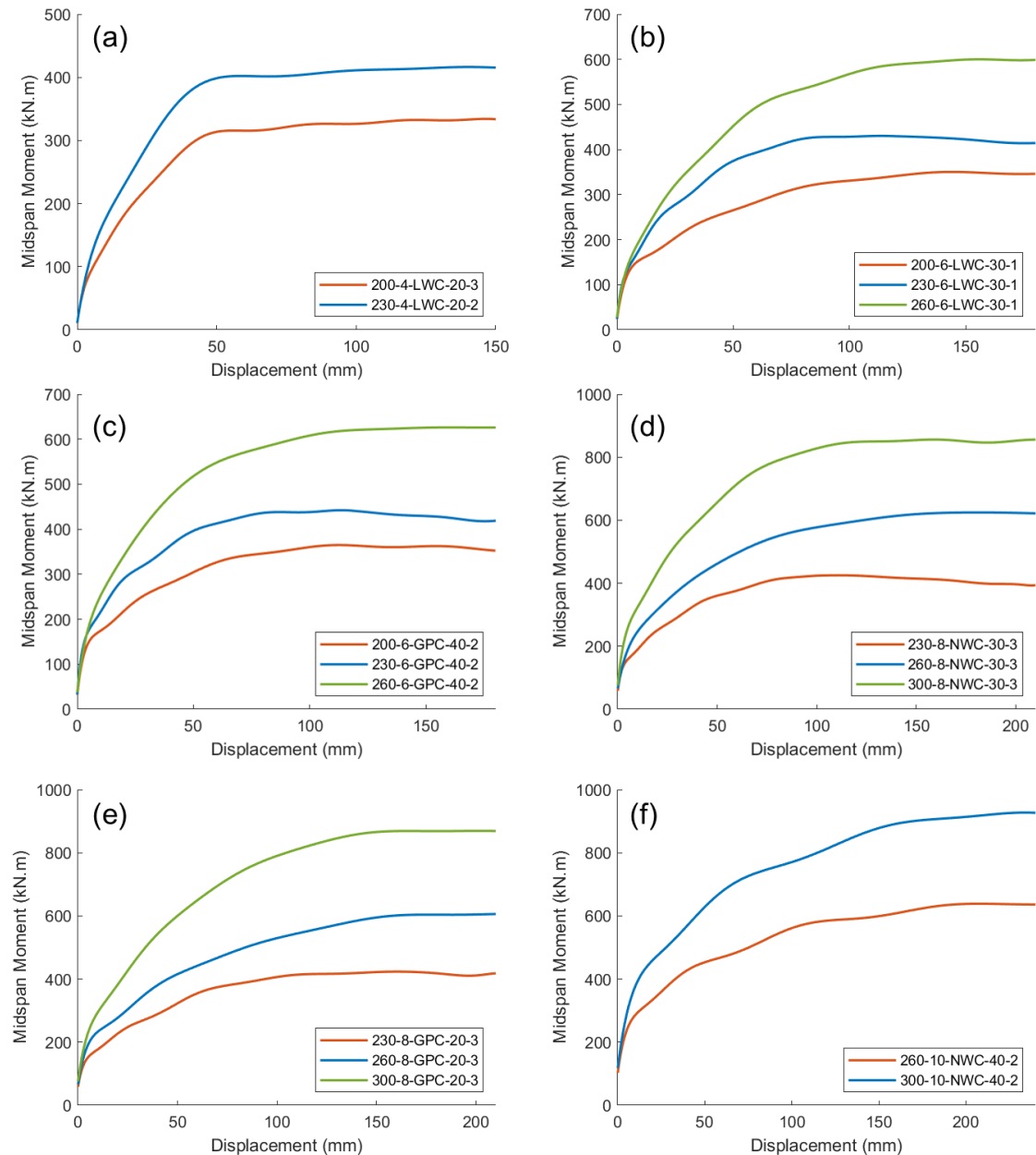


Figure 5-29: Effect of varying PUSS depth on moment vs displacement curves

As expected, increasing the size of PFC steel beams and the depth of the slabs enhances the moment capacity and initial stiffness of the moment versus displacement curves. Deeper sections exhibit higher moment capacities and

initial stiffness, allowing for their effective use in longer spans. Furthermore, utilizing deeper sections for similar spans shifts the yielding point upwards, resulting in yield moment values closer to the maximum moment capacities. Conversely, reducing the section size initiates the yield region at earlier loading stages and elongates the yield region, necessitating extreme deflections to achieve maximum moment capacities, particularly in longer spans.

5.6.3 Effect of Slab Span

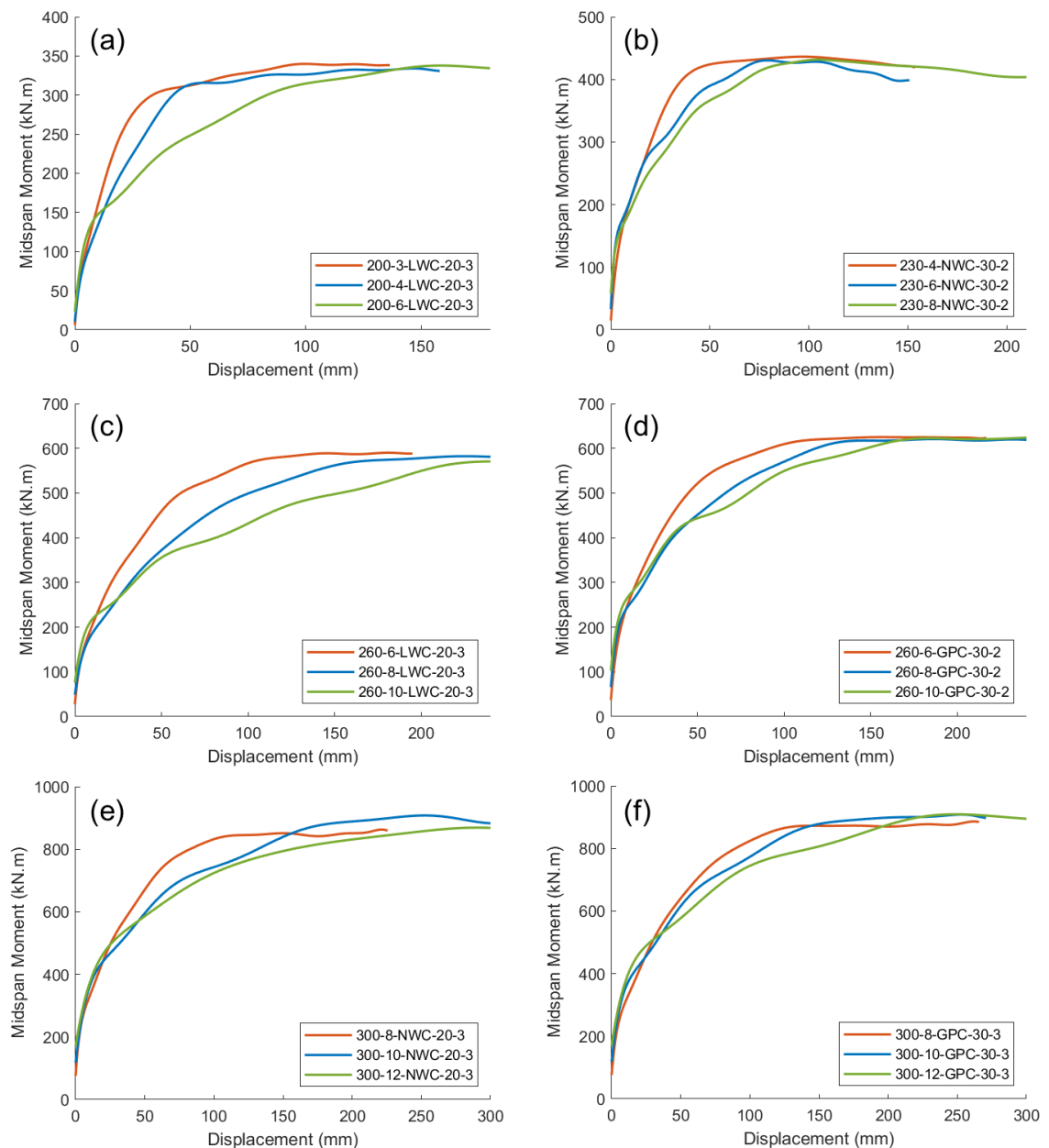


Figure 5-30: Effect of varying PUSS span on moment vs displacement curves

For each of the examined PUSS depths, three distinct spans are evaluated. These spans are selected based on practical design criteria of each depth. Figure 5-30 presents six graphs, each illustrating midspan moment versus displacement

curves of FE models with similar parameters but varying spans. The graphs reveal that while slabs with different spans demonstrate comparable moment capacities, increasing the span reduces the yield moment and prolongs the yielding region. This requires significant deflections to reach peak moments, thereby limiting the permissible design loads for longer spans.

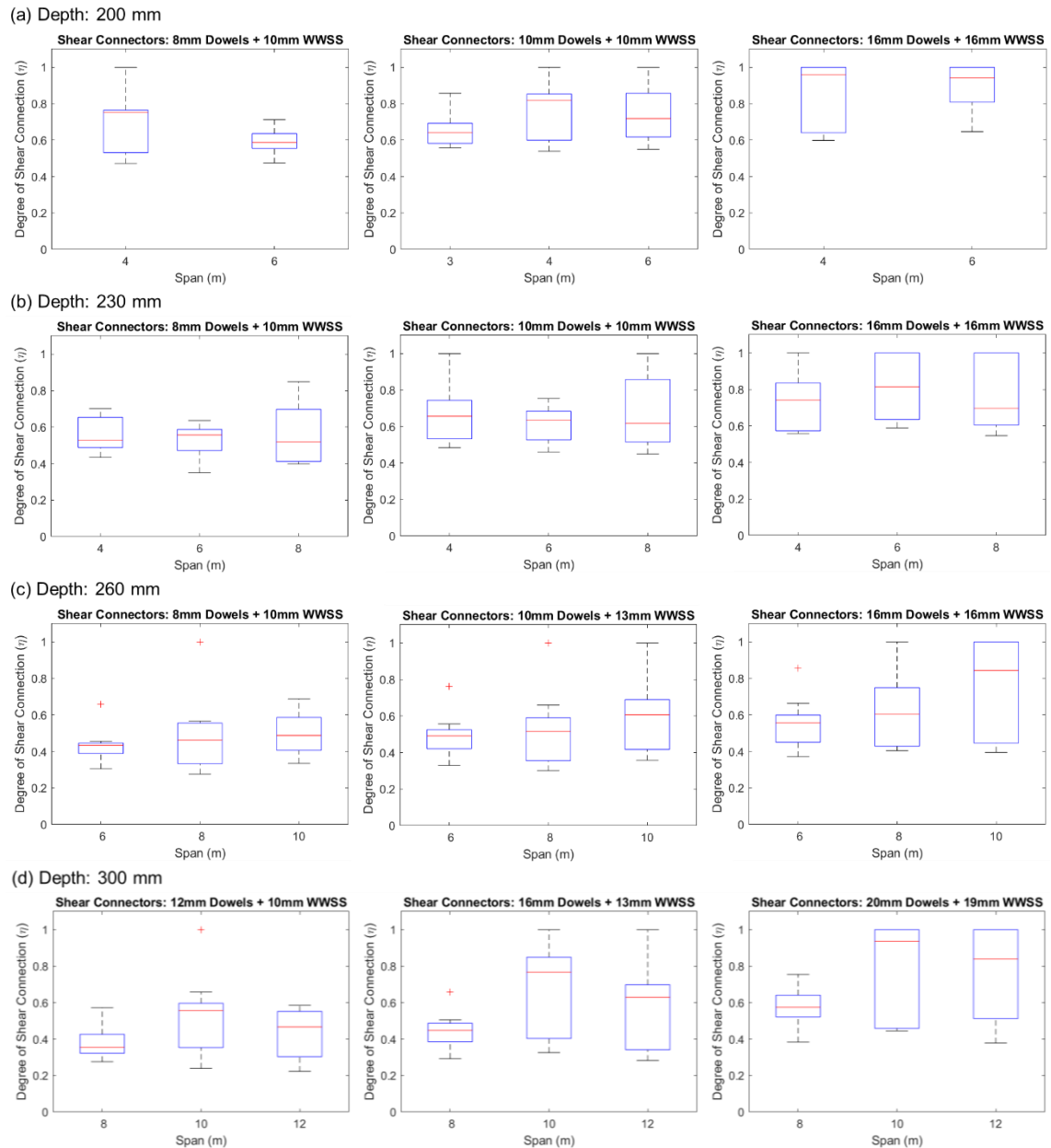


Figure 5-31: Effect of varying PUSS span on the degree of shear connection

In exploring the effect of the previous parameters, it is important to note that their individual impacts may not be as significant as the collective interactions with other variables. Therefore, to explore their combined influence alongside with the size of the implemented shear connectors, Figure 5-31 provides an overall look of all the FE models, and highlights how these parameters affect the degree of shear connection while maintaining consistent sizes of shear connectors. The

figures demonstrate that, on average, varying the spans of the slabs while keeping the depths and shear connectors sizes constant results in nearly similar degrees of shear connection. However, some models show an increase in the degree of shear connection with increasing span, as depicted in Figure 5-31 (c) and (d) for 16 mm dowels + 16 mm WWSS and 20 mm dowels + 19 mm WWSS, respectively. On the other hand, inspection of the figure reveals that the degree of shear connection decreases when similar shear connectors are implemented in deeper slabs, due to the increasing moment capacities.

5.6.4 Effect of Concrete Type and Strength

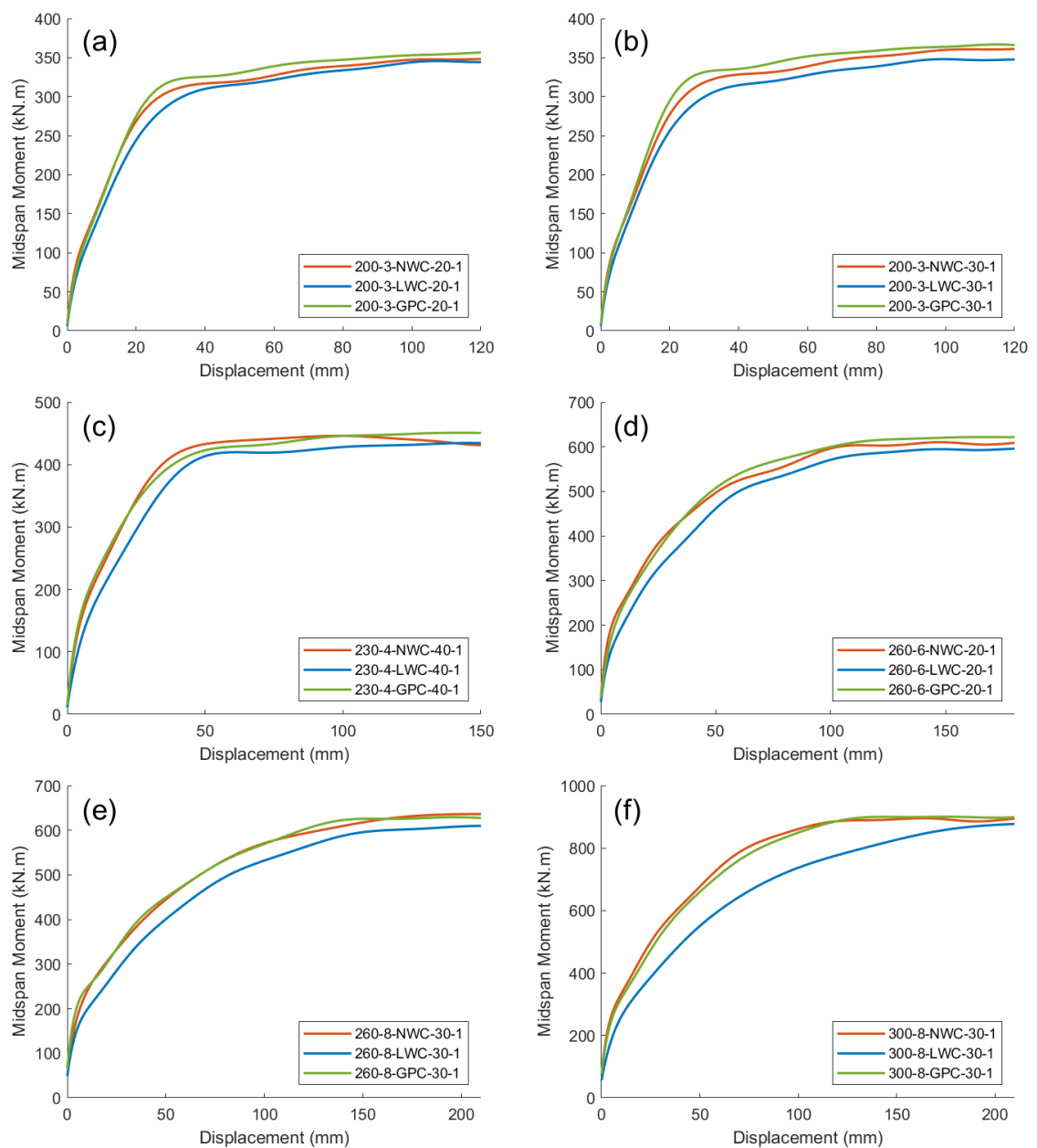


Figure 5-32: Effect of varying PUSS concrete type on moment vs displacement curves

Figure 5-32 illustrates the impact of different concrete types, maintaining consistent strengths, on the midspan moment vs. displacement curves. The curves reveal that while the various concrete types achieve nearly identical peak moments, the initial stiffness of models with LWC is noticeably lower than that of the other two types due to its lower modulus of elasticity. This results in larger deflections under similar loads. In contrast, both NWC and GPC demonstrate almost identical performance. Furthermore, Figure 5-33 examines the effect of varying concrete strengths while keeping the concrete type constant. It is observed that using higher strength concrete marginally increases the moment capacities and slightly enhances the initial stiffness.

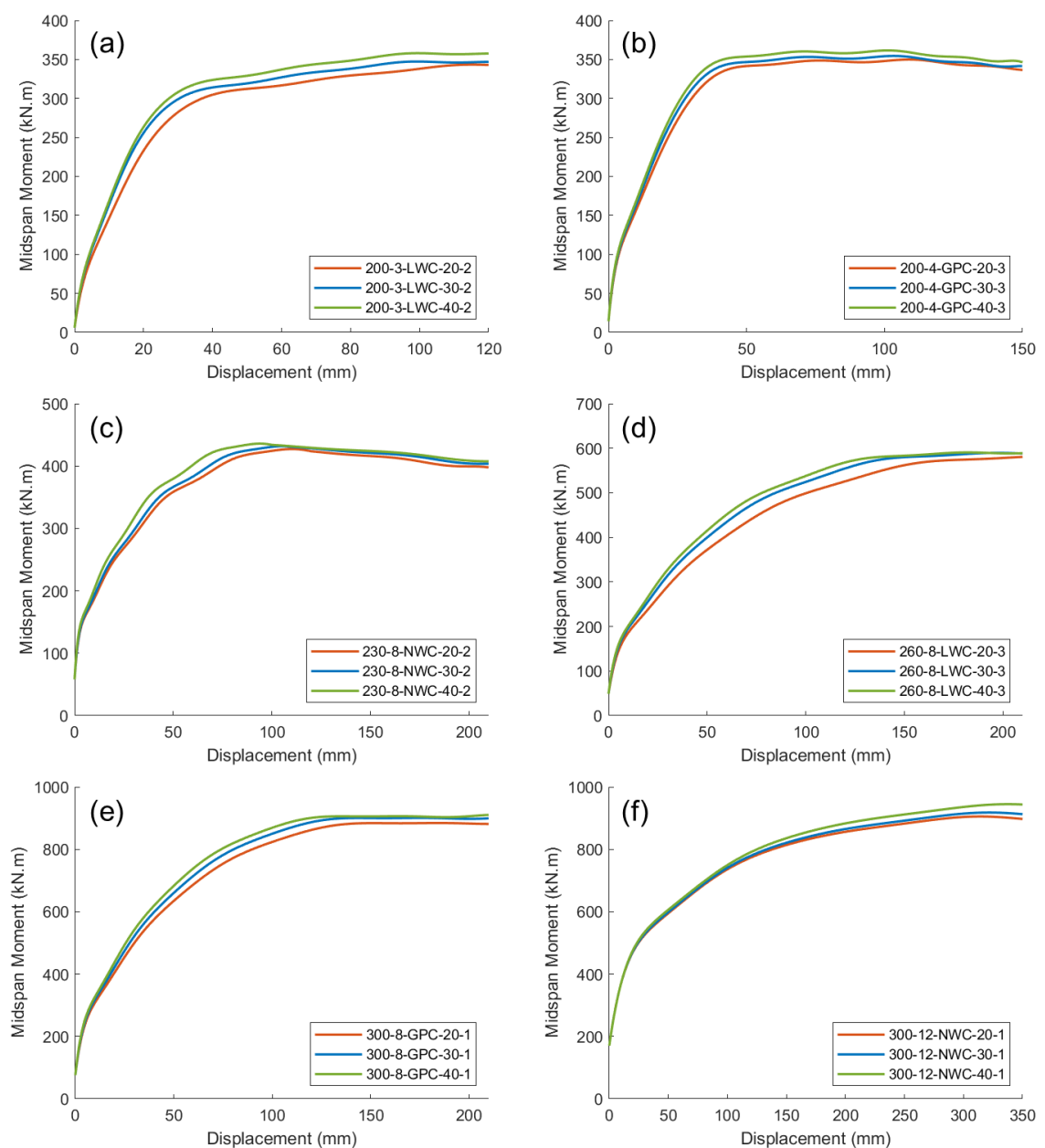


Figure 5-33: Effect of varying PUSS concrete strength on moment vs displacement curves

5.6.5 Effect of Degree of Shear connection

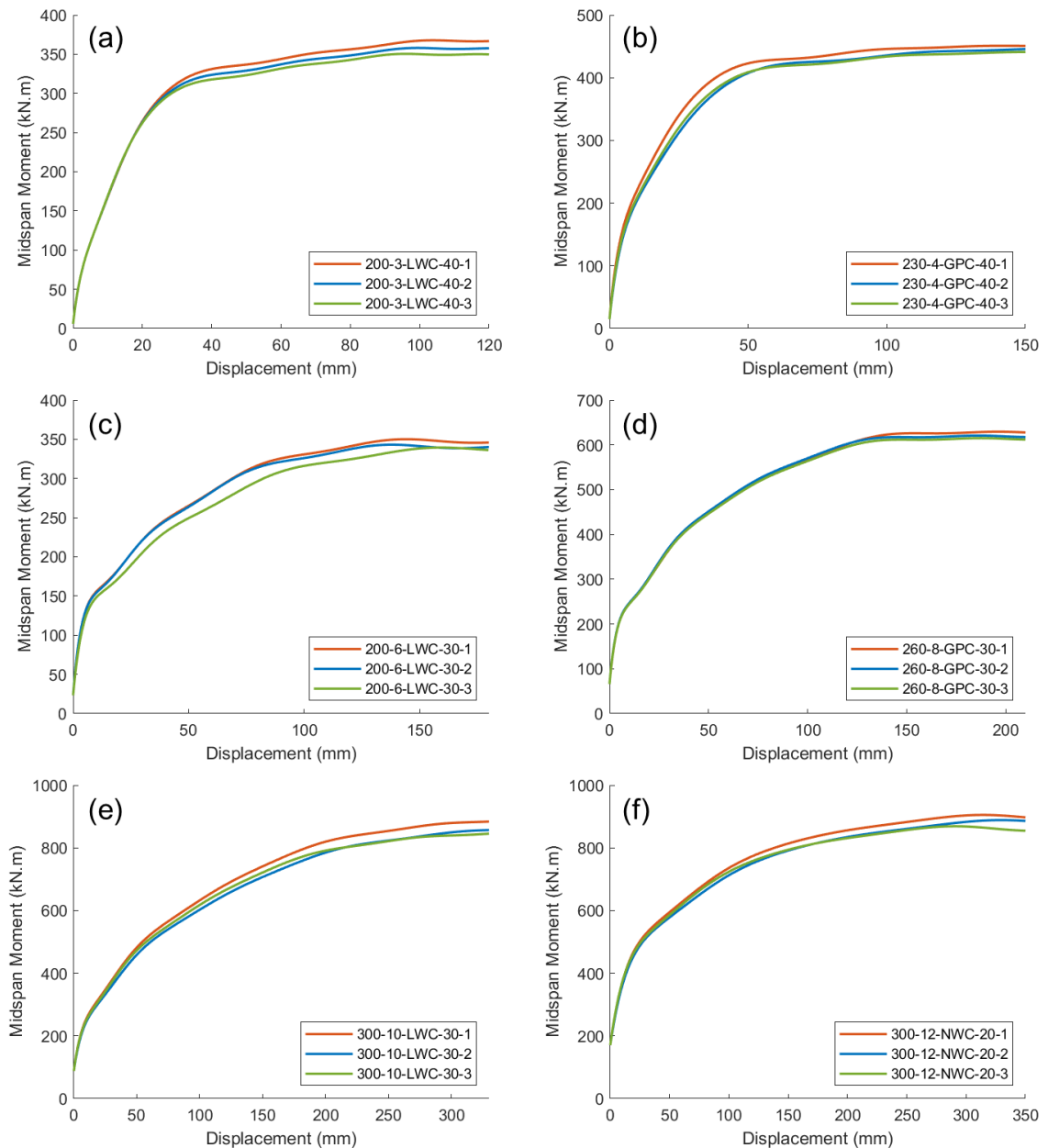


Figure 5-34: Effect of varying PUSS degree of shear connection on moment vs displacement curves

The degree of shear connection is directly influenced by the type and configuration of the shear connectors used in PUSS units. Accurate evaluation relies on precise equations for calculating the shear resistance of each connector. Knowing the degree of shear connection enables the estimation of the moment capacity of the PUSS section through the stress block method. In analysing the FE outcomes to assess the degree of shear connection, the process is conducted in reverse: the moment capacity is first determined, and then the stress block method is applied to evaluate the degree of shear connection.

Figure 5-34 demonstrates that decreasing the degree of shear connection results in lower maximum moment capacities. However, the reduction in maximum moment (as a percentage) is not directly proportional to the decrease in the degree of shear connection. For instance, a 40% reduction in the degree of shear connection only leads to about a 4% decrease in maximum moment capacity. This discrepancy can be attributed to two main factors. Firstly, even without any shear connection (0 degree of shear connection), PUSS retains most of its moment capacity, primarily derived from the steel sections. Secondly, the parabolic shape of the moment vs. degree of shear connection curve, associated with the stress block method (Figure 5-35), indicates that as the degree of shear connection increases, the corresponding increase in moment capacity becomes progressively less significant.

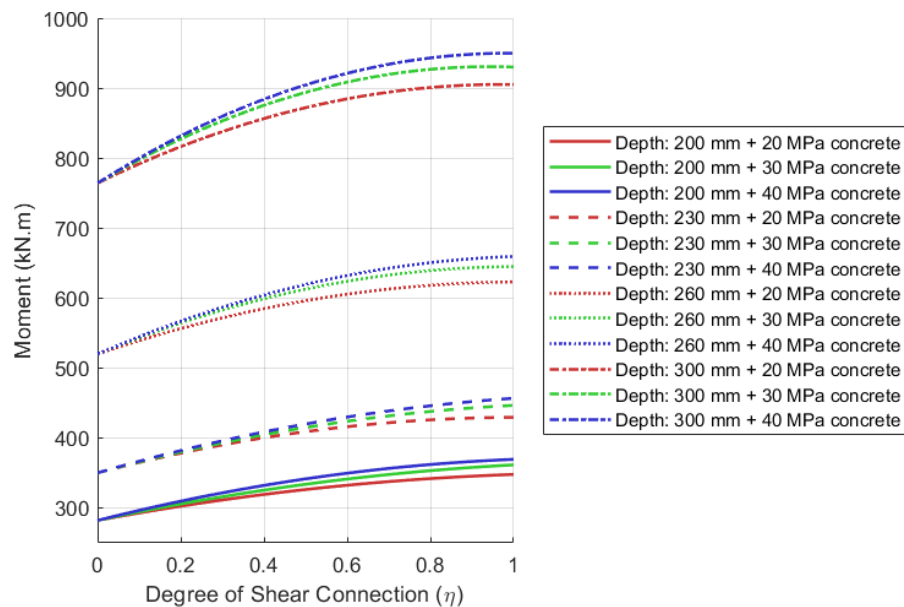


Figure 5-35: Stress block method curves

The small contribution of concrete to the overall moment capacity of PUSS slab is primarily due to the slab's geometric configuration, with the concrete slab situated within the depth of the steel sections. Figure 5-36 demonstrates that the depth of concrete in compression increases linearly with the degree of shear connection. Additionally, it shows that higher strength concrete results in a reduced depth of concrete in compression, which explains the limited increase in moment capacity with increased concrete strength. Conversely, Figure 5-37 reveals that increasing the degree of shear connection lowers the depth of the plastic neutral axis (PNA) of the PUSS units, eventually aligning with the depth of concrete in compression at full shear connection. Furthermore, the figure indicates that higher concrete strength also reduces the depth of the PNA.

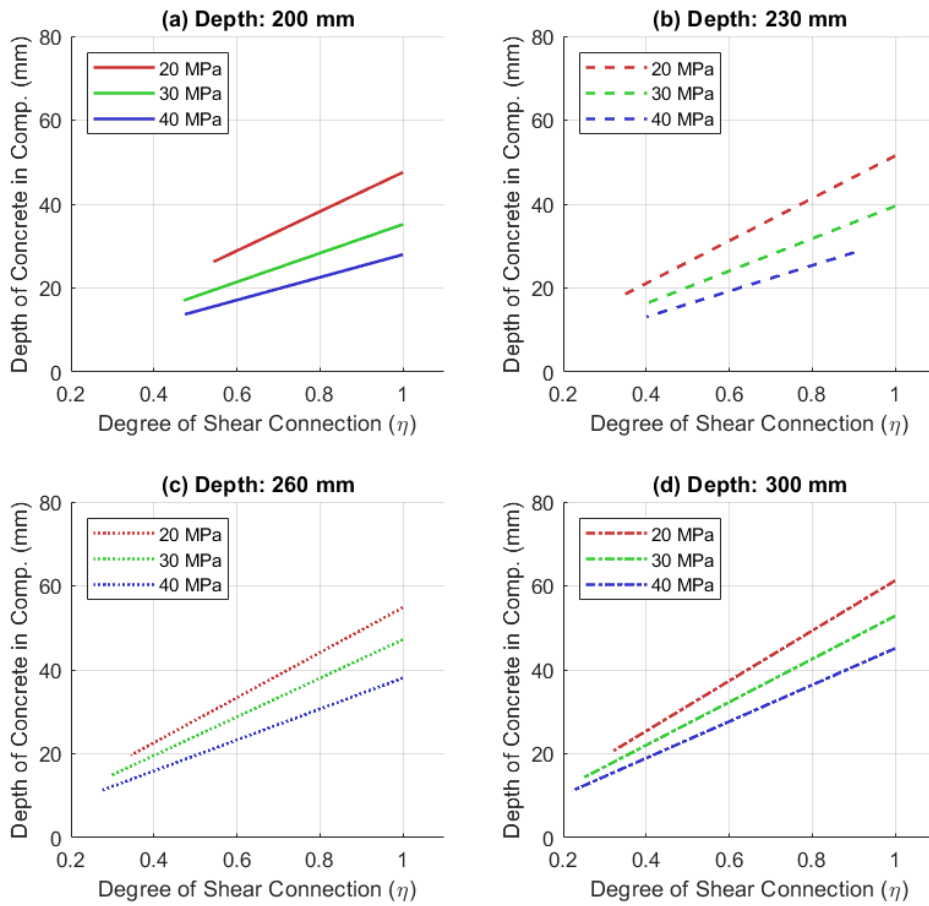


Figure 5-36: Effect of degree of shear connection on depth of concrete in compression

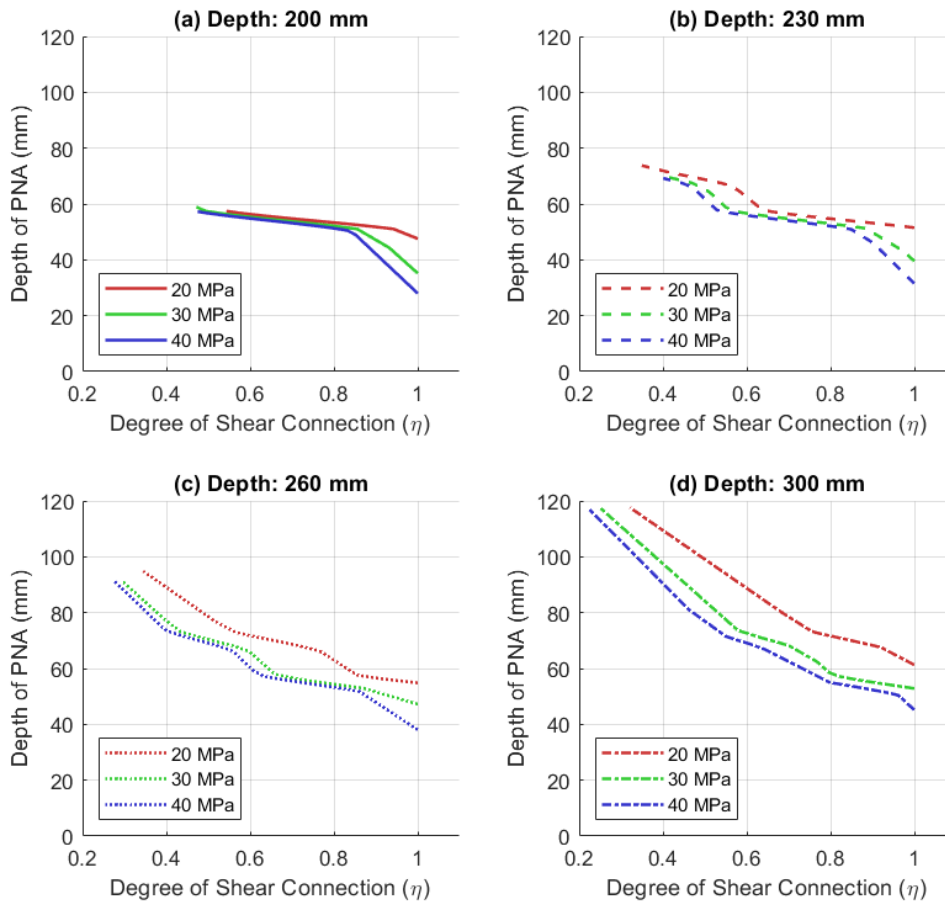


Figure 5-37: Effect of degree of shear connection on depth of PNA

5.6.6 Comparison of FEA Outcomes and Calculations

The comparison between the FEA outcomes and hand calculations is presented in the below figures in terms of moment capacities and degrees of shear connection for each model.

Figure 5-38 illustrates the ratio of maximum moments derived from FEA models to those derived from hand calculations across different depths and spans of PUSS units. The overall match between FEA and the hand calculations is excellent, with an average ratio of 0.983 and a maximum difference of less than 9%.

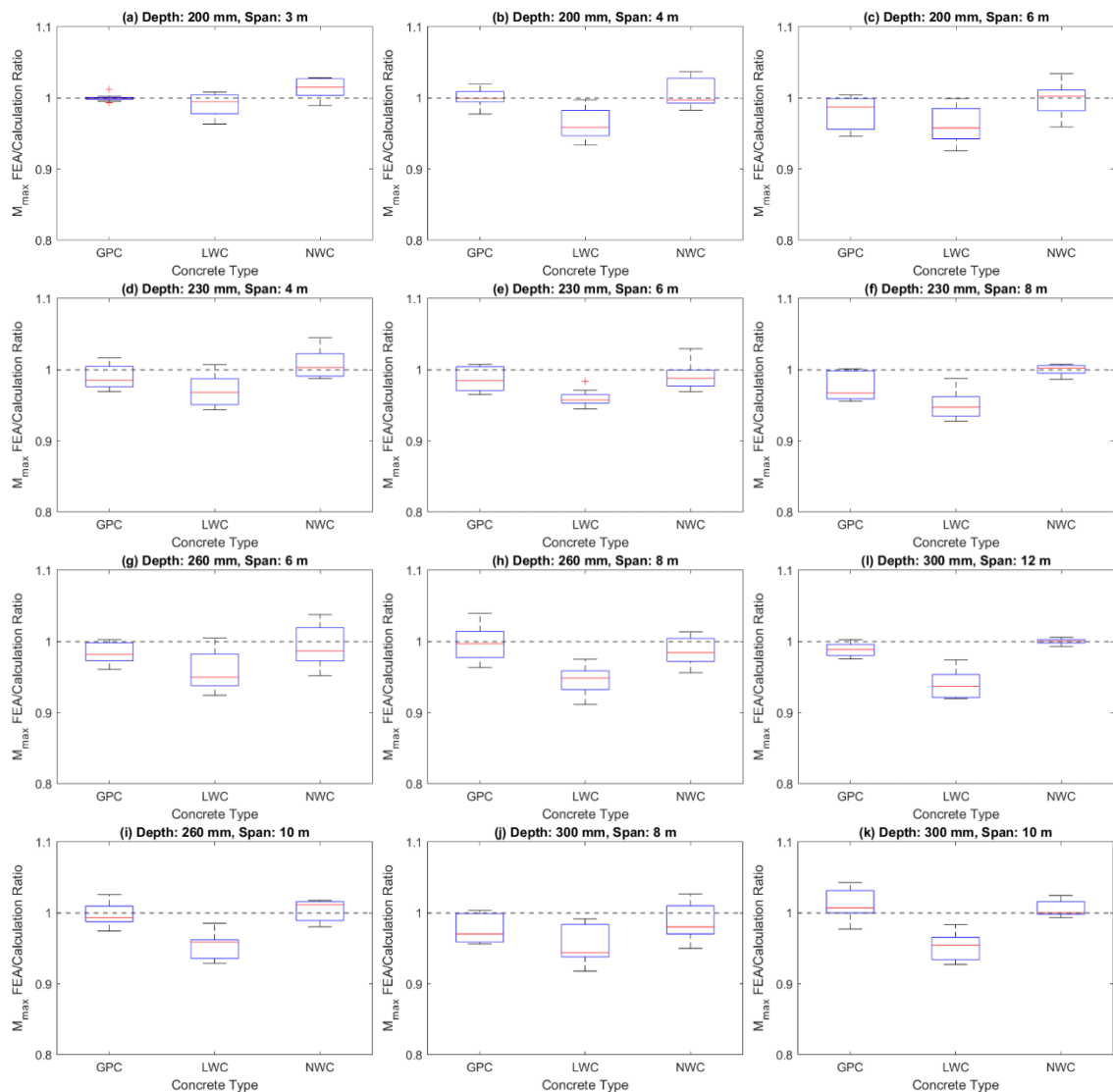


Figure 5-38: Maximum moment FEA/calculation ratio for all FE models

For slabs with depth of 200 mm (Figure 5-38 (a), (b), & (c)) the ratios are close to 1 for all concrete types (GPC, LWC, NWC) and spans. However, slight variations are observed in the models with LWC concrete, particularly at longer spans. Similar trends are observed for models with depth of 230 mm (Figure 5-38 (d),

(e), & (f)). In the deeper 260 mm and 300 mm slabs (Figure 5-38 (g) to (l)), the FEA results align well with the hand calculations, though LWC continues to display more noticeable differences, especially for spans of 10 m and 12 m. From that, it can be concluded that the observed discrepancies are mainly associated with models including LWC, especially at greater depths and spans, suggesting that LWC's mechanical properties contribute to the reduction in the degree of shear connection and, consequently, the moment capacity.

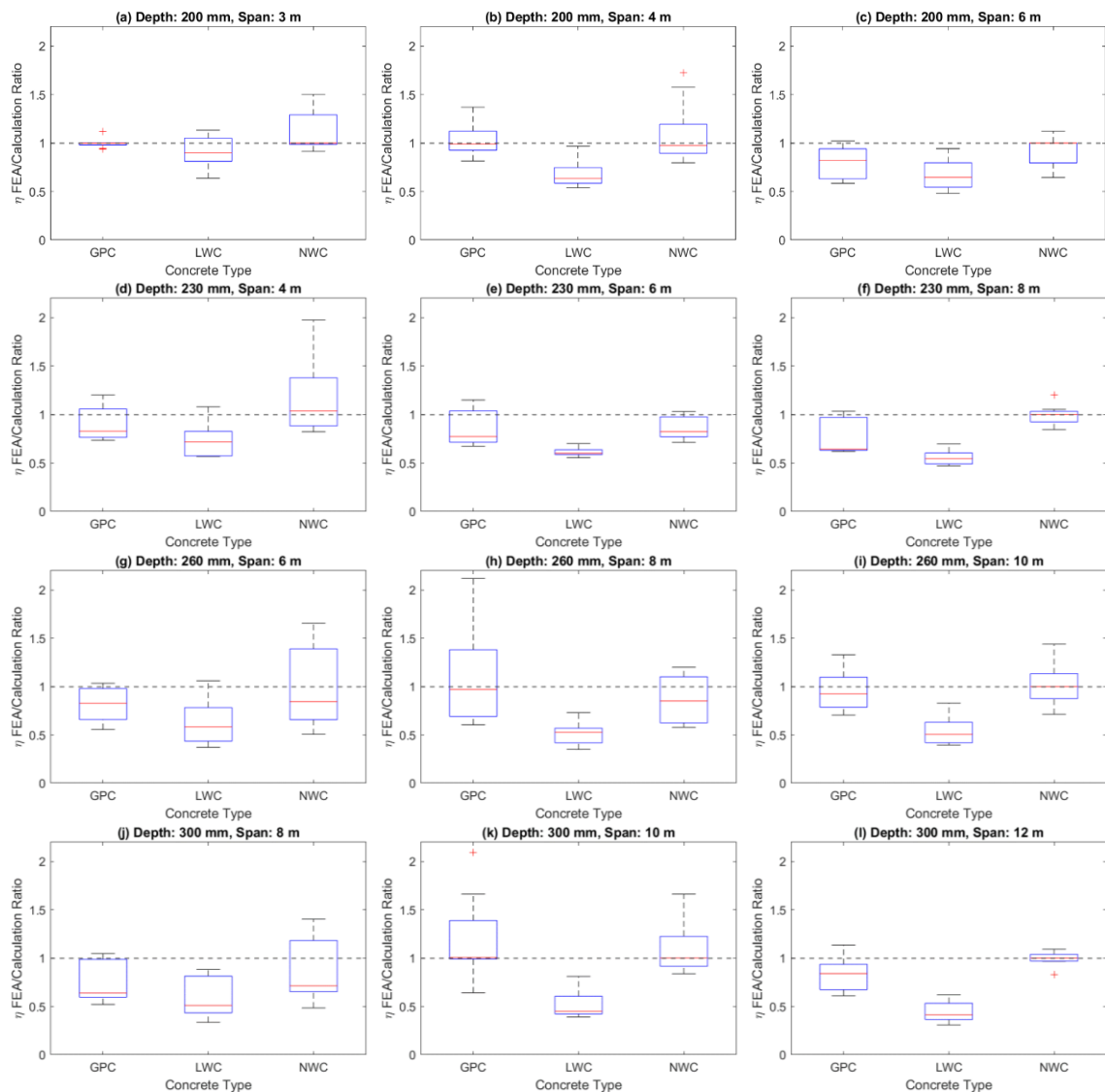


Figure 5-39: Degree of shear connection FEA/calculation ratio for all FE models

Figure 5-39 highlights the ratios of the degree of shear connection derived from FEA models to those calculated by hand. The ratios show much higher variability compared to moment capacities, with an average ratio of 0.843 and a maximum difference of about 70%. Similar to the moment capacities, the highest differences are consistently observed in models with LWC, especially at greater depths and spans. The larger discrepancies in the degree of shear connection ratios can be

attributed to the sensitivity of this parameter. Small differences in moment capacity calculations can lead to significant variations in the degree of shear connection.

Based on the comparison and analysis of the previous figures, it is evident that the FEA and hand calculations for the degree of shear connection shows some discrepancies. These discrepancies highlight the need for a refinement in the equation used to estimate the shear resistance of shear connectors (Equation 2-4). Adjusting this equation will improve the accuracy of hand calculations for the degree of shear connection, ensuring better alignment with FEA results, particularly for LWC and models with higher depths and spans.

5.7 Summary

This chapter presents a comprehensive FEA parametric study that comprises 324 models. The parametric results are analysed to gain a better understanding of the performance of the prefabricated ultra-shallow composite slabs (PUSS) in bending. The analysis focused on the effects of various parameters including slab depth, span, concrete type and strength, and the degree of shear connection on the flexural behaviour of the slabs.

The FEA models are meticulously set up with consistent loading conditions, ensuring reliability in the comparative analysis of different parameter configurations. The key findings from the parametric studies can be summarised as follows:

1. Increasing the slab depth significantly enhances the moment capacity and initial stiffness of the slabs. Deeper slabs, incorporating larger PFC steel sections, exhibits higher moment capacities and stiffness, making them suitable for longer spans. Conversely, shallower slabs reaches their yield points at lower loads, extending the yield region and requiring extreme deflections to achieve maximum moment capacities.
2. While the moment capacities remains relatively constant across different spans for slabs of similar depths, increasing the span results in a lower yield moment and an elongated yield region, reducing the allowable design loads for longer spans.
3. The combined effects of slab depth and span with shear connector size indicates that similar degrees of shear connection could be maintained

across different spans for slabs of similar depths and sizes of shear connectors. However, for greater depths, the degree of shear connection tends to decrease, emphasising the need to optimise shear connector design for different slab configurations.

4. The type of concrete used NWC, LWC and GPC shows distinct impacts on the slabs' performance. LWC, with its lower modulus of elasticity, results in lower initial stiffness compared to NWC and GPC. Increasing the concrete strengths slightly increases the moment capacities and initial stiffness of the slabs.
5. The degree of shear connection influences the moment capacity of PUSS units. The FEA results demonstrates that reducing the degree of shear connection leads to a reduction in moment capacity. However, the reduction in moment capacity is not directly proportional to the reduction in the degree of shear connection, highlighting the complex interaction between shear connectors and overall slab performance.
6. The comparison between FEA results and hand calculations reveals a good match in terms of moment capacities, with an average ratio of 0.983. The discrepancies are more pronounced in models with LWC, especially for greater depths and spans. For the degree of shear connection, the FEA results shows higher variability, with an average ratio of 0.843 and differences up to 70%. This underscores the need for more accurate equations to estimate the shear resistance of connectors.

In conclusion, the parametric study provides valuable insights into the flexural behaviour of PUSS slabs under varying parameters. The results emphasise the importance of considering the interaction between different parameters to optimise slab design. The next chapter, "Analytical Study," focuses on refining the equations used to estimate shear resistance of shear connectors to improve the accuracy of predicting the degree of shear connection, especially for slabs incorporating LWC.

5.8 FEA Parametric Study Limitations

While the presented FEA parametric study provides valuable insights into the behaviour of PUSS with variable parameters under flexural loading, it is important to acknowledge the limitations that define the scope and the constraints of the findings.

The validation of the developed FE models is based on four full-scale experimental tests, which covered different parameters, but the relatively limited number of tests imposes limitations on the applicability of the model to of the studied parameters. A broader experimental database, especially including more tests with longer spans, would strengthen the confidence in the FEA results and improve the predictions of the models.

Moreover, the material properties used for steel components, NWC and LWC are based on actual tests conducted on experimental tests samples, ensuring consistency with the physical experiments. However, the GPC material models are developed based solely on values reported in the literature. While this approach is justified by previous studies, it might introduce some uncertainty in the mechanical behaviour of GPC.

A key limitation of the parametric study is the presence of fluctuations or “trembling” in some of the resulted curves, particularly in models with longer spans and deeper cross-sections. This behaviour is inconsistent with the validation models, which display smoother responses. This inconsistency is attributed to several contributing factors. Firstly, the longer parametric models are more complex than the validation models, leading to higher element counts and increased numerical sensitivity. Secondly, the applied displacements in longer-span models are much larger, which amplifies localised numerical disturbances. In addition, although the models were executed using High-Performance Computing (HPC) resources (ARC3 and ARC4) at the University of Leeds, each simulation is constrained to a maximum runtime of 48 hours. To ensure all models completed within this window, step times were limited (not exceeding 500 seconds for the largest models) to ensure completing the analysis within the maximum running time. This may have affected solution stability and response smoothness. It is believed that extending the step time would reduce such fluctuations, but this is not feasible under the available computational resources.

Lastly, although the dynamic/explicit method is highly effective in solving complex nonlinear problems and avoiding convergence issues, it is sensitive to time increment control. Mass scaling and smoothed displacement amplitude were applied to minimise inertial effects and ensure quasi-static behaviour. However, the computational efficiency required for large-scale modelling occasionally necessitated trade-offs between resolution and runtime.

Chapter 6

Analytical Study of Shear Connectors Capacity

6.1 Introduction

The analysis of the experimental and FEA results provides a comprehensive understanding of the flexural behaviour of PUSS floorings and a large set of data for PUSS floorings with various parameter combinations. In this chapter, the data is further examined to derive a formula, using regression analysis, which reasonably predicts the shear resistance capacity of each shear connector used in PUSS flooring system. This allows the calculation of the degree of shear connection provided by the implemented shear connection system. In addition, this chapter discusses how this calculation method can be applied in evaluating and designing the bending capacity of PUSS units.

6.2 Shear Capacity of Shear Connectors Formulas

Although the existing formulas in codes of practice and literature for evaluating the shear capacities of shear connectors in flooring systems are not directly applicable to the shear connection system implemented in PUSS, assessing their suitability against the data obtained from the experimental and FEA results helps in deriving a new reliable formula.

6.2.1 Existing Formulas for Shear Capacity of Headed Shear Studs

As previously discussed in the literature review chapter (Chapter 2), several formulas provided by codes of practice and structural institutes exist to evaluate the shear resistance capacity of shear connectors, particularly for headed shear stud connectors embedded in normal concrete. To develop a new formula suited for the horizontally oriented shear connection system in PUSS, the shear capacities of shear connectors derived from the experimental and FEA data are first compared with those calculated from equations in existing design codes. The design codes used for comparison include Annex C of Eurocode 4 (Equation 2-10) (CEN, 2005), which evaluates the shear strength of horizontally oriented shear stud connectors responsible for splitting of concrete in the direction of slab thickness, as well as ANSI/AISC 360–10 (2010) (Equation 2-8) and AASHTO (2020) (Equation 2-9) which calculate the shear capacity of headed shear studs embedded in concrete.

Equation 2-8

$$P_s = 0.5A_s\sqrt{f_{ck}E_c} \leq 0.75f_uA_s$$

Equation 2-9

$$P_s = \emptyset 0.5A_s\sqrt{f_{ck}E_c} \leq 0.75f_uA_s$$

Where: P_s is the shear resistance of headed shear stud connectors,
 A_s is the cross-sectional area of the shear stud,
 E_c is the modulus of elasticity of concrete,
and \emptyset is the resistance factor for the shear connectors = 0.85.

Equation 2-10

$$P_{Rd,L} = 1.4k_v(f_{ck}da'_r)^{0.4} \left(\frac{a}{s}\right)^{0.3} / \gamma_v \leq 0.8f_u\pi d^2 / \gamma_v$$

Where: $P_{Rd,L}$ is the shear resistance of horizontally lying shear stud connectors,
 $k_v = 1$ for shear connection in an edge position and 1.14 for a middle position,
 f_{ck} is the characteristic concrete cylinder compressive strength,
 d is the diameter of the shank of the stud with $19 \leq d \leq 25$ mm,
 a'_r is the effective edge distance to the centre of the shear stud = $a_r - c_v - \emptyset_s/2 \geq 50$ mm,
 a is the horizontal spacing of studs with $110 \leq a \leq 440$ mm,
 s is the spacing of stirrups with both $a/2 \leq s \leq a$ and $s/a'_r \leq 3$,
 γ_v is a partial factor and its recommended value is 1.25,
 f_u is the ultimate strength of shear stud steel but not greater than 500 N/mm²,
 a_r is the vertical distance from the edge of the slab to the centre of the stud,
 c_v is the vertical concrete cover,
and \emptyset_s is the diameter of the stirrups with $\emptyset_s \geq 8$ mm.

The aforementioned equations were originally developed for headed shear stud connectors embedded in NWC, but each has some advantages over the others relative to the shear connection system in PUSS. The formula in Annex C of Eurocode 4 was designed for horizontally oriented shear studs, matching the orientation of shear connectors in PUSS. The latter two formulas are more

general in form but incorporate the modulus of elasticity of concrete, making them more suitable for systems involving different types of concrete, such as LWC.

6.2.2 Existing Formula for Shear Capacity of WWSS and Steel Dowels in PUSS

The previous experimental and FEA investigations on the performance of WWSS and steel dowel shear connectors in PUSS by Ahmed and Tsavdaridis (2020), under direct static push-out tests, suggested a formula to predict the shear strength (P_{sd}) of these shear connectors (Equation 2-4).

Equation 2-4

$$P_{sd} = 1.873(f_{ck}da_r)^{0.835} \leq 0.8f_uA_s$$

Where: P_{sd} is the shear resistance of headed shear stud or steel dowel,
 d is the diameter of the shear stud or steel dowel,
and a_r is the distance from first stud or dowel to the top of concrete.

Although the proposed formula is intended to be applicable for PUSS with both NWC and LWC, it demonstrates that the shear capacity of the shear connectors in PUSS is influenced by f_{ck} , d and a_r without accounting for parameters that consider the effects of different types of concrete. As previously discussed in section 5.6.6, the comparison between the degrees of shear connection derived from FEA models with those calculated using Equation 2-4 revealed greater discrepancies in models with LWC, especially at increased depths and spans. This highlights the need for a refinement of the equation based on the flexural performance of PUSS units, with the inclusion of parameters related to the concrete type.

6.2.3 Proposed Formula for Shear Capacity of Shear Connectors in PUSS

Nonlinear regression analysis was carried out on the experimental and FEA flexural tests results, considering the effects of all the explored parameters to develop a reliable formula for evaluating the shear strength ($P_{Rd,h}$) of the horizontally oriented shear connectors in PUSS. The formulation process began by analysing the structure of the existing design formulas presented earlier in sections 6.2.1 & 6.2.2. A generalised equation structure was constructed during this process which incorporated all the relevant parameters found in these

formulas, such as compressive strength of concrete (f_{ck}), elastic modulus of concrete (E_c), shear connector diameter (d) and cross-sectional area (A_s) as well as other key geometrical distances. Each parameter was expressed in a power-law form, multiplied together and scaled by a leading constant, such that the formula took the general form: $P_{Rd,h} = c_1 \cdot f_{ck}^{c_2} \cdot E_c^{c_3} \cdot d^{c_4} \dots$ where c_1, c_2, \dots, c_n are coefficients to be calibrated and optimised, and the parameters correspond to the physical and material properties that govern shear connectors' shear capacity.

Using the combined dataset of 328 results from the experimental and FEA studies, the generalised equation form was applied to predict the total shear capacity and the degree of shear connection provided by the group of shear connectors in each model. All relevant input parameters were substituted into the equation, and the predicted values were compared against the corresponding shear capacities obtained directly from the experimental and numerical results. The goal of the regression process was to calibrate the equation such that its outputs closely match the actual capacities from the dataset.

A nonlinear regression analysis was performed to examine the contribution of each parameter to prediction accuracy. Insignificant parameters (those that did not meaningfully improve the correlation) were removed to produce a reduced and more robust set of predictors, and particular attention was given to including the significant predictors (independent variables with the highest contribution to shear strength). The regression analysis was performed using iterative nonlinear optimisation techniques to calibrate the coefficients, targeting minimal variations between the values predicted from the formula and experimental/FEA values. The final formula was selected based on its ability to produce an average mean value around 1.0 and the lowest possible CV, ensuring a balance between accuracy and simplicity. In this context, the mean ratio reflects the average of formula-predicted shear capacity (or degree of shear connection) divided by the experimentally or numerically derived capacity (or degree), while the CV quantifies the dispersion of these two values. This iterative and data-driven approach resulted in the development of the new proposed formula, presented in Equation 6-1.

Equation 6-1

$$P_{Rd,h} = 13.8(\sqrt{f_{ck}E_c}da'_r)^{0.586} \leq 0.8f_uA_s/\alpha_v$$

Where: $P_{Rd,h}$ is the shear resistance of horizontally oriented shear stud or steel dowel in PUSS,
 f_{ck} is the characteristic concrete cylinder compressive strength,
 E_c is the modulus of elasticity of concrete,
 d is the diameter of the shear connector,
 a'_r is the effective edge distance to the centre of the shear connector = $a_r - c_v - \phi_s/2 \geq 50$ mm (see Figure 6-1),
 f_u is the ultimate strength of shear stud or steel dowel,
 A_s is the cross-sectional area of the shear stud,
 α_v is a partial factor and its recommended value is 1.14,
 a_r is the vertical distance from the edge of the slab to the centre of the stud,
 c_v is the vertical concrete cover,
and ϕ_s is the diameter of the stirrups.

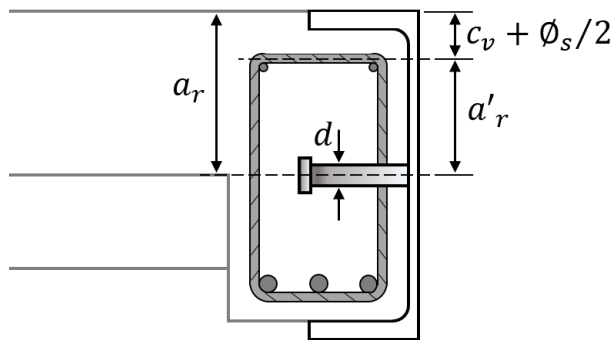


Figure 6-1: Geometrical parameters of Equation 6-1

The degree of shear connection, as well as the total shear resistance provided by the group of shear connectors on one side of the PUSS units, as calculated using the various formulas presented earlier, are compared with the experimental and FEA results, as illustrated in Figure 6-2 to Figure 6-5. Additionally, Table 6-1 and Table 6-2 assess the fit quality of each of these formulas against the data obtained from the experimental and FEA results.

To produce Table 6-1 and Table 6-2, the means and coefficients of variations (CV) of the ratios of both the degree of shear connection and the shear capacity provided by the group of shear connections on one side of PUSS (Experiment/FEA to prediction), are calculated across all the considered 328

experiments and FEA models. The results show that the proposed formula (Equation 6-1) demonstrates the best fit compared to the other calculation methods. Both of its means of ratios are approximately 1, suggesting high accuracy in the predictions. Additionally, it has the lowest level of dispersion around the mean, as indicated by the lowest coefficients of variation which is less than 30%.

In contrast, the other calculation methods appear to have lower accuracy and overestimate the shear capacities of the connectors, as evidenced by their mean of ratios (Experiment/FEA to prediction) being less than 1 (except in case of the formula proposed by Ahmed and Tsavdaridis (2020) for experimental results, where sample size is very small). Moreover, their associated CVs show greater variability. Focusing on the FEA data (since it has more dataset compared to the experimental data), the Eurocode 4 (Annex C) formula provides a reasonable fit, though it still exhibits higher variability compared to the new proposed formula. The AASHTO and ANSI/AISC 360–10 methods show varying levels of accuracy and consistency, with AASHTO displaying slightly higher mean ratios but greater variability, while ANSI/AISC demonstrates lower mean ratios alongside the highest coefficients of variation, indicating more inconsistent predictions overall. Finally, the formula proposed by Ahmed and Tsavdaridis (2020), despite being specifically developed for PUSS, was solely based on push-out tests. The formula showed good fit with the experimental flexural tests results, however, comparison with the FEA results revealed a need for refinement, as the mean ratios for this method are 0.843 for degree of shear connection and 0.750 for shear capacity, with relatively high coefficients of variation at 35.2% and 35.8%. This highlights the importance of the newly proposed formula, which not only provides a more accurate prediction but also reduces variability in the results.

The visual comparison in Figure 6-2 to Figure 6-5 further supports the findings from Table 6-1 and Table 6-2 regarding the accuracy of the various prediction methods. In both figures, the data points representing the new formula (Equation 6-1) are much closer to the blue lines, which shows better agreement between experimental/FEA results and predictions (i.e., a ratio of 1.0). This indicates that the proposed formula consistently provides the best fit, with predictions aligning closely with the experimental and FEA values. In contrast, the points corresponding to the remaining methods are more scattered, particularly in

Figure 6-5, where many points lie to the far right from the line. This suggests that these methods tend to overestimate the shear capacities, especially at higher values. The new formula's proximity to the line across a wide range of data points demonstrates not only its accuracy but also its reliability in predicting both the degree of shear connection and the shear capacity, outperforming the existing methods.

Table 6-1: Evaluation of fitting of various formulas to Experiment results

Prediction Method	Degree of shear connection (Experiment to prediction ratio)		Shear capacity of all shear connectors at one side of PUSS (Experiment to prediction ratio)	
	Mean	CV	Mean	CV
EC4 - Annex C	0.829	24.4%	0.640	16.9%
ANSI/AISC 360-10	0.783	28.4%	0.489	22.1%
AASHTO	0.803	26.2%	0.575	22.1%
Ahmed and Tsavdaridis (2020)	1.116	6.8%	1.171	11.8%
New formula - Equation 6-1	1.013	4.5%	1.040	7.2%

Table 6-2: Evaluation of fitting of various formulas to FEA results

Prediction Method	Degree of shear connection (FEA to prediction ratio)		Shear capacity of all shear connectors at one side of PUSS (FEA to prediction ratio)	
	Mean	CV	Mean	CV
EC4 - Annex C	0.897	32.6%	0.825	35.8%
ANSI/AISC 360-10	0.882	34.4%	0.774	42.7%
AASHTO	0.967	38.0%	0.876	43.9%
Ahmed and Tsavdaridis (2020)	0.843	35.2%	0.750	35.8%
New formula - Equation 6-1	1.002	31.2%	0.970	29.9%

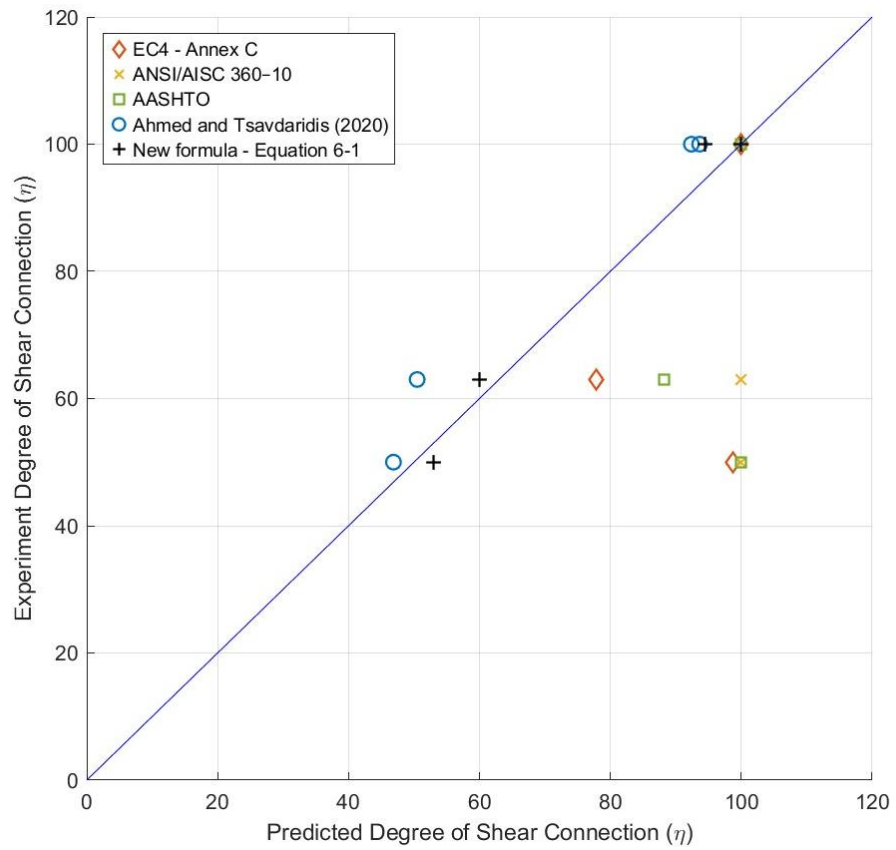


Figure 6-2: Comparison between the degree of shear connection obtained from Experiment results and predictions calculated using various formulas

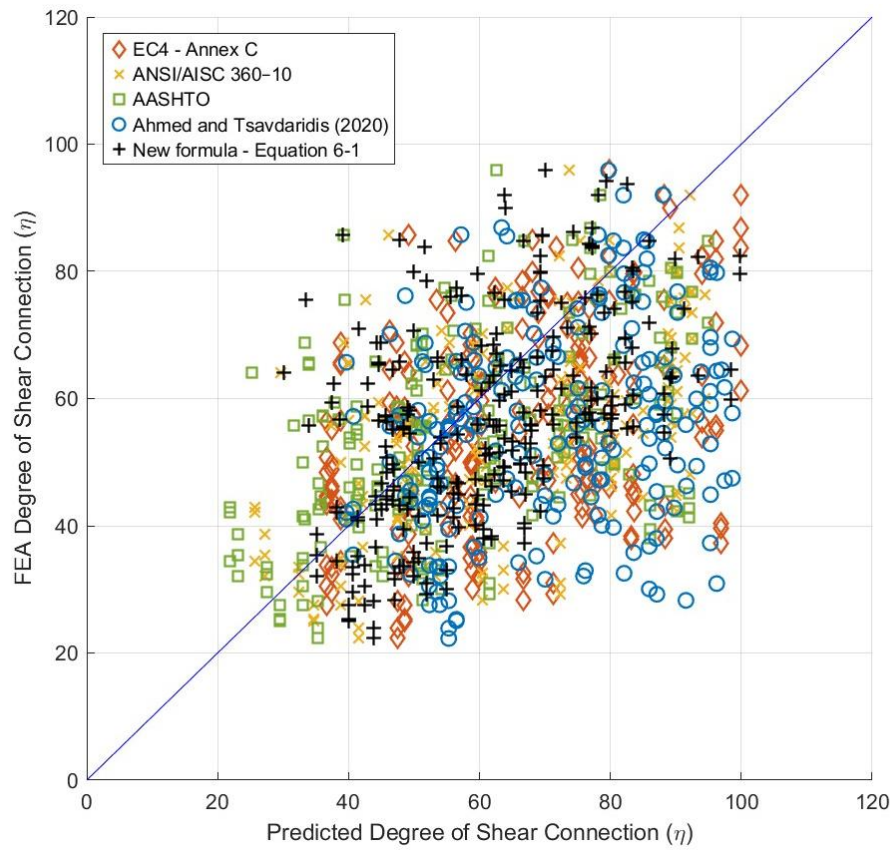


Figure 6-3: Comparison between the degree of shear connection obtained from FEA results and predictions calculated using various formulas

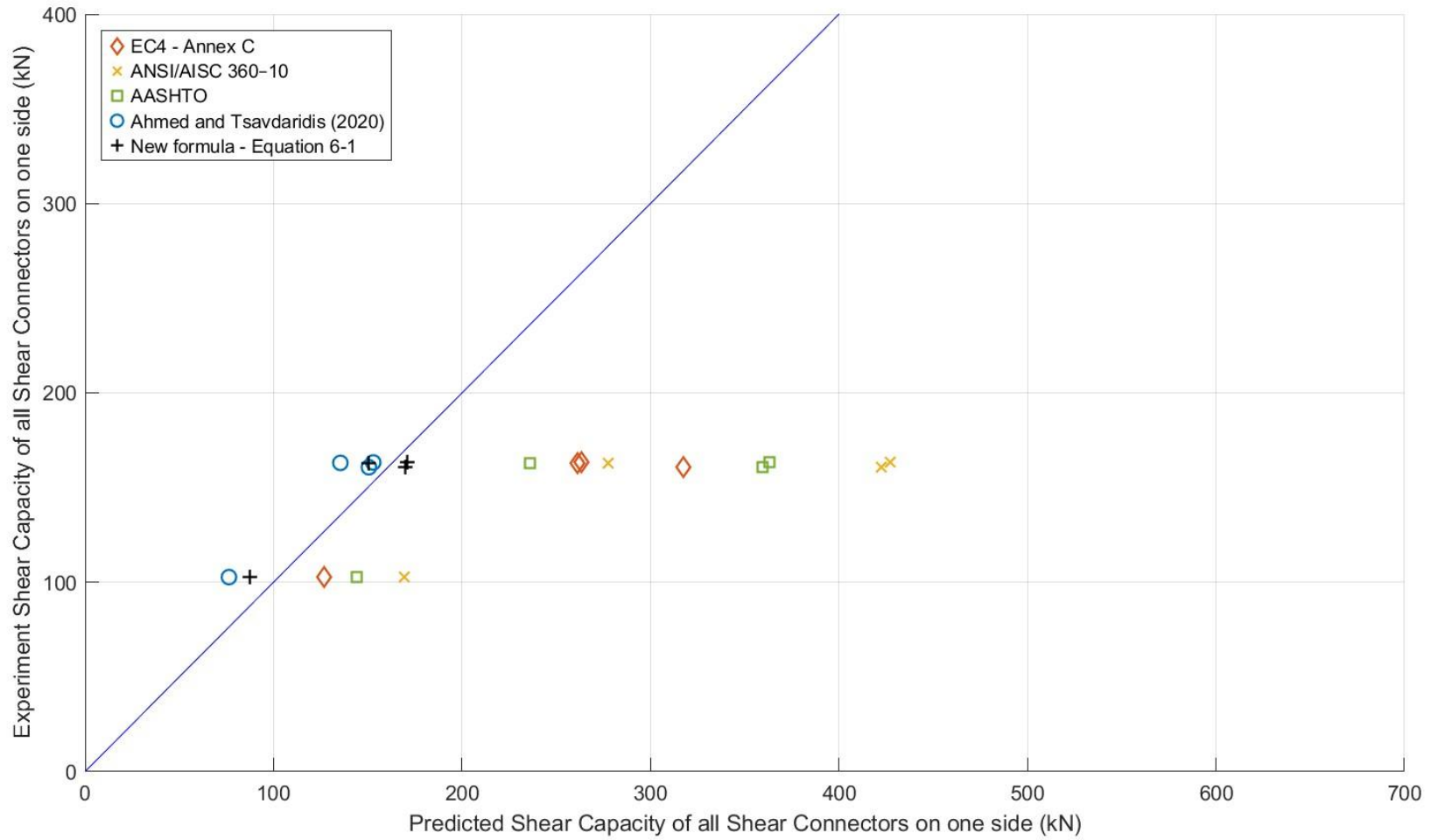


Figure 6-4: Comparison between the shear capacity of all shear connectors on one side of PUSS units obtained from Experiment results and predictions calculated using various formulas

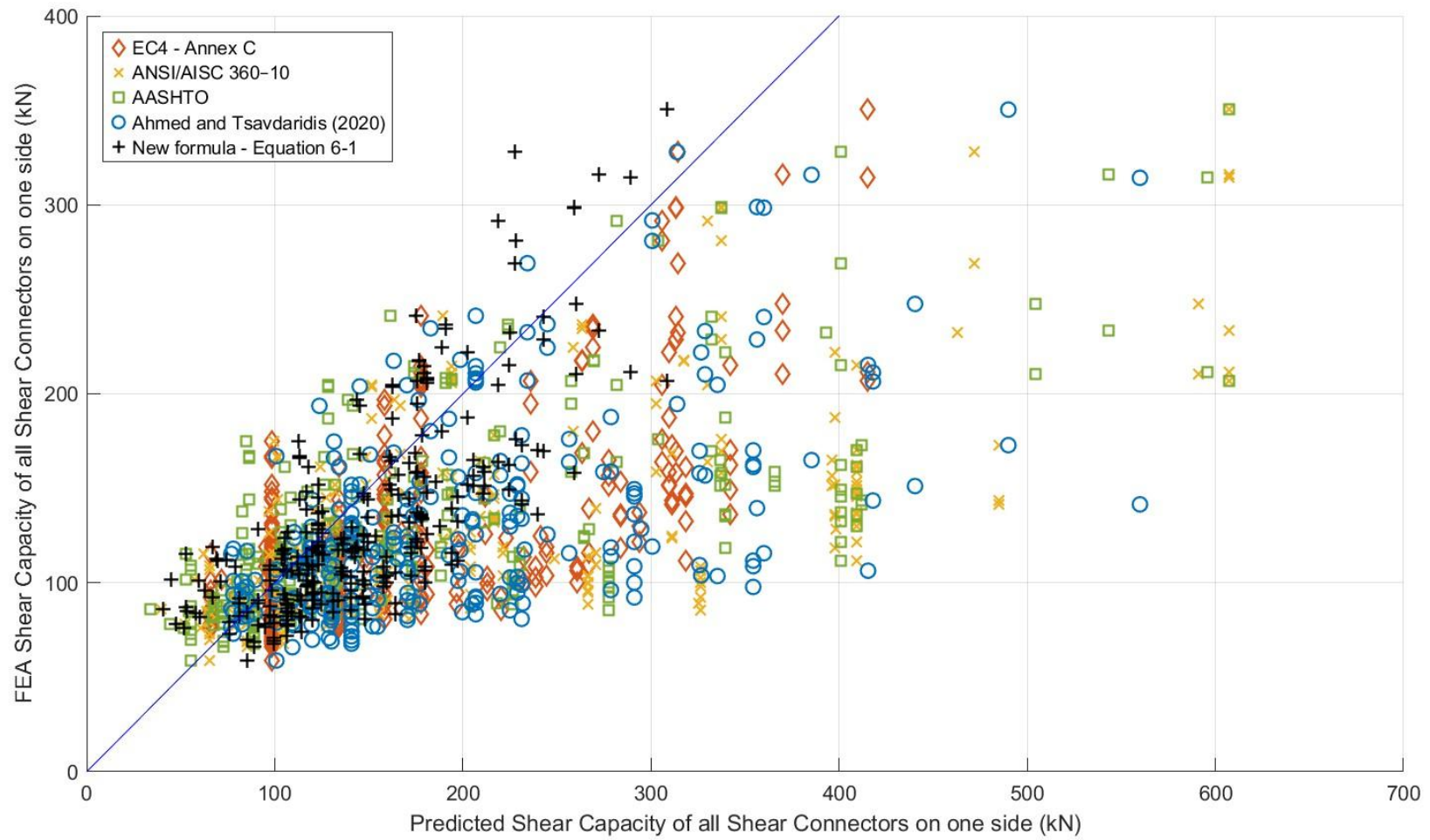


Figure 6-5: Comparison between the shear capacity of all shear connectors on one side of PUSS units obtained from FEA results and predictions calculated using various formulas

6.3 Bending Resistance Design of Prefabricated Ultra-Shallow Slabs

The specifications of Eurocode 4 (CEN, 2004b) specifies two primary methods for designing the moment capacity of composite sections: the linear interaction method (simplified method) and the stress block method (plastic theory or plastic stress distribution method). As illustrated in Figure 6-6, the linear interaction method shows a linear increase in the moment capacity of the composite section as the degree of shear connection increases, while the stress block method exhibits a parabolic relationship. This section presents the design moment methodologies for PUSS units using both methods. The methodologies are demonstrated through an example of a PUSS unit with a depth of 300 mm, having a steel section PFC 300x100x46. The details of the slab's cross-section are shown in Figure 6-7 (due to symmetry, only one half of the slab's width, 1 m, is presented).

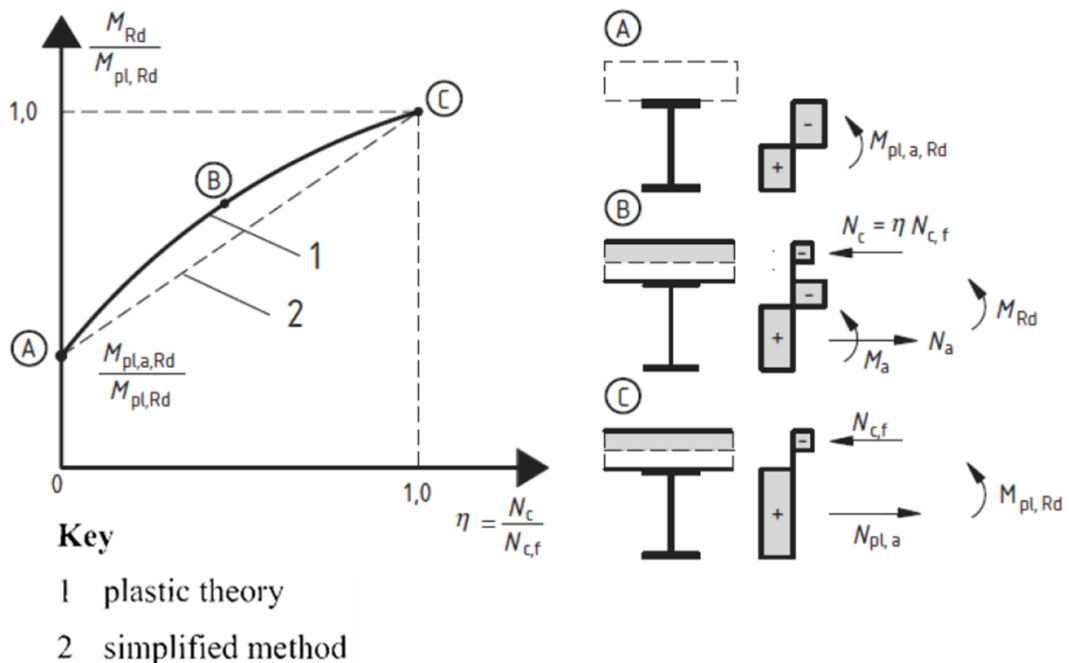


Figure 6-6: Comparison of the moment capacity vs degree of shear connection curves between plastic theory and the simplified method (CEN, 2004b)

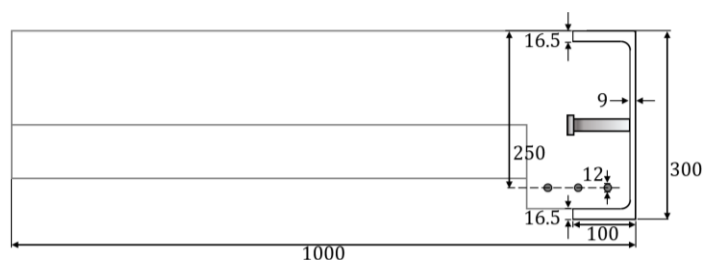


Figure 6-7: Details of half PUSS unit cross-section used in design methodology example

6.3.1 Stress Block Method

The specifications of Eurocode 4 (CEN, 2004b) establish the following assumptions for applying the stress block method:

- The composite cross-section remains plane.
- The tensile strength of concrete is neglected.
- The compressive forces in top steel reinforcement may be neglected.
- The effective areas of structural steel in tension and compression are uniformly stressed to its design yield stress f_{yd} .
- The effective area of steel reinforcement in tension or compression is uniformly stressed to its design yield stress f_{sd} .
- The effective area of concrete in compression resists a uniform stress of $0.85f_{cd}$ over the entire depth of the compressed area, where f_{cd} is the design cylinder compressive strength of concrete.

To calculate the depth of the plastic neutral axis (PNA), the depth of concrete in compression and the design moment of the composite section with full or partial shear connection using the stress block method, equilibrium of the forces within the cross-section is applied. Figure 6-8 gives an example of stress block distribution in a composite beam with a solid slab.

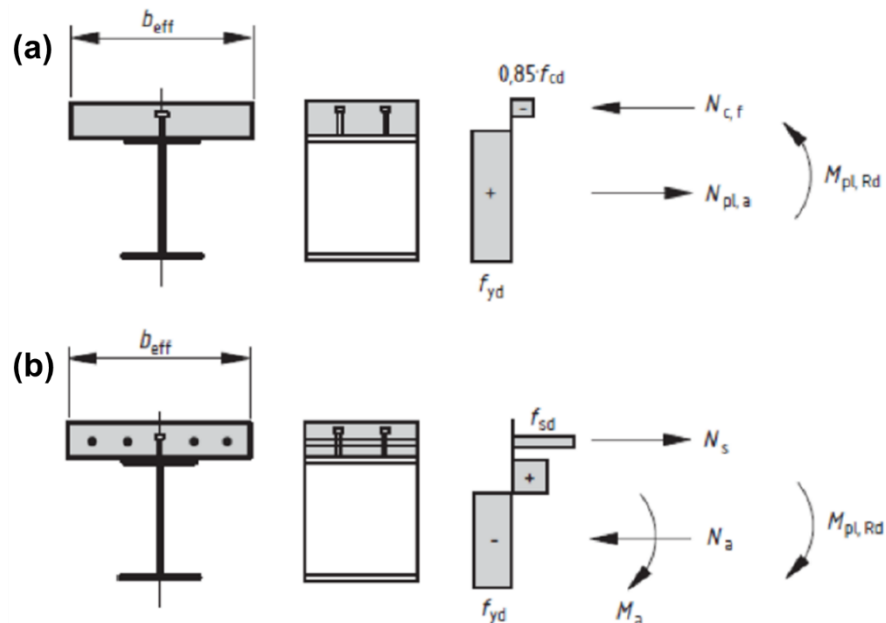


Figure 6-8: Examples of plastic stress distribution in a composite beam with a solid slab with full shear connection in (a) sagging and (b) hogging bending (CEN, 2004b)

For the worked example, the structural steel section is assumed to be S355 steel, with a design yield stress f_{yd} of 355 N/mm² (for both tension and compression).

The steel reinforcement is assumed to have a design yield stress f_{sd} of 500 N/mm², and the concrete is considered as normal weight concrete with a design cylinder compressive strength f_{cd} of 30 N/mm². The following sections present the steps involved in the calculation of the design moment capacity of PUSS, starting with the calculation of the moment resistance of the steel section alone, the moment resistance of the composite section with full shear connection, and the moment resistance of the composite section with partial shear connection.

The criteria to determine whether or not the composite section has a partial or full shear connection is the evaluation of the longitudinal shear resistance of the shear connectors, R_q (or N_c as named in Eurocode 4), and compare it to the compressive resistance of concrete in the composite section with full shear connection, R_c (or $N_{c,f}$ as named in Eurocode 4). At full shear connection, $R_c \leq R_q$, and the ratio of R_q to R_c is defined as the degree of shear connection, $\eta = R_q/R_c$. The specified limits of η in Eurocode 4 are $0.4 \leq \eta \leq 1.0$.

6.3.1.1 Moment Capacity of Steel Section (M_s)

Figure 6-9 illustrates the plastic stress block distribution over the cross-section. To determine the depth (D) of the PNA, equilibrium of the tension and compression forces is applied (Equation 6-2). Substituting the relevant areas and stresses into the equation gives a value of $D = 150$ mm.

Equation 6-2

$$R_{c/f} + R_{c/w} = R_{t/w} + R_{t/f}$$

Where: $R_{c/f} = A_{c/f}f_{yd}$, is the compressive resistance of the top flange area ($A_{c/f}$),
 $R_{c/w} = A_{c/w}f_{yd}$, is the compressive resistance of web area ($A_{c/w}$) in compression,
 $R_{t/w} = A_{t/w}f_{yd}$, is the tensile resistance of web area ($A_{t/w}$) in tension,
 $R_{t/f} = A_{t/f}f_{yd}$, is the tensile resistance of the bottom flange area ($A_{t/f}$).
and f_{yd} is the design yield stress of the steel section.

After that, the moment about the PNA is calculated to determine the moment capacity of the steel section (M_s) using Equation 6-3. By substituting the respective resistances and distances to the PNA, the calculated $M_s = 223.00$ kN.m.

Equation 6-3

$$M_s = R_{c/f}D_{c/f} + R_{c/w}D_{c/w} + R_{t/w}D_{t/w} + R_{t/f}D_{t/f}$$

Where: M_s is the plastic moment resistance of the steel section,
 $D_{c/f}$ is the distance between the centroid of $A_{c/f}$ and PNA,
 $D_{c/w}$ is the distance between the centroid of $A_{c/w}$ and PNA,
 $D_{t/w}$ is the distance between the centroid of $A_{t/w}$ and PNA,
and $D_{t/f}$ is the distance between the centroid of $A_{t/f}$ and PNA.

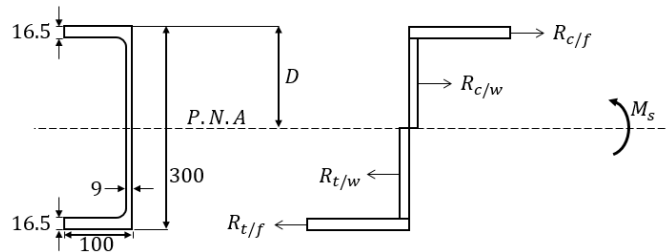


Figure 6-9: Stress block diagram of PFC 300x100x46 steel section

Since the structural steel in the composite section is composed also of steel reinforcement, we need to calculate the moment resistance of the steel section with reinforcement ($M_{s+rebars}$). Figure 6-10 shows the plastic stress block distribution over the cross-section of steel section and reinforcements. To determine the depth (D) of the PNA for this, equilibrium of the tension and compression forces is applied (Equation 6-4). Substituting the relevant areas and stresses into the equation gives a value of $D = 176.55$ mm.

Equation 6-4

$$R_{c/f} + R_{c/w} = R_{t/w} + R_{t/R} + R_{t/f}$$

Where: $R_{t/R} = A_{t/R}f_{sd}$, (or N_s as named in Eurocode 4) is the tensile resistance of the area of the reinforcement in tension ($A_{t/R}$),
and f_{sd} is the design yield stress of the steel reinforcement.

Next, the moment about the PNA is calculated to determine the moment capacity of the steel section with rebars ($M_{s+rebars}$) using Equation 6-5. By substituting the respective resistances and distances to the PNA, the calculated $M_{s+rebars} = 237.71$ kN.m.

Equation 6-5

$$M_{s+rebars} = R_{c/f}D_{c/f} + R_{c/w}D_{c/w} + R_{t/w}D_{t/w} + R_{t/R}D_{t/R} + R_{t/f}D_{t/f}$$

Where: $M_{s+rebars}$ is the plastic moment resistance of the steel section with reinforcement,

and $D_{t/R}$ is the distance between the centroid of $A_{t/R}$ and PNA.

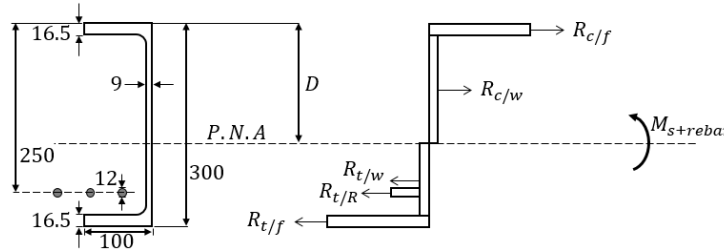


Figure 6-10: Stress block diagram of PFC 300x100x46 steel section with steel reinforcement

6.3.1.2 Moment Capacity of PUSS with Full Shear Connection ($M_{pl,Rd}$)

In the case of full shear connection, the whole concrete area above the depth of the PNA has a uniform compressive stress as depicted in Figure 6-11. To determine the depth (D) of the PNA and the compressive resistance of concrete area in compression at full shear connection (R_c), equilibrium of the tension and compression forces is applied (Equation 6-6). Substituting the relevant areas and stresses into the equation gives a value of $D = 36.84$ mm and $R_c = 892.73$ kN.

Equation 6-6

$$R_{c/f} + R_{c/w} + R_c = R_{t/w} + R_{t/R} + R_{t/f}$$

Where: $R_c = A_c * 0.85f_{cd}$, (or $N_{c,f}$ as named in Eurocode 4) is the compressive resistance of concrete area in compression (A_c), at full shear connection,

and f_{cd} is the design cylinder compressive strength of concrete.

Following that, the moment about the PNA is calculated to determine the moment capacity of the composite section at full shear connection ($M_{pl,Rd}$) using Equation 6-7. By substituting the respective resistances and distances to the PNA, the calculated $M_{pl,Rd} = 316.05$ kN.m.

Equation 6-7

$$M_{pl,Rd} = R_{c/f}D_{c/f} + R_{c/w}D_{c/w} + R_cD_c + R_{t/w}D_{t/w} + R_{t/R}D_{t/R} + R_{t/f}D_{t/f}$$

Where: $M_{pl,Rd}$ is the plastic moment resistance of the composite section with full shear connection,

and D_c is the distance between the centroid of A_c and PNA.

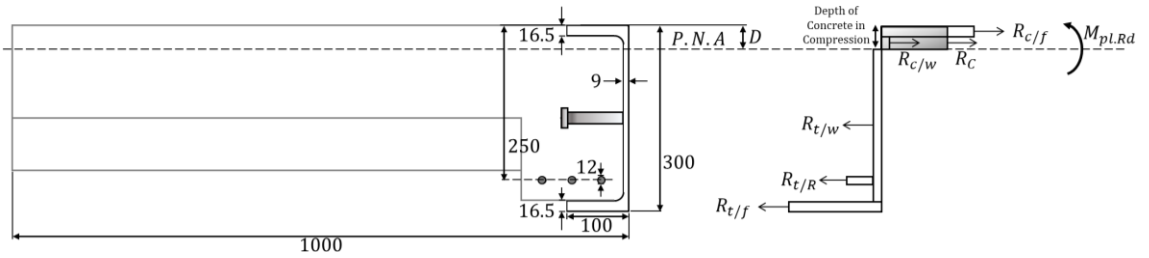


Figure 6-11: Stress block diagram of PUSS in full shear connection

6.3.1.3 Moment Capacity of PUSS with Partial Shear Connection (M_{Rd})

In the case of partial shear connection, not the whole concrete area above the depth of the PNA is stressed. Instead, only the concrete up to the depth that develops a compressive resistance equal to the longitudinal shear resistance of the shear connectors (R_q) is uniformly compressed. Therefore, the first step in calculating the moment capacity of PUSS with partial shear connection is to determine the depth of concrete in compression based on the degree of shear connection (η). For instance, with $\eta = 0.7$, the longitudinal shear resistance $R_q = 0.7 R_c = 624.91$ kN. Using Equation 6-8, the corresponding depth of concrete needed to develop this compressive resistance is calculated as 26.24 mm. As illustrated in Figure 6-12, for PUSS in partial shear connection, the depth of the concrete in compression is less than the depth (D) of the PNA. As a result, to maintain equilibrium, the depth of PNA in the case of partial shear connection is larger than in the case of full shear connection.

Equation 6-8

$$R_q = A_q * 0.85 f_{cd}$$

Where: A_q is the concrete area in compression at partial shear connection.

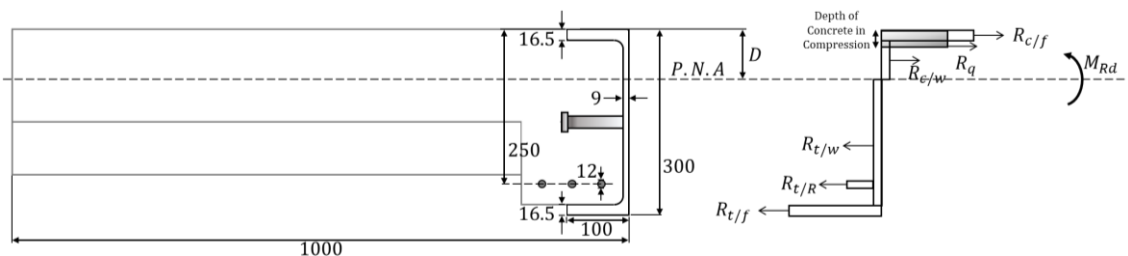


Figure 6-12: Stress block diagram of PUSS in partial shear connection

To determine the depth (D) of the PNA, equilibrium of the tension and compression forces is applied (Equation 6-9). Substituting the relevant areas and stresses into the equation gives a value of $D = 78.75$ mm.

Equation 6-9

$$R_{c/f} + R_{c/w} + R_q = R_{t/w} + R_{t/R} + R_{t/f}$$

Where: R_q is the compressive resistance of concrete area in compression, which is equal to the longitudinal shear resistance of the shear connectors

Subsequently, the moment about the PNA is calculated to determine the moment capacity of the composite section with partial shear connection (M_{Rd}) using Equation 6-10. By substituting the respective resistances and distances to the PNA, the calculated $M_{Rd} = 309.01$ kN.m.

Equation 6-10

$$M_{Rd} = R_{c/f}D_{c/f} + R_{c/w}D_{c/w} + R_qD_q + R_{t/w}D_{t/w} + R_{t/R}D_{t/R} + R_{t/f}D_{t/f}$$

Where: $M_{pl,Rd}$ is the moment resistance of the composite section with partial shear connection,

and D_q is the distance between the centroid of A_q and PNA.

A similar procedure is followed to determine the depth of concrete in compression, the D of the PNA, R_q , and M_{Rd} at different η . Table 6-3 presents the results corresponding to various degrees of partial shear connection.

Table 6-3: Results corresponding to various degrees of partial shear connection

η	R_q (kN)	Depth of concrete in compression (mm)	Depth (D) of PNA (mm)	M_{Rd} (kN.m)
0	0.00	0.00	176.55	237.71
0.05	44.64	1.94	169.56	246.46
0.1	89.27	3.89	162.58	252.95
0.15	133.91	5.83	155.59	259.73
0.2	178.55	7.78	148.61	266.15
0.25	223.18	9.72	141.62	272.19
0.3	267.82	11.67	134.64	277.83
0.35	312.45	13.61	127.65	283.08
0.4	357.09	15.56	120.67	287.94
0.45	401.73	17.41	113.68	292.41
0.5	446.36	19.18	106.70	296.51
0.55	491.00	20.94	99.71	300.22
0.6	535.64	22.71	92.72	303.54
0.65	580.27	24.48	85.74	306.47
0.7	624.91	26.24	78.75	309.01
0.75	669.54	28.01	71.77	311.16
0.8	714.18	29.78	64.78	312.92
0.85	758.82	31.54	57.80	314.29
0.9	803.45	33.31	50.81	315.26
0.95	848.09	35.08	43.83	315.85
1	892.73	36.84	36.84	316.05

6.3.2 Linear Interaction Method

The linear interaction method is a simplified approach for calculating the moment capacity of composite sections with partial shear connection (M_{Rd}). It assumes a linear increase in moment capacity as the degree of shear connection increases. Consequently, after evaluating $M_{pl.Rd}$ and $M_{pl.a.Rd}$ (or M_s) as previously done for the stress block method, M_{Rd} can be calculated for different η using Equation 6-11 (which is a modified form of Equation 2-5).

Equation 6-11

$$M_{Rd} = M_{pl.a.Rd} + \eta(M_{pl.Rd} - M_{pl.a.Rd})$$

Where: $M_{pl.a.Rd}$ (or M_s) is the plastic moment resistance of the steel section.

Figure 6-13 compares the variation of M_{Rd} as η increases, showing the results from both the stress block method and the linear interaction method. The shape of the stress block method curve aligns with the curves presented earlier in Figure 5-35.

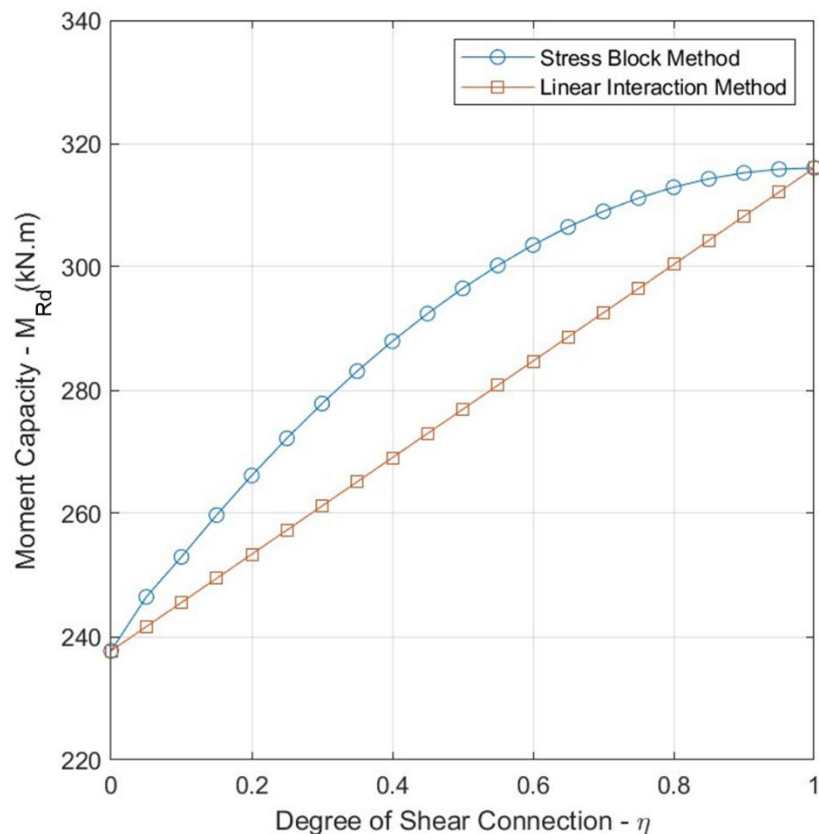


Figure 6-13: Comparison of the variation of M_{Rd} between stress block method and linear interaction method

6.3.3 Quantity and Size of shear Connectors

Load distribution shape over the floor composite section and the span of the slab determine the maximum allowable load that can be applied to reach the design moment capacity of the PUSS unit. Assuming a uniformly distributed load (w) over the area of the slab, and assuming this load is equivalent to the load that results in $M_{max} = M_{pl,Rd}$, as illustrated in Figure 6-14, the structural analysis produce the below shear and moment diagrams. Additionally, the diagram of the longitudinal shear flow (q) can be produced using Equation 4-1 ($q = VQ / I$), where q is the shear flow between the steel section and concrete slab (Figure 6-15), expressed in units of shear force per unit of length, V is the shear force, Q is the first moment of area of steel section with respect to the neutral axis and I is the moment of inertia of the entire cross-section about the neutral axis. Note that w includes flooring live and dead loads factored appropriately in accordance with Eurocode 4 (CEN, 2004b).

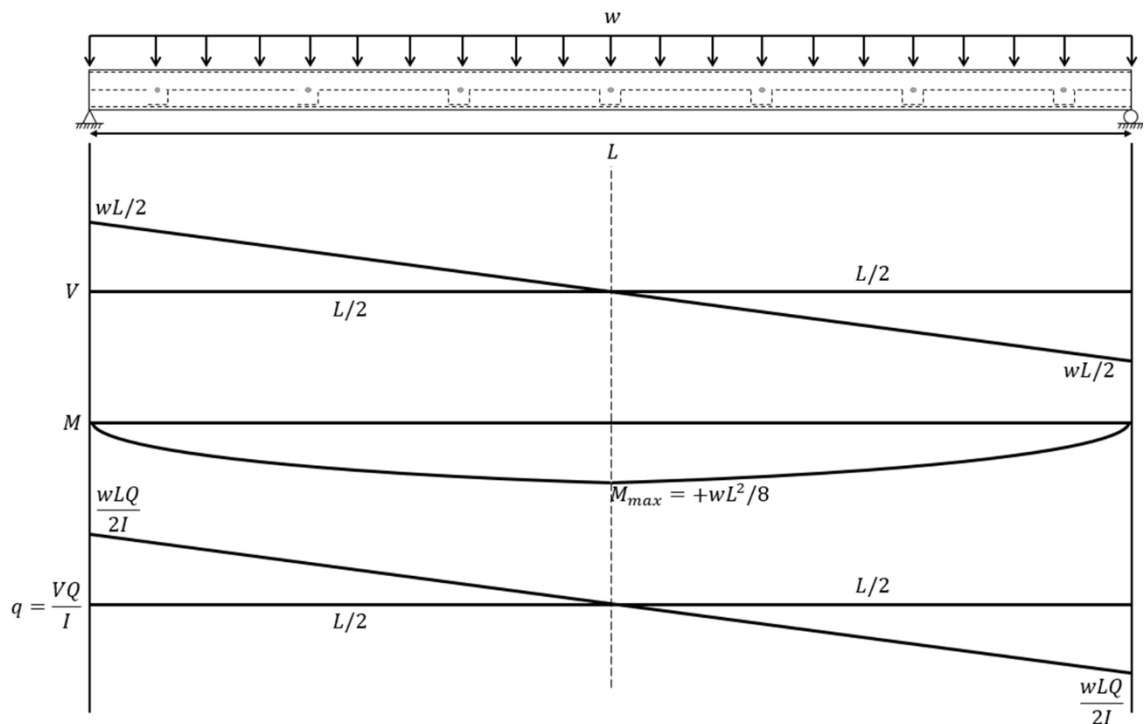


Figure 6-14: Shear force (V), bending moment (M) and shear flow (q) diagram of PUSS unit with uniformly distributed load (w)

The area under the shear flow (q) diagram in each shear span provides the total longitudinal shear force that must be resisted by all the shear connectors along the shear span. To determine the size and number of shear connectors required to achieve full shear connection, Equation 6-1 is employed to evaluate the shear resistance ($P_{Rd,h}$) of individual horizontally oriented shear connectors (shear studs or steel dowels) of various sizes. The required number and sizes of shear

connectors are then selected and distributed along the span ensuring that the total $P_{Rd,h}$ of the shear connectors is equal or greater than the calculated total longitudinal shear force. For cases involving design of composite sections with partial shear connection, the calculated total longitudinal shear force is factored by the relative degree of shear connection (η). Consequently, the required longitudinal shear force required to be resisted by the shear connectors is reduced, allowing for smaller sizes and/ or fewer shear connectors.

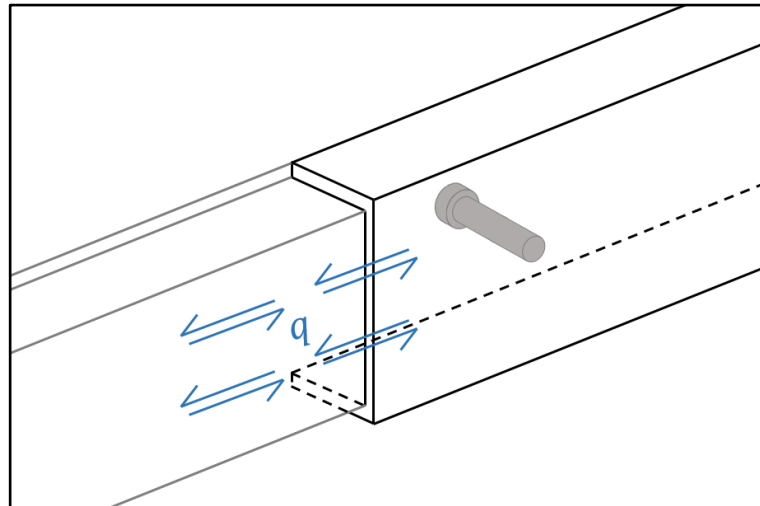


Figure 6-15: Longitudinal shear flow (q) between the concrete slab and steel section of PUSS unit

It is noteworthy, as depicted in Figure 6-14, that despite the span length, the maximum moment should not be exceeded. This indicates that increasing the span length reduces the maximum allowable load (w), and the area under the shear force (V) and, consequently, the shear flow (q) diagrams remain constant for the same PUSS section. This leads to conclude that regardless of span length, the required number and size of shear connectors also remain constant. This observation is in alignment with conclusions drawn from both experimental and FEA investigations, which revealed that only a small number of shear connectors is needed in PUSS to achieve the full degree of shear connection in comparison to other shear connection systems that utilise vertical shear studs.

6.4 Analytical Study Limitations

While the proposed empirical formula (Equation 6-1) shows better agreement with experimental and FEA results and outperforms existing design equations, there are several limitations that must be acknowledged regarding its development and validation.

Although the proposed formula achieves mean ratios close to 1.0 and the lowest coefficients of variation among all methods, a degree of scatter remains in the results. This variability is partially attributed to the numerical effects observed in the parametric study models, such as the trembling in load-deflection curves, particularly in long-span and high depth sections. These effects stem from factors including mesh density, boundary complexity, and limited runtime during the FEA simulation process, as discussed in Chapter 5. As the formula was derived using regression analysis on data from these simulations, it inherently gets such limitations.

In addition, the validity of the proposed formula has not been evaluated through reliability analysis due to the absence of sufficiently similar systems in existing literature. The unique shear connection system in PUSS, consisting of horizontally oriented web-welded steel dowels and WWSS connectors, is not replicated in other known slab or composite beam systems to a degree that enables direct statistical comparison. Although horizontally WWSS exist in some systems, they are not combined with steel dowels as in PUSS, limiting their applicability for validation.

These constraints should be considered when applying the proposed formula in practical design. Future work should focus on broader experimental programmes and comparative studies to enable more robust reliability assessments.

6.5 Summary

This chapter introduces a new empirical formula for predicting the shear resistance of the horizontally oriented shear connectors employed in Prefabricated Ultra-Shallow Slab (PUSS) flooring system, as expressed in Equation 6-1. The proposed equation is developed through regression analysis conducted on the extensive dataset obtained from both the experimental results (Chapter 4) and the comprehensive FEA parametric study (Chapter 5). This approach ensures optimising the structure (form) of the formula, and incorporating the most significant parameters influencing shear resistance calculation.

The predicted shear resistance of the shear connectors and the corresponding degrees of shear connection obtained from the calculation methodology utilising Equation 6-1 demonstrated the best overall agreement with all the considered

328 experiments and FEA models, compared to the calculation results obtained from other formulas present in design codes and literature. This is evidenced by an average ratio of approximately 1.0 for the experiment/FEA results to predicted values of both degree of shear connection and total shear resistance of shear connectors on one side of PUSS, accompanied by the lowest coefficients of variation.

In addition, this chapter outlines a design methodology of the bending capacity of PUSS flooring in accordance with Eurocode 4 (CEN, 2004b), utilising both the stress block method and the linear simplified method, along with the detailing of shear connectors requirements.

The significance of proposed formula lies in its potential to update Eurocode 4 (CEN, 2004b), particularly in the context of using horizontally oriented shear connectors. Furthermore, the design methodology presented can serve as a design guide example for the application of Eurocode 4 (CEN, 2004b) guidelines in designing structural elements that incorporate new shear connection systems.

Chapter 7

Conclusions and Recommendations

7.1 Overview

The Prefabricated Ultra-Shallow Slab (PUSS) flooring system offers an innovative solution to the challenges of designing slim, long-span floors while mitigating the environmental impact associated with traditional flooring systems and their supporting structure. The shear transfer mechanism formed by the novel horizontally oriented shear connection system develops the necessary composite action without increasing slab depth. In addition, PUSS's shallow profile, voids beneath the slab, and use of lightweight materials, reduce material consumption and overall weight, significantly lowering the environmental footprint both the flooring and the supporting structural elements. Moreover, the system's controlled offsite prefabrication further enhances sustainability by minimising construction waste and the need for extensive formwork.

Considering its relatively recent introduction, research on the performance of the PUSS flooring system remains limited, although existing studies have underscored its advantages and its potential as a sustainable, lightweight and high-strength alternative to the existing flooring systems. Previous assessments of the system have demonstrated reductions in Global Warming Potential (GWP), energy consumption, time, and costs when compared to other prefabricated systems such as hollow core slabs. However, these assessments were constrained to specific spans and loading conditions, without accounting for the effects of various parameters on overall performance. Additionally, the predominant focus of the previous experimental and numerical investigation was on the performance of the implemented shear connection system under direct shear, without evaluating the performance of the shear connectors and the entire slab under bending, which is the primary load type carried by the floor.

This PhD thesis aims to expand the existing knowledge on the environmental and structural performance of PUSS, advocating for the adoption of such practical and sustainable system in building design. The comprehensive comparative LCA presented in this thesis explores how variations in key factors, such as span and live load, impact the environmental performance of the system. Moreover, the analysis of both experimental and numerical investigations conducted in this

research deepens the understanding of the flexural behaviour of the slabs and shear connectors, contributes to the development of a design methodology, and addresses the limited research available on horizontally oriented shear connectors.

7.2 Research Objectives

This section reflects how the research objectives outlined in Chapter 1 have been addressed throughout this thesis:

Objective 1. Literature Review on Sustainability and Composite Flooring Systems

In Chapter 2, a comprehensive literature review was conducted on topics critical to understanding the performance of PUSS flooring systems. The review included an in-depth exploration of sustainability in construction, existing shallow composite flooring systems, relevant codes of practice concerning composite sections and shear connectors, as well as experimental and numerical studies focused on performance of shear connectors in composite sections.

Objective 2. Life Cycle Assessment (LCA) Study

Chapter 3 presents a detailed comparative LCA study of the PUSS flooring system, evaluating its environmental impacts (GWP and EE) across multiple live load and span scenarios. The findings demonstrate the superiority of PUSS, particularly when constructed with LWC or GPC, over conventional hollow core slabs.

Objective 3. Experimental Four-Point Bending Tests

In Chapter 4, full-scale four-point bending tests were conducted on PUSS units to assess the effects of concrete type, slab depth, and degree of shear connection on flexural performance. The experiments provided valuable data for understanding the behaviour of PUSS under bending.

Objective 4. Finite Element Analysis (FEA) Parametric Study

Chapter 5 focused on validating the experimental tests through FEA and conducting a parametric study involving 324 models. The study investigated the effects of key parameters on the flexural behaviour

and performance of shear connectors, highlighting critical findings related to the moment capacity and the degree of shear connection.

Objective 5. Development of an Empirical Formula for Shear Resistance

Based on the experimental and FEA data, Chapter 6 introduces an optimised empirical formula to predict the shear resistance of shear connectors used in PUSS. The formula provides a more accurate prediction compared to existing methods and has potential applications in design codes like Eurocode 4.

Objective 6. Design Methodology for Moment Capacity of PUSS Composite Sections

Chapter 6 also provides a design methodology for calculating the moment capacity of PUSS composite sections, offering practical guidance for engineers and designers.

7.3 Research Conclusions

The primary objectives of this research is to study the performance of the PUSS flooring system through a comprehensive approach, encompassing Life Cycle Assessment (LCA), experimental tests, finite element analysis (FEA), and analytical studies. The following sections present the contributions and findings related to each objective, as explored in the respective chapters of the thesis:

7.3.1 Conclusions of the Life Cycle Assessment (LCA) Study

The comprehensive comparative Life Cycle Assessment (LCA) study conducted in this research provides valuable insights into the environmental impacts of PUSS flooring system using different concrete types compared to the widely used hollow core slabs. The assessment specifically evaluates Global Warming Potential (GWP) and embodied energy (EE) across various scenarios involving different live loads and span. Additionally, the analysis includes a sensitivity evaluation of transportation distances and end-of-life (EOL) recycling allocation methods. The following key conclusions emerged from the study:

- **Global Warming Potential (GWP):** The results indicate that PUSS with Geopolymer Concrete (GPC) exhibits the most favourable environmental performance considering GWP, reducing it by 40% to 50% compared to hollow core slabs. PUSS with Lightweight Concrete (LWC) follows closely, achieving reductions between 37% and 46%. Conversely, PUSS with

Normal Weight Concrete (NWC) demonstrates reductions ranging from 24% to 33%. This highlights the significant potential for environmental benefits when utilising alternative concrete types in flooring systems.

- **Embodied Energy (EE):** In terms of EE, PUSS with LWC stands out as the best performer, conserving between 21% and 35% of the total EE compared to hollow core slabs. PUSS with GPC also shows substantial energy savings, achieving reductions between 17% and 32%. However, PUSS with NWC provides the least improvement in energy efficiency, with reductions ranging from 6% to 20%. This suggests that LWC not only reduces weight but also enhances overall energy performance. Furthermore, given that LWC's GWP performance is closely aligned with that of GPC, it emerges as an excellent choice for sustainable construction, reinforcing the potential of lightweight materials in achieving eco-friendly building solutions.
- **Manufacturing Phase:** The LCA results emphasise the importance of material selection in determining the environmental impacts of flooring systems. The PUSS flooring systems benefit from reduced material consumption, particularly in the manufacturing phase, which accounts for a significant portion of the total GWP and EE. The study reveals that the manufacturing phase contributes between 86% and 94% of the total GWP and 83% to 93% of the total EE for all flooring systems assessed. In this phase, PUSS with LWC and GPC exhibited lower carbon emissions and energy consumption compared to hollow core slabs due to their lighter weight and reduced material requirements.
- **Transportation and On-Site Construction:** The analysis indicates that transportation contributes significantly to the overall environmental impacts, accounting for between 5.75% and 11.5% of total GWP and 7% to 14.5% of total EE. PUSS flooring systems, being lighter than hollow core slabs, resulted in lower transportation emissions, with reductions of 15% to 45% in GWP and EE across different concrete types. Furthermore, the on-site construction phase showed negligible contributions to GWP and EE, typically around 1% or less, as a result of prefabrication practices, which reduced the need for extensive on-site construction equipment.
- **End-of-Life Phase:** The end-of-life phase analysis highlights the significance of recycling potential, particularly for steel components in

PUSS flooring. The study found that PUSS units could recover between 10% and 18% of GWP and EE through recycling, significantly outperforming hollow core slabs, which only recovered 4% to 7%. This recovery aspect emphasises the advantages of using PUSS in terms of sustainability and waste reduction.

- **Robustness of Findings:** The sensitivity analysis conducted on transportation distances and recycling allocation methods demonstrated that these variations did not change the relative rankings of the flooring systems. This underscores the reliability of the findings, indicating that PUSS flooring systems consistently outperform hollow core slabs across various scenarios and conditions.

In conclusion, the LCA study presented in this thesis not only confirms the environmental benefits of the PUSS flooring system but also illustrates the critical role of material selection and construction practices in enhancing sustainability in the construction sector. The results advocate for the increased adoption of PUSS flooring systems, particularly in environmentally conscious designs, highlighting their potential to mitigate the impacts associated with traditional flooring solutions.

7.3.2 Conclusions of the Experimental Four-Point Bending Tests

The experimental phase of this research is focused on understanding the flexural behaviour of PUSS through four-point bending tests on four specimens. The investigation focuses on examining the effects of concrete type, degree of shear connection, and slab depth on the overall structural performance. The findings from these tests provide important insights into the structural behaviour of PUSS, as detailed below:

- **Performance of Concrete Types:** PUSS specimens constructed with LWC and NWC demonstrated comparable bending performance and moment capacities, provided the concrete strengths were similar. However, specimens made with LWC exhibited a greater tendency for larger crack development due to LWC's lower modulus of elasticity. This resulted in an average loss of strength of about 7% in the later stages of testing, indicating that while LWC offers benefits in terms of weight, it may compromise strength under severe loading conditions.
- **Initial Stiffness and Load Capacity:** Initial stiffness values were lower in PUSS specimens with LWC compared to those with NWC. Nonetheless,

the lighter weight of LWC enabled the LWC specimens to support slightly higher live loads, thus contributing to a more efficient overall load-bearing capacity.

- **Impact of the Degree of Shear Connection:** A direct correlation was observed between the degree of shear connection and the moment capacity of PUSS units. Specimens with lower degrees of shear connection experienced a notable decrease in moment capacity, with failures occurring in some shear connectors at higher displacements. This resulted in separation between the concrete slab and steel sections, emphasising the critical role that shear connections play in the structural integrity of PUSS.
- **End-Slip Observations:** All PUSS specimens with full shear connection exhibited end-slips lower than the 6 mm threshold at the end of the tests. However, specimens with a reduced shear connection degree recorded end-slips exceeding 6 mm only after some shear connectors had failed. The significance of this finding lies in the necessity to reconsider the 6 mm limit set by Eurocode 4 for ductile shear connectors, as this standard may not adequately apply to the horizontal shear connectors utilised in PUSS.
- **Ductile Behaviour of the Composite System:** The shear connection system in PUSS facilitated ductile behaviour, enabling the slabs to deflect significantly beyond SLS and ULS thresholds without the shear connectors failing. This characteristic underscores the effectiveness of the applied shear connection system and affirms the overall integrity of the composite structure.
- **Effectiveness of Shear Connection System:** The employed shear connection system, which integrates web-welded shear studs and horizontal steel dowels, demonstrated high resistance to longitudinal shear and effectively maintained the structural bond between the concrete and steel sections. Importantly, none of the shear connectors displayed permanent deformation at the test's conclusion, even those that failed, indicating the robustness of this connection method. Furthermore, only a small number of shear connectors is required in PUSS to achieve the full degree of shear connection, especially in comparison to other shear connection systems that utilise vertical studs. This efficiency not only

simplifies the design but also contributes to overall material savings and sustainability.

- **Shear Resistance Formula:** The research also demonstrated that the formula for calculating shear resistance of shear connectors in PUSS, developed from prior work by Ahmed and Tsavdaridis (2020) (Equation 2-4), yields results within a 10% deviation from experimental outcomes. This confirms its suitability for designing PUSS units of similar dimensions. However, there is potential for enhancement of this formula by incorporating additional parameters through further experimental validation or parametric Finite Element Analysis (FEA).

These conclusions demonstrate the critical contributions of this research to understanding the flexural behaviour of PUSS, particularly in terms of structural integrity, material performance, and design methodology, paving the way for more sustainable building practices.

7.3.3 Conclusions of the Finite Element Analysis (FEA) Parametric Study

The Finite Element Analysis (FEA) parametric study conducted in this research provides significant insights into the flexural behaviour of Prefabricated Ultra-Shallow Slab (PUSS) units under bending. This study involves the development of 324 models to explore various parameters, including slab depth, span, concrete type and strength, and the degree of shear connection. The following conclusions can be drawn from the analysis:

- **Effect of Slab Depth and Span:** The investigation demonstrates that increasing the slab depth significantly enhances both the moment capacity and initial stiffness of the PUSS units. Deeper slabs, utilising larger parallel flange channel (PFC) steel sections, exhibit greater moment capacities and stiffness, making them more suitable for longer spans.

The study also reveals that while moment capacities remain relatively constant across varying spans for slabs of similar depths, increasing the span leads to a reduction in the yield moment and elongation of the yield region. This relationship effectively reduces the allowable design loads for longer spans, indicating a critical design consideration for PUSS units.

Additionally, the analysis indicates that similar degrees of shear connection can be maintained across different spans when the slabs are of similar depths and shear connector sizes. However, when maintaining the same shear connectors while increasing slab depth, a decrease in the degree of shear connection is observed. This underscores the necessity for optimizing shear connector design in relation to slab configurations, as it becomes crucial to ensure that the connectors effectively engage with the concrete to maximise composite action and moment capacity in deeper slabs.

- **Concrete Type and Strength Impact:** The results also highlight that the type of concrete — NWC, LWC, and GPC —significantly influences slab performance. LWC, characterised by its lower modulus of elasticity, results in reduced initial stiffness compared to NWC and GPC. Moreover, increasing concrete strength slightly enhances moment capacities and initial stiffness.
- **Degree of Shear Connection:** The findings illustrate that the degree of shear connection has a direct effect on the moment capacity of PUSS units. The results indicate that a reduction in the degree of shear connection leads to a decrease in moment capacity; however, this reduction is not proportional, highlighting the complex interactions between shear connectors and overall slab performance.
- **Comparison with Existing Formula:** A comparison between the FEA results and hand calculations using Equation 2-4 reveals an average ratio of 0.843 for the degree of shear connection, indicating a discrepancy between FEA and hand calculations. The variability is particularly pronounced in models utilising LWC, especially at greater depths and spans, with potential differences reaching up to 70%. This significant variation underscores the necessity for improved equations to accurately estimate shear resistance and ensure better alignment with FEA outcomes.

In summary, the parametric study provides essential insights into the flexural behaviour of PUSS slabs under various parameters. The findings stress the importance of considering the interaction of different parameters to optimise slab design.

7.3.4 Conclusions of the Analytical Study of Shear Connectors Capacity

The analytical study of shear connectors' capacity builds on extensive experimental and finite element analysis (FEA) data, ultimately deriving a reliable formula to predict the shear resistance of the connectors used in PUSS flooring system. The following key conclusions have been drawn from this chapter:

- **Empirical Formula Development:** A new empirical formula (Equation 6-1) is developed through nonlinear regression analysis of experimental and FEA results. This formula accurately predicts the shear resistance ($P_{Rd,h}$) of the horizontally oriented shear connectors in PUSS, considering various influential parameters. The derived equation is essential for calculating the degree of shear connection and contributes significantly to design PUSS's bending capacity and understanding its flexural behaviour.
- **Comparison with Existing Formulas:** The performance of the newly proposed formula are evaluated against existing design codes and formulas. The comparison demonstrates that the new formula provides a more accurate prediction, with an average ratio of approximately 1 when compared to the experimental and FEA results. Furthermore, it exhibits the lowest coefficients of variation, indicating a higher degree of reliability and consistency in its predictions.
- **Design Methodology for Bending Capacity:** This chapter outlines a comprehensive design methodology for calculating the bending capacity of PUSS units according to Eurocode 4. By utilising both the stress block method and the linear interaction method, the design approach accommodates the unique characteristics of the PUSS system, offering a practical guide for engineers in the design of composite flooring systems.

In conclusion, the analytical study provides essential insights and tools for accurately predicting shear connector capacity in PUSS flooring systems, reinforcing the potential for enhanced design practices in composite construction.

7.4 Recommendations for Future Research

The findings from this research underscore the potential of PUSS flooring system in advancing sustainable construction practices. However, further research is needed to enhance the understanding of PUSS flooring and its applications in

structural engineering practice. Based on the insights gained throughout the research, the following specific recommendations are proposed for future research:

- **Expanded Experimental Campaign on Key Structural Parameters:**

A wider experimental programme is recommended to address the limitations of the current study and to strengthen applicability of the findings. Future studies include a broader range of full-scale PUSS specimens, particularly wider 2m slabs with longer spans that reflect the intended design applications. This expanded testing will provide valuable data for improving and validating the developed FE model, as well as enhancing its reliability in predicting the behaviour of PUSS systems under diverse practical conditions.

- **Extension of FEA Parametric Study:**

To further enhance the robustness and applicability of the FE models, future parametric studies should first be validated against a broader set of experimental results. Once validated, the models should be extended to investigate additional structural parameters not covered in the present research. These include the weld position of shear connectors along the PFC web height, various shear connector layouts, and different slab widths. Numerically exploring these parameters would provide a deeper understanding of their influence on composite action and flexural performance. In addition, employing longer step times in future simulations is recommended to minimise fluctuations and improve the stability of results, particularly for large-scale models. These enhancements would refine the predictive accuracy of the FEA framework and expand its practical relevance for the design and optimisation of PUSS systems.

- **Development and Testing of Eco-Friendly PUSS Solutions:**

Future studies should explore the integration of more sustainable practices into PUSS by incorporating new low-carbon materials and alternative structural elements. This includes the integration of greener concrete mixes, such as GPC combined with lightweight aggregates, while ensuring that concrete maintains sufficient structural strength. In parallel, the replacement of hot-rolled steel sections with cold-formed steel components. These practices reduce the material usage and overall system weight, producing more eco-friendly floorings. Experimental tests,

including direct shear and flexural tests, are recommended to assess the structural performance of these alternative floorings in comparison to the previously tested units. These findings will provide valuable insights for optimising PUSS design and advancing its sustainability.

- **Dynamic and Fatigue Behaviour Evaluation:**

To provide more comprehensive design guidelines of PUSS flooring and enhance their applicability in diverse environments, additional research should consider the influence of dynamic loading on its behaviour, including vibrations from pedestrians, machinery, and seismic activity. Fatigue testing of the flooring units and the integrated shear connectors under repeated loading should also be carried out to evaluate service life.

- **Investigations of PUSS Integration with Composite Beams:**

Future research should investigate the interaction between PUSS units and the supporting structural framework, particularly composite beams. Experimental testing of full composite floor assemblies is recommended to evaluate load transfer mechanism from PUSS units to surrounding beams and frames. Such studies would provide insight into overall system stiffness, deflection compatibility between adjacent units, and the effectiveness of shear transfer. These investigations are essential for developing accurate design guidelines and ensuring serviceability under realistic loading conditions.

References

- Abdullah, R. 2004. *Experimental evaluation and analytical modeling of shear bond in composite slabs*. PhD Thesis. Virginia Polytechnic Institute and State University.
- Ahmed, I.M. 2019. *Shear connection of a prefabricated lightweight steel-concrete composite flooring system*. PhD Thesis. University of Leeds.
- Ahmed, I.M. and Tsavdaridis, K.D. 2018. Life cycle assessment (LCA) and cost (LCC) studies of lightweight composite flooring systems. *Journal of Building Engineering*. 20, pp.624-633.
- Ahmed, I.M. and Tsavdaridis, K.D. 2019. The evolution of composite flooring systems: applications, testing, modelling and eurocode design approaches. *Journal of Constructional Steel Research*. 155, pp.286-300.
- Ahmed, I.M. and Tsavdaridis, K.D. 2020. Shear connection of prefabricated slabs with LWC-Part1: Experimental and analytical studies. *Journal of Constructional Steel Research*. 169, 106016.
- Ahmed, I.M. and Tsavdaridis, K.D. 2022. Shear connection of prefabricated ultra-lightweight concrete slab systems (PUSS™). *Structures*. 36, pp.65-97.
- Alali, A.A. and Tsavdaridis, K.D. 2021. Flexural Behaviour of Prefabricated Ultra-Shallow Steel-Concrete Composite Slabs. In: *Proceedings of the 9th European Conference on Steel and Composite Structures (EUROSTEEL 2021)*, 1-3 September 2021, Sheffield, UK. Available from: <https://doi.org/10.1002/cepa.1362>
- Alali, A.A. and Tsavdaridis, K.D. 2023. Flexural Behaviour of Prefabricated Ultra-Shallow Composite Slabs with Horizontally Oriented Shear Connectors. In: *Proceedings of the 10th Hellenic National Conference of Steel Structures*, 19-21 October 2023, Athens, Greece. Available from: https://www.researchgate.net/publication/378297980_FLEXURAL_BEHAVIOUR_OF_PREFABRICATED_ULTRA-SHALLOW_COMPOSITE_PUSS_R_SLABS_WITH_HORIZONTALLY_ORIENTED_SHEAR_CONNECTORS
- Alali, A.A. and Tsavdaridis, K.D. 2024. Experimental Investigation on Flexural Behaviour of Prefabricated Ultra-Shallow Steel Concrete Composite Slabs.

- Journal of Constructional Steel Research*. 217, 108632. Available from:
<https://doi.org/10.1016/j.jcsr.2024.108632>
- Alam, N., Maraveas, C., Tsavdaridis, K. D., & Nadjai, A. 2021. Performance of Ultra Shallow Floor Beams (USFB) exposed to standard and natural fires. *Journal of Building Engineering*, 38, 102192
- Alam, N., Nadjai, A., Hanus, F., & Vassart, O. 2021. Experimental and numerical investigations on slim floor beams exposed to fire. *Journal of Building Engineering*, 42, 102810.
- Al Bakri, A.M.M., Kamarudin, H., Nizar, I.K., Sandu, A.V., Binhussain, M., Zarina, Y. and Rafiza, A.R. 2013. Design, processing and characterization of fly ash-based geopolymers for lightweight concrete application. *Revista de Chimie (Bucharest)*. 64(4), pp.382-387.
- Allacker, K., Mathieux, F., Manfredi, S., Pelletier, N., De Camillis, C., Ardente, F. and Pant, R. 2014. Allocation solutions for secondary material production and end of life recovery: Proposals for product policy initiatives. *Resources, Conservation and Recycling*. 88, pp.1-12.
- Almusallam, T.H. and Alsayed, S.H. 1995. Stress–strain relationship of normal, high-strength and lightweight concrete. *Magazine of Concrete Research*. 47(170), pp.39-44.
- American Association of State Highway and Transportation Officials (AASHTO) 2020. *AASHTO LRFD bridge design specifications*. 9th ed. Washington, DC: AASHTO.
- American National Standards Institute (ANSI) 2010. *AISC 360–10: Specification for structural steel buildings*. Chicago: ANSI.
- Anderson, J. and Moncaster, A. 2020. Embodied carbon of concrete in buildings, Part 1: Analysis of published EPD. *Buildings & Cities*.
- ArcelorMittal. 2019. Composite floor decking. [Online]. Available from:
https://constructalia.arcelormittal.com/files/AMC_floors_guide_EN_June2019_LR--b47b21285b39514432cf4da5d75b23f1.PDF
- Asdrubali, F., Grazieschi, G., Roncone, M., Thiebat, F. and Carbonaro, C. 2023. Sustainability of building materials: Embodied energy and embodied carbon of masonry. *Energies*. 16(4), 1846.

- Bakharev, T. 2006. Thermal behaviour of geopolymers prepared using class F fly ash and elevated temperature curing. *Cement and Concrete Research*. 36(6), pp.1134-1147.
- Baldassino, N., Roverso, G., Ranzi, G. and Zandonini, R. 2019. Service and ultimate behaviour of slim floor beams: an experimental study. *Structures*. 17, pp.74-86.
- Balasbaneh, A.T., Sher, W., Yeoh, D. and Koushfar, K. 2022. LCA & LCC analysis of hybrid glued laminated Timber–Concrete composite floor slab system. *Journal of Building Engineering*. 49, 104005.
- Beckmann, O., & Cyllok, M. 2023. LOAD TRANSFER FROM HOLLOWCORE SLABS TO DELTABEAM® SLIM FLOOR BEAMS IN CASE OF A FIRE. *ce/papers*, 6(1), 381-392.
- Borghini, T. M., Oliveira, L. A. M., & El Debs, A. L. H. C. 2021. Numerical investigation on slim floors: comparative analysis of ASB and CoSFB typologies. *Revista IBRACON de Estruturas e Materiais*, 14(4), e14402.
- Brander, M. and Davis, G. 2012. Greenhouse gases, CO₂, CO_{2e}, and carbon: What do all these terms mean. *Econometrica, White Papers*.
- British Standards Institution (BSI) 1990. *Structural use of steelwork in building. Design in composite construction. Code of practice for design of simple and continuous composite beams* (BS 5950-3.1:1990+A1:2010). London: BSI.
- British Standards Institution (BSI) 2009. *Testing hardened concrete – Part 6: Tensile splitting strength of test specimens* (BS EN 12390-6). London: BSI.
- British Standards Institution (BSI) 2011a. *Cement – Part 1: Composition, specifications and conformity criteria for common cement* (BS EN 197-1). London: BSI.
- British Standards Institution (BSI) 2011b. *Sustainability of construction works — Assessment of environmental performance of buildings — Calculation method* (BS EN 15978:2011). London: BSI.
- British Standards Institution (BSI). 2019a. *Sustainability of construction works. Environmental product declarations. Core rules for the product category of construction products* (BS EN 15804:2012+A2:2019). London: BSI.

- British Standards Institution (BSI) 2019b. *Testing hardened concrete – Part 3: Compressive strength of test specimens* (BS EN 12390-3). London: BSI.
- Chen, S., Limazie, T. and Tan, J. 2015. Flexural behavior of shallow cellular composite floor beams with innovative shear connections. *Journal of Constructional Steel Research*. 106, pp.329-346.
- Chen, S. and Limazie, T. 2018. Composite slim floor beams with innovative shear connections. *Proceedings of the Institution of Civil Engineers-Structures and Buildings*. 171(1), pp.29-37.
- Cherubini, E., Franco, D., Zanghelini, G.M. and Soares, S.R. 2018. Uncertainty in LCA case study due to allocation approaches and life cycle impact assessment methods. *The International Journal of Life Cycle Assessment*. 23, pp.2055-2070.
- Chicco, D., Warrens, M.J. and Jurman, G. 2021. The coefficient of determination R-squared is more informative than SMAPE, MAE, MAPE, MSE and RMSE in regression analysis evaluation. *PeerJ Computer Science*. 7, e623.
- Chinn, J. 1965. Pushout tests on lightweight composite slabs. *AISC Engineering Journal*. 2(4), pp.129-134.
- Coldebella, G., Ferreira, F.P.V. and De Nardin, S. 2022. Shear forces transfer in steel-concrete slim floor with circular web opening and PCHCS. *Structures*. 38, pp.1295-1307.
- Cornelissen, H., Hordijk, D. and Reinhardt, H. 1986. Experimental determination of crack softening characteristics of normal weight and lightweight concrete. *Heron*. 31(2), pp.45-46.
- Crisinel, M. and Marimon, F. 2004. A new simplified method for the design of composite slabs. *Journal of Constructional Steel Research*. 60(3-5), pp.481-491.
- Cui, Y., Ai, W., Tekle, B. H., Liu, M., Qu, S., & Zhang, P. 2023. State of the art review on the production and bond behaviour of reinforced geopolymer concrete. *Low-carbon Materials and Green Construction*, 1(1), 25.
- Dai, X., Lam, D., Sheehan, T., Yang, J. and Zhou, K. 2020. Effect of dowel shear connector on performance of slim-floor composite shear beams. *Journal of Constructional Steel Research*. 173, 106243.

Dassault Systèmes. 2022. *ABAQUS 2022 Documentation*. [Online]. Available from:

https://help.3ds.com/2022/english/DSSIMULIA_Established/SIMULIA_Established_FrontmatterMap/sim-r-DSDocAbaqus.htm?contextscope=all&id=ec01bc8c83d743a6a30123c5a034edca

Davies, C. 1967. Small-scale push-out tests on welded stud shear connectors. *Concrete*. 1(9), pp.311-.

Díaz, C., Victoria, M., Querin, O.M. and Martí, P. 2018. FE model of three-dimensional steel beam-to-column bolted extended end-plate joint. *International Journal of Steel Structures*. 18, pp.843-867.

Dong, Y.H., Jaillon, L., Chu, P. and Poon, C.S. 2015. Comparing carbon emissions of precast and cast-in-situ construction methods – A case study of high-rise private building. *Construction and Building Materials*. 99, pp.39-53.

Duma, D., Zaharia, R., Pintea, D., Both, I., & Hanus, F. 2022. Analytical Method for the Bending Resistance of Slim Floor Beams with Asymmetric Double-T Steel Section under ISO Fire. *Applied Sciences*, 12(2), 574.

Duxson, P., Fernández-Jiménez, A., Provis, J.L., Lukey, G.C., Palomo, A. and van Deventer, J.S. 2007. Geopolymer technology: the current state of the art. *Journal of Materials Science*. 42(9), pp.2917-2933.

Easterling, W.S., Gibbings, D.R. and Murray, T.M. 1993. Strength of shear studs in steel deck on composite beams and joists. *Engineering Journal*. 30(2), pp.44-55.

European Committee for Standardization (CEN) 2004a. *Eurocode 2: Design of Concrete Structures, Part 1-1: General Rules and Rules for Buildings* (BS EN 1992-1-1). Brussels: CEN.

European Committee for Standardization (CEN) 2004b. *Eurocode 4: Design of composite steel and concrete structures – Part 1-1: General rules and rules for buildings* (BS EN 1994-1-1). Brussels: CEN.

European Committee for Standardization (CEN) 2005. *Eurocode 4: Design of composite steel and concrete structures – Part 2: General rules and rules for bridges* (BS EN 1994-2). Brussels: CEN.

- Fang, J., Zhou, L., Fan, J., Dai, C., Li, F., & Liao, F. 2024a. Shear behavior of perforated steel plate shear connectors in innovative modular steel channel–concrete composite floor systems. *Thin-Walled Structures*, 197, 111626.
- Fang, J., Zhou, L., Shi, J., Dai, C., Li, F., & Liao, F. 2024b. Flexural behavior of modular steel channel–concrete composite floor systems with bolted connections. *Engineering Structures*, 300, 117217.
- Fang, J., Zhou, L., Zhu, Y., Li, F., Dai, C., Zhou, Q., & Liao, F. 2023. Experimental study on flexural behavior of modular prefabricated channel–concrete composite beams with dry connections. *Journal of Building Engineering*, 68, 106194.
- Ferreira, F.P.V., Tsavdaridis, K.D., Martins, C.H. and De Nardin, S. 2021. Steel-Concrete Composite Beams with Precast Hollow-Core Slabs: A Sustainable Solution. *Sustainability*. 13, 4230.
- Figueiredo Filho, D.B., Júnior, J.A.S. and Rocha, E.C. 2011. What is R² all about?. *Leviathan (São Paulo)*, (3), pp.60-68.
- Forterra. 2020. *Hollowcore Load-Span Tables*. [Online]. Available from: <https://www.forterra.co.uk/wp-content/uploads/2020/12/Hollowcore-Loadspan-Tables-V3-3.pdf>
- FP McCann. 2021. *Precast Flooring Solutions*. [Online]. Available from: https://fpmccann.co.uk/wp-content/uploads/2021/06/Flooring_2022_v5.1.pdf
- Ganesan, N., Abraham, R., Raj, S.D. and Sasi, D. 2014. Stress–strain behaviour of confined geopolymer concrete. *Construction and Building Materials*. 73, pp.326-331.
- Genikomsou, A.S. and Polak, M.A. 2015. Finite element analysis of punching shear of concrete slabs using damaged plasticity model in ABAQUS. *Engineering Structures*. 98, pp.38-48.
- Gorkum, C.V. 2010. *CO₂ emissions and energy consumption during the construction of concrete structures*. Delft University of Technology, Holland, pg, 1-143.
- Grand View Research, 2024. *UK Geopolymer Concrete Market Outlook Report 2024–2030*. [Online] Available from:

<https://www.grandviewresearch.com/horizon/outlook/geopolymer-concrete-market/uk> [Accessed: May 2024].

- Grant, J.A., Fisher, J.W. and Slutter, R.G. 1977. Composite beams with formed steel deck. *Engineering Journal*. 14(1).
- Grazieschi, G., Asdrubali, F. and Thomas, G. 2021. Embodied energy and carbon of building insulating materials: A critical review. *Cleaner Environmental Systems*. 2, 100032.
- Hahnel, G., Whyte, A. and Biswas, W.K. 2021. A comparative life cycle assessment of structural flooring systems in Western Australia. *Journal of Building Engineering*. 35, 102109.
- Hammond, G. and Jones, C.A. 2011. *BSRIA guide: Embodied Carbon The Inventory of Carbon*. Bracknell: BSRIA.
- Hardjito, D., Cheak, C.C. and Ing, C.H.L. 2008. Strength and setting times of low calcium fly ash-based geopolymer mortar. *Modern Applied Science*. 2(4), pp.3-11.
- Hawkins, N. 1973. The strength of stud shear connectors. *Institution of Engineers (Australia) Civ Eng Trans*. (1).
- Hawkins, N.M. and Ghosh, S.K. 2006. Shear strength of hollow-core slabs. *PCI Journal*. 51(1), pp.110-114.
- Heath, A., Paine, K., Goodhew, S., Ramage, M., & Lawrence, M. 2013. The potential for using geopolymer concrete in the UK. *Proceedings of the Institution of Civil Engineers-Construction Materials*, 166(4), 195-203.
- Hechler, O. and Braun, M. 2010. New structural concepts in high-rise building, *Highrise towers and tall buildings 2010: Design and construction of safe and sustainable highrise structures*. In: International Conference at the Technische Universität München. Overseas Publishers Association.
- Hechler, O., Braun, M., Obiala, R., Kuhlmann, U., Eggert, F. and Hauf, G. 2013. CoSFB—Composite Slim-Floor Beam: Experimental Test Campaign and Evaluation. In: *Composite Construction in Steel and Concrete VII*, 28-31 July 2013, Palm Cove, North Queensland, Australia. American Society of Civil Engineers.

- Hegger, J., Roggendorf, T. and Kerkeni, N. 2009. Shear capacity of prestressed hollow core slabs in slim floor constructions. *Engineering Structures*. 31(2), pp.551-559.
- Hicks, S. 2003. Current trends in modern floor construction. *New Steel Construction*. 11(1), pp.32-33.
- Hill, C., Norton, A. and Dibdiakova, J. 2018. A comparison of the environmental impacts of different categories of insulation materials. *Energy and Buildings*. 162, pp.12-20.
- Hillerborg, A. 1985. The theoretical basis of a method to determine the fracture energy G_F of concrete. *Materials and Structures*. 18, pp.291-296.
- Hjulsbro Steel AB. 2020. *Environmental Product Declaration for PC-strand – Prestressed steel for reinforcement of concrete. In accordance with ISO 14025 and EN 15804:2012+A2:2019*. EPD-IES-0002400:002 (S-P-02400). [Online]. Available from: <https://www.hjulsbrosteel.com/>
- Hosseinpour, E., Baharom, S., Badaruzzaman, W.H.W. and Al Zand, A.W. 2018. Push-out test on the web opening shear connector for a slim-floor steel beam: Experimental and analytical study. *Engineering Structures*. 163, pp.137-152.
- Huang, Y., Spray, A. and Parry, T. 2013. Sensitivity analysis of methodological choices in road pavement LCA. *The International Journal of Life Cycle Assessment*. 18, pp.93-101.
- Huo, B. 2012. *Experimental and analytical study of the shear transfer in composite shallow cellular floor beams*. PhD thesis, City University London.
- Hussein, Z.M., Khalil, W.I. and Ahmed, H.K. 2018. Structural behavior of sustainable Hollow Core Slabs reinforced with hybrid fibers. *ARPJ Journal of Engineering and Applied Sciences*. 13(24), pp.9328-9334.
- International Federation for Structural Concrete (*fib*). 2000. *Special Design Considerations for Precast Prestressed Hollow Core Floors*. *fib*.
- International Federation for Structural Concrete (*fib*). 2013. *fib Model Code for Concrete Structures 2010*. Ernst & Sohn. ISBN 978-3-433-03061-5.
- International Organization for Standardization (ISO). 2006a. *Environmental management - Life cycle assessment - Principles and framework* (BS EN ISO 14040). Geneva: ISO.

- International Organization for Standardization (ISO). 2006b. *Environmental management - Life cycle assessment - Requirements and guidelines*. Brussels (BS EN ISO 14044). Geneva: ISO.
- International Organization for Standardization (ISO). 2019. *Metallic materials – Tensile testing – Part 1: Method of test at room temperature* (BS EN ISO 6892-1). Geneva: ISO.
- Jaillon, L. and Poon, C.S. 2008. Sustainable construction aspects of using prefabrication in dense urban environment: a Hong Kong case study. *Journal of Construction Management and Economics*. 26(9), pp.953-966.
- Jang, H.J., Ahn, Y.H. and Tae, S.H. 2022. Proposal of major environmental impact categories of construction materials based on life cycle impact assessments. *Materials*. 15(14), 5047.
- Johnson, R., Oehlers, D. and BS. 1981. Analysis and design for longitudinal shear in composite T-beams. *Proceedings of the Institution of Civil Engineers*. 71(4), pp.989-1021.
- Komnitsas, K., Zaharaki, D. and Perdikatsis, V. 2007. Geopolymerisation of low calcium ferronickel slags. *Journal of Materials Science*. 42(9), pp.3073-3082.
- Kuhlmann, U. and Breuninger, U. 2002. Behaviour of horizontally lying studs with longitudinal shear force. *Composite Construction in Steel and Concrete IV*. pp.438-449.
- Kuhlmann, U. and Kürschner, K. 2006. Structural behaviour of horizontally lying shear studs. *Composite Construction in Steel and Concrete V*. pp.534-543.
- Kurda, R., Silvestre, J.D. and De Brito, J. 2018. Life cycle assessment of concrete made with high volume of recycled concrete aggregates and fly ash. *Resources, Conservation and Recycling*. 139, pp.407-417.
- Kyriakopoulos, P., Peltonen, S., Spyrakos, C., & Vayas, I. 2022. Experimental and Analytical Investigation of Shallow Floor Composite Beams under Extreme Deformation. *Journal of Structural Engineering*, 149(2), 04022213.
- Kyriakopoulos, P., Peltonen, S., Vayas, I., Spyrakos, C., & Leskelä, M. 2021. Experimental and numerical investigation of the flexural behavior of shallow floor composite beams. *Engineering Structures*, 231, 111734.

- Kwasny, J., McGrath, T., Lawther, S., Soutsos, M., Sha, W., Cox, S., Chen, J. F., and Lopes, R. F. C. .2019. Lagoon fly ash: A potential source of the precursor for geopolymer binders. In *EuroCoalAsh 2019* (pp. 322-333).
- Lawson, M., Beguin, P., Obiala, R. and Braun, M. 2015. Slim-floor construction using hollow-core and composite decking systems. *Steel Construction*. 8(2), pp.85-89.
- Lawson, R., Bode, H., Brekelmans, J., Wright, P. and Mullett, D. 1999. *Slimflor and slimdek construction: European developments*.
- Lawson, R.M., Mullett, D.L. and Rackham, J. 1997. *Design of asymmetric slimflor beams using deep composite decking*. Berkshire: Steel Construction Institute.
- Li, X., Zhu, Y. and Zhang, Z. 2010. An LCA-based environmental impact assessment model for construction processes. *Building and Environment*. 45(3), pp.766-775.
- Limazie, T. and Chen, S. 2017. Effective shear connection for shallow cellular composite floor beams. *Journal of Constructional Steel Research*. 128, pp.772-788.
- Longley. 2019. *Hollowcore Precast Flooring*. [Online]. Available from: <https://www.longley.uk.com/wp-content/uploads/2014/09/4pp-Hollowcore-Precast-Flooring-Leaflet-NOV-2019-WEB-1.pdf>
- López-Mesa, B., Pitarch, Á., Tomás, A. and Gallego, T. 2009. Comparison of environmental impacts of building structures with in situ cast floors and with precast concrete floors. *Building and Environment*. 44(4), pp.699-712.
- Majdub, M.S., Baharom, S., Al Zand, A.W., Mutalib, A.A. and Hosseinpour, E. 2022. Innovation of Shear Connectors in Slim Floor Beam Construction. *Journal of Engineering*. 2022.
- Malhotra, V.M. 2000. Role of supplementary cementing materials in reducing greenhouse gas emissions. In: *Concrete technology for a sustainable development in the 21st century*. 5, pp.6.
- Maraveas, C. 2017. Fire resistance of DELTABEAM® composite beams: a numerical investigation. *Journal of Structural Fire Engineering*, 8(4), 338-353.

- Masson-Delmotte, V., Zhai, P., Pirani, A., Connors, S.L., Pean, C., Berger, S., Zhou, B., et al. 2021. *IPCC, 2021: Climate Change 2021: The Physical Science Basis*. Contribution of Working Group I to the Sixth Assessment Report of the Intergovernmental Panel on Climate Change.
- Mateus, R. and Bragança, L. 2011. Sustainability assessment and rating of buildings: Developing the methodology SBToolPT–H. *Building and Environment*. 46(10), pp.1962-1971.
- Mateus, R., Neiva, S., Bragança, L., Mendonça, P. and Macieira, M. 2013. Sustainability assessment of an innovative lightweight building technology for partition walls–comparison with conventional technologies. *Building and Environment*. 67, pp.147-159.
- Meyer, C. 2009. The greening of the concrete industry. *Journal of Cement and Concrete Composites*. 31(8), pp.601-605.
- Mones, R.M. and Breña, S.F. 2013. Hollow-core slabs with cast-in-place concrete toppings: A study of interfacial shear strength. *PCI Journal*. 58(3), pp.124-141.
- Mullett, D.L. 1992. *Slim Floor Design and Construction*. The Steel Construction Institute.
- Mullett, D.L. 1998. *Composite Floor System*. Blackwell Science Ltd.
- Nath, P. and Sarker, P.K. 2014. Effect of GGBFS on setting, workability and early strength properties of fly ash geopolymer concrete cured in ambient condition. *Construction and Building Materials*. 66, pp.163-171.
- Nethercot, D. 2003. *Composite construction*. Boca Raton, FL: CRC Press.
- Neupane, K. 2016. Fly ash and GGBFS based powder-activated geopolymer binders: A viable sustainable alternative of portland cement in concrete industry. *Mechanics of Materials*. 103, pp.110-122.
- Nicholson, A.L., Olivetti, E.A., Gregory, J.R., Field, F.R. and Kirchain, R.E. 2009. End-of-life LCA allocation methods: Open loop recycling impacts on robustness of material selection decisions. In: *2009 IEEE international symposium on sustainable systems and technology*, pp.1-6.

- Ollgaard, J.G., Slutter, R.G. and Fisher, J.W. 1971. Shear strength of stud connectors in lightweight and normal weight concrete. *AISC Engineering Journal*. April, pp.71-10.
- Orr, J., Gibbons, O. and Arnold, W. 2020. *How to calculate embodied carbon v1.0*. IStructE.
- PEIKKO. 2014. *DELTABEAM Slim Floor Structure - Technical Manual*. Lahti, Finland.
- Peltonen, S. and Leskelä, M.V. 2006. Connection behaviour of a concrete dowel in a circular web hole of a steel beam. *Composite Construction in Steel and Concrete V*. pp.544-552.
- Pereira Júnior, S. E., Ferreira, F. P. V., Tsavdaridis, K. D., & De Nardin, S. 2023. Flexural behavior of steel–concrete ultra-shallow floor beams (USFBs) with precast hollow-core slabs. *Engineering Structures*, 278, 115524.
- Provis, J.L., 2018. Alkali-activated materials. *Cement and Concrete Research*, 114, pp.40–48.
- Provis, J.L. and Van Deventer, J.S.J., 2014. *Alkali Activated Materials: State-of-the-Art Report, RILEM TC 224-AAM*. Dordrecht: Springer Netherlands. [Online]. Available from: <https://doi.org/10.1007/978-94-007-7672-2>
- Qureshi, J. and Lam, D. 2012. Behaviour of headed shear stud in composite beams with profiled metal decking. *Advances in Structural Engineering*. 15(9), pp.1547-1558.
- Rackham, J.W., Hicks, S.J. and Newman, G.M. 2006. *Design of Asymmetric Slimflor Beams with Precast Concrete Slabs*. The Steel Construction Institute.
- Rahman, M.K., Baluch, M.H., Said, M.K. and Shazali, M.A. 2012. Flexural and shear strength of prestressed precast hollow-core slabs. *Arabian Journal for Science and Engineering*. 37, pp.443-455.
- Rey-Álvarez, B., Sanchez-Montanes, B. and García-Martínez, A. 2022. Building material toxicity and life cycle assessment: A systematic critical review. *Journal of Cleaner Production*. 341, 130838.

- Ríos, J.D., Cifuentes, H., Martínez-De La Concha, A. and Medina-Reguera, F. 2017. Numerical modelling of the shear-bond behaviour of composite slabs in four and six-point bending tests. *Engineering Structures*. 133, pp.91-104.
- Ryu, G.S., Lee, Y.B., Koh, K.T. and Chung, Y.S. 2013. The mechanical properties of fly ash-based geopolymer concrete with alkaline activators. *Construction and Building Materials*. 47, pp.409-418.
- Salas, D.A., Ramirez, A.D., Ulloa, N., Baykara, H. and Boero, A.J. 2018. Life cycle assessment of geopolymer concrete. *Construction and Building Materials*. 190, pp.170-177.
- Sheehan, T., Dai, X. and Lam, D. 2018. Flexural behaviour of asymmetric composite beam with low degree of shear connection. *Journal of Constructional Steel Research*. 141, pp.251-261.
- Sheehan, T., Dai, X., Yang, J., Zhou, K. and Lam, D. 2019. Flexural behaviour of composite slim floor beams. *Structures*. 21, pp.22-32.
- Simms, W.I. and Hughes, A.F. 2011. *Composite Design of Steel Framed Buildings*. SCI publication P359. The Steel Construction Institute.
- Sjunnesson, J. 2005. *Life Cycle Assessment of Concrete*. Lund University, Lund, Sweden: Department of Technology and Society, Environmental and Energy Systems Studies.
- Slutter, R.G. and Driscoll, G.C. 1965. Flexural strength of steel and concrete composite beams.
- Suwan, T. 2016. *Development of self-cured geopolymer cement*. PhD Thesis. Brunel University London.
- Thannimalay, L., Yusoff, S. and Zawawi, N.Z. 2013. Life cycle assessment of sodium hydroxide. *Aust. J. Basic Appl. Sci.* 7(2), pp.421-431.
- Topçu, I.B., Toprak, M.U. and Uygunoğlu, T. 2014. Durability and microstructure characteristics of alkali activated coal bottom ash geopolymer cement. *Journal of Cleaner Production*. 81, pp.211-217.
- Tsavdaridis, K.D., D'Mello, C. and Hawes, M. 2009. Experimental Study of Ultra Shallow Floor Beams with Perforated Steel Sections. In: *Nordic Steel 09, 2-4 September 2009*, Malmo, Sweden. Nordic Steel, pp.312-319.

- Tsavdaridis, K.D., D'Mello, C. and Huo, B.Y. 2013. Experimental and computational study of the vertical shear behaviour of partially encased perforated steel beams. *Engineering Structures*. 56, pp.805-822.
- Tsavdaridis, K. D., McKinley, B., Kacaroglu, B. N., Corfar, D. A., & Lawson, R. M. 2024. Bending test of long-span ultra-shallow floor beam (USFB) with two lightweight concretes. *Structures*, 66, 106895.
- UK Export Finance. 2021. *Climate Change Strategy, 2021-2024*. pp.1-26.
- UNFCCC. 1997. *Kyoto Protocol to the United Nations Framework Convention on Climate Change*. Kyoto, FCCC/CP/1997/L.7/Add.1, pp.1-24.
- UNFCCC. 2012. *Doha amendment to the Kyoto Protocol*. Doha, pp.1-6.
- UNFCCC. n.d. What is the United Nations Framework Convention on Climate Change? *United Nations Climate Change*. [Online]. Available from: <https://unfccc.int/process-and-meetings/what-is-the-united-nations-framework-convention-on-climate-change>
- Valente, I.B. and Cruz, P.J. 2009. Experimental analysis of shear connection between steel and lightweight concrete. *Journal of Constructional Steel Research*. 65(10-11), pp.1954-1963.
- Van den Heede, P. and De Belie, N. 2012. Environmental impact and life cycle assessment (LCA) of traditional and 'green' concretes: Literature review and theoretical calculations. *Cement and Concrete Composites*. 34(4), pp.431-442.
- Vukotic, L., Fenner, R.A. and Symons, K. 2010. Assessing embodied energy of building structural elements. In: *Proceedings of the Institution of Civil Engineers-Engineering Sustainability*. 163(3), pp.147-158.
- Wang, Y., Yang, L., Shi, Y. and Zhang, R. 2009. Loading capacity of composite slim frame beams. *Journal of Constructional Steel Research*. 65(3), pp.650-661.
- Way, A.G.J., Cosgrove, T.C. and Brettle, M.E. 2007. *Precast Concrete Floors in Steel Framed Buildings*. The Steel Construction Institute.
- Wong, F. and Tang, Y.T. 2012. Comparative embodied carbon analysis of the prefabrication elements compared with in-situ elements in residential

- building development of Hong Kong. *International Journal of Civil and Environmental Engineering*. 6(2), pp.89-94.
- Xu, C., Sugiura, K., Wu, C. and Su, Q. 2012. Parametrical static analysis on group studs with typical push-out tests. *Journal of Constructional Steel Research*. 72, pp.84-96.
- Yan, J.B., Wang, J.Y., Liew, J.R. and Qian, X. 2016. Applications of ultra-lightweight cement composite in flat slabs and double skin composite structures. *Construction and Building Materials*. 111, pp.774-793.
- Yang, K.H., Song, J.K. and Song, K.I. 2013. Assessment of CO₂ reduction of alkali-activated concrete. *Journal of Cleaner Production*. 39, pp.265-272.
- Yee, A.A. 2001a. Social and environmental benefits of precast concrete technology. *PCI Journal*. 46(3), pp.14-19.
- Yee, A.A. 2001b. Structural and economic benefits of precast/prestressed concrete construction. *PCI Journal*. 46(4), pp.34-42.
- Zhang, H., Huang, W., Liu, B., Han, C., Li, Q., & Chen, C. 2022. Flexural behavior of precast concrete hollow-core slabs with high-strength tendons. *Journal of Building Engineering*, 59, 105050.
- Zhang, H., Li, L., Yuan, C., Wang, Q., Sarker, P. K., & Shi, X. 2020. Deterioration of ambient-cured and heat-cured fly ash geopolymer concrete by high temperature exposure and prediction of its residual compressive strength. *Construction and Building Materials*, 262, 120924.

Appendix A

LCA Study Detailed Inventory Results for Each Load/ Slab Span Scenario

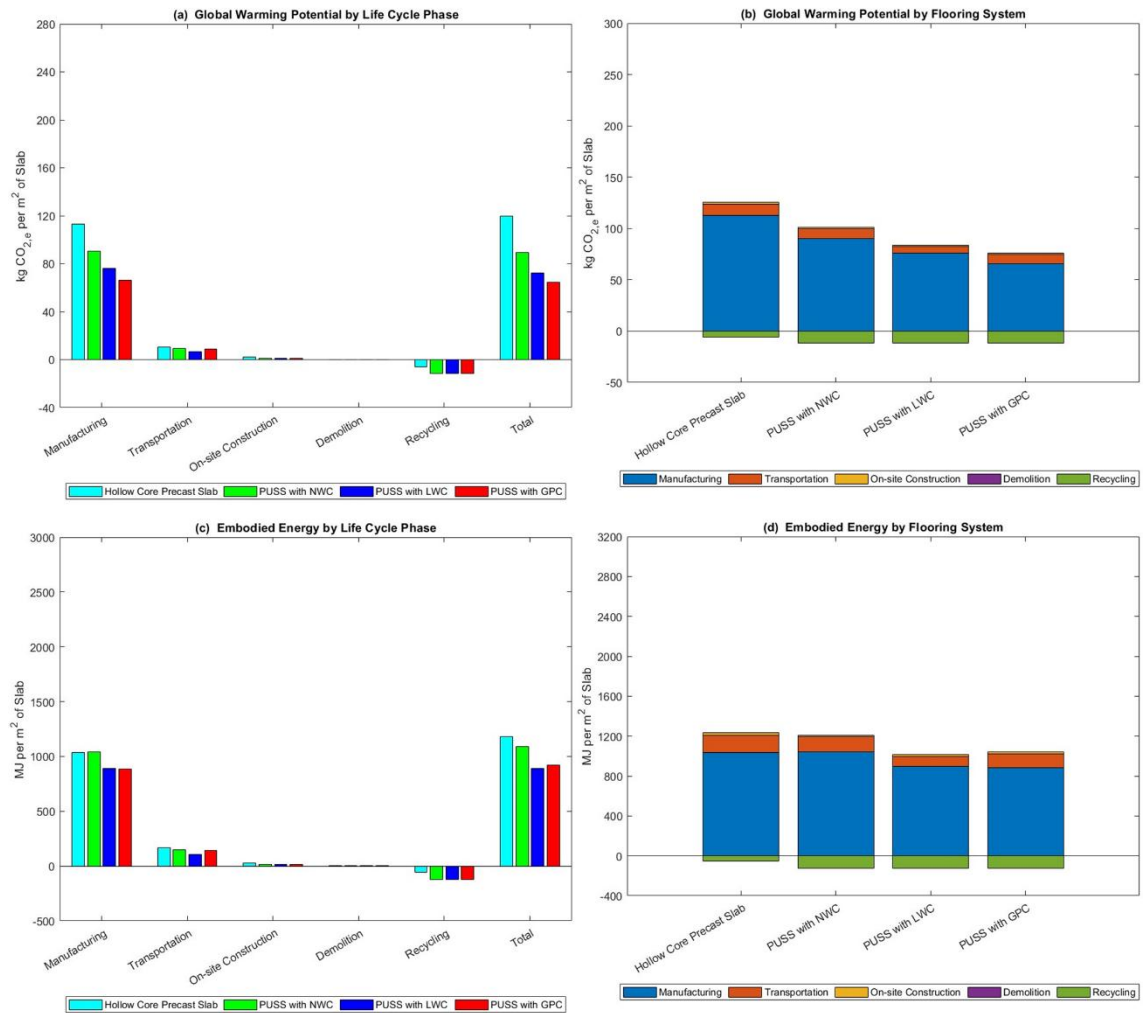


Figure A-1: Results for LL= 2 kN/m² & span= 6 m (a) GWP by life cycle stage (b) GWP by flooring system (c) EE by life cycle stage (d) EE by flooring system

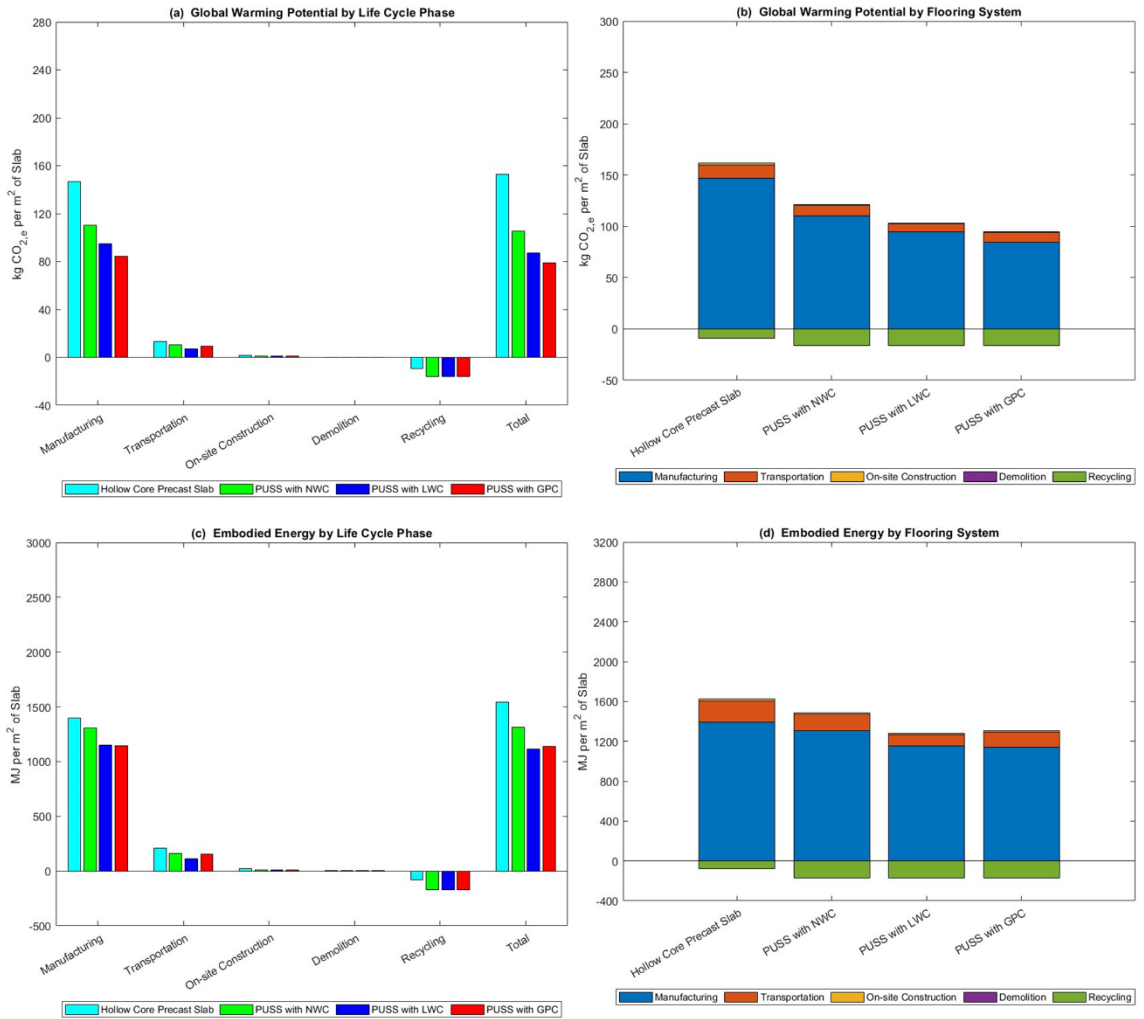


Figure A-2: Results for LL= 2 kN/m² & span= 8 m (a) GWP by life cycle stage (b) GWP by flooring system (c) EE by life cycle stage (d) EE by flooring system

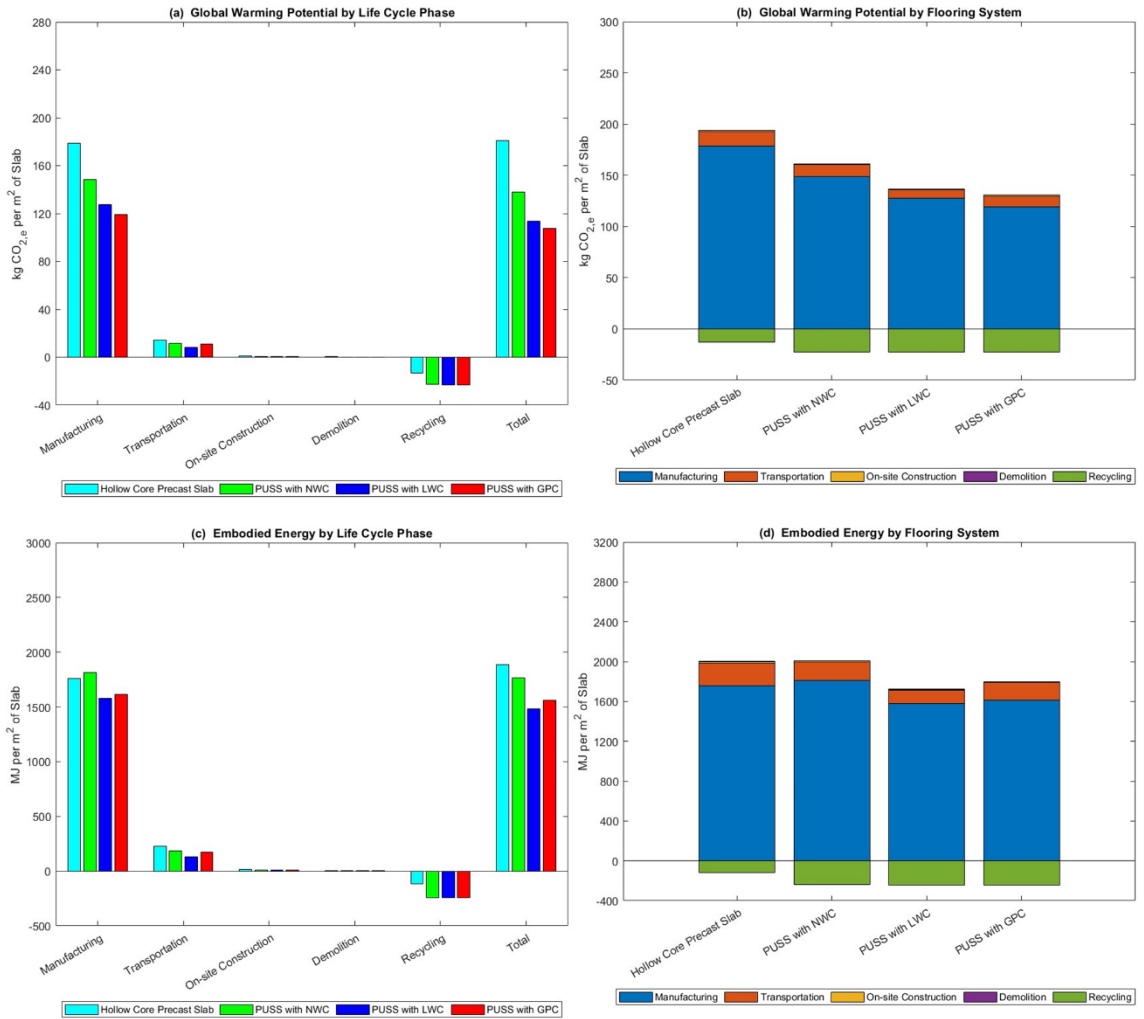


Figure A-3: Results for LL= 2 kN/m² & span= 10 m (a) GWP by life cycle stage (b) GWP by flooring system (c) EE by life cycle stage (d) EE by flooring system

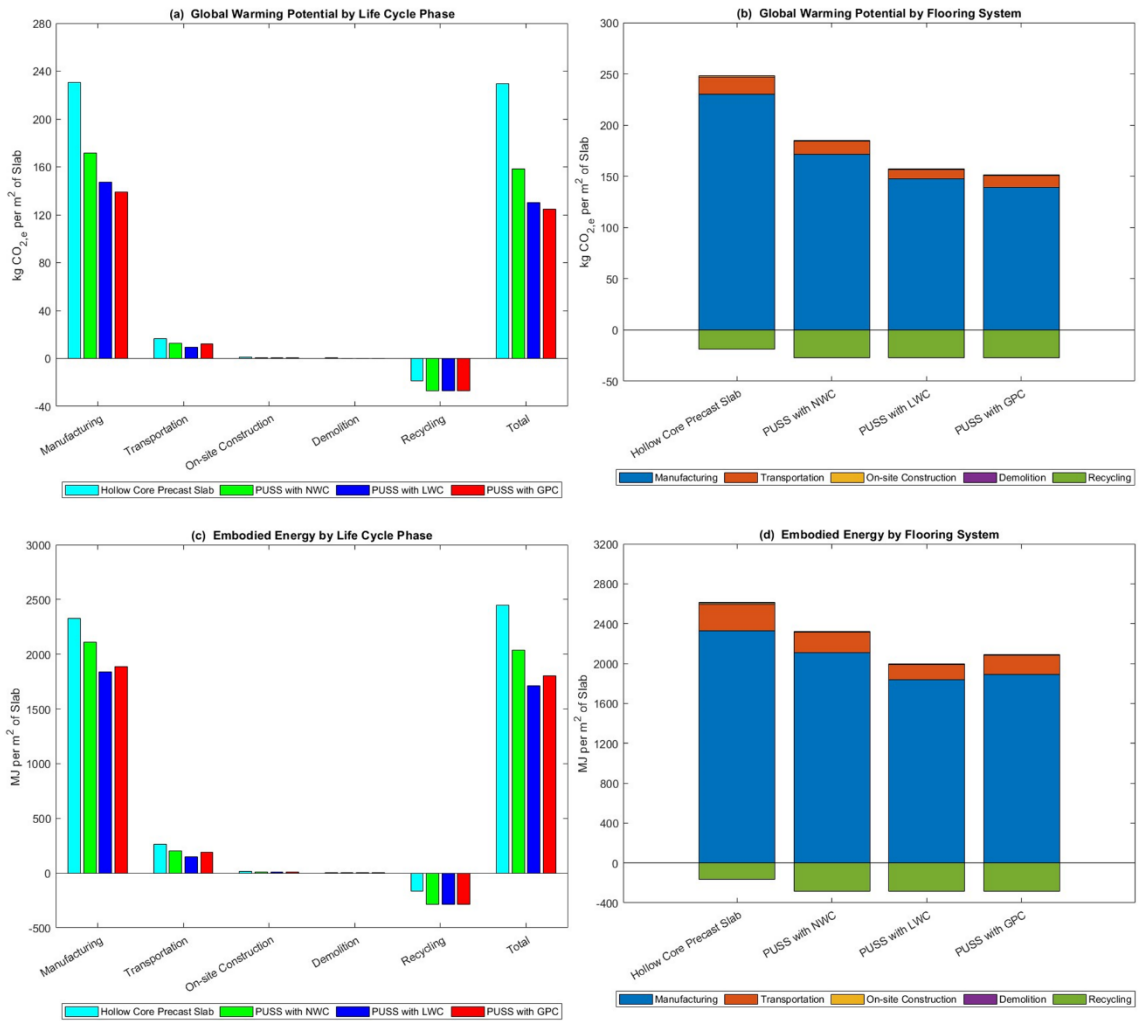


Figure A-4: Results for LL= 2 kN/m² & span= 12 m (a) GWP by life cycle stage (b) GWP by flooring system (c) EE by life cycle stage (d) EE by flooring system

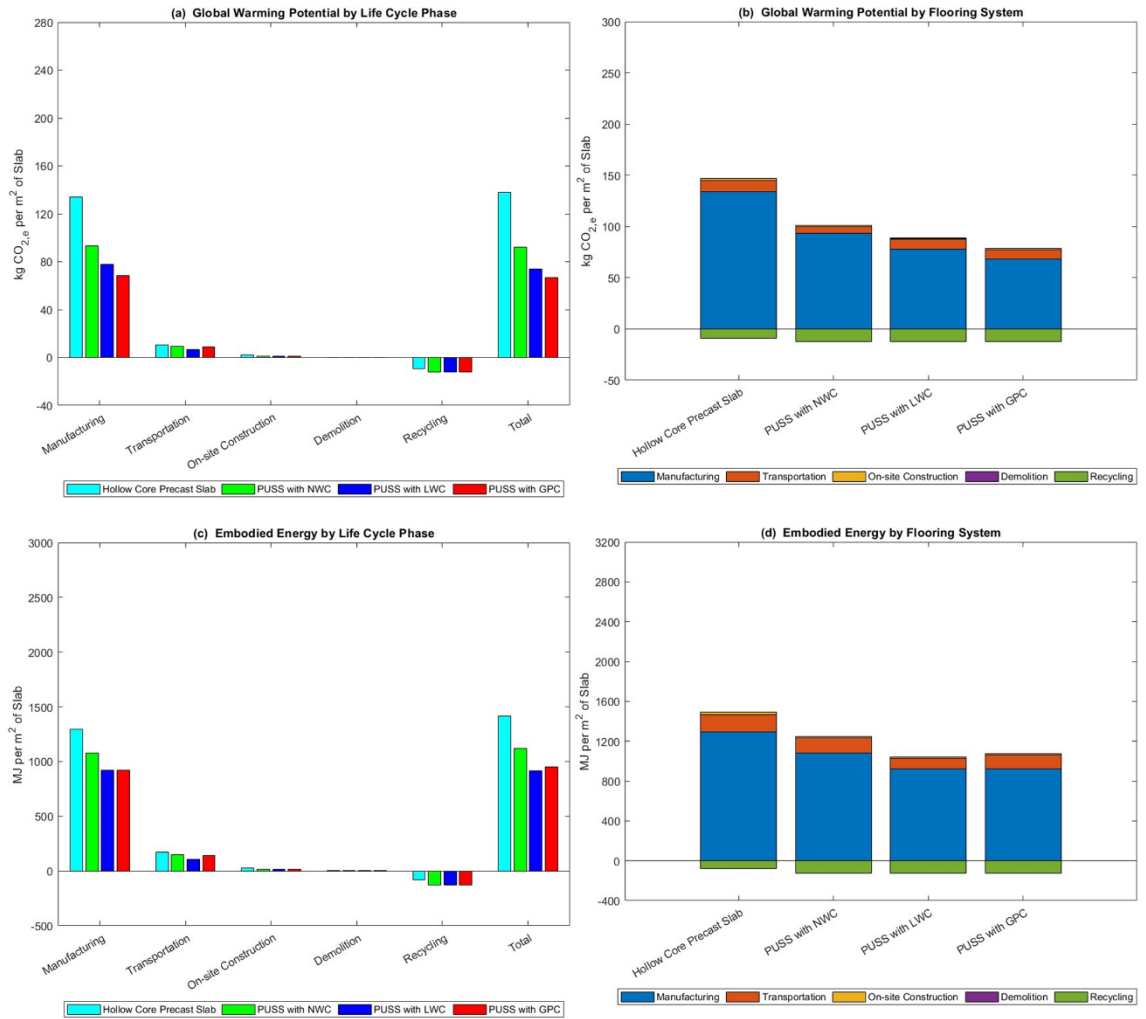


Figure A-5: Results for LL= 3 kN/m² & span= 6 m (a) GWP by life cycle stage (b) GWP by flooring system (c) EE by life cycle stage (d) EE by flooring system

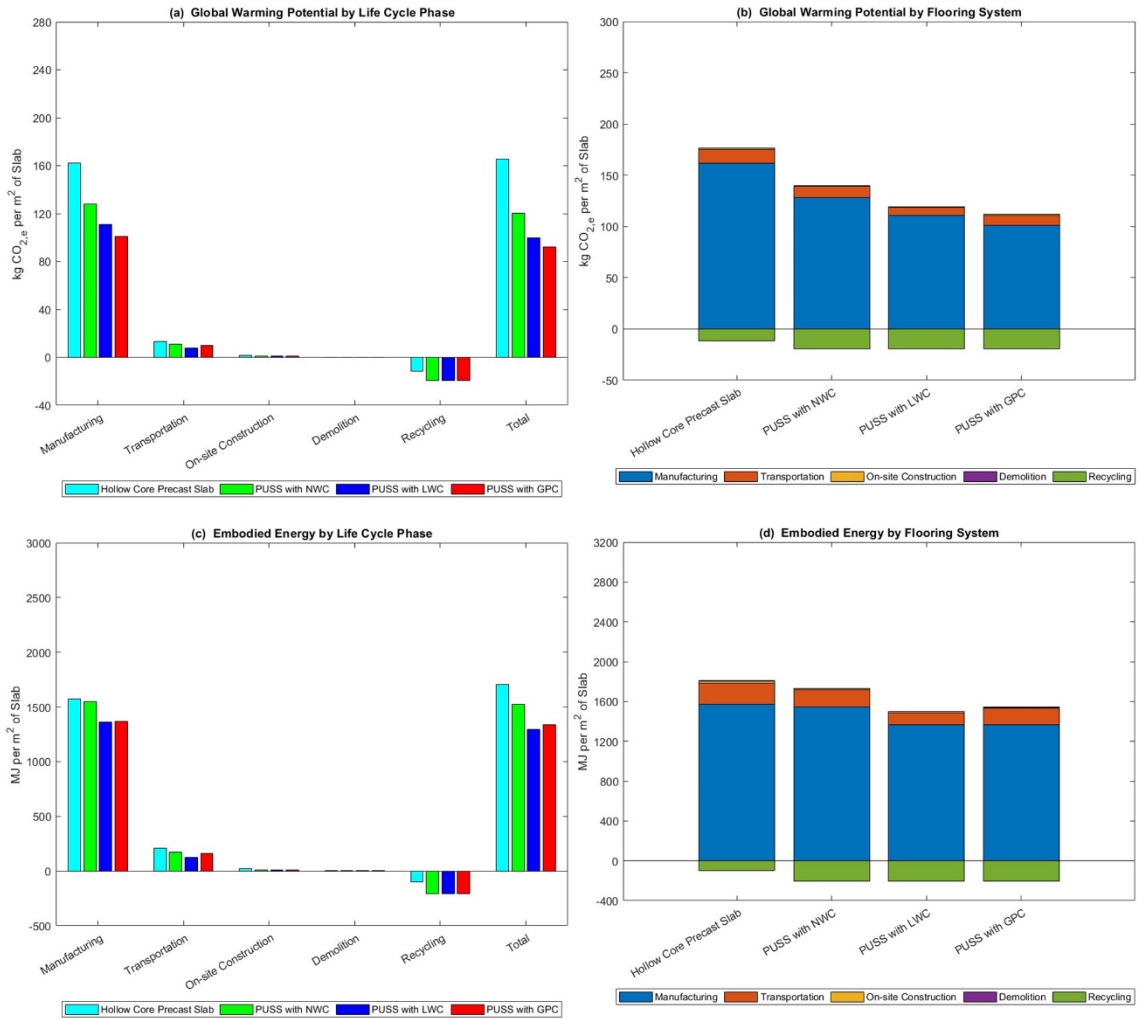


Figure A-6: Results for LL= 3 kN/m² & span= 8 m (a) GWP by life cycle stage (b) GWP by flooring system (c) EE by life cycle stage (d) EE by flooring system

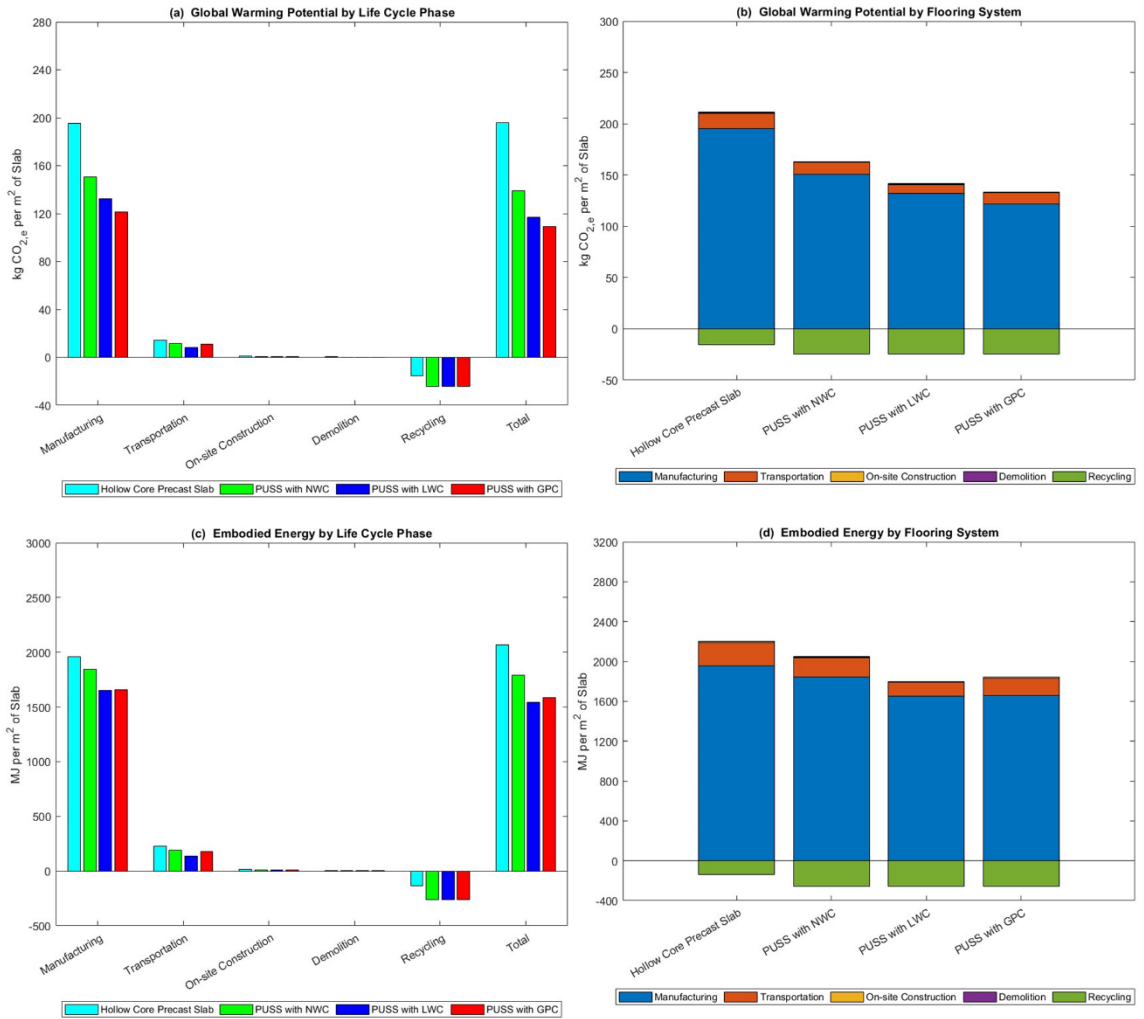


Figure A-7: Results for LL= 3 kN/m² & span= 10 m (a) GWP by life cycle stage (b) GWP by flooring system (c) EE by life cycle stage (d) EE by flooring system

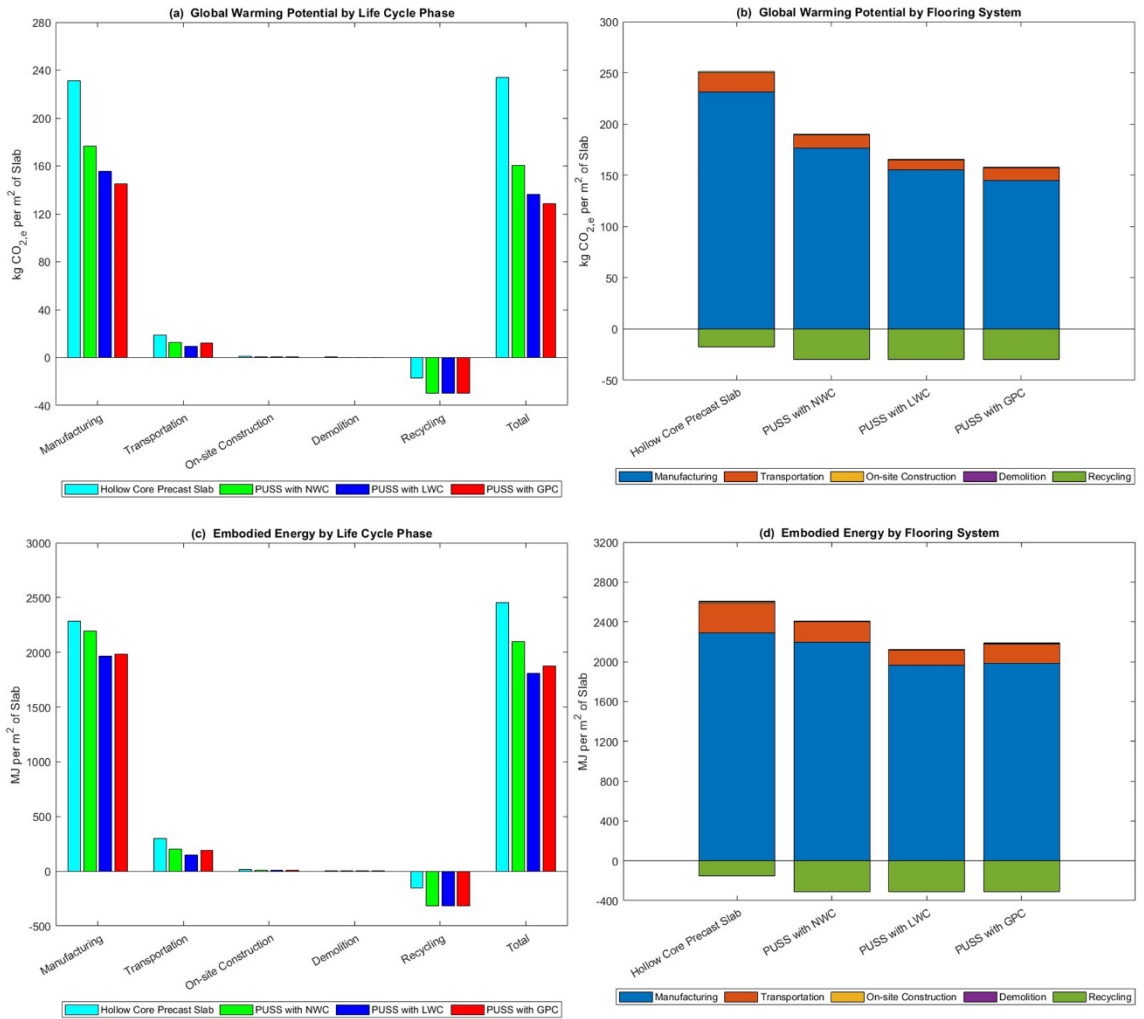


Figure A-8: Results for LL= 3 kN/m² & span= 12 m (a) GWP by life cycle stage (b) GWP by flooring system (c) EE by life cycle stage (d) EE by flooring system

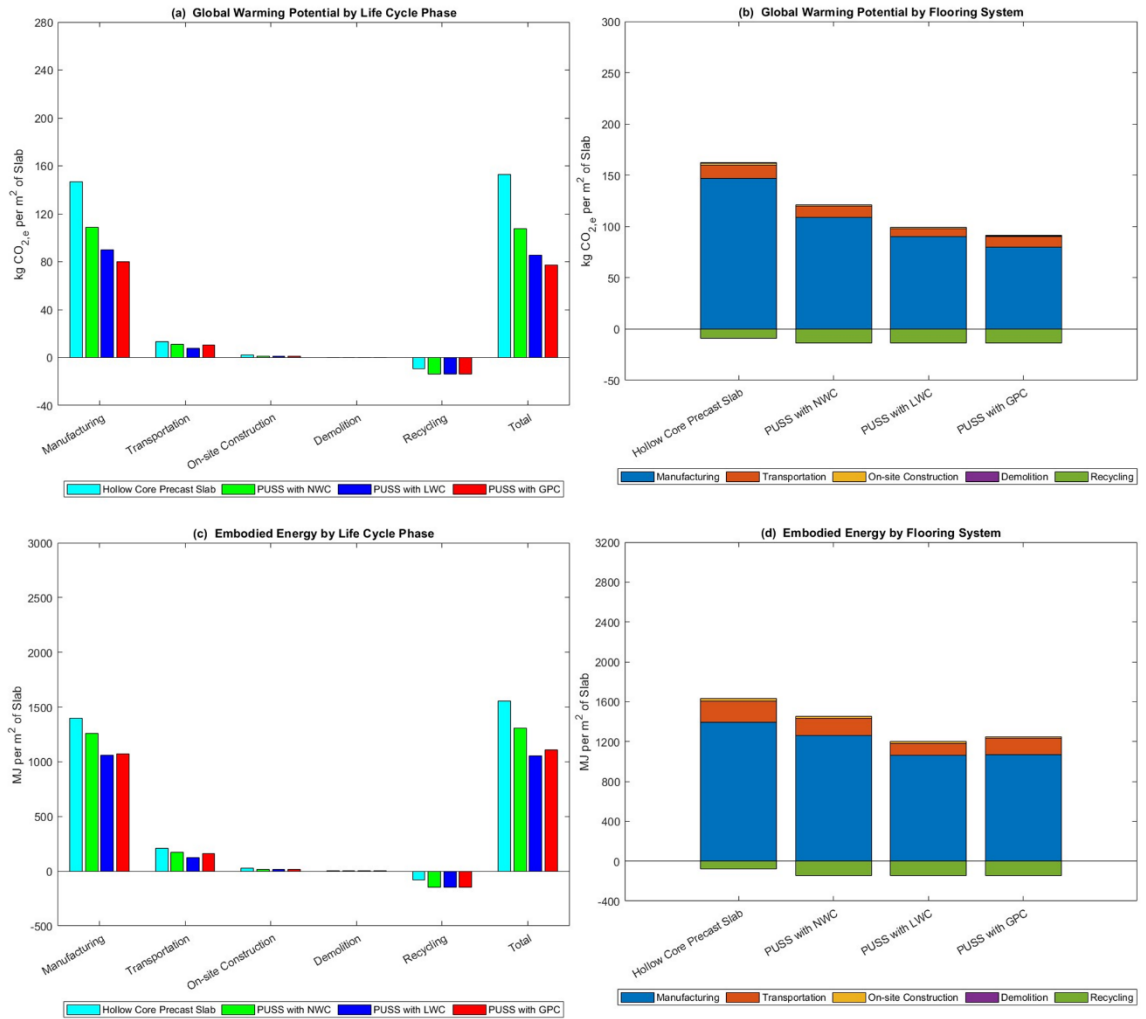


Figure A-9: Results for LL= 4 kN/m² & span= 6 m (a) GWP by life cycle stage (b) GWP by flooring system (c) EE by life cycle stage (d) EE by flooring system

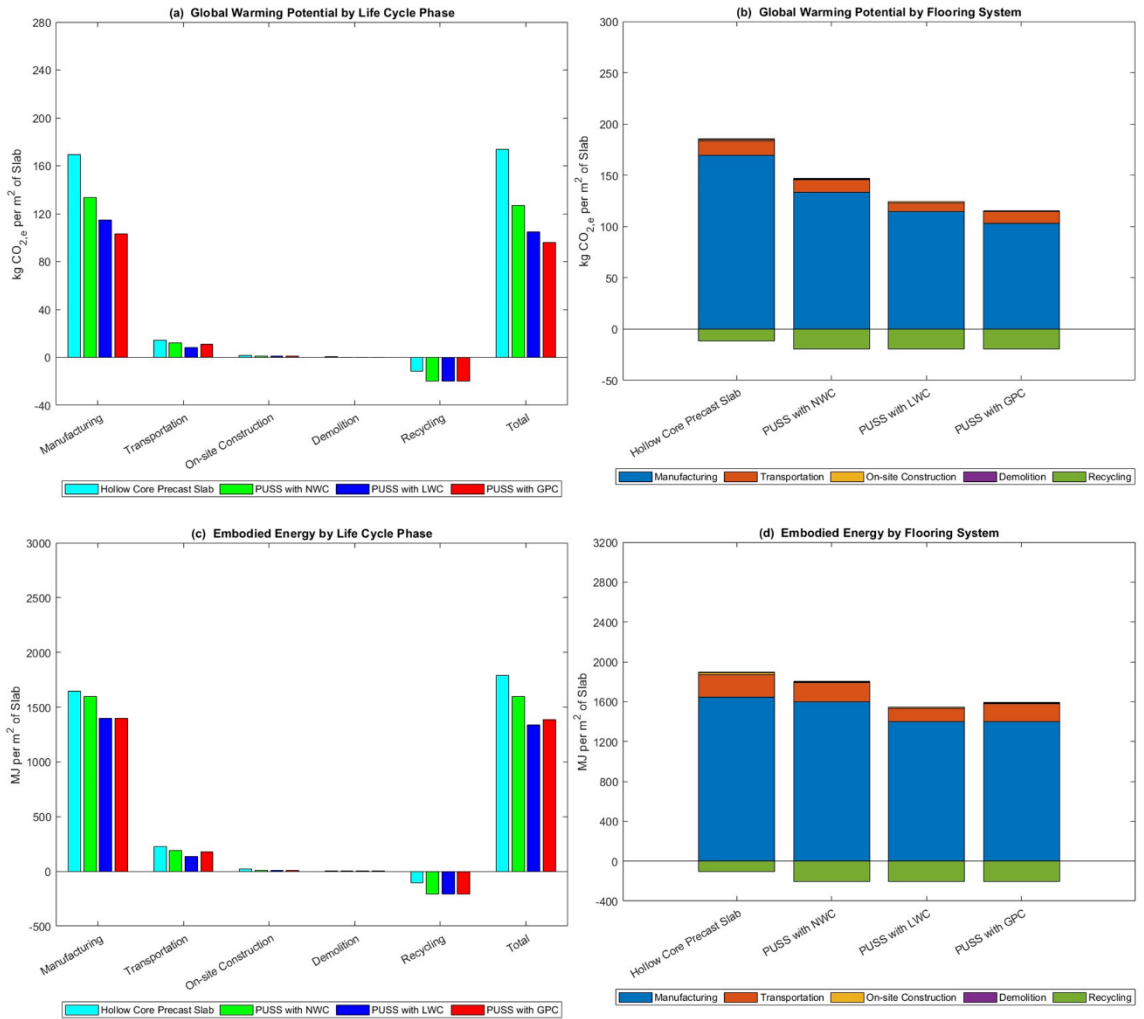


Figure A-10: Results for LL= 4 kN/m² & span= 8 m (a) GWP by life cycle stage (b) GWP by flooring system (c) EE by life cycle stage (d) EE by flooring system

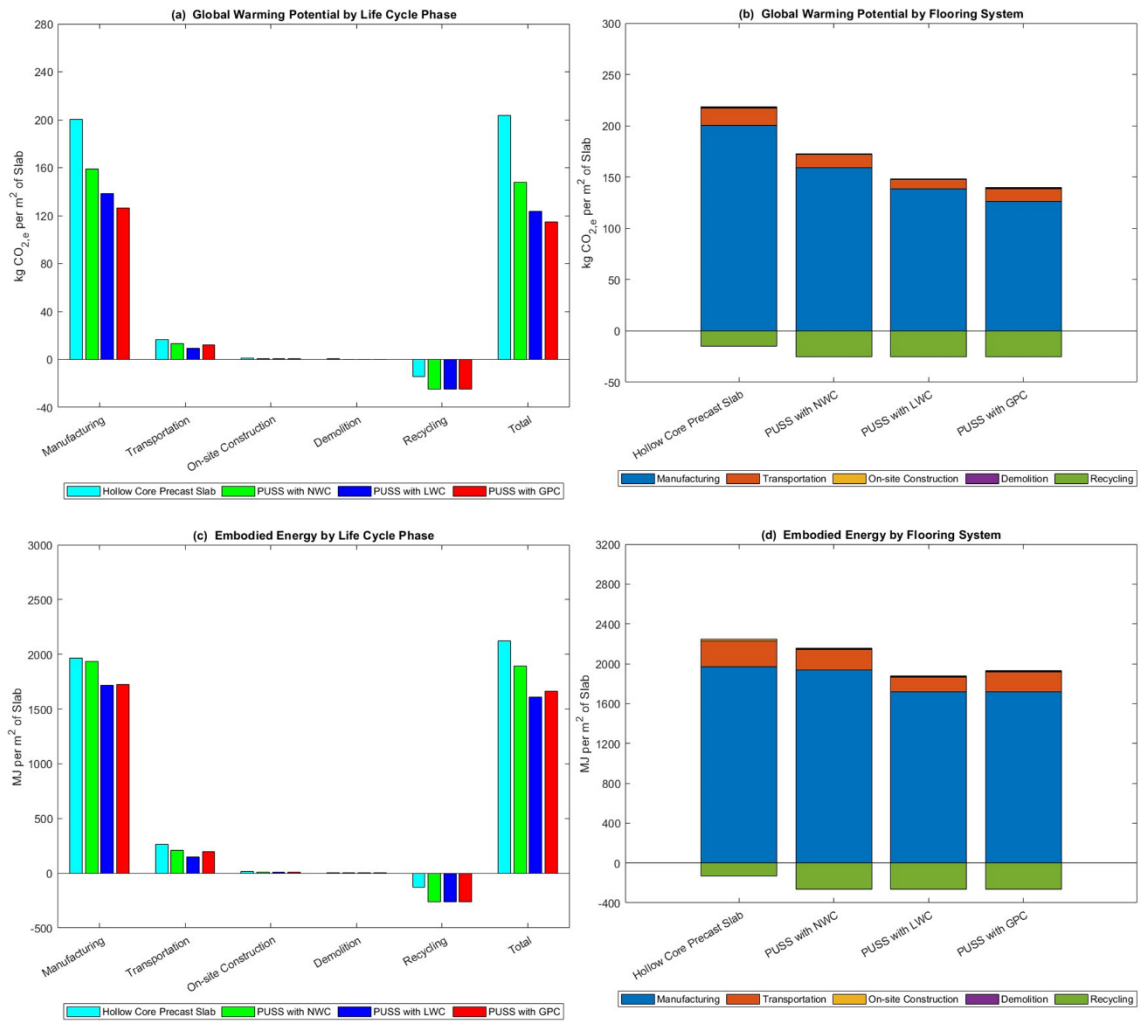


Figure A-11: Results for LL= 4 kN/m² & span= 10 m (a) GWP by life cycle stage (b) GWP by flooring system (c) EE by life cycle stage (d) EE by flooring system

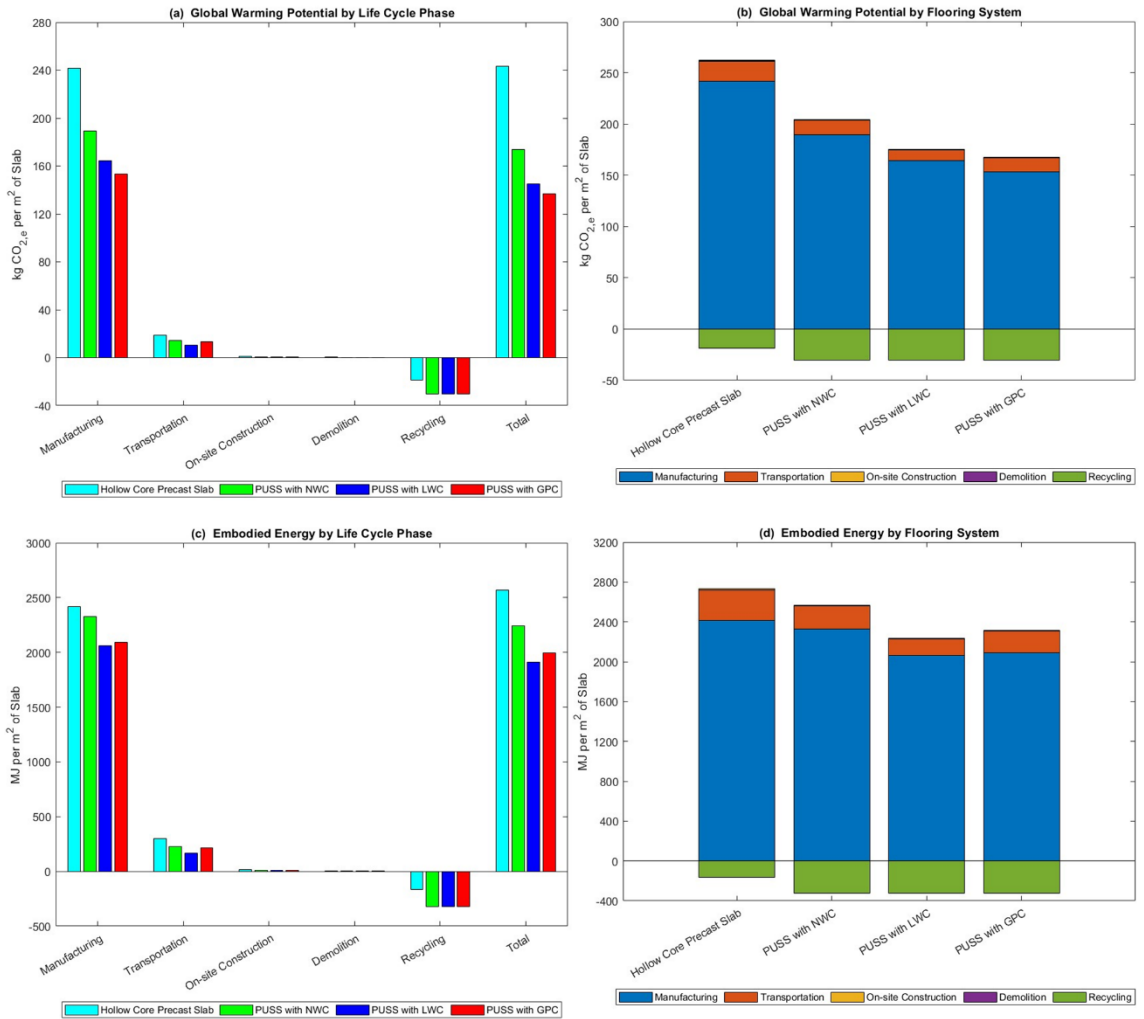


Figure A-12: Results for LL= 4 kN/m² & span= 12 m (a) GWP by life cycle stage (b) GWP by flooring system (c) EE by life cycle stage (d) EE by flooring system

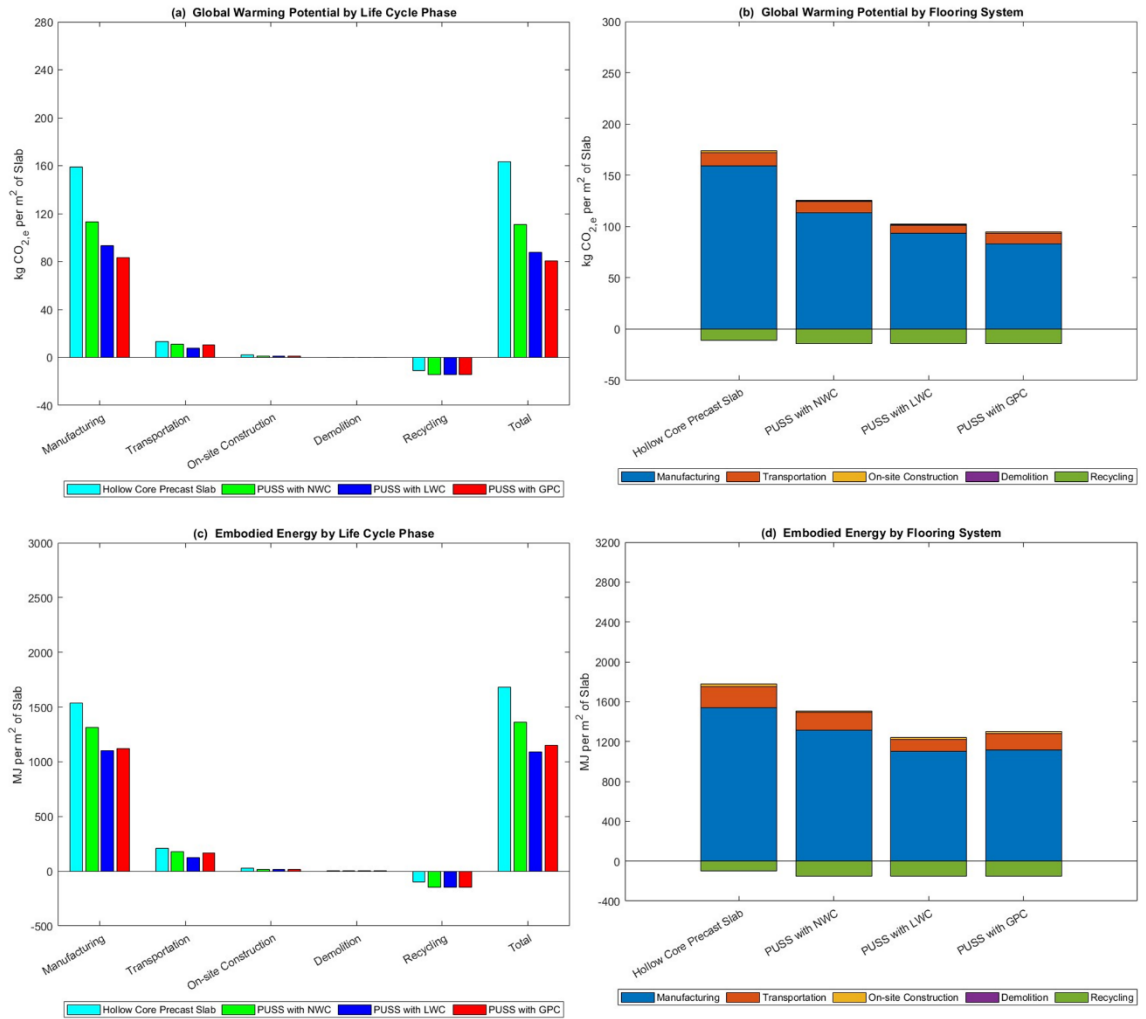


Figure A-13: Results for LL= 5 kN/m² & span= 6 m (a) GWP by life cycle stage (b) GWP by flooring system (c) EE by life cycle stage (d) EE by flooring system

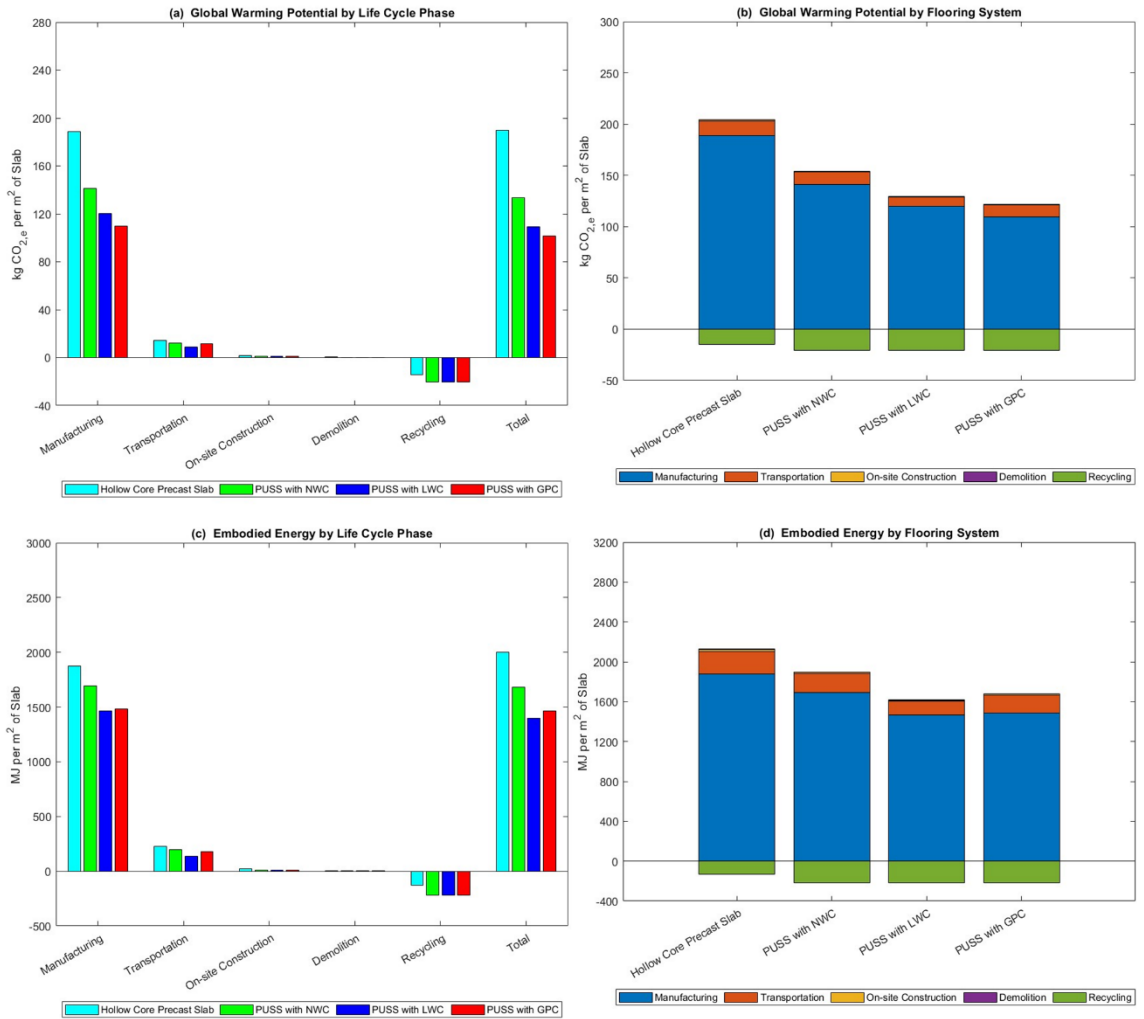


Figure A-14: Results for LL= 5 kN/m² & span= 8 m (a) GWP by life cycle stage (b) GWP by flooring system (c) EE by life cycle stage (d) EE by flooring system

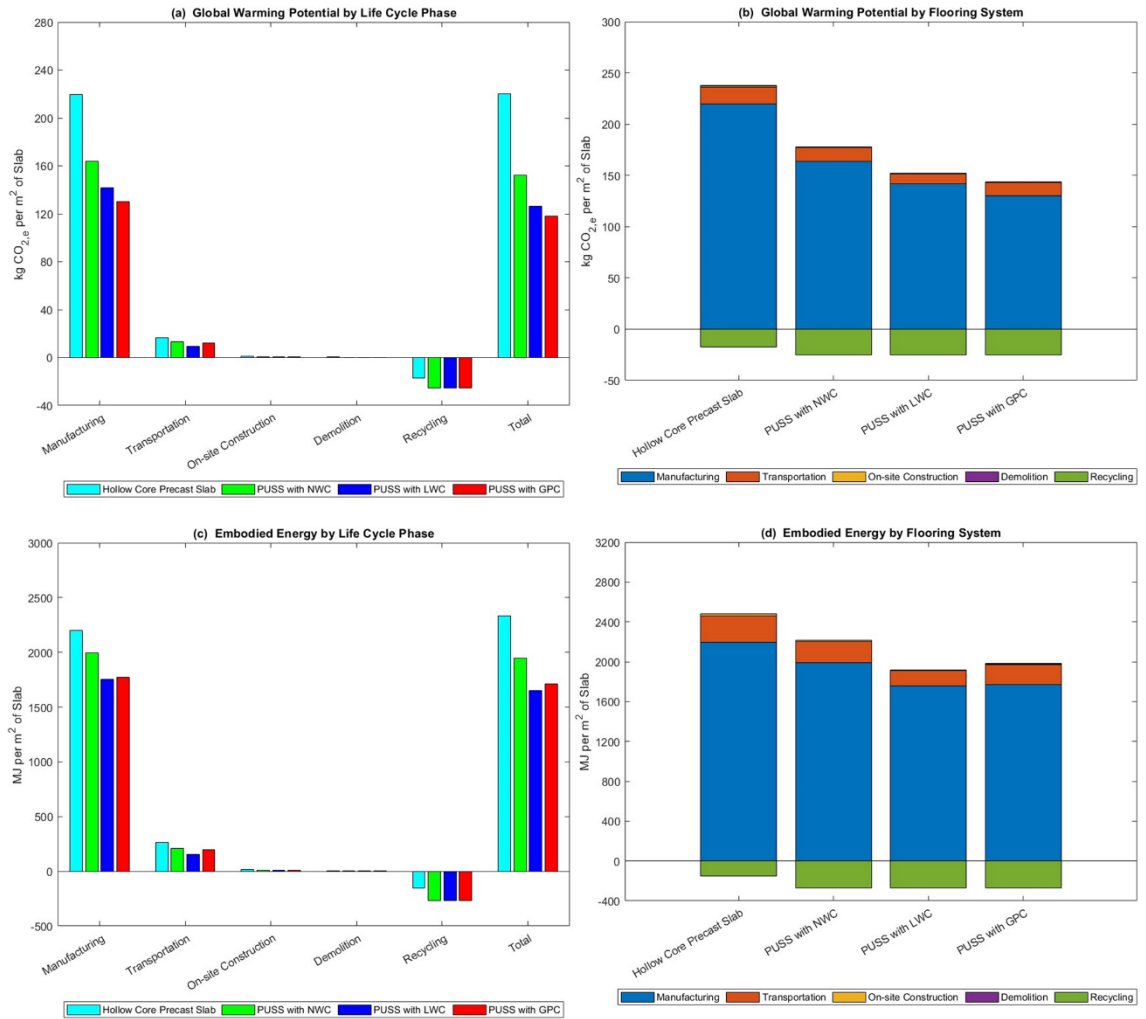


Figure A-15: Results for LL= 5 kN/m² & span= 10 m (a) GWP by life cycle stage (b) GWP by flooring system (c) EE by life cycle stage (d) EE by flooring system

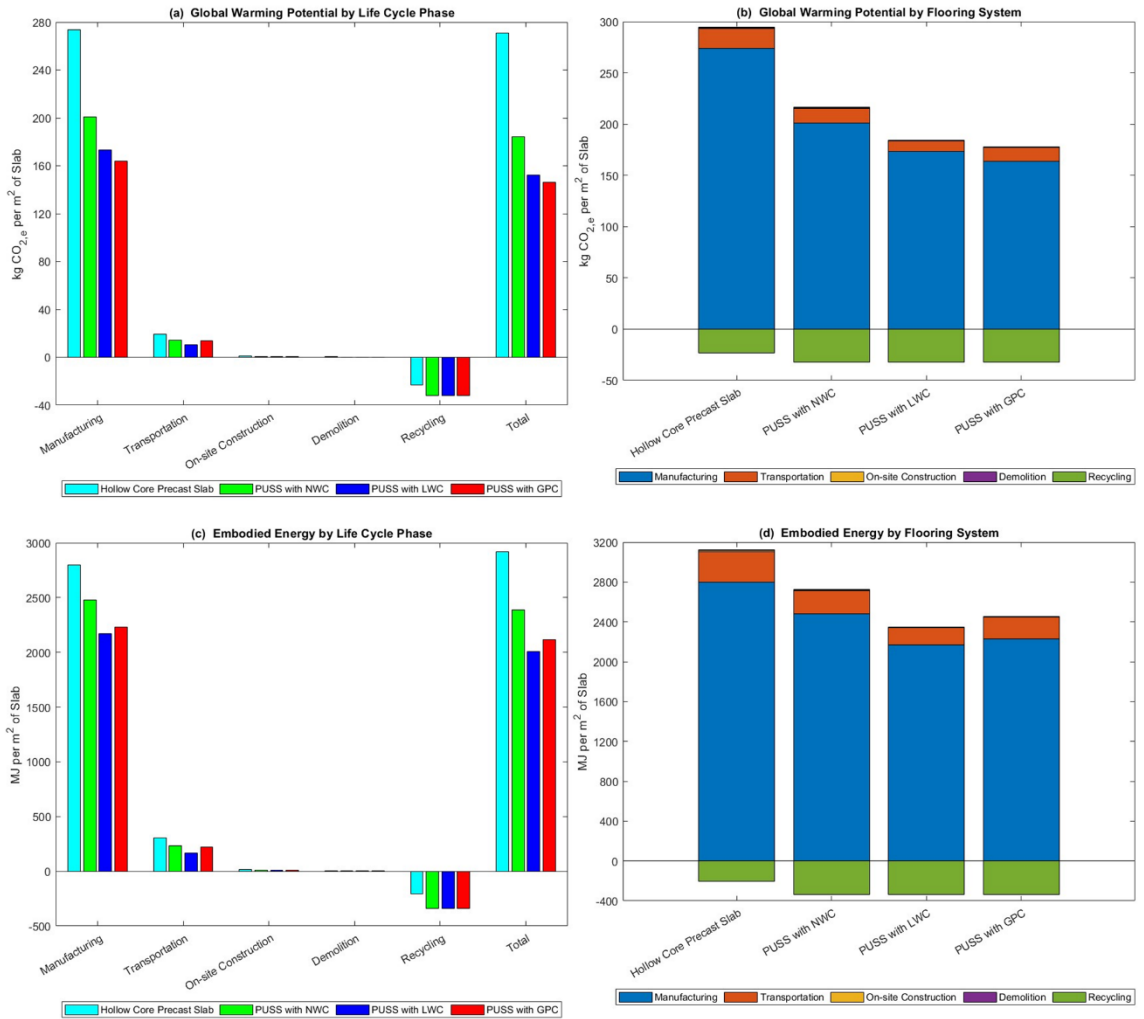
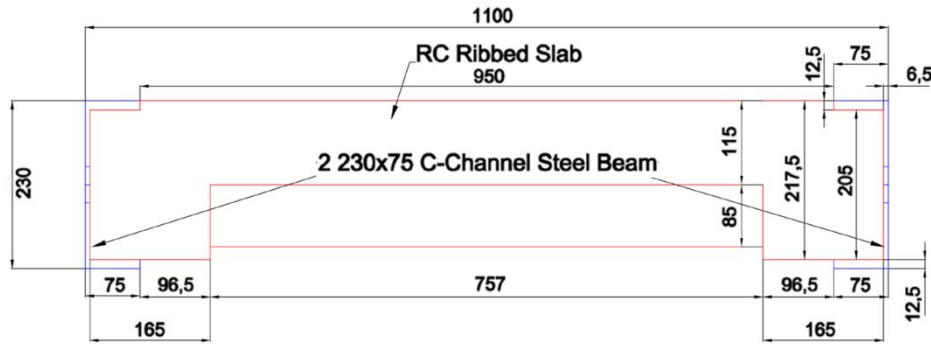


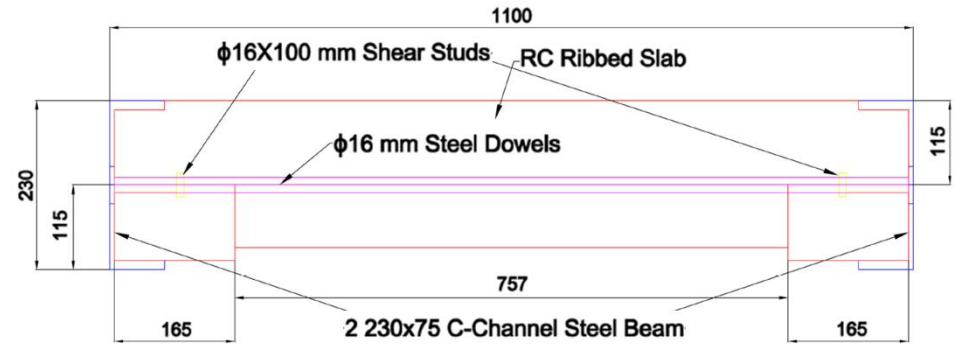
Figure A-16: Results for LL= 5 kN/m² & span= 12 m (a) GWP by life cycle stage (b) GWP by flooring system (c) EE by life cycle stage (d) EE by flooring system

Appendix B
Detailed Drawings of Test Specimens

(a) External dimensions of the short side showing the shear connections locations



(b) Detailed dimensions of the short side



(c) Transparent View of the short side showing steel reinforcement details

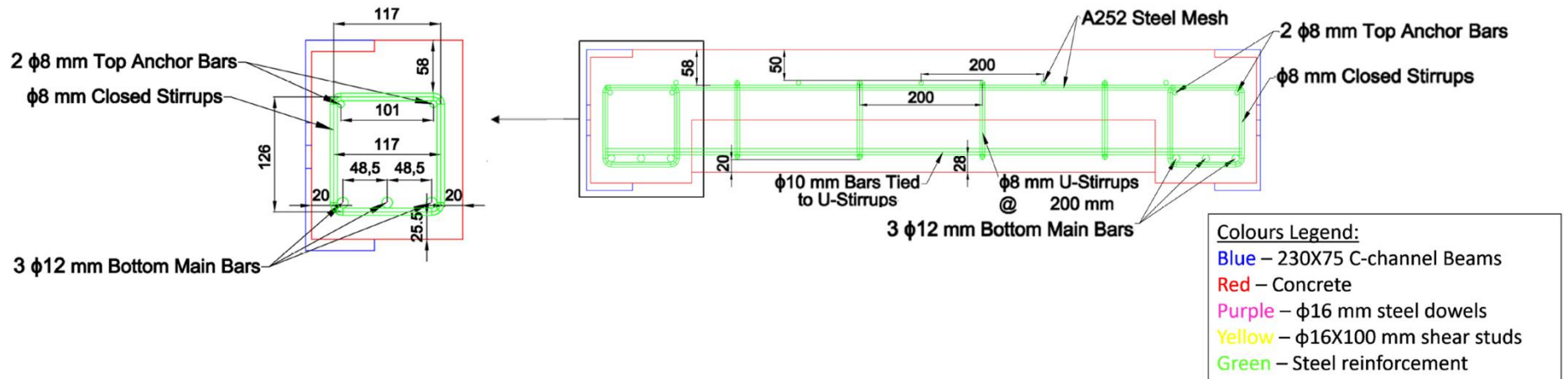
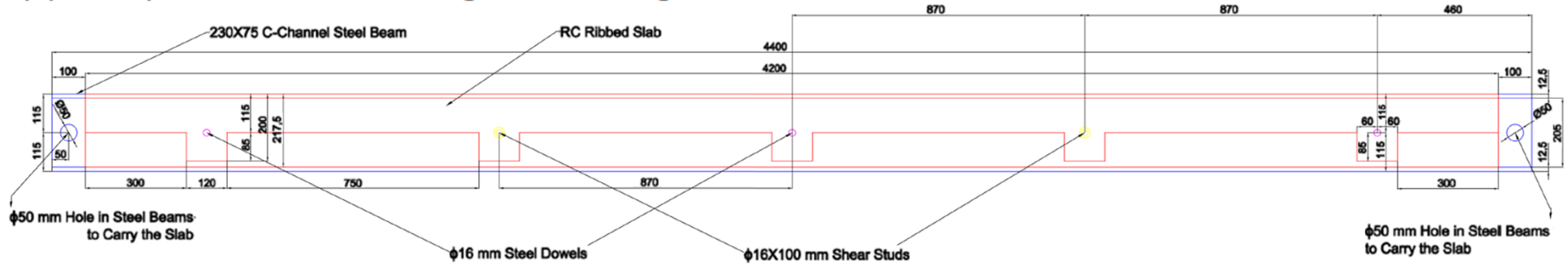
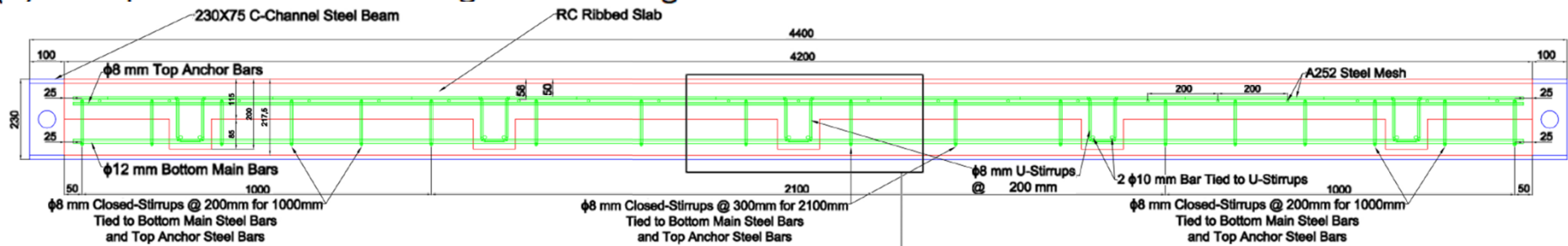


Figure B-1: Transverse cross-section details for tests specimens 1 & 2 (as well as specimen 3 but without WWSS)

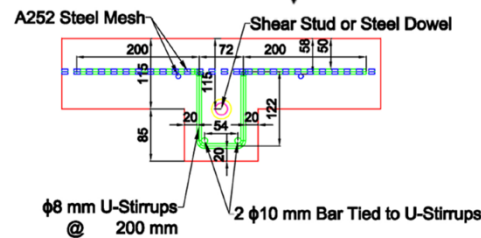
(a) Transparent view of the long side showing the shear connections and dimensions details



(b) Transparent View of the long side showing steel reinforcement details



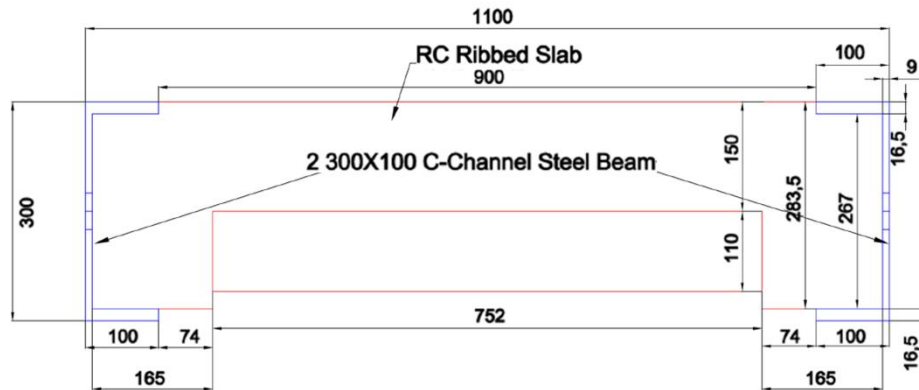
(c) Reinforcement details in ribs locations



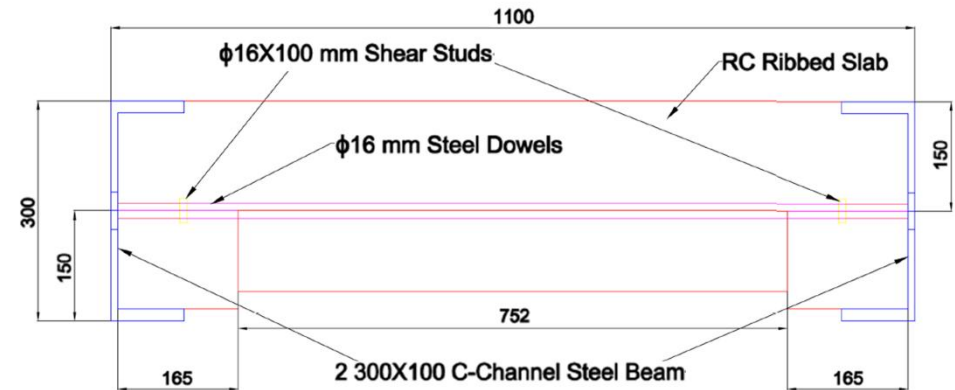
Colours Legend:	
Blue	– 230X75 C-channel Beams
Red	– Concrete
Purple	– $\phi 16$ mm steel dowels
Yellow	– $\phi 16 \times 100$ mm shear studs
Green	– Steel reinforcement

Figure B-2: Longitudinal cross-section details for specimens 1 & 2 (as well as specimen 3 but without WWSS)

(a) External dimensions of the short side showing the shear connections locations



(b) Detailed dimensions of the short side



(c) Transparent View of the short side showing steel reinforcement details

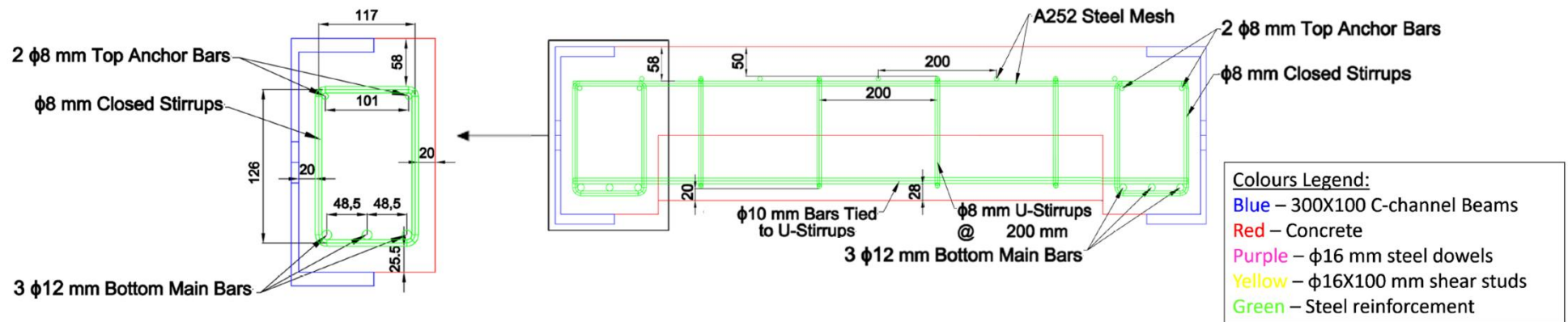


Figure B-3: Transverse cross-section details for specimen 4

